ELECTRON TUNNELING AND NOISE IN SPINTRONIC SYSTEMS

A Thesis submitted in partial fulfillment of the requirements for the degree of Doctor of Philosophy

Isidoro Martínez Ramírez

FACULTAD DE CIENCIAS
UNIVERSIDAD AUTÓNOMA DE MADRID

Departamento de Física de la Materia Condensada
Universidad Autónoma de Madrid, Madrid, Spain

Thesis supervisor: **Farkhad Aliev Kazanski**

July 2018

Publications relevant for the thesis

1. J. P. Cascales, J-Y. Hong, **I. Martínez**, M-T. Lin, T. Szczepanski, V. K. Dugaev, J. Barnas and F. G. Aliev, "Superpoissonian shot noise in organic magnetic tunnel junctions", Applied Physics Letters **105**, 233302 (2014)

2. **I. Martínez**, J. P. Cascales, J.-Y. Hong, M.-T. Lin, M. Prezioso, A. Riminucci, V. A. Dediu, and F. G. Aliev. "Electron transport and noise spectroscopy in organic magnetic tunnel junctions with PTCDA and Alq3 barriers", Proc. of SPIE Vol. **9931** 99313P-1 (2016)

3. T. Szczepanski, V. K. Dugaev, J. Barnas, **I. Martínez**, J. P. Cascales, J.-Y. Hong, M.-T. Lin, and F. G. Aliev, "Shot noise in magnetic tunneling structures with two-level quantum dots", Phys. Rev. B **94**, 235429 (2016)

4. **I. Martínez**, C. Tiusan, M. Hehn, M. Chshiev, F.G. Aliev, "Symmetry broken spin reorientation transition in epitaxial MgO/ Fe/MgO layers with competing anisotropies", Scientific reports, **submitted** (2018). arXiv:1805.01304.

5. **I. Martínez**, J.P. Cascales, J.-Y. Hong, C.-F. Hung, M.-T. Lin, T. Frederiksen, F. G. Aliev, "Spin-controlled molecular vibrational dynamics and switching", **to be submitted** (2018)

6. **I. Martínez**, J.P. Cascales, C. Tiusan, M. Hehn, P. Högl, J. Fabian, A. Matos-Abiague, I. Zutic, F. G. Aliev, "Towards fully coherent superconducting spintronics", **to be submitted** (2018)

Other publications

7. J. P. Cascales, **I. Martínez**, D. Díaz, J.A. Rodrigo, and F. G. Aliev, "Transient lateral photovoltaic effect in patterned metal-oxide-semiconductor films" Applied Physical Letters, **104**, 231118 (2014)

8. **I. Martínez**, J. P. Cascales, A. Lara, P. Andrés and F. G. Aliev, "Magnetic state dependent transient lateral photovoltaic effect in patterned ferromagnetic metal-oxide-semiconductor films", AIP Advances **5**, 117207 (2015)
9. **I. Martínez**, J. P. Cascales, A. Lara, P. Andrés, and F. G. Aliev, "Transient lateral photovoltaic effect in patterned ferromagnetic metal-oxide semiconductor films", Proc. SPIE **9358** 93580O-1 (2015)
10. J. P. Cascales, **I. Martínez**, F. Katmis, C-Z Chang, Rubén Guerrero, J. S. Moodera, and F. G. Aliev, "Band structure of topological insulators from noise measurements in tunnel junctions", Appl. Phys. Lett. **107**, 252402 (2015)
11. Patent: **I. Martínez**, J.P. Cascales, F. G. Aliev, "Sensor inductivo sensible a la posición basado en efecto fotovoltaico lateral y sistema de medida que lo comprende/Position sensitive detector based on lateral photovoltaic effect and set-up", publication number: **ES2553472**, expedition date: 08/11/2016, Universidad Autónoma de Madrid
12. **I. Martínez**, M. Ribeiro, P. Andrés, L. E. Hueso, F. Casanova, and F. G. Aliev, "Photodoping-Driven Crossover in the Low-Frequency Noise of MoS2 Transistors", Phys. Rev. Applied **7**, 034034 (2017)

A mi familia.

"Mens sana in corpore sano"

– **Juvenal**

Agradecimientos

Quisiera agradecer en primer lugar toda la ayuda que he recibido por parte de los miembros con los que he trabajado del grupo MAGNETRANS. Empezando por mi director de tesis, Farkhad Aliev, el cual me dió la oportunidad de continuar con mi carrera en la Física, y me ha enseñado el significado de ser un investigador, lo que es el rigor y lo que se puede conseguir esforzándose al máximo en el trabajo.

En segundo lugar, y siguiendo con la analogía de los *maestros Jedi*, a Juan Pedro Cascales le tengo que agradecer haberme enseñado casi todo lo que sé del laboratorio y dejarme un sistema experimental que prácticamente es "darle al botón y medir". Sólo mencionar que aún me acuerdo de cuando me salvó la mano sifonando helio al principio. A Antonio Lara, que ha estado aquí desde siempre y me ha ayudado con absolutamente todos los problemas que se han ido presentando durante estos años. A los dos, que sepáis que echo de menos aquellos días de piscina y chistes.

A los demás miembros con los que no he coincidido en el laboratorio, a David Herranz y a Rubén Guerrero sobre todo por dejar un sistema experimental montado y funcionando. También a los que han pasado por el laboratorio ayudando al desarrollo del mismo como Pablo Andrés por su trabajo con las simulaciones micro-magnéticas y a José Rodrigo de la Universidad Complutense de Madrid por el montaje de nuestro sistema óptico.

Qué sería de nosotros sin los técnicos del departamento a los que tantas cervezas se les deben. Gracias a José Luis por su ayuda con la electrónica, a Santiago, a José María, a Rafa y los técnicos del SEGAINVEX por su ayuda con las piezas que necesitábamos, y a Andrés Buendía y a Chema por su inestimable ayuda también con piezas y sobre todo con las demás cosas relacionadas con el criostato. A Javier Díaz, a Carlos y a Gonzalo, por proveernos de helio líquido siempre que lo hemos necesitado. A Macarena por procurarnos un sitio limpio donde trabajar. Y a las secretarias del departamento, Luisa, Ángeles y Elsa, por ayudarme con todos los trámites burocráticos y hacerme la vida mucho más fácil.

I would like to thank professors Minn-Tsong Lin and Jhen-Yong Hong (National Taiwan University) for growing the organic magnetic tunnel junctions and specially for helping me in my visit to their laboratory in Taipei which was a great experience for me. Thanks also to professors Coriolan Tiusan and Michel Hehn (University of Nancy) for the growth of the epitaxial superconducting magnetic tunnel junctions. Finally thanks to all of our collaborators for their guide and discussions, Petra Högl, prof. Jaroslav Fabian (University of Regensburg), prof. Alex Matos-Abiague and prof. Igor Zutiċ (State University at Buffalo), prof. Thomas Frederiksen (Donostia International Physics Center) and prof. Juan Carlos Cuevas (UAM).

Gracias a toda la gente de la UAM que he conocido estos años, Pablo Molina, las Lauras, la gente de las pachangas de fútbol (que hace mucho que no echamos por cierto), a la gente de bajas temperaturas, Antón, Edwin, Pepe, Jose Luis, Isa, Fran, Víctor, Sara etc. Ya sé que echáis de menos ir a comer a Psicología a las 13:30 exactamente. También a mi grupo de natación, con el que despejo la mente por las tardes.

A mis amigos de la Dehesa, a la que ya no vamos casi, les agradezco que en las pocas veces que me han visto últimamente siempre me han animado a seguir adelante.

A Rocío le tengo que agradecer muchas cosas, el haberme aguantado durante este período que sé que no ha sido fácil, sobre todo los últimos meses y el haberme apoyado moralmente durante todos estos años.

Finalmente a mi familia y en especial a mis padres y a mi hermano. A mi madre, que también me ha tenido que aguantar y siempre está con una sonrisa cuando la necesitas. Y a mi padre, que lo sabe todo, y siempre tiene una solución para todos los problemas que he tenido en mi vida. A todos vosotros os dedico esta tesis.

Contents

Scientific collaboration

Parts of this thesis have profited from scientific collaborations. The author would like to state the contributions by the respective researchers:

- The superconducting magnetic tunnel junctions based on Vanadium were grown by the group of prof. Coriolan Tiusan and prof. Michel Hehn within a collaboration project with the Institute Jean Lamour, Nancy Universitè (France).
- The organic magnetic tunnel junctions made of PTCDA molecules were grown by the group of professor Minn-Tsong Lin in a collaboration project with the National Taiwan University (NTU). The author of this thesis visited prof. Lin's lab and participated in the growth of the samples used in this thesis.
- The modeling of conductance anisotropy in ballistic transport regime has been developed by the groups of prof. Jaroslav Fabian with the help of Petra Högl, from the University of Regensburg (Germany), prof. Alex Matos-Abiague and prof. Igor Zutiċ, from the University at Buffalo (USA).
- The theoretical model of the vibrational heating mechanisms for molecular vibrations has been conducted by prof. Thomas Frederiksen, from the Donostia International Physics Center (Spain).
- The NVIDIA corp. has contributed with a TITAN X GPU needed for making micro-magnetic simulations.

The author would like to express his gratitude for the productive collaborations.

Resumen

Esta tesis se ha desarrollado en el laboratorio MAGNETRANS, en el departamento de Física de la Materia Condensada de la UAM. Los dos temas principales de esta tesis han sido, por un lado el estudio de transporte y ruido en uniones túnel magnéticas superconductoras epitaxiales, y por otro lado el estudio de ruido a baja frecuencia y espectroscopía de túnel inelástico en uniones túnel magnéticas moleculares con la barrera compuesta por moléculas de Perylenetetracarboxylic dianhydride (PTCDA).

El estudio de películas finas ha permitido un adelanto en muchas áreas tecnológicas como en dispositivos magnéticos de grabación, dispositivos electrónicos semiconductores, LEDs, células solares y dispositivos de almacenamiento de información. A mediados del siglo XX había estudios que se centraban en las propiedades magnéticas de los materiales en uso. Sin embargo en las últimas décadas la investigación ha virado hacia estudiar el transporte de espín a través de heteroestructuras dando origen al campo de la *espintrónica*.

La espintrónica es el campo de estudio del momento angular intrínseco del electrón (*espín*) además de su carga fundamental. El origen de la espintrónica data de experimentos de túnel a través de uniones ferromagnético/superconductor llevadas a cabo por Meservey y Tedrow y experimentos con uniones túnel magnéticas hechos por Jullière en 1970. Sin embargo no sería hasta 1985 cuando la espintrónica emergiese como un campo de estudio propio con los experimentos de inyección de corriente de espín polarizada desde un metal ferromagnético

a un metal normal realizados por Johnson y Silsbee y el posterior descubrimiento de la magnetoresistencia gigante (GMR) hecho independientemente por Albert Fert *et al.* y Peter Grünberg *et al.* en 1988 (ganadores del Nobel en 2007). Estos descubrimientos dieron lugar al nacimiento de los dispositivos espintrónicos tales como discos duros (principios de siglo), válvulas de espín o uniones túneles magnéticas.

Actualmente la espintrónica es la base de muchas ramas de investigación, por ejemplo en sensores de campo magnético, detectores de campo lejano (*espincaloritrónica*), opto-espintrónica, baterías de spin, computadores cuánticos, etc. Sin embargo donde más éxito ha tenido la espintrónica es en dispositivos para el almacenamiento de datos. El límite práctico para la utilización de estos dispositivos es la relación señal/ruido (*signal to noise ratio o SNR*). Debido a esta limitación es impresicindible el estudio de las distintas fuentes de ruido en estos dispositivos. Su comprensión es fundamental para su utilización y mejora hacia un desarrollo de dipositivos espintrónicos más pequeños con alto rendimiento.

Estudiaremos los diferentes aspectos fundamentales de transporte electrónico y ruido en voltaje a bajas frecuencias (hasta 102.4 kHz) en nuevos tipos de uniones túnel magnéticas con barreras orgánicas e inorgánicas. La motivación principal es investigar los mecanismos físicos detrás del transporte de carga y espín en uniones túnel magnéticas donde un electrodo ferromagnético se ha sustituído por un material superconductor o donde la barrera está compuesta por moléculas orgánicas.

Este trabajo está organizado en los siguientes capítulos:

- El **capítulo 1** presenta una breve introducción al campo de la espintrónica y la motivación de ésta tesis introduciendo conceptos básicos sobre dispositivos túnel magnéticos y ruido en sistemas espintrónicos.

- El **capítulo 2** explica las técnicas experimentales usadas y los métodos de análisis de datos empleados.

- El **capítulo 3** se centra en la descripción, medidas de conductancia y estados magnéticos en las uniones compuestas por V/

MgO/Fe, V/MgO/Fe/MgO/Fe y Fe/MgO/V/MgO/Fe a temperaturas por encima de la temperatura crítica del Vanadio. Se estudia el comportamiento de la imanación de la capa ferromagnética blanda de Fe de 10 nm de espesor, donde se dan las condiciones de competición entre la anisotropía de forma y de superficie, cuando es sometida a un campo magnético externo a bajas temperaturas.

- El **capítulo 4** estudia las propiedades en el transporte de espín en uniones V/MgO/Fe, V/MgO/Fe/MgO/Fe y Fe/MgO/V/MgO/Fe además de en uniones V/MgO/Au usadas como muestras de control. Se investiga la posible conversión de pares de Cooper entre tipo "singlete" y tipo "triplete" a través de medidas de conductancia donde las anomalías están asociadas a quasi-partículas con largo alcance de penetración. Adicionalmente, con la ayuda de colaboradores, se ha desarrollado un modelo teórico para calcular la anisotropía magnética de la conductancia a voltaje cero.

- El **capítulo 5** investiga la interacción electrón-fonón en uniones túnel magnéticas moleculares basadas en moléculas de PTCDA usando medidas de conductancia y ruido a baja frecuencia. También se ha propuesto, en colaboración con teóricos, un modelo que describe las anomalías en ruido causadas por las interacciones electrón-fonón.

- El **capítulo 6** resume las conclusiones generales de la tesis.

Chapter 1

Introduction

1.1. Overview and motivation

Thin films have enabled a wide range of technological breakthroughs in areas such as magnetic recording media, electronic semiconductor devices, LEDs, material coatings, solar cells and the matter of concern of this manuscript, storage. Magnetic thin films have been widely studied for this purpose. At the beginning (by the middle of 20th century) the studies were focused on the properties of the magnetic materials used, but during the last two decades research has turned towards studying the transport of spin through heterostructures giving rise to the field of *spintronics*.

Spintronics is the field of study of the intrinsic angular momentum (*spin*) of the electron in addition to its fundamental electronic charge. In this section we will briefly go over the recent history of spintronics which will serve as context and motivation for the results presented in this thesis.

The origins of spintronics can be traced to the tunneling experiments through ferromagnet/superconductor pioneered by Meservey and Tedrow and initial experiments on magnetic tunnel junctions by Jullière in the 1970s, although emerging as a proper field when observing the spin-polarized electron injection from a ferromagnetic metal to a normal metal by Johnson and Silsbee (1985) and the discovery

of the giant magnetoresistance (GMR) independently by Albert Fert et al. and Peter Grünberg et al. in 1988 (Nobel Prize awarded in 2007). This discoveries gave birth to a large variety of spintronic devices such as hard disk drives (early 2000's), spin valves or magnetic tunnel junctions (MTJs).

Magnetic tunnel junctions come up from replacing the non-magnetic spacer layer in old magnetic multilayered systems with a non-magnetic insulating layer. Is in this type of structures where the tunnel magnetoresistance effect (TMR) occurs. In the case of magnetic field sensors, TMR based devices should have overridden GMR based ones due to their lower power consumption, size, easy data reading, etc. The signal to noise ratio (SNR) of the TMR based devices has been until recently insufficiently high for general applications however, modern hard disk drives and magnetoresistive random access memories (MRAMs) are based on the TMR effect. In the case of spintronic oscillators, the phase noise and the low power delivered despite their reduced size, dispelled their general use in more complex devices. Because of these limitations, the understanding and control of noise sources in spintronic devices is a crucial aspect that is often overlooked.

The main motivation of this thesis is to investigate different fundamental aspects of electron transport and low frequency (up to 102.4 kHz) voltage fluctuations (*noise*) in novel types of MTJs with organic and inorganic barriers. The MTJs studied in this thesis include different materials or configurations all of which are currently the focus of intense investigation in the area of spintronics. The main motivation is to clarify the physical mechanisms behind electron and spin transport, such as magnetic tunnel junctions where one electrode has been replaced by a superconducting material or where the barrier is made of organic molecules.

The manuscript is organized in the following chapters:

- **Chapter 1** presents a brief introduction to the spintronics field and the motivation behind this thesis introducing basic concepts about magnetic tunnel devices and noise in spintronic systems.

- **Chapter 2** introduces the experimental techniques and the data analysis methods employed.

- **Chapter 3** focuses in the description, conductance measurements and magnetic states of the V/MgO/Fe, V/MgO/Fe/MgO/FeCo and Fe/MgO/V/MgO/FeCo samples at temperatures above the critical temperature of the superconducting transition of Vanadium. The magnetization of the soft (10 nm thick) ferromagnetic electrode, with competing shape and surface anisotropies, conforming these samples is studied at low temperatures and in the presence of an external applied magnetic field.

- **Chapter 4** studies the superconducting electron and spin transport properties in V/MgO/Fe, V/MgO/Fe/MgO/FeCo and Fe/MgO/V/MgO/FeCo samples and additionally in V/MgO/Au samples taken as "control samples". The possibility of singlet-triplet cooper pair conversion is investigated through measurements where long-range particle penetration is responsible of conductance anomalies. Moreover a theoretical model made in collaboration is proposed here to calculate the conductance magnetic anisotropy.

- **Chapter 5** studies the electron-phonon interaction in organic (PTCDA based) MTJs using conductance and low frequency noise measurements. A vibrational-heating model is proposed, with the help of collaborators, to describe the noise anomalies caused by electron-phonon interaction.

- **Chapter 6** summarizes the general conclusions of this thesis.

1.2. Magnetoresistance

Magnetoresistance is the property of a material or heterostructure to change its electrical resistance when a magnetic field is applied. There are a variety of effects that can be called magnetoresistive: some occur in bulk non-magnetic metals or clean structured semiconductors (e.g. geometrical magnetoresistance), while others take place in magnetic materials (e.g. anisotropic magnetoresistance (AMR)). Finally, the matter of concern here, in multilayer systems (e.g. magnetic tunnel

junctions, GMR, TMR, etc) magnetoresistance may take place. The emphasis is going to be towards explaining TMR, however it would be pedagogical to explain AMR and GMR first.

The **anisotropic magnetoresistance** (AMR) physical origin arises from the interplay between magnetization and spin-orbit interaction. It was discovered by William Thomson in 1857 (Lord Kelvin)[1] in iron and nickel (ferromagnetic materials). The electron cloud about each nucleus deforms slightly as the direction of the magnetization rotates, and this deformation changes the probability of scattering undergone by the conduction electrons when traversing the lattice. The magnetic anisotropy in magnetic conductors is characterized by the resistivity of the material and depends on the angle between the external applied magnetic field and current running through the material. A simplified picture of the effect is shown in figure 1.1.

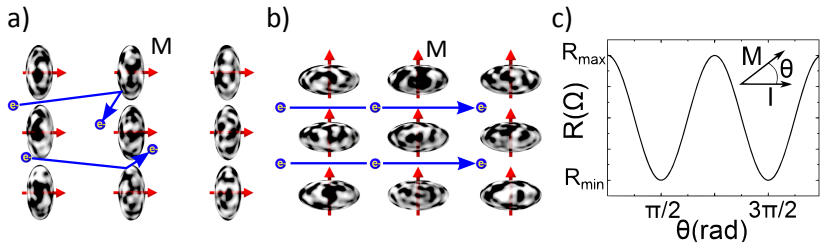

Figure 1.1: AMR effect. The distorted electron clouds of each atom scatter more electrons when the field is applied parallel a) to the direction of the current, while the scattering is minimal when they are perpendicular b). c) Variation of the resistance with the angle between current and magnetization. Figure adapted from ref.[2]

As mentioned before, the discovery of the **giant magnetoresistance**[3,4] (GMR) was done in a multilayered system of ferromagnetic (FM) and non-magnetic (NM) conductive layers which show antiferromagnetic coupling[5,6]. The simplest configuration would be a two ferromagnetic layered structure separated by a thin non-magnetic layer (see figure 1.2). This configuration is called a *spin valve*. The origin of the GMR effect is the spin dependent scattering of electrons in the magnetic layers forming the structure. The schematic in figure 1.2 is

referred as the *two-current model*, where the current through the junction is separated in two parallel currents, one of spin-up and one of spin-down electrons. Depending whether the magnetization direction of both ferromagnets is parallel (P state) or anti-parallel (AP state) there will be two resistance levels. The low state resistance (P state) where the majority of electrons have a spin parallel to the magnetization direction thus having a minimum scattering, and the high state resistance (AP state) where the majority of electrons coming from the first FM layer will have a high probability of scattering in the second FM layer. These two resistance states are used to read data bits in magnetic hard disk drives.

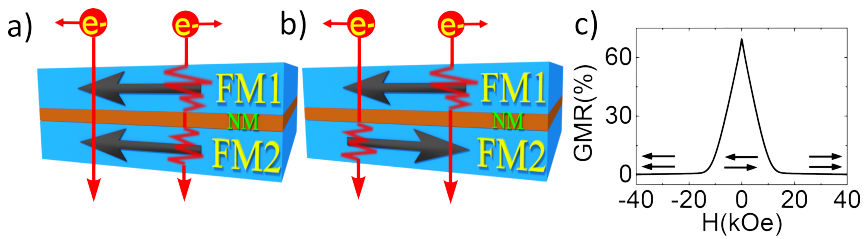

Figure 1.2: GMR effect. a) Minimal scattering when the magnetization of the layers are parallel (P state). b) Multilayers with alternating magnetization (anti-ferromagnetic system) present high scattering probabilities (AP state). c) Typical dependence of the resistance with the applied field for two exchange coupled ferromagnetic layers[7]. Figure adapted from ref.[2]

1.2.1. Tunnel Magnetoresistance (TMR)

A Magnetic Tunnel Junction (MTJ) is a device consisting of two FM electrodes separated by a thin insulating layer. If the insulator is thin enough (typically a few nanometers), electrons can tunnel from one electrode into the other. Since this process is forbidden in classical physics, the TMR is a strictly quantum mechanical phenomenon. The physics of these quantum systems is known as *Mesoscopic and Nanoscopic Physics*, indicating that the system dimensions involved

are somewhere in between the macroscopic physics and the nanoscopic world of the atoms.

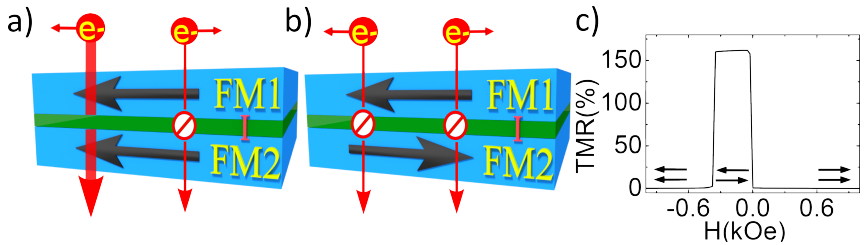

Figure 1.3: Simplified picture of the TMR effect for 100 % polarized ferromagnets. a) In the P state the spin majority electrons from the top electrode easily find available majority states in the bottom layer to tunnel into. b) In the AP state the spin majority electrons from the top layer may only tunnel into the scarcely available minority states of the bottom layer. c) TMR vs external magnetic field.

It is necessary to emphasize that from now on we are going to differentiate between *in-plane magnetization* when the magnetization direction is along the surface of the layers and *out-of-plane magnetization* when the magnetization is perpendicular to the layer surface although unless otherwise stated we will refer to *in-plane magnetization* as simply *magnetization*.

Classically, the magnetization direction of both FM layers is changed with an externally applied magnetic field H_{ext} and each FM has a different coercive field H_c^1 and H_c^2 thereby if $H_c^1 > H_c^2$ the FM1 will be the hard FM layer and the FM2 will be the soft FM layer. Sweeping H_{ext} (see figure 1.3 c) we are able to control whether the magnetization angle between both FM electrodes is parallel (P state in figure 1.3 a) or anti-parallel (AP state in figure 1.3 b).

Similarly as what happens in the GMR effect, the TMR effect is defined as the difference of resistance between the P state and the AP state normalized by the P state resistance:

$$TMR = \frac{R_{AP} - R_P}{R_P} \tag{1.1}$$

Before diving into more complexity, we will describe in more detail the tunneling transport phenomena in these type of structures.

1.3. Electron tunneling

One of the main experimental tools throughout this thesis will be the study of physical mechanisms of electron transport in hybrid structures through the characterization of the electron tunneling conductance. Therefore it is of fundamental importance to understand first the basics of the tunneling procedures in simple structures. After that we will introduce magnetic and superconducting materials.

1.3.1. Rectangular potential barrier

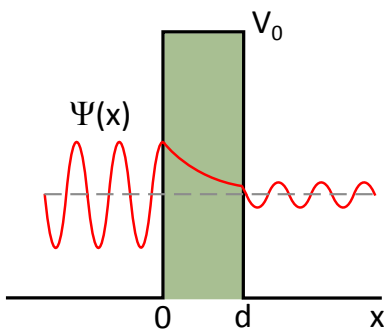

Figure 1.4: Schematic of a rectangular potential barrier of width d showing the transmission wave function. Figure adapted from ref.[2]

In classical physics, a particle needs to have at lest the energy of the potential barrier to overcome it. In quantum mechanics however, a particle with less energy than the barrier potential could tunnel through with a probability that decays exponentially with the barrier width (figure 1.4). Let's consider a rectangular potential barrier of width d and height V_0, and an incoming wave from the left. The solutions to the wavefunction in each region are:

$$\begin{aligned} \psi_1(x) &= e^{ikx} + re^{-ikx} & x &\leq 0 \\ \psi_2(x) &= Ae^{i\kappa x} + Be^{-i\kappa x} & 0 &\leq x \leq d \\ \psi_3(x) &= te^{ikx} & d &\leq x \end{aligned}$$

where $k = \sqrt{\frac{2mE}{\hbar^2}}$ is the wavevector in vacuum, $\kappa = \sqrt{\frac{2m(E-V_0)}{\hbar^2}}$ is the wavevector inside the barrier, r denotes the reflected amplitude and t the transmitted. Applying the continuity conditions on the wavefunction an its derivative at $x = 0$ and $x = d$, one obtains the value of the coefficients A and B. The case which we are interested is when the particle energy is $0 < E < V_0$, which in the case of weak tunneling ($T \ll 1$) yields a transmission probability $T \propto e^{-2\kappa d}$.

As is described in ref.[2], considering the three dimensional problem where the particle propagates in the Z direction and tunnels through a rectangular potential barrier. Addressing the problem using separation of variables solves the problem with a plane wave in the X and Y directions (let us call it $\Phi(z)$) propagating in the Z direction, i.e.:

$$\Psi(x, y, z) = \Phi(z)e^{i(k_x x + k_y y)}$$

In $\Phi(z)$, k should be replaced by k_z with κ and k_z presenting the following dependence with $\mathbf{k}_\parallel = (k_x, k_y)$:

$$k_z = \sqrt{2m\frac{E}{\hbar^2} - k_\parallel^2} \quad \text{and} \quad \kappa = \sqrt{2m\frac{(V_0 - E)}{\hbar^2} - k_\parallel^2}$$

Electron tunneling processes have found numerous applications in physics, chemistry and technology. As to physical applications, closely related to the present thesis, one could mention the Josephson effect, the tunneling magnetoresistance, or just the well known diodes or transistors.

Now consider the particle tunneling between two metals. In figure 1.5a) without an applied potential difference ($V_0 = 0$) and at zero temperature, tunneling is not possible because both electrode levels are filled. The electric field changes the shape of the barrier bringing some empty levels in correspondence with the filled ones on the other

side of the barrier. In this case the tunneling can happen with the transmission probability previously calculated.

The current through a tunnel junction may be expressed as a function of the applied voltage V[8]:

$$I(V) = \int_{-\infty}^{+\infty} \rho_L(E)\rho_R(E+eV)|M|^2 f(E)(1-f(E+eV))dE \quad (1.2)$$

where ρ is the density of states of the left (ρ_L) or right (ρ_R) electrode, $|M|^2$ is the transmission probability, f(E) the occupied states of the left electrode and (1-f(E)) the unoccupied states of the right electrode.

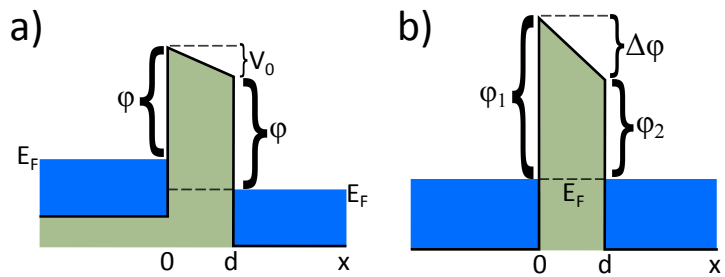

Figure 1.5: Energy diagram for tunneling between a) two identical metals with an applied potential difference V_0 (Simmon's model[8]) and b) two different metals with an asymmetric electrode barrier (Brinkman's model[9]).

Using Simmon's fit[8] (see figure 1.5), which is a very useful approximation of the equation 1.2 for the tunneling current, we may obtain some important parameters of the barrier fitting the following equation of the current density $J(V)$ to an I-V curve:

$$\begin{aligned} J(V) = J_0 \Bigg\{ \left(\bar{\varphi} - \frac{eV}{2}\right) \exp\left[-A\left(\bar{\varphi} - \frac{eV}{2}\right)^{1/2} \right] \\ - \left(\bar{\varphi} + \frac{eV}{2}\right) \exp\left[-A\left(\bar{\varphi} + \frac{eV}{2}\right)^{1/2} \right] \Bigg\} \end{aligned} \quad (1.3)$$

with $J_0 = \dfrac{e}{(2\pi)^2\hbar d^2}$, $A = \dfrac{2d}{\hbar}\sqrt{2m}$ and where the fitting parameters are the barrier height $\bar{\varphi}$ and the barrier thickness d (in Å).

In practice we will use a slightly more complex approximation with the Brinkman's model[9] which takes into account the case of an asymmetric barrier where the two electrodes of the junction have different barrier potential:

$$J(V) = G_0\left[V - \left(\frac{A_0\Delta\varphi}{32\,\bar{\varphi}^{3/2}}\right)(eV)^2 + \left(\frac{3A_0^2}{128\,\bar{\varphi}}\right)(eV)^3\right] \tag{1.4}$$

with $G_0 = \dfrac{e^2\sqrt{2m}\,\bar{\varphi}^{1/2}}{(2\pi)^2\hbar^2 d}\exp\left(-\dfrac{2d}{\hbar}\sqrt{2m\bar{\varphi}}\right)$, $A_0 = \dfrac{4d}{3\hbar}\sqrt{2m}$ and the fitting parameters are the barrier mean height $\bar{\varphi}$, the barrier asymmetry $\Delta\varphi$ and the barrier thickness d (in Å).

1.3.2. Tunneling procedures between magnetic materials

Magnetization of the electrodes (ferromagnets) greatly affects the tunneling processes that we are studying. In the model[10] that was proposed by Julliére in 1975 for tunnel junctions with amorphous barriers, the difference in resistance between the two magnetic states is determined by the spin polarization of the ferromagnets. Thereby electron spin role appears on the scene.

The band structure $E(k)$ of a ferromagnet (FM) can be described as the sum of two sets of bands, one with electrons with spin up ($\uparrow$) and the other with electrons with spin down ($\downarrow$). Electrons within the FM will tend to align their spin with the direction of the FM magnetization shifting the two bands, the *majority spin* band where most of the electrons with spin aligned to the magnetization will be located and the *minority spin* band where the rest of the electrons with opposite spin will be located. An electron current passing throughout a FM will be polarized. To describe the degree of polarization we can define a **spin polarization** P parameter as:

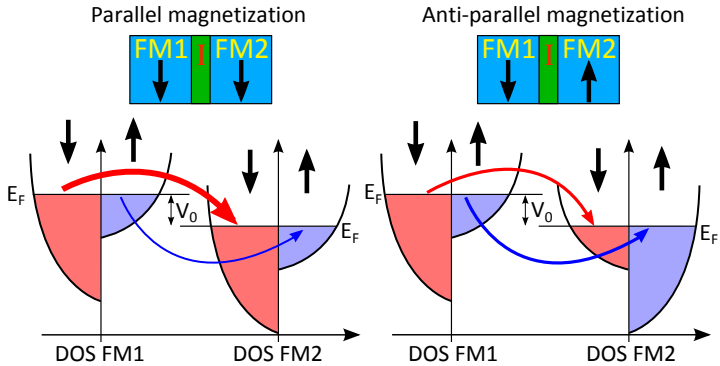

Figure 1.6: Julliére model[10] explains the difference of resistance between P and AP magnetic states because of the shifting of the density of states (DOS) in the FM. Majority electrons easily find available energy states in P state while much fewer majority electrons find vacancies in AP state.

$$P = \frac{n_i^{\uparrow} - n_i^{\downarrow}}{n_i^{\uparrow} + n_i^{\downarrow}} \tag{1.5}$$

where $n_{i\sigma}$ is obtained from the spin dependent density of states. Non-magnetic materials have the same number of spin up and spin down electrons yielding $P = 0$ whereas a fully spin-polarized FM at E_F gives $P = 1$. In the case of different FM electrodes, P_i denotes the polarization of each one ($i = 1, 2$) and then the TMR may be expressed as a function of the polarization:

$$TMR = \frac{G_P - G_{AP}}{G_P} = \frac{\left(n_1^{\uparrow} n_2^{\uparrow} + n_1^{\downarrow} n_2^{\downarrow}\right) - \left(n_1^{\uparrow} n_2^{\downarrow} + n_1^{\downarrow} n_2^{\uparrow}\right)}{n_1^{\uparrow} n_2^{\uparrow} + n_1^{\downarrow} n_2^{\downarrow}} = \\ = \frac{2P_1 P_2}{1 - P_1 P_2} \tag{1.6}$$

The model above works in the regime where the tunneling barrier has to be thick enough in order to have a very small overlap of the electron wavefunctions. Julliére's model implies that the TMR depends

exclusively on the density of states (DOS) of the electrodes near the Fermi level E_F thus being effective only for small applied voltages. It does not take into account the influence of the filtering properties of the barrier or the influence of interface states[11].

Having in mind this considerations, the Julliére model is valid mainly for MTJs with amorphous barriers such as AlO_x, where multiple symmetries of the electron wavefunction merge with evanescent states within the barrier and have finite tunneling probabilities[12]. Moreover the model assumes that tunneling probabilities are equal for all the Bloch states in the electrodes which corresponds to symmetry independent or **incoherent tunneling**, meaning that there is no preferred symmetry in momentum space for the tunneling electrons.

To help the reader, so far the concepts explained are shared introduction to both organic and superconducting spintronics. Now we split paths and continue with concepts leading to superconducting spintronics setting aside organic spintronics till section 1.6. We are going to introduce the concept of coherent magnetic tunneling which is essential in the case of having epitaxial junctions (in contrast to incoherent tunneling in amorphous junctions) as is the case with the superconducting spintronics experiments.

1.3.3. Coherent magnetic tunneling in Fe/MgO/Fe

The concept of coherent magnetic tunneling[12] implicates the condition of wavefunction matching at the interface in contrast to the wavefunction coupling mentioned previously in amorphous barriers. Fe, Ni and Co (and some of their alloys) owe their magnetic properties to unfilled 3*d* orbitals, and Bloch states with different symmetries of wave functions exist in these materials. In this context, **coherent tunneling** indicates that electrons with a given symmetry tunnel maintaining their symmetry state into the other electrode (see figure 1.9b). We are going to focus on the matching properties of the Fe/MgO/Fe structure which will be the case study for some of our samples.

Electrons conducting in iron, may have one of the following symmetries: Δ_1 (*spd* hybridized states which usually have a large **positive**

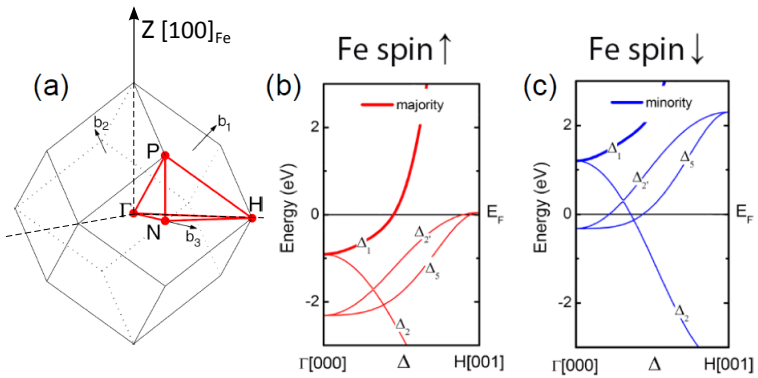

Figure 1.7: a) Reciprocal representation of the bcc Fe lattice. Z direction corresponds to the propagation of electrons perpendicular to the (100) plane in real space. Bulk band structure diagram for the b) majority and c) minority spin of bcc Fe[12]. Figure adapted from ref.[13]

spin polarization at E_F), Δ_2, and Δ_5 (d states which often have a much smaller or even **negative spin polarization** at E_F). The Δ_1 band is fully spin-polarized at the Fermi energy, which makes the P state conductance much larger than the AP state one. Therefore, a very large TMR effect is expected, a similar situation could be found for other FM metals and alloys based on Fe and Co (bbc FeCo, bcc CoFeB, and some Heusler alloys)[14].

In order to avoid electron structural disturbances, the lattice mismatch between different materials should be minimized. Let us now therefore explain briefly the lattice matching properties of these materials looking at figure 1.8. Crystalline MgO [001] barriers can be epitaxially grown over bcc Fe [001] with a 3% lattice mismatch (see the matching lattices in figure 1.8), which is compensated by lattice dislocations formed at the interface. Such a high quality interface allows coherent tunneling to take place. Theoretical calculations predicted a huge increase of the TMR value, for epitaxial Fe[001]/MgO[001]/Fe[001] tunnel junctions with crystalline MgO barriers[15,16], and were later confirmed experimentally[17,18].

As long as coherent tunneling electron symmetries are conserved,

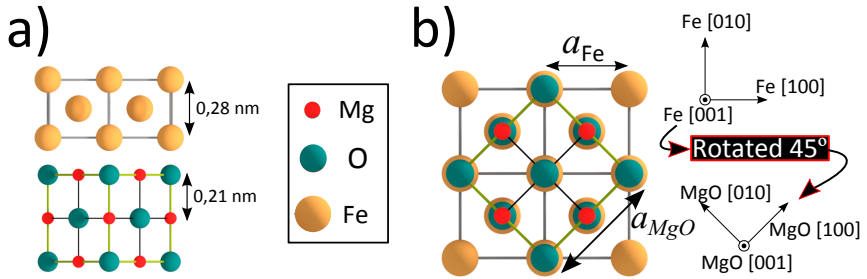

Figure 1.8: Epitaxial growth of Fe on MgO with only a 3% lattice mismatch. The Fe lattice is rotated by 45° with respect to to the MgO lattice[12]. Figure has been adapted from ref.[12].

and those symmetries are linked to the spin orientation, we could have a highly spin-polarized tunneling current between irons because of majority carriers having Δ_1 symmetry (see figure 1.7b). Incidentally, since this spin polarized state is prohibited in the AP state, this would lead to a high TMR ratio. However, for this effect to occur, the filtering of the other symmetries (Δ_2 , Δ_5) by the MgO barrier is essential (see figure 1.9).

The influence of the thickness of the insulating barrier is rather complex as in the small thickness regime the contribution of $k \neq 0$ electrons to the tunneling current is enhanced. The tunnel transmission becomes strongly affected by resonant tunneling mechanism[19]. These resonant effects increase locally the conductance distribution in particular points in the two-dimensional Brillouin zone. In order to study how these effects influence the tunneling transport, the dynamic conductance measurements are typically used. Apart from this technique, it seems necessary to use additional tools from which one could obtain extra information on tunneling, such as from noise measurements.

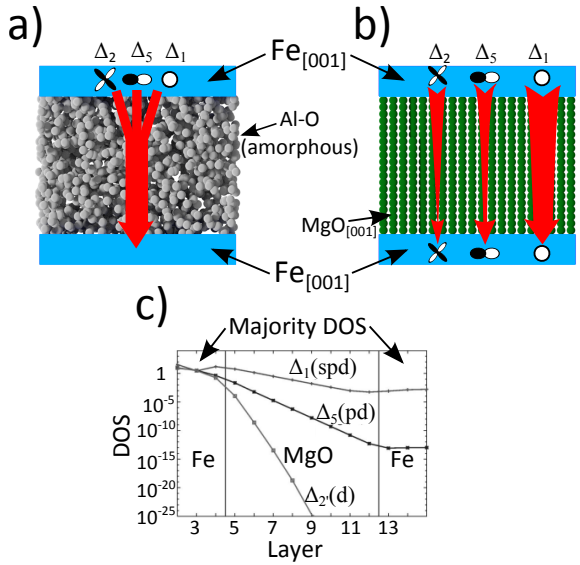

Figure 1.9: Electron tunneling through a) an amorphous Al-O barrier where symmetries merge between them and b) an crystalline MgO [001] barrier[12] where all symmetries except Δ_1 are filtered. c) Tunneling DOS for $k_{\parallel} = 0$ for Fe(100)—8MgO—Fe(100) and for the particular majority parallel alignment (the other possible configurations show similar behavior). The Δ_1 symmetry is weakly filtered through the 8 MgO layers. Figures adapted from refs.[12,15]

1.3.4. Tunneling between different single crystalline materials: case of study in V/MgO/Fe

We will now consider what happens when an electron tunnels **coherently** from one material to a different one. We are going to illustrate the example using iron (Fe) and vanadium (V) because they are the two materials involved in our measurements.

As we have discussed in the previous 1.3.3 subsection, electrons tunneling coherently conserve their symmetry while tunneling. This means that in order to tunnel (have a high tunneling probability) they must find the same symmetry at the other side of the barrier.

Examining the band structure for bcc V and Fe in the (100) direc-

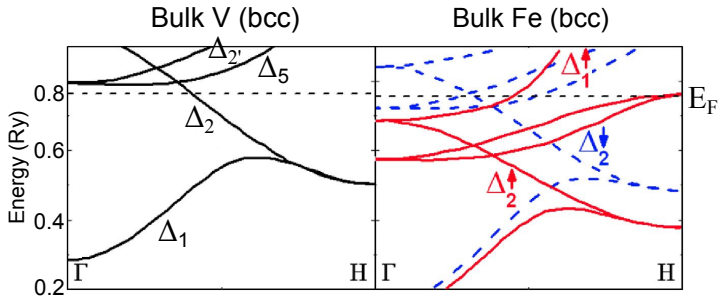

Figure 1.10: Band structure model for electron transport between V and Fe. In Fe, the solid red lines are majority carriers and dashed blue lines correspond to minority carriers. Figure adapted from refs. [20,21]

tion (figure 1.10), we see that the dominant conduction band of V at the Fermi level is of Δ_2 symmetry. However, Δ_2 symmetry is absent in the Fe majority channel near the Fermi level (E_F)[15]. Thereby the conductivity through Fe↔V is mediated only by a small portion of the minority channel electrons whose symmetry match. The effect is a dramatic increase of the normal resistivity, which can be compared conveniently with previous MTJs measured in this laboratory made of Fe/MgO/Fe[2]. Moreover, due to the strong spin filtering of the MgO barrier (see figure 1.9) the conduction of Δ_2 states is strongly suppressed which contributes acutely to the effect.

Electron tunneling symmetries however could be modified by spin-orbit effects. These procedures are essential in layered systems where interfaces break the inversion symmetry of the material's crystalline structure creating electric and magnetic surface fields.

1.3.5. Spin-orbit coupling (SOC)

The so called spin-orbit coupling (SOC) (also called spin-orbit effect or spin-orbit interaction (SOI)) refers to the general interaction of the electron spin with its motion. Depending on the crystal symmetries of a material the SOC takes on different functional forms, particularly in systems lacking space inversion symmetry (be it in bulk, hybrid structures, junctions) SOC induces spin-orbit fields which rep-

resent an emergent phenomenon in modern spintronics[22,23].

To describe electron spin in the presence of SOC, one of the most common approaches is the one presented by Fabian *et al.* in ref.[23] in which they consider a FM/semiconductor/normal-metal MTJ. The semiconductor is assumed to lack bulk inversion symmetry. The bulk inversion assymetry of the semiconductor together with the structure inversion asymmetry of the heterojunction give rise to the Dresselhaus (D) and Bychkov-Rashba (BR) SOIs, respectively. The model Hamiltonian describing the tunneling across the heterojunction reads:

$$H = H_0 + H_{BR} + H_D;$$

Here

$$H_0 = \frac{-\hbar^2\nabla^2}{2m_i^*} + V_i - \frac{\Delta_i}{2} n_i \cdot \boldsymbol{\sigma}; i = l, c, r$$

where m_i^* and V_i are the effective mass and potential energy, respectively, in the FM ($i = l$), semiconductor ($i = c$), and normal-metal ($i = r$) regions. Δ_i is the exchange energy, n_i defines the magnetization direction with respect to the [100] direction and $\boldsymbol{\sigma}$ is a vector whose components are the Pauli matrices.

$$H_D = \mathbf{k} \cdot \boldsymbol{\sigma}(\gamma(z)\nabla_z^2 + \gamma_{l,r}\nabla_z) = (k_x\sigma_x - k_y\sigma_y)(\gamma(z)\frac{d^2}{dz^2} + \gamma_{l,r}\frac{d}{dz});$$

The Dresselhaus parameter $\gamma(z)$ has a finite value γ in the semiconductor region, where the bulk inversion asymmetry is present, and vanishes elsewhere, i.e., $\gamma_l = \gamma_r = 0$. For the system here studied, the Bychkov-Rashba SOI inside the semiconductor can be neglected and one is left only with the interface contributions.

$$H_{BR} = \frac{1}{\hbar}\sum_{i=l,r} \alpha_i(\boldsymbol{\sigma} \times \mathbf{p})\delta(z - z_i) = \frac{1}{\hbar}\sum_{i=l,r} \alpha_i(\sigma_x p_y - \sigma_y p_x)\delta(z - z_i);$$

where, $\alpha_l(\alpha_r)$ denotes the SOI strength at the left (right) interface $z_l = 0(z_r = d)$.

With this theoretical description we relate how SOC (Bychkov-Rashba interaction strength is α_i, Dresselhaus interaction strength is γ influences the electron spin $\boldsymbol{\sigma}$. The theory is based on the experiments from ref.[24] where they use a Fe/GaAs/Au junction. That approach is also valid for our system (Fe/MgO/V) because instead of a 8 nm thick GaAs semiconductor we have a thin (2 nm thick) MgO insulator and the SOC effects here arise due to interfacial surface asymmetry.

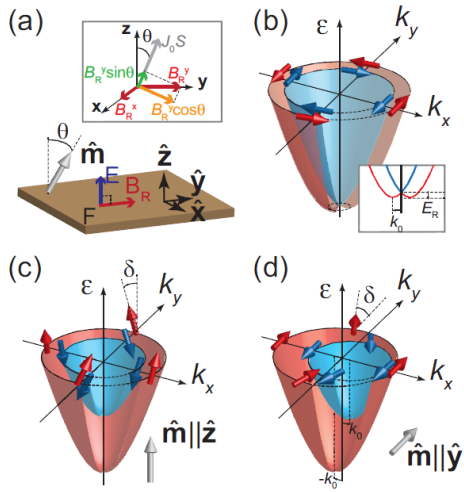

Figure 1.11: Rashba SOC at the interface of a FM layer. a) Rashba magnetic field (B_R) and the exchange splitting (J_0S). E is the Rashba electric field and θ the magnetization direction. Band structure and spin orientation for majority (red) and minority (blue) carriers in the case of b) a non-magnetic electrode, c) FM electrode with out-of-plane magnetization ($\theta = 0$), d) FM electrode with in-plane magnetization ($\theta = \pi/2$). δ is the effective spin orientation. Figure adapted from ref.[25].

We should mention also that SOC anisotropy may the responsible for having a perpendicular magnetic anisotropy (PMA) which often arises in ultra-thin FM layers when the thickness of the layer is small (typically of a few nm) because of the competition between the shape volume anisotropy versus the surface anisotropy. The Rashba

magnetic field appears because of the structure inversion asymmetry happening at the interface of a material as we have mentioned already. The resulting Rashba field is proportional to the cross product of the interfacial electric field and the electron momentum ($\boldsymbol{B_R} \propto \boldsymbol{k} \times \boldsymbol{E}$). An adapted sketch explaining this effect can be found in figures 1.11 and 1.12, where in addition to explaining SOC effects, they specifically address them in insulator/FM/(insulator or metal) junctions.

Figure 1.11 shows how the dispersion relations (band structure) may be affected by the SOC at the interface, therefore how the spin of electrons is shifted (δ) depending on the direction of the magnetization (θ) in the FM. It is important to emphasize again that in MTJs when an electron tunnels, the strongest influence in the tunneling procedures comes from the local characteristics (magnetization, symmetry matching and filtering, electric fields, etc.) near the interfaces of the insulator. We will discuss (in chapter3) how magnetic anisotropies (in particular surface anisotropies) affect the magnetization direction in our MTJs in the case of competing in-plane versus out-of-plane anisotropies.

The orientation of the effective magnetization of the FM is studied in figure 1.12. It shows how the Rashba magnetic field $\boldsymbol{B_R}$ is acting upon the electrons tunneling in the mentioned MTJ. It is known that the large surface electric field give rise to a spin-splitting of the conduction electrons due to Rashba SOC[25]. For a magnet, this same splitting is modified by the exchange field resulting in a large magnetic anisotropy that can explain the electric field, thickness and material dependence reported in many experiments.

For a perfectly symmetric heterostructure shown in figure 1.12a) we can see how there is an electric field $\boldsymbol{E}$ at each interface region of the FM. For a given wavevector $\boldsymbol{k}$, the Rashba field $\boldsymbol{B_R}$ proportional to $\boldsymbol{k} \times \boldsymbol{E}$, has an opposite sign at the two surfaces and the average field is zero. If a gate voltage is applied across the structure then the symmetry is broken and a net Rashba field influence the electrons (see figure 1.12b). The gate voltage dependence of the anisotropy is shown in figure 1.12c). The interfacial electric field $\boldsymbol{E}$ causes a lateral shift of the parabola as indicated by V_0 for the case i). The interfacial field is shifted far beyond the external field range (for cases ii) and iii)

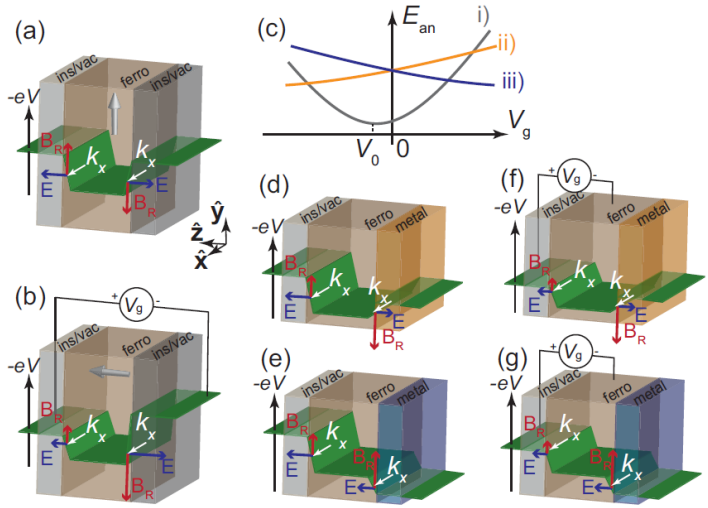

Figure 1.12: Rashba magnetic field dependence on interfacing materials and gate voltage. At each interface, the Rashba magnetic field $\boldsymbol{B_R} \propto \boldsymbol{k} \times \boldsymbol{E}$ is proportional to the cross product of the electron wave vector and the surface electric field. a) The average $\boldsymbol{B_R}$ is zero. b) An external gate voltage V_g breaks the symmetry (the average $\boldsymbol{B_R}$ is not zero). c) V_g dependence of the anisotropy energy. The asymmetry may also appear due to having the FM (e.g. a $3d$ FM such as Fe) between two different materials: in parts d) and f) the metal is a $4d$ transition metal and in parts e) and d) its a $5d$ metal. Figure adapted from Ref.[25].

arising a close to linear dependence. The materials used in the growth of the junctions influence also the net Rashba field, particularly the materials used for capping the FM electrode. Usually a normal metal is used as a cap (in our case is Au), figure 1.12d) and e) shows how the net Rashba field arises when using a $4d$ or $5d$ transition metal. The latter situation is particularly favorable since the intrinsic Rashba fields have the same sense and add. In addition, the $5d$ elements (e.g. Au, Pt, Ta) have larger SOC, resulting in a larger α_R and hence are more likely to produce a sizable PMA. Experiments in ref.[26] indeed show an opposite field dependence for such systems with Pd($4d$) and

Pt($5d$) N-layers.

1.3.6. Anisotropic tunneling magnetoresistance due to SOC (TAMR)

We are going to discuss how, besides PMA, the presence of SOC could show up in the form of an anisotropic tunneling magnetoresistance between ferromagnet and normal metal.

In a spin valve, the TMR comes from the change of resistance due to the relative orientation between the two FM electrodes magnetization, which is due to the differences in the spin polarizations of majority and minority carriers at the Fermi energy. However the absolute orientation of the magnetization in the FM with respect to the MTJ (the crystallographic orientations) influences also the TMR. This crystalline anisotropy affecting the TMR has been named tunneling anisotropic magnetoresistance (TAMR)[27,28]. It is interesting the fact that, regarding TAMR, there is no need to have two different FM electrodes to measure TMR, only one is enough. This effect in single FM junctions has been studied in (Ga,Mn)As/Al_2O_3/Au[27] and Fe/GaAs /Au[24] sandwiches. The TAMR then will have different values for the in-plane and the out-of-plane configurations (the reference is the layer plane). In analogy to the TMR, the TAMR ratio is defined as:

$$TAMR_{[ref]} = \frac{R(\phi) - R_{[ref]}}{R_{[ref]}} \tag{1.7}$$

where $[ref]$ indicates the crystallographic direction taken as a reference (say, an easy, or hard axis) and ϕ denotes the angle with respect to the $[ref]$ direction.

From the many studies of the TAMR effect[22,27,28,24], it has become clear that the responsible mechanisms could be different depending on the systems. One of the point of views with the broadest agreement is presented in refs.[23,24] where the authors propose that the uniaxial anisotropy in epitaxial tunnel junctions comes from the interference of Dresselhaus and Bychkov-Rashba spin-orbit interactions. This approach is in agreement with our Fe/MgO/V junction system, and

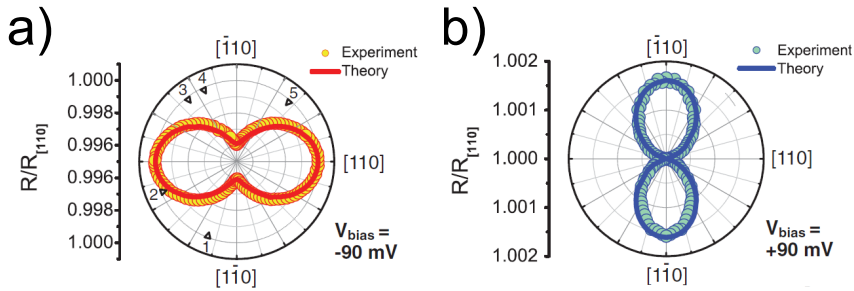

Figure 1.13: In-plane rotations showing different TAMR behaviors at low temperatures. Parts a) and b) show the in-plane rotations from Moser et al. in Fe/GaAs/Au MTJs made at H_{mod} =5 kOe. Both the calculated and measured TAMR is roughly 0.3% either for positive a) or negative b) applied bias. Figure adapted from Ref.[24].

additionally we can introduce another magnetocrystalline anisotropy called perpendicular magnetic anisotropy (PMA) which to some extent appears in thin FM films[29]. PMA and its effects on the magnetic states of our junctions are some of our experimental results thus will be discussed in a separate chapter 3.4.3.

We have gone step by step explaining the possible mechanisms of electrons conducting through our MTJs above the critical temperature of (bulk) Vanadium ($T_C = 5.4K$). Decreasing the temperature below T_C makes the superconductive effects to emerge. Superconductivity is a complex macroscopic quantum phenomena which is not going to be formally treated here, but we will only take the necessary ingredients to explain and understand the effects and results obtained. We will start describing the conductance mechanisms in superconducting tunnel junctions (SCTJs) and finally we will introduce the interaction of magnetism with superconductivity.

1.4. Tunneling involving superconducting materials

At present, the *superconducting electronics* field is a well-established branch of engineering[30,31]. There are already a great amount of applications of this in different areas such as information technology, radiofrequency technology, electrical and magnetic measures of high precision or electromedicine.

A good motivation may start by enumerating the advantages of the *superconducting electronics* with respect to the well-established semiconductor electronics. For example, once the electrical resistances disappears so do the parasitic heat losses which occur in the circuit resistances and connections of semiconductor devices. The superconductor components have therefore exceptionally high frequency tolerance compared to the semiconductor electronics, such as, if they are used as sensors, their sensitivity can be only constrained by the Heisenberg uncertainty principle.

The race in electronics towards the miniaturization of its different components have given many problems such as the heat losses in the integrated circuits of semiconductors will be appreciable, or when one has a nanometric-size electronic device, the dimensions of the system are comparable to the Fermi wave length of the electrons within the system.

Devices considered in this thesis are not based on the idea of communication between superconductors (which is typical in superconducting electronics) but rather designed to investigate the interaction between superconductivity and ferromagnetism mediated by spin-orbit interaction. In this section we will start describing what a superconducting junction (SCJ) is and how the electron transport is treated theoretically. Then we will explain briefly the Blonder-Tinkham-Klapwijk (BTK) model[32] concentrating in its tunneling limit. Afterwards we will explain the Andreev reflection conducting process and finally we will add ferromagnetism degree of freedom into the problem.

1.4.1. Superconducting junctions

We may start by a brief clarification on the difference between an electron current flowing through a junction (meaning extensive junction) and the general theoretical approach. Often, the theoretical method to explain the current flow through a junction is considering one electron tunneling through a single conducting channel. This is called a single quantum point contact (SQPC) and it can be extrapolated to the case of an extensive junction if the sample is almost fully epitaxial which means that each conducting channel has a similar electron transmission. The transmission (τ) of the junction will determine if the electron conduction regime is in the tunneling range (low transmission) or in the metallic contact range (high transmission).

Let τ_i be the probability of an electron tunneling in a SQPC (where $0 \leq \tau_i \leq 1$). Thereby, that the current through a SQPC depends on this transmission probability ($I(\tau_i)$). In an extensive film, the amount of conduction channels (SQPC) is proportional to its cross-sectional area A. Ideally, if the interface has been perfectly growth, the transmission probability of each channel will be similar and very small inasmuch tunneling probabilities are so ($\tau_i \ll 1$), then:

$$I(\tau) = \sum_n I_i(\tau_i) = \tau \sum_n I_i = \tau I$$

where τ_i is the transmission probability of each channel, I_i is a single channel contribution to the current, n is the number of channels, τ is the mean transmission value and I is the total current through the junction. The picture is that if every channel is a resistor, then a junction is just a bunch of resistors in put in parallel, thus the total conductance through the junction will be the direct sum of the individual conductances of each channel.

When a junction has any of the electrodes made of a superconducting material, if the temperature drops below a critical value T_C, superconductivity arises and makes tunneling at low voltages (below the superconducting gap Δ) quite exotic[33]. Giaever (1960) discovered it in a $Al/Al_2O_3/Pb$ junction (see figure 1.14b,c) when measuring the current versus voltage curve (I-V curve). The derivative of the I-V

curve, the differential conductance G, resembles the Bardeen-Cooper-Schriefer (BCS) density of states for quasiparticle excitations (see figure 1.14a). Looking at figure 1.14a showing the density of states of a NIS junction its clear that tunneling processes are forbidden for energies below the gap Δ of the superconductor. Thus, a priori, the conductance of low-energy electrons ($eV < \Delta$) will be zero, and the conductance of high-energy electrons ($eV > \Delta$) will be the expected value of a *normal/insulator/normal* (*NIN*) tunnel junction.

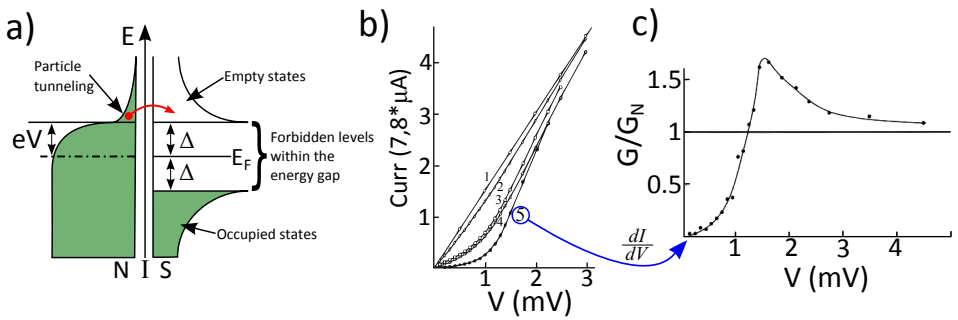

Figure 1.14: a) *Normal/Insulator/Superconductor* (*NIS*) junction energy diagram at T = 0K. The particle can only tunnel if $eV > \Delta$. b) Tunnel current through a $Al/Al_2O_3/Pb$ junction as a function of voltage. Curve (5) corresponds to T=1.6 K, H=0 Oe (Pb superconducting). c) Normalized (at normal state) conductance from curve (5) in part b). Figures adapted from ref.[34].

Nevertheless, there are possibilities for the electron to tunnel even at energies below the SC gap. To explain the basics of the subgap electron transmission procedures, one must start with the BTK model.

1.4.2. BTK model

Blonder, Tinkham and Klapwijk developed a model based on the scattering formalism to describe N-S and S-S contacts[35, 32, 36]. In their model the excitations of a clean superconductor are described by the Bogoliubov-de Gennes equations[37]. In order to simulate the scattering that takes place in the junctions they used a repulsive δ-like

potential located in the interface between electrodes, whose strength is controlled by a parameter $Z = H/\hbar\nu_F$ which is the transparency of the barrier, proportional to the barrier height H and inversely proportional to the Fermi velocity ν_F, and is related to the transmission parameter $\tau = 1/(1 + Z^2)$. As it is explained in detail in ref.[32], the BTK model has been developed for the case of a N-S junction. The model obtains the current as a function of Z, ranging from the case of a tunnel barrier, where it's recovered the results of the traditional tunnel theory ($Z \gg 1$), to the case where there is no scattering in the interface ($Z = 0$).

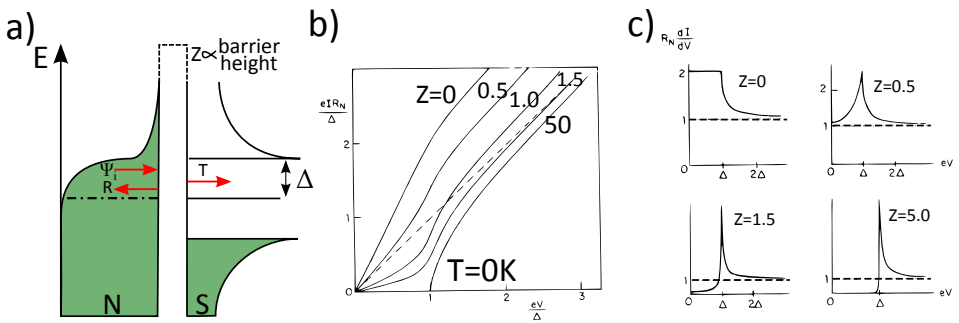

Figure 1.15: a) Single particle (Ψ_i) tunneling in a NS junction. b) IV curve for different transparencies: $Z = 0$ metallic contact limit and $Z \gg 1$ tunnel regime. c) Differential conductance for different barrier transparencies. Figure adapted from ref.[32].

Traditionally, quantum transport in microelectronic is calculated using one of the following approaches: The scattering formalism in which transport properties are expressed in terms of the scattering matrix of the system. This can be pictured as replacing the device by an appropriate scattering matrix. BTK model[35] uses this approach for the superconducting case. Another technique is that of the semiclassical Green functions. In this case the problem consist of determining the Green functions for the uncoupled electrodes and finally connect them in the interfaces by means of suitable boundary conditions. Finally there is a different point of view developed by Cuevas[38] which consists in using a Hamiltonian approach with infinite order pertur-

bation terms.

Before continuing with the quantum transport formalism of a *NIS* junction, lets first consider the processes happening at the interface. As we have discussed previously there are two main regimes depending on the energy the incident electrons have, namely the subgap ($eV < \Delta$) and the overgap ($eV > \Delta$) regime. Henceforth we are going to delve into the subgap regime processes given that the overgap regime is straightforward the case of a simple *NIN* junction.

When a normal metal is adjacent to a superconductor, the superconducting condensate 'leaks' from the superconductor part into the overlaying metal layer. This behavior is known as the *proximity effect*[39]. Essentially we are looking at the way the electronic reservoirs are communicating and the picture is that the interface is not a sharp abrupt change from single electrons (in the normal metal) to Cooper pairs (in the superconductor) but more like there is a region of influence in the neighborhood of the interface. To clarify this we can divide the proximity effect in two: First, the Andreev reflection, where a normal electron incident into the S/N interface is paired with an electron inside the Fermi sea by the S energy gap, leaving a hole excitation, and second, the propagation length of this electron/hole phase-correlated pair.

1.4.3. Conventional Andreev Reflection

At the boundary between a normal metal and a superconductor Andreev Reflection[40] occurs. Conventionally, in this process an electron above the Fermi level is converted into a hole below the Fermi level with opposite spin and a Cooper pair is formed inside the superconductor (see figure 1.16a).

Depending on different junction parameters such as the thickness of the barrier, the quality of the layer matching characteristics or the spin filtering of the barrier, Andreev reflection can present a very important charge transmitting channel. Indeed, continuing with the previous discussion of the quantum transport formalism using the approach made by Cuevas[38] taking into account the contribution to the charge transport, which is called 'branch crossing' in the BTK language, that

is no other than the Andreev reflection term we have the equation for the differential conductance of a *NIS* junction:

$$G_{NS} = \frac{4e^2}{h} \begin{cases} \dfrac{\tau^2}{(2-\tau)^2 - 4(1-\tau)(eV/\Delta)^2} & eV \leq \Delta \\ \dfrac{\tau}{\tau + (2-\tau)\sqrt{1-(\Delta/eV)^2}} & eV > \Delta \end{cases} \tag{1.8}$$

in terms of the gap of the superconductor Δ and the barrier transmission coefficient τ which in the small bias regime where the normal system exhibits an Ohmic response is taken as a constant. It is clear that in the tunneling regime, where we have a small transmission coefficient τ, the overall differential conductance ought to be also small.

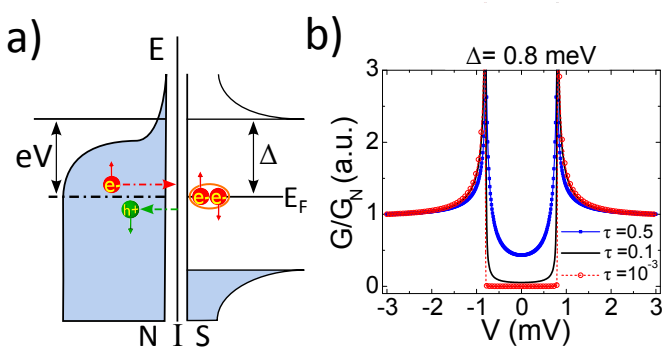

Figure 1.16: a) Conventional Andreev Reflection sketch in a NIS junction. b) Normalized conductance of a NIS junction changing the barrier transmission coefficient (tunneling regime $\tau \ll 1$), calculated with equation 1.8.

Now we have a charge transmission procedure that can explain to some extent the finite conductance value in the subgap regime. There are other mechanisms that can make the subgap conductance finite, such as the *gapless superconductivity*[41] which is associated with the presence of magnetic impurities or the presence of external magnetic

fields in thin films. Moreover, when carriers go through a SC/FM interface they experience an spin-dependent phase angle resulting in spin-mixing and the formation of a bound state called the Andreev bound state (ABS). With point contact Andreev reflection (PCAR) measurements it is possible to extract the value of the spin mixing angle[42]. In addition, experiments with carbon nanotubes grown between SC leads show properties of these molecules such as the energy levels, their relative spin orientation and the coupling to the leads[43], which is relevant for applications such as SQUIDs.

So far we have considered a NIS junction configuration and while we will extensively discuss the influence having a FM substituting the NM in the next section, we can include at this point the expansion of equation 1.8 given by Ref.[44] considering a FIS junction. In this case, there are two transmission coefficients, one for majority ($\tau_\uparrow$) and one for minority ($\tau_\downarrow$) carriers, the reflection probabilities being $r_\sigma = \sqrt{1-\tau_\sigma}$ where $\sigma = \uparrow, \downarrow$ and the expansion reads:

$$G_{FS} = \frac{4e^2}{h}\begin{cases} \dfrac{\tau_\uparrow\tau_\downarrow}{(1+r_\uparrow r_\downarrow)^2 - 4r_\uparrow r_\downarrow (eV/\Delta)^2} & eV \leq \Delta \\ \dfrac{\tau_\uparrow\tau_\downarrow + (\tau_\uparrow + \tau_\downarrow - \tau_\uparrow\tau_\downarrow)\sqrt{1-(\Delta/eV)^2}}{\left[1 - r_\uparrow r_\downarrow + (1+r_\uparrow r_\downarrow)\sqrt{1-(\Delta/eV)^2}\right]^2} & eV > \Delta \end{cases} \tag{1.9}$$

This formula in the absence of spin polarization ($\tau_\uparrow = \tau_\downarrow$) reduces to the BTK result (equation 1.8). The normal state conductance is given by $G_N = (e^2/h)(\tau_\uparrow + \tau_\downarrow)$ and the current polarization is defined by $P = |\tau_\uparrow - \tau_\downarrow|/(\tau_\uparrow + \tau_\downarrow)$.

This model fits perfectly to an Al/Co point contact (see Figure1.17) described in the paper[44] and is a good and easy model for extracting some quantitative parameters such as the carrier transparencies ($\tau_\uparrow$ and $\tau_\downarrow$) and the current polarization (P).

The measurements from figure 1.17 were made at $T \approx 100$mK and the parameters from the fit to model 1.9 give all similar values which in average are $\Delta = 0.19$meV, $\tau_\uparrow = 0.40, \tau_\downarrow = 0.98, P = 41\%$. This result is coherent for a direct contact (metallic contact) between a NM and

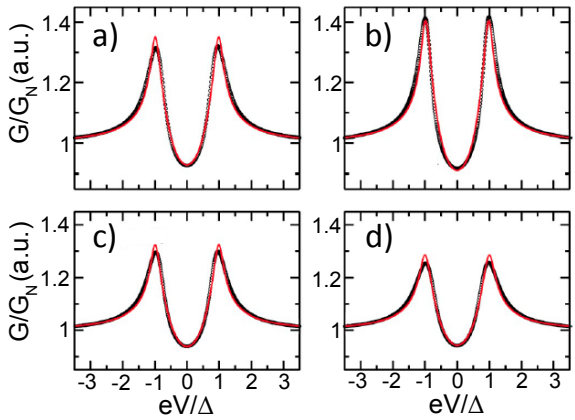

Figure 1.17: Normalized conductance (black dots) of an Al/Co point contact and the fit to equation 1.9 (red solid line) for different Co thicknesses. a) d_{Co} = 6nm, b) d_{Co} = 12nm, c) d_{Co} = 24nm and d) d_{Co} = 50nm. Figure adapted from ref.[44].

a FM indeed giving a high transmission an a moderately strong spin polarization.

This is already a very complete model in spite of the fact that it doesn't take into account spin-flip processes that might take place at the interface (spin-active interface) between two materials, so lets focus in the interplay between Andreev Reflection and ferromagnetism in the presence of a spin-active interface.

1.4.4. Unconventional Andreev Reflection

Previous models of Andreev reflection have only take into account the formation of conventional Cooper pairs (anti-parallel coupling) but not a parallel spin coupling (**spin triplet**). Such correlations could be induced at the interface between a SC and a FM due to SOC or magnetic inhomogeneities. This section aims to describe the origin of spin triplet correlation at FM/SC interfaces.

In a superconductor (SC), the conduction electrons of opposite spin and momentum form Cooper pairs near the Fermi surface[46] and

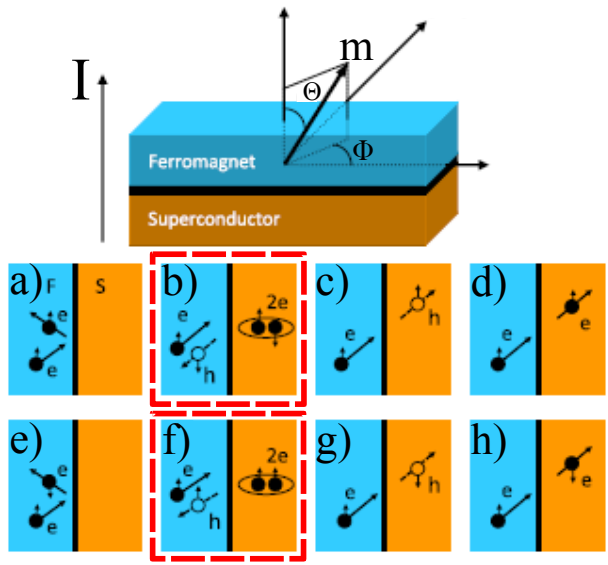

Figure 1.18: Top: FS junction. $\boldsymbol{m}$ is the magnetization vector in spherical coordinates defined by the polar angle Θ and azimuthal angle Φ. The electron current I, flows perpendicular to the interface. Bottom: Scattering processes at the FS interface with SOC. Electron (holes) are depicted by full (empty) circles. Vertical arrows denote the spin. a) Specular reflection, b) Andreev reflection, c) holelike transmission, and d) electronlike transmission. e)-h) Corresponding spin-flip counterparts. Figure adapted from Ref.[45]

in a ferromagnet (FM) the conduction electrons tend to align with the ferromagnet magnetization, this two effects are in principle mutually exclusive. Traditionally, the mix of ferromagnetism and superconductivity has seemed incompatible because the magnetic exchange field in a ferromagnet tends to polarize the spin of the electrons thus breaking apart the opposite-spin singlet the Cooper pairs are. However, experiments found Josephson coupling between superconducting electrodes separated afar by a ferromagnetic spacer[47]. This has been considered a proof of the equal-spin triplet pairing *spin triplet*, which is not affected by the exchange field and can therefore propagate over long distances

into the FM. Several works[39,48,49,50,51,52] studying quasiparticle and electron interference effects in the conductance across the FM/SC interfaces demonstrate the long-range propagation of superconducting correlations, and imply the occurrence of unconventional equal-spin Andreev reflection.

In particular, Bergeret et al.[51,52] study theoretically the singlet to triplet spin conversion in SC/FM structures in the presence of SOC. In ref.[51] a SU(2) (special unitary group) has been developed to unify all models describing the long-range proximity effect in SC/FM structures providing in addition new sources for the singlet-triplet conversion.

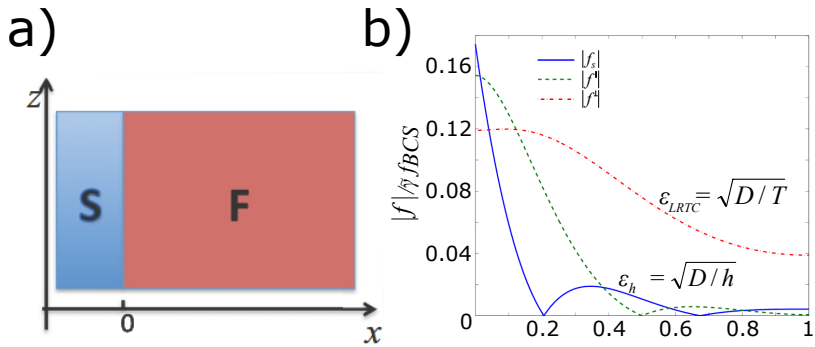

Figure 1.19: Part a) shows the SF interface for the geometry system used. Part b) shows the spatial dependence of the amplitude of all components of the condensate function. The exchange field $\boldsymbol{h}$ in F is homogeneous and points in the z direction. The SOC is isotropic inside the F. Figure adapted from Ref.[52]

Looking at ref.[52] we find an extensive theoretical demonstration of how SOC, among other interfacial effects such as magnetic inhomogeneities, may act as a source of long-range triplet correlations (LRTC) in SC/FM structures. The Usadel's equation to describe the superconducting condensate is:

$$D\nabla^2\hat{f} - 2|\omega|\hat{f} - i\mathrm{sgn}(\omega)\{\hat{h},\hat{f}\} = 0 \tag{1.10}$$

where the superconducting condensate components $\hat{f} = f_s\hat{1} + f_t^a\sigma^a$ are the singlet scalar component f_s and the triplet vector component

$f_t^{\parallel}$ and $f_t^{\perp}$ which are the spatial parallel and perpendicular components with respect to the exchange field ($\hat{h}$) of the ferromagnet, ω is the Matsubara frequency, D is the diffusion constant and T the temperature. The authors conclude that LRTC are possible if the SC/FM structure has SOC due to the lack of inversion symmetry (explained in 1.3.5) and if the FM has perpendicular magnetization.

Three spin-related effects are needed for explaining how a supercurrent could be generated and sustained in a *s-wave*(SC)/half-metal(FM)/*s-wave*(SC) junction: *spin-mixing*, *spin-filtering* and *spin-flip* processes[48]. As explained in section 1.3.2 in a FM the transmission probabilities of majority and minority carriers differ not only in magnitude but also through the phases they pick up upon scattering at the interface, effect named *spin-mixing*.

The *spin-flip* process is related to the Rashba SOC happening at the interface due to the lack of space inversion symmetry, and in the non-superconducting state has been addressed in section 1.3.5. In ref.[45] the authors theoretically address the interplay of magnetism and spin-orbit fields when the Andreev reflection mechanism is in play. The most robust anisotropy is the out-of-plane one (plane being the interface) and more subtle is the in-plane anisotropy. They find also that the resulting magnetic anisotropy, termed magnetoanisotropic Andreev Reflection (MAAR), should be giant in comparison to the TAMR[27,28] (its normal-state counterpart) reaching a universal behavior in the half-metallic case (see Figure 1.20b).

We can address now the challenge posed with the model describe in equation 1.9(from Ref.[44]). Figure 1.18b) shows how the subgap conductance can be finite for a strong spin polarization ($P > 80\%$) involving indispensably SOC at the interface, otherwise it vanishes.

As in the case of the TAMR, the MAAR definition (reference system shown in Figure 1.18a) is given for the in-plane and the out-of-plane configurations by:

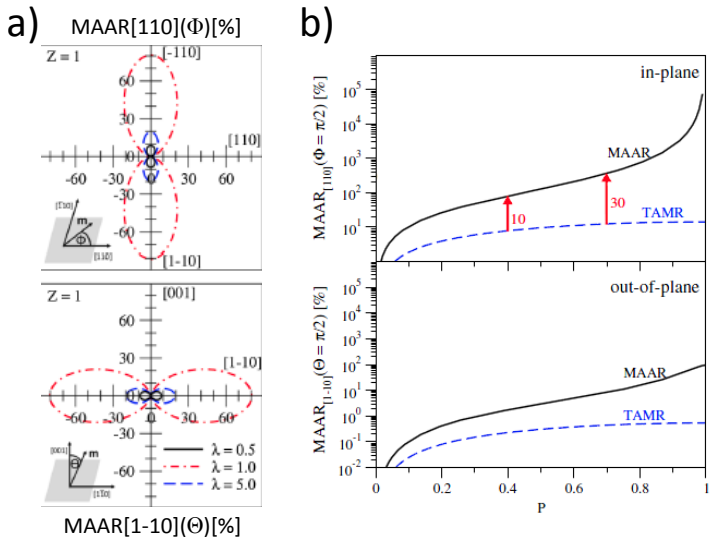

Figure 1.20: Part a) shows the calculated in-plane (top) and out-of-plane (bottom) MAAR for different SOC strengths at $P = 0.4$. Part b) shows the calculated in-plane (top) and out-of-plane (bottom) MAAR and TAMR as a function of spin polarization P at a selected SOC strength. Red arrows show the ratio between MAAR/TAMR. All calculations were made at zero bias conductance $G(V = 0)$ and for a moderate barrier transparency ($Z = 1$). Figure adapted from Ref.[45]

$$MAAR_{[110]}(\Phi) = \frac{G(\Theta, 0) - G(\Theta, \Phi)}{G(\Theta, \Phi)}\bigg|_{\Theta=90^\circ}$$

$$MAAR_{[1-10]}(\Theta) = \frac{G(0, \Phi) - G(\Theta, \Phi)}{G(\Theta, \Phi)}\bigg|_{\Phi=-90^\circ}$$

The out-of-plane MAAR depends, in general on Φ, but authors[45] choose the yz ($\Phi = -90^\circ$) plane as its reference. The calculated MAAR (shown in Figure 1.20a) shows a nonmonotonic dependence on SOC. In the presence of a moderate barrier ($Z = 1$) MAAR gets strongly enhanced due to the additional contribution from spin-flip

AR. Compared to TAMR (see Figure 1.20b), the (calculated) magnitude of MAAR is giant, varying by orders of magnitude upon chaning the spin polarization P (we have mentioned the experimentally measured in-plane TAMR in Fe/GaAs/Au junctions is less than a percent[24]). For a strong spin polarized current the ratio MAAR/TAMR climbs to mor than 10^2. The experimental realization of MAAR (in contrast to TAMR) should be complicated because magnetization of the FM is rotated by an external magnetic field whose presence can affect the SC decreasing the SC gap thus influencing the value of the zero bias conductance.

We finish here the theoretical introduction related to electron tunnel in superconducting spintronics. Before addressing the other main subject (organic spintronics) it is necessary first to introduce the concept of noise fluctuations in the low frequency range.

1.5. Low frequency noise (LFN)

This section describes the main contributions to low frequency noise ($<$ 102.4kHz) that are observed in spintronic devices. As it is explained in chapter 2, we measure the voltage signal response (which will have a certain amount of noise) of the electron transport through magnetic tunnel junctions. But before going to each particular noise source, let us first give a brief definition of what is noise.

1.5.1. Formal description of noise fluctuations

Noise is defined as the random fluctuations of a physical quantity. In electronic devices, this quantity is the voltage and/or the current measured at the device terminals. In general, the random nature of this inherent noise comes from the thermal motion and intrinsic properties of the building blocks of this devices, such as the generation and recombination of carriers, the discreteness of the current, the influence of magnetic fluctuations on the carriers transport or the existence of carrier traps. Noise measurements can give us information of all this properties of the system that, sometimes, are not accessible by other

techniques though in any case can complement any study made using some other technique. Besides, noise is in general a figure of merit of a device, as it determines the noise floor and thus the signal-noise ratio (SNR) of a system.

1.5.1.1. Stochastic processes

First we define a time dependent variable $x(t)$ which will have fluctuations. This fluctuations are the expected value of the squared deviation from the mean $\langle \delta x^2 \rangle$, that is, the variance. The first of these processes ever studied was the random motion of microscopic particles submerged in a fluid, namely Brownian motion[53].

This phenomenon, named after the botanist Robert Brown, consists on the movement of big or slow particles compared to smaller or quicker ones forming the environment of the big ones. For example, he was looking through a microscope at particles trapped in cavities inside pollen grains in water (environment), he noted that the particles moved through the water, but he was not able to determine the mechanisms that caused this motion. The Brownian motion of a particle in a liquid is due to the instantaneous imbalance in the combined forces exerted by collisions of the particle with the much smaller liquid molecules (which are in random thermal motion) surrounding it.

Given a system in thermodynamic equilibrium state, the *fluctuation-dissipation* theorem states that the thermal fluctuations of a physical variable are related to the impedance of the physical variable[54]. It assumes that the response of a system in equilibrium to a small applied force is the same as its response to a spontaneous fluctuation. The thermal noise in a resistor is a manifestation of this theorem, where the voltage is the generalized force and the role of dissipation is played by the electrical resistance and the temperature[55]. Another example of the fluctuation dissipation theorem is the magnetic noise observed in soft ferromagnets, which comes from a frequency independent imaginary permeability at low temperature[56].

So now let us define a stochastic variable $X(t)$, with a distribution function $F_X(x)$ defined as the probability P of the variable X being equal or smaller than a certain value x:

$$F_X(x) = P(X \leq x)$$

The derivative of the distribution function with respect to x is the probability density:

$$f_X(x) = \frac{dF_X(x)}{dx}$$

The statistics moments m_n associated to the random variable may be defined using the probability density by:

$$m_n = \int_{-\infty}^{+\infty} x^n f_X(x) dx$$

The first moment corresponds to the mean value of our random variable. The central moments μ_n of the variable are given by:

$$\mu_n = \int_{-\infty}^{+\infty} (x - m_1)^n f_X(x) dx$$

The first central moment $(x - m_1)$ corresponds to the fluctuation (δx) of our random variable x with respect to the mean value, so μ_1 corresponds to the average value of δx, which for a random process is zero. The second central moment μ_2 corresponds to the average value of δx^2, i.e. the variance σ^2. Figure 1.21 shows the first four statistic moments.

The Central Limit Theorem (CLT) states that if the process under study can be modeled as a sum of N random variables, then independently of the distribution of each variable, the distribution of the sum will approach a gaussian distribution if N is large enough. Only the first two moments, mean and variance, are non-zero for a gaussian distribution. *Therefore, if we can guarantee that our process has a gaussian probability density, determined by a mean m_1 and a variance μ_2, determining these two quantities experimentally will be enough to characterize the random process.* In the context of electronic transport through spintronic devices, the first and second moments may be obtained by measuring the voltage (mean) and its variance, which we extract from the Fourier transform of the voltage fluctuations (see below).

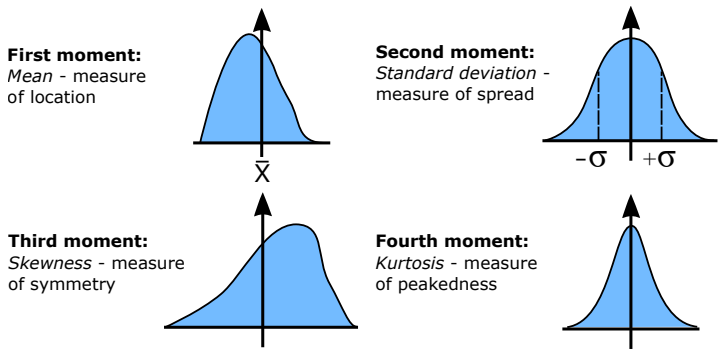

Figure 1.21: Diagram showing the first four statistic moments. Figure adapted from ref.[2]

1.5.2. Time series analysis

The noise in electronic devices may be understood using the fluctuation-dissipation theorem if we take the voltage as the general force. Then, if we design an experiment which measures the variance of our generalized force, ($\langle V^2 \rangle$), at the thermal equilibrium and at some fixed frequency bandwidth Δf, the **spectral density function** S_V may be defined as *the variance of the voltage per unit of frequency*:

$$S_V = \frac{\langle \Delta V^2 \rangle}{\Delta f} \tag{1.11}$$

The frequency-dependent spectral density is obtained by differentiating the variance with respect to the frequency:

$$S_V(f) = \frac{d\langle \Delta V^2 \rangle}{df} \tag{1.12}$$

Thereby, *the spectral density show us how a signal or a time series is distributed with frequency.*

For convenience we are going to discuss an alternative way of defining the spectral density of a process using the correlation function.

The correlation function is a measure of the similarity between two signals $X(t)$, $Y(t)$, when one of them is delayed by a lag τ. The

definition slides the $Y(t)$ function along the time axis, and calculates the integral of their product at each position. When the functions match, the correlation is maximized. The formula is:

$$R_{XY}(\tau) = \lim_{T\to\infty} \frac{1}{2T} \int_{-T}^{T} X(t)Y(t+\tau)dt \tag{1.13}$$

The autocorrelation function of a variable $X(t)$ is defined as the correlation of the signal with itself:

$$R_{XX}(\tau) = \lim_{T\to\infty} \frac{1}{2T} \int_{-T}^{T} X(t)X(t+\tau)dt \tag{1.14}$$

Finally, the Wiener-Khinchin theorem relates the autocorrelation function to the power spectral density via the Fourier transform:

$$S(f) = \int_{-\infty}^{+\infty} R_{XX}(\tau)e^{-i2\pi f\tau}d\tau \tag{1.15}$$

$$R_{XX}(\tau) = \int_{-\infty}^{+\infty} S(f)e^{i2\pi f\tau}df \tag{1.16}$$

From now on we will refer the fluctuations as a spectral density instead of a variance.

Now, in spintronics, the signals we are interested in measuring have a very small amplitude, and they need to be treated (amplified, filtered, etc) appropriately through some electronic system, say an amplifier. One could think of the amplifier as a 'black box' with an input signal $V_{in}(t)$ and an output signal $V_{out}(t)$. Both are related through their power spectral densities $S_V^{in}(f)$, $S_V^{out}(f)$ and the transfer function $H(f)$ of the amplifier through the relation:

$$S_V^{out}(f) = S_V^{in}(f)|H(f)|^2 \tag{1.17}$$

valid only if the setup does not add any noise, which is never the case. The modeling of the amplifiers noise and how to avoid it is explained in chapter 2.

The minimum level of noise intrinsic to the system is called noise floor. Thus all the noise measured should be significantly higher than the noise floor. The SNR is defined as the ratio between the signal

power and the noise floor power. Ideally, the SNR should be as high as possible.

There are two main techniques of obtaining the spectral densisty of a signal: either using the fast Fourier transform (FFT) or a filtering technique.

The FFT method is the one used for low frequency measurements, where a resolution from a fraction of Hz up to tens of kHz is needed. In order to obtain the spectrum, the signal is sampled by $2N$ points during a times T with a resolution in time of Δt. The FFT of this discrete time trace is calculated, giving a spectrum with N data points (or **bins**) up to a maximum frequency $f_{max} = 1/2\Delta t$ and a frequency step of $\Delta f = 1/T$.

In the filtering technique, the spectral density for a range of frequencies (or span) is obtained by sweeping the central frequency of the filter. Since the band-width is inversely proportional to the duration of one measurement, having a high resolution in frequency (a small frequency step) would take a very long time. So this technique is used for the detection of high frequency dynamics (in the range of GHz), where having a resolution of kHz is quite sufficient. As we are dealing with low frequency noise we will use the FFT method for extracting a signal's spectral density.

Now we will describe the most relevant, intrinsic to magnetic tunnel junctions, low frequency noise sources shown in figure 1.22.

1.5.3. White noise

White noise or frequency independent noise. This random fluctuation has a constant power spectral density, therefrom comes its name from an analogy with the white light, which contains light of all visible frequencies. In spintronic systems, this fluctuation has two components: thermal and shot noise.

1.5.3.1. Thermal noise

Thermal or Johnson-Nyquist noise was discovered in 1928 by John B. Johnson at Bell Labs[57], who described his results to his co-worker

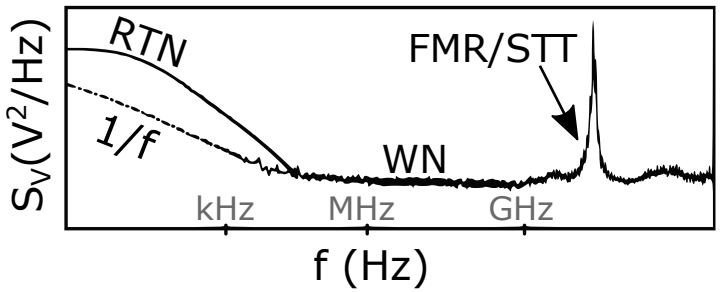

Figure 1.22: Diagram of the main noise contributions in spintronic systems. Note that this thesis focus in low frequency noise (up to a hundreds of kHz), thus the ferromagnetic resonance (FMR) will not be discussed. Figure adapted from ref.[2]

Harry Nyquist who produced a theory explaining the observation[55]. The thermal noise in a conductor at thermodynamic equilibrium depends on its resistance and temperature. It is due to the random motion of the electric charges caused by thermal agitation. As previously mentioned, this noise is the manifestation of the fluctuation-dissipation theorem[54] relating the dissipation in a dynamic system (resistance), to the thermal fluctuations of the system (voltage fluctuations) at equilibrium. The spectra density S_V of the voltage due to thermal noise is given by:

$$S_V = 4k_BTR \tag{1.18}$$

where k_B is Boltzman's constant, T is the equilibrium temperature and R is the electrical resistance of the device. Measuring thermal noise can be used to calibrate our experimental setups quite straightforwardly (see chapter 2).

1.5.3.2. Shot noise

In statistics, the *Poisson distribution* expresses the probability of a number of events occurring in a fixed interval of time (or space) if the events occur with a known average rate (or mean), and are independent of the time elapsed since the last event. The name is in honor

of Siméon Denis Poisson (1781-1840) who introduced it and its first practical application was carried out by Ladislaus Borkiewicz in 1898 when he studied the number of Prussian soldiers accidentally killed by horse kicks. A wide variety of processes obey Poisson statistics, from the emission of electrons in a vacuum tube to the photons gathered per pixel in a CCD camera, or the number of molecules found in a small volume at a time lapse.

A discrete random variable X is said to follow a Poisson distribution with a mean $\lambda > 0$, if the probability of having k events in a given interval $P(X = k)$ for $k = 0, 1, 2 \ldots$ is given by:

$$f(k; \lambda) = P(X = k) = \frac{\lambda^k e^{-\lambda}}{k!} \tag{1.19}$$

When the average number of events occurring in the fixed interval of time or space becomes very large, i.e., $\lambda \to \infty$, the Poisson distribution is equivalent to the Gaussian distribution, as seen in figure 1.23a.

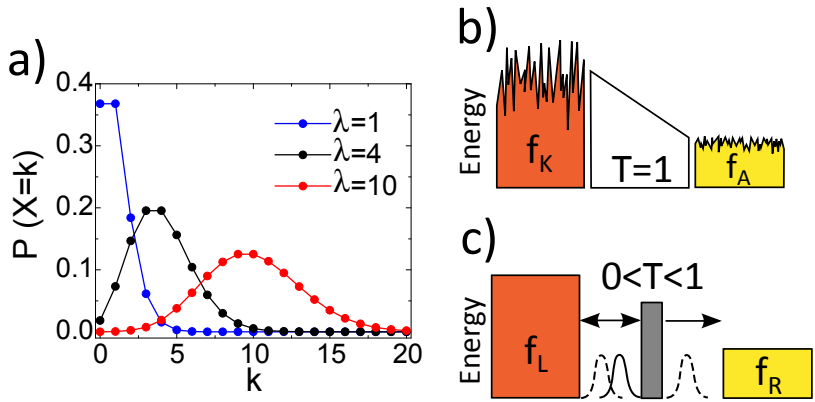

Figure 1.23: a) Poisson distribution for different number of events λ. b) Thermionic emission randomness coming from the cathode-anode emission. c) Quantum tunneling randomness coming from the transmission probability. Figure adapted from ref.[2]

In electronic devices, the discreteness of the electron current is the cause of the shot noise. It was first detected by Schottky in 1918 in a

vacuum tube, where electrons are emitted from the cathode electrode to the anode. In this system, the thermionic emission is the random process (see figure 1.23b), in contrast to quantum tunneling where the random process comes from the transmission probability (see figure 1.23c). Both systems follow a Poisson probability distribution where, focusing at the vacuum tube one, the mean squared fluctuation of the number of emission events equals the average count of the emission events. Thereby, the spectral density of the current fluctuations is given by Schottky's formula $S = 2eI$, where e is the charge of the electron and I the average current. The value $2eI$ is referred to as the Poissonian or full shot noise. Shot noise presents a frequency independent spectrum (whit noise) up to a certain cut-off frequency, typically in the GHz range. This cut-off frequency in the time domain is near the times an electron takes to travel through the conductor[58].

In mesoscopic devices like point contacts or tunnel junctions however, the randomness dwell from the transmission probability T of an electron tunneling from one lead to another. Indeed, the tunneling regime is only when this transmission is very small ($T \ll 1$), which yields an expression for the shot noise such as[59]:

$$S_I = \frac{e^3|V|}{\pi\hbar}\sum_n T_n(1-T_n) \tag{1.20}$$

where V is the bias voltage, T_n is the transmission probability in the n channel and h is Planck's constant. This equation yields the Poissonian value only in the limit of a low transparency system, such as we mentioned, a tunnel junction. Variations in the transparency of the system may lead to sub-Poissonian or, even, super-Poissonian shot noise[59].

For convenience we are going to define also the Poissonian voltage shot noise:

$$S_V = 2eIR_d^2 \tag{1.21}$$

where R_d is the differential resistance of the device. This equation describes white noise only at zero temperature, since for $T > 0$ and $V = 0$ the system would exhibit zero fluctuations at zero bias,

which violates the fluctuation-dissipation theorem. Avoiding this is straightforward by adding the thermal noise.

Shot noise and thermal noise are often, and incorrectly, viewed as additive and independent noise sources. This independence has been questioned for a long time and it can be shown that both types of noise have the same explanation if the electrical conductance is treated as a quantum-mechanical transmission phenomenon[60].

The joint expression for voltage white noise[60] (shot noise and thermal) for a tunnel junction is:

$$S_V = 2eIR_d^2 \coth\left(\frac{eV}{2k_BT}\right) \tag{1.22}$$

We will derive this equation in the following subsection in an intuitive way.

1.5.4. Unified equation for tunnel junctions

Instead of using the mathematical derivation presented above[59], we are now going to derivate it from the same physical model but using several assumptions from various branches of physics and signal analysis[61].

Consider an ideal tunnel junction: two metal contacts A and B separated by a thin insulating barrier (vacuum or dielectric). The junction is connected to an ideal voltage source which applies a constant bias voltage V.

Be $I(t)$ the current flowing through the circuit, which is kept at a constant temperature T. The current is an electric current made of electrons (discrete carriers), thus each have charge q.

Considering electrons as quantum-mechanical particles, there is a finite probability per unit of time that an electron (instantaneously) tunnels from lead A to B (noted by P_{AB}) and vice versa (noted by P_{BA}).

Suppose the detector of our thought experiment allows us to watch individual electrons tunneling through the barrier, because its sampling time τ is small enough. The bandwidth of the measurements would be:

$$\Delta f = \frac{1}{2\tau} \tag{1.23}$$

Three different events are possible:

1. An electron tunnels $A \to B$. Then $I(1) = +q/\tau$, occurring with a probability $P_{I(1)} = \tau P_{AB}$.
2. No electrons tunnel, so $I(0) = 0$, occurring with a probability $P_{I(0)} = 1 - (P_{AB} + P_{BA})\tau$.
3. An electron tunnels $B \to A$. Then $I(-1) = -q/\tau$, occurring with probability $P_{I(-1)} = \tau P_{BA}$.

Since this are all the possible outcomes, the average and mean square values of the current are:

$$\langle I \rangle = \sum_{i=-1}^{1} I(i) p_{I(i)} = q(P_{AB} - P_{BA}) \tag{1.24}$$

$$\langle I^2 \rangle = \sum_{i=-1}^{1} I(i)^2 p_{I(i)} = \frac{q^2}{\tau}(P_{AB} + P_{BA}) \tag{1.25}$$

Let us think of the electron tunneling event as a transition between two states A or B. Then n_A, n_B represent the occupation of the states A and B. If the system is in a steady state, n_A and n_B are constant and the following is true:

$$P_{AB} n_A = P_{BA} n_B \tag{1.26}$$

This assumption is extracted from the *detailed balance* principle[62], which informally states that for kinetic systems which are decomposed into elementary processes, then "*At equilibrium, each elementary process should be equilibrated by its reverse process*".

The two states A and B have energies E_A and E_B so $E_A - E_B = qV$. Since the occupation numbers satisfy the Boltzmann distribution[63]:

$$\frac{n_A}{n_B} = e^{-\frac{qV}{k_B T}} \tag{1.27}$$

Combining equations 1.26 and 1.27, we arrive at:

$$\frac{P_{BA}}{P_{AB}} = e^{-\frac{qV}{k_B T}}$$

thus

$$\langle I \rangle = qP_{AB}(1 - e^{-\frac{qV}{k_B T}})$$
$$\langle I^2 \rangle = \frac{q^2}{\tau} P_{AB}(1 + e^{-\frac{qV}{k_B T}})$$

which combined, along with equation 1.23, yields:

$$\langle I^2 \rangle = 2q\langle I \rangle \frac{1 + e^{-\frac{qV}{k_B T}}}{1 - e^{-\frac{qV}{k_B T}}} \Delta f = 2q\langle I \rangle \coth\left(\frac{qV}{2k_B T}\right)\Delta f$$

Finally, denoting the resistance of the junction by R, the voltage spectral density is:

$$S_V = S_I R^2 = \frac{\langle I^2 \rangle}{\Delta f} R^2 = 2q\langle I \rangle R^2 \coth\left(\frac{qV}{2k_B T}\right)$$

1.5.5. $1/f$ noise

This type of noise, also named as pink noise or flicker noise, is an ubiquitous type of noise found in many physical, biological and even economic systems. For example the fluctuations of the sea level, the intensity in a music recording, the human heart rates or the electrical currents in semiconductor devices all present $1/f$ noise.

It was discovered in 1925 by Johnson, in an experiment designed to test Schottky's theory of shot noise in vacuum tubes. After almost a century of research, the origin of $1/f$ noise in solid state remains unclear and only phenomenological models are used to characterize it.

The noise spectra in spintronic devices (as well as in electronic ones or other systems in nature) present a dependence, in some range of frequency, of the form $1/f^{\beta}$, with β generally close to 1. These

fluctuations are attributed to fluctuations in the conductance, for example, in Si MOSFETs, the resistance of the channel fluctuates due to electron capture into and emission from traps that lie in the oxide layer. In a MOSFET with a large area ($> 1\mu m^2$), $1/f$ noise appears from a superposition of the effects of a large number of traps with various activation energies and relaxation times[64, 65].

A fluctuation which is characterized by a single relaxation time τ is defined by a spectral density which follows a Lorentzian function of frequency:

$$S_X(f) = \langle X^2 \rangle \frac{4\tau}{1 + \omega^2 \tau^2}$$

Considering that the kinetics of the fluctuating quantity $X(t)$ may be described as a superposition of several relaxation processes with different relaxation times (or even a continuous distribution of relaxation times), schematically represented in figure 1.24. Then the spectral density of such a process is given by the average of the Lorentzian spectral density of this distribution weighted by the number of subsystems $p_X(\tau)$ each with a different relaxation time τ and the corresponding variance of fluctuations. The spectral density if then given by:

$$S_X(f) = \int_0^\infty p_X(\tau) \frac{4\tau}{1 + \omega^2 \tau^2} d\tau \tag{1.28}$$

The spectral density is inversely frequency dependent $S_X(f) \propto 1/f$ at some interval of frequency if $p_X(\tau) \propto 1/\tau$. Du Pré[66] and Van der Ziel[67] proposed that the fluctuations are a result of the superposition of activation processes with different relaxation times ($\tau = \tau_0 e^{-(E/k_B T)}$) with activation energies E. Then if the distribution activation energies $F_X(E)$ is chosen to be constant, the distribution relaxation times $p_X(\tau)$ has the required form, since:

$$p_X(\tau)d\tau = F_X(E)dE \Rightarrow p_X(\tau) = F_X(E)/(d\tau/dE) = k_B T F_X(E)/\tau$$

and if $F_X(E) = cnt.$, then $p_X(\tau) \propto 1/\tau$.

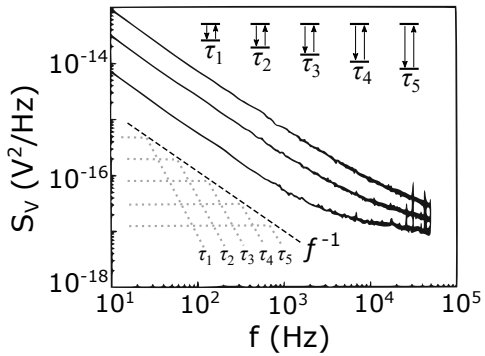

Figure 1.24: Sketch of $1/f$ noise as a sum of defects with different relaxation times. Figure adapted from ref.[2]

There is a phenomenological description of the $1/f$ noise propose by Hooge[68] which describes the $1/f$ noise in terms of the variation of the density of charge carriers, which is proportional to the dimensionless **Hooge parameter** α. The Hooge parameter allows comparing the $1/f$ noise power in different devices, and is given by:

$$S_V = \frac{\alpha V^2}{\Omega f^\beta} \tag{1.29}$$

where V is the applied DC voltage and Ω the volume or lateral size of the conductive region. In the case of tunnel junctions, the noise power is normalized by the cross-sectional area A of the junction, so the Hooge parameter typically has dimentios of μm^2.

$$S_V = \frac{\alpha V^2}{A f^\beta} \tag{1.30}$$

The exponent β varies between 0.9 and 1.4, and variations from this range are usually due to additional noise contributions, such as random telegraph noise[69] or generation-recombination processes[65].

Almost all electronic devices have $1/f$ noise associated with low frequency fluctuations in resistance. Spintronic devices, like GMR or TMR systems, are influenced by defects in their structure which give rise to $1/f$ noise. Besides, due to the link between magnetic order and

conductivity in spintronic devices, these may exhibit an additional $1/f$ noise source. This term is directly related to the magnetization noise that can be described using the fluctuation-dissipation theorem.

1.5.6. Thermal magnetic fluctuations

In ferromagnetic systems, the energy losses can be described by the complex susceptibility $\chi(\omega) = \chi'(\omega) + i\chi''(\omega)$. This quantity is dependent on frequency and its real and imaginary parts are described as the in-phase and out-phase, respectively, response of the magnetization to a small AC magnetic field. By using this quantity the thermal fluctuations of the magnetization ($S_M(\omega)$) can be expressed [70] as:

$$S_M(\omega) = \Omega \frac{4k_B T}{\omega} \chi''(\omega) \tag{1.31}$$

where Ω is the volume of the ferromagnetic body. The observation of this noise in a ferromagnet was reported at low frequencies [70, 71]. The obtained power spectrum is in accord with ferromagnetic frequency independent losses, thus the fluctuations exhibit $1/f$ noise.

1.5.7. Magnetic noise in spintronics

We have already mentioned that in magnetoresistive devices, due to the link between magnetization and resistivity, the measured resistance fluctuations come from the electrode's magnetic noise. This relationship was first reported in multilayer structures which exhibited GMR [72]. In that work, Hardner accurately predicted $1/f$ noise from a fluctuation-dissipation relation using the imaginary (or out-of phase) susceptibility of the system, and it was found that the fluctuations in resistance where proportional to the magnetization noise and the derivative $dR(H)/dH$ (see figure 1.25). Also it shows that at H=0 Oe the $1/f$ noise predicted by the fluctuation-dissipation theorem underestimates the resistance noise actually observed. This failure of the fluctuation-dissipation theorem is, in fact, expected as in this field region the main noise contribution is the domain wall dynamics, as long as domain walls are out of thermodynamic equilibrium. This out of

equilibrium noise is called Barkhausen noise and has been observed in other spintronic devices as magnetic tunnel junctions[73]. Indeed this kind of noise is not $1/f$ noise but seems rather $1/f^2$ noise, which is consistent with random walk dynamics and avalanches, as is expected in domain wall dynamics which may contribute to noise in the small field range.

The equilibrium noise is exhibited by every spintronic system, e.g. magnetic tunnel junctions, limits the use of GMR or TMR systems in magnetic field sensing and high frequency applications. In general, the design of sensors using crossed anisotropy[74] or easy axis biasing[75] neglects the Barkhausen noise. However, the presence of this kind of noise and its proportionality to the sensitivity (dR/dH) is a big drawback for using them in general applications.

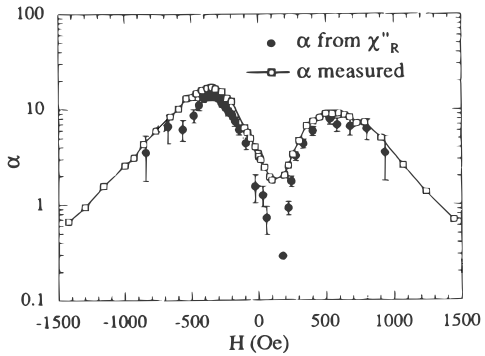

Figure 1.25: Hooge parameter α obtained from the resistance noise measurements and the AC susceptibility. Figure adapted from ref.[72]

1.5.8. Random telegraph noise (RTN)

Random telegraph noise is an electronic noise characterized by a time-dependent signal where step-like transitions between two or more discrete voltage (or current) levels take place at random times, as shown in figure 1.26a. RTN can be originated by different mechanisms depending on the structure being studied, like random trapping

and releasing of charge carriers at defect sites in bulk semiconductor crystals or local changes in the magnetization of a FM electrode.

The characteristic times τ_i of the levels can be obtained from the histogram of the time trace, or by a theoretical fit of the noise power spectrum, shown in figure 1.26b. For a two-level RTN, the spectral density is given by the Lorentzian[76]:

$$S_V^{RTN} = \frac{4\Delta V^2}{(\tau_{up} + \tau_{down})} \frac{T^2}{(1 + (2\pi T f)^2)} \tag{1.32}$$

with $T = (1/\tau_{up} + 1/\tau_{down})^{-1}$, where τ_{up} and τ_{down} are the characteristic dwell times of each level. This equation can be generalized for multilevel RTN.

Analyzing this type of noise may be quite useful for determining different properties, depending on the nature of the fluctuations. If the RTN is due to charge trapping/detrapping, for example in oxide traps in MOSFETS[77], then properties like the trap depth may be extracted from the dependence of $\ln(\tau_{up}/\tau down)$ with the voltage. An Arrhenius-type dependence is supposed for each characteristic time, and so one obtains:

$$\ln(\tau_{up}/\tau_{down}) = K - \frac{q}{k_B T}\left(\frac{x_T}{t} V + \dots\right)$$

where K is a constant, x_T the trap depth, t the oxide thickness and V the applied voltage. Other terms which depend on the temperature may be added to estimate surface potentials, etc.

Another origin of the resistance fluctuations may be the occurrence of magnetization fluctuations in the electrodes of a MTJ. In this case, the fluctuating magnetic moment may be calculated from the logarithmic dependence with the applied magnetic field. Again using an Arrhenius law for each characteristic time, one arrives at[76]:

$$\ln(\tau_{up}/\tau_{down}) = K + \frac{2\Delta m}{k_B T} H \tag{1.33}$$

where K is a constant, Δm is the fluctuating magnetic moment and H is the applied magnetic field.

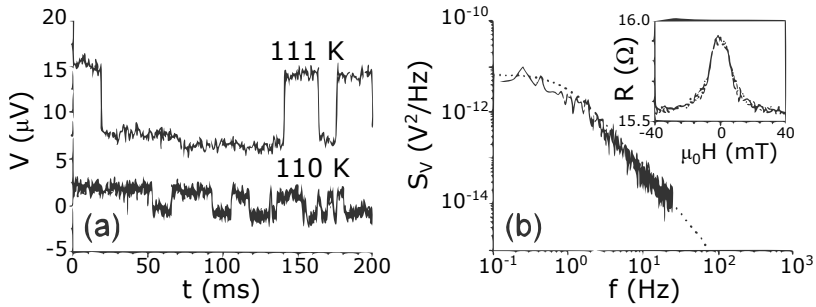

Figure 1.26: Typical RTN a) time trace with step-like fluctuations and b) a Lorentzian noise spectrum, fit with equation 1.32 calculated from the up and down lifetimes. Figure adapted from ref.[76]

We are going to address now the subject of organic spintronics, which is the other type of samples measured during this thesis. Hereafter we will describe the theory of electron tunneling through organic barriers as well as the resulting noise fluctuations. To clarify the reader, in the following part we don't have coherent tunneling because the layers are not epitaxially grown, and all of the samples under study have an organic **P**erylene**t**etra**c**arboxylic **di****A**nhydride $C_{24}H_8O_6$ (PTCDA) barrier sandwiched between two FM. Regarding the application of the external magnetic field, we have made only studies changing the magnetization of the FM from parallel (P) to anti-parallel (AP) (in-plane) magnetic configurations.

1.6. Organic spintronics

In this section we are going to study the role of the barrier in MTJs when its made of an organic material, i.e. the so-called organic magnetic tunnel junctions (OMTJs). The concept of single molecules or small groups of them conducting electrical current originated in the seventies[78]. Currently organic electronics is among the most promising candidates to substitute traditional Si based electronics. General interest in organic semiconductors arouse because of their promising features, such as the capability to form self-assembled layers, mechan-

ical flexibility, lower fabrication costs or higher efficiency. Nowadays they are used in everyday technology as, OLEDs, OFETs, photovoltaic cells, etc.

Historically, the first step in the search of new materials suitable for organic spintronics at room temperature, a direct spin polarized injection regarding an organic semiconductor was made by Dediu *et al.*[79] using sexithienyl (T_6). The authors reported on having a strong magnetoresistance (up to 30%) on planar heterojunctions of LSMO/T_6/LSMO. These junctions have been grown using thick organic semiconductor barriers (about 150 nm thick) in order to avoid pinholes inside the organic barrier. Another early study from Xiong *et al.*[80] this time using Alq_3 as the organic spacer in LSMO/Alq_3/Co heterojunctions directly noticed that layers of Alq_3 below 100 nm thick present a linear IV response which is a clear sign of having pinholes inside the barrier. The authors report a 40% TMR value in thicker Alq_3 heterojunctions.

The solution for decreasing the thickness down to several monolayers of this organic heterojunctions came through the incorporation of an aluminum oxide buffer layer, by the hand of Santos *et al.*[81]. The authors studied the Alq_3 barrier thickness dependence of conductance using a thin (0.6 nm thick) Al_2O_3 buffer layer between the FM electrode and the organic Alq_3 spacer. The ultrathin Al_2O_3 layer avoided the creation of pinholes leading to a thinner but still good-quality barrier. A few years later, a similar study made by Schoonus *et al.*[82] corroborated the exponential dependence of the sample resistance with increasing thickness (see figure 1.27). Both studies[81,82] found a relatively small value of the TMR ($\sim$ 10%) in these samples made of a thin Alq_3 film deposited over a Al_2O_3 buffer layer.

A different route to avoid the pinhole formation in OMTJs is through the decrease of the lateral junction size. In that direction, Barraud *et al.*[83] found that by downscaling to nanosized junctions (see figure 1.28a) made of LSMO/Alq_3/Co may provide TMR values close to 300% (see figure 1.28c). The thickness Alq_3 spacer was controlled by a nanoindent made in the Alq_3 performed with a conductive tip AFM allowing the thickness control (see figure 1.28b). In this work[83] the authors suggest the possibility of studying the role of the organic

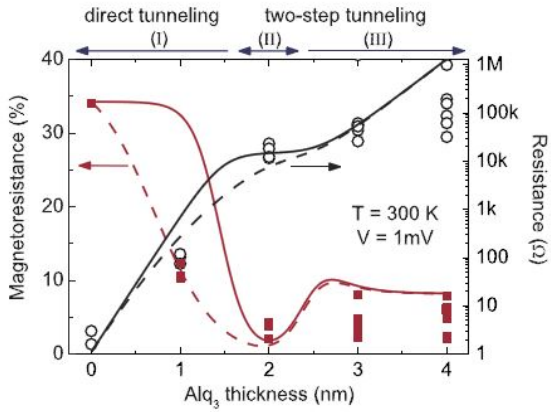

Figure 1.27: Room-temperature resistance (circles, right axis) and TMR (squares, left axis) for variable Alq_3 thicknesses. Dotted and full lines are models taking into account hybridization of the Alq_3/Co interface. Figure adapted from ref.[82]

barrier in the junction magnetoresistance through inelastic electron tunneling spectroscopy (IETS).

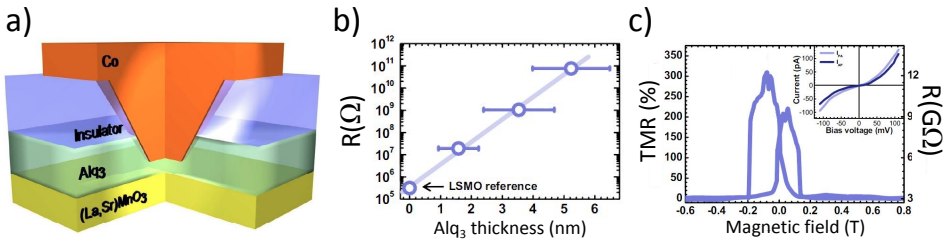

Figure 1.28: a) Schematic of the OMTJ. b) Sample resistance vs. Alq_3 thickness showing an exponential dependence. c) TMR vs. applied field measured at 2 K and 10 mV. The inset IV curves were recorded at 2 K in the P and AP states. Figure adapted from ref.[83]

1.6.1. Vibrational spectroscopy

It is known that electrons tunneling through organic barriers loose some energy during the process generating molecular vibrations called phonons. These interactions can be studied with IETS yielding the spectra of the molecular adsorbates with high resolution and high sensitivity. Due to that it has proven to be an effective tool to characterize the quality of a molecular barrier.

The work presented by Galbiati *et al.*[84] address the investigation of transport through molecules by a combined TMR and IETS study. This time the authors use a $Co/Al_2O_3(2.5\ nm)/Alq_3(20\ nm)/Co$ junctions ($100 \times 100\mu m^2$ size) to sort out if the effective spin dependent transport is carried out by the organic spacer or not, comparing their results with short-circuited junctions fabricated on the same wafer.

The value of TMR$\sim$ 20% (see figure 1.29b) in the reference sample confirms the quality of the Al_2O_3 barrier. The value of TMR$\sim$ 8% (see figure 1.29a) in the sample with the Alq_3 barrier however doesn't clarify the question whether the MR signal comes from the organic or from the inorganic spacer. To verify this point, the authors adopt the IETS technique (see figure 1.29c) where one can relate the peaks observed in the second derivative of the current (d^2I/dV^2) signal to the molecular vibrations exited by the electrons tunneling through the barrier. The comparison between the reference sample and the sample with the organic Alq_3 barrier clearly show peaks which are only visible in the Alq_3 one. Moreover those peaks are identified (see figure 1.29c) comparing them to the infrared and Raman spectra of Alq_3. Thereby, IETS allows to make a fingerprint of the transport through molecules inside each junctions[85,86].

To further confirm that IETS is a powerful tool to discriminate between spin injection into the organic layer and an inorganic shot-circuited contact, in this same paper[84] the authors fabricated another sample "sample 2"(see figure 1.30c) which was located during the growth nearby "sample 1" in the same wafer and presents the same structure and both have been grown exactly under the same conditions.

Even though TMRs from sample 1 (figure 1.29a) and 2 (figure

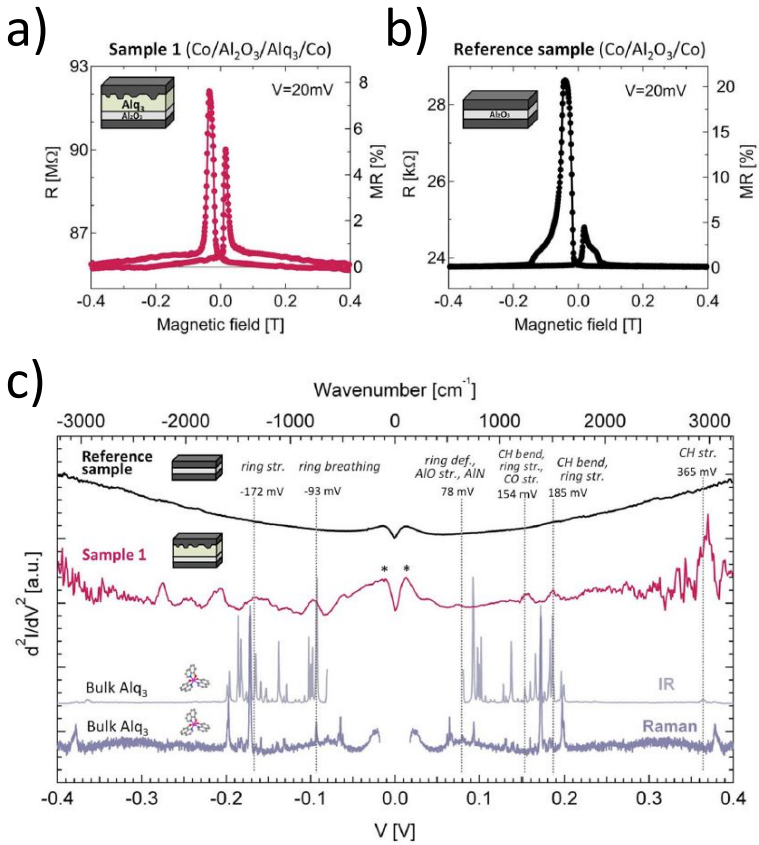

Figure 1.29: TMRs taken with V=20 mV of the sample with the organic barrier named sample 1 a) and the reference sample b), the insets show a schematic representation of the junction with the expected morphology of the top interface. Part c) compares the IETS of both samples showing the correlation of the IETS peaks with the bulk Alq_3 Raman spectra. Measurements were made at 2 K. Figure adapted from ref.[84]

1.30b) might look similar, their IETS (figure 1.30a) plainly displays a totally different behavior.

It is increasingly clear that, although the structural details of organic interfaces are rarely known, they play a critical role for the

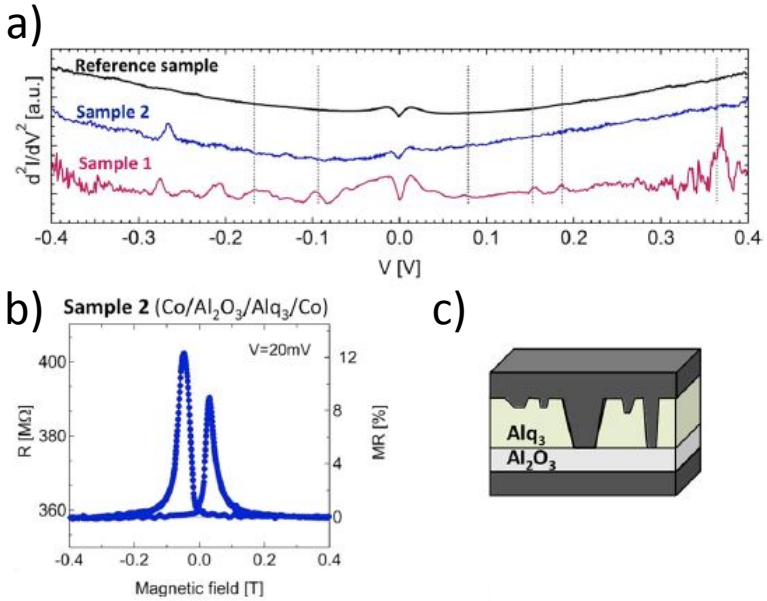

Figure 1.30: Part a) shows the comparison of the IETS curves for samples 1, 2 and reference. Part b) shows the TMR of sample 2 taken with V=20 mV. Measurements were made at 2 K. Part c) shows the sketch of the sample 2 with the pinhole structure. Figure adapted from ref.[84]

injection and extraction of charge carriers and for the resulting TMR. The theoretical model from Shi *et al.*[87] demonstrate the experimentally observed rapid decrease of the TMR in an organic spin valve with increasing applied bias in addition to relating short range tunneling process in thin films, which is very sensitive to details on the organic DOS, with a macroscopic device model.

1.6.2. PTCDA organic barrier

So far the reader should have noticed the general use of Alq_3 as the organic spacer in researches. Here we explain why PTCDA has replaced Alq_3 as the ideal molecule to conform the organic barrier in OMTJs.

Many investigation regarding organic spintronics have attempted to insert thin insulating layers (e.g. Al_2O_3) between the organic and the FM layers to improve the spin injection efficiency[81,88,89]. However, such insulating layers give rise to a measurable TMR becoming effective tunneling barriers on their own (see TMR in figure 1.27). We aim to study the spin transport mechanisms through organic layers without any other effective barrier influence. Although initial organic spin valves that achieved measurable TMRs used thick Alq_3 layers, other organic layers were being exploited and PTCDA was beginning to show success in conforming organic thin-film transistors and organic LEDs presenting good adhesion and small roughness when deposited on chosen substrates[90]. In the work presented by Li *et al.*[91] the authors report a TMR ratio of $\sim$ 20% with a 1.25 nm thick PTCDA barrier.

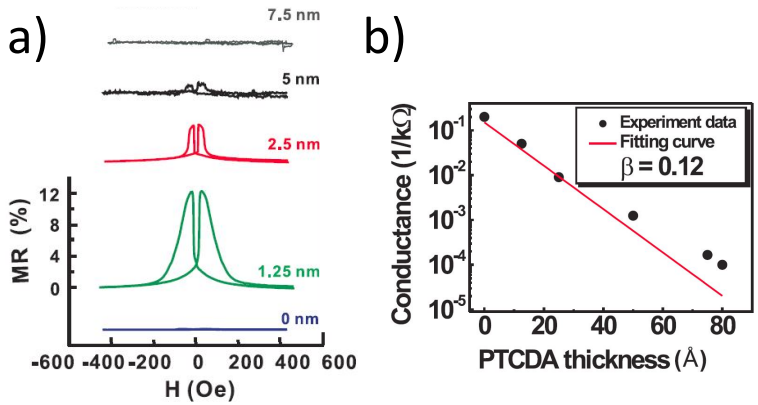

Figure 1.31: Part a) shows the TMR curves dependence on the PTCDA thickness measured at room tempreature. Part b) shows the junction conductance vs PTCDA thickness showing the characteristic exponential behavior. The PTCDA barrier was grown over the AlO_x layer. Figure adapted from ref.[91]

At the interface between the organic PTCDA layer and the FM electrodes of either side, a thin AlO_x layer was made by partially oxidizing an aluminum layer in an oxygen plasma. As is well known, the metals are likely to react the anhydride (C-O) end groups of

the PTCDA molecule resulting in the formation of a mixed oxidation layer[92]. The AlO_x layer is the key point in suppressing pinhole formation at the interface with both FM layers as well as not showing any TMR ratio when there is no PTCDA spacer (see figure 1.31a). This is an indication that the partially oxidized Al layer alone do not act as an effective spin-transport barrier for the 0.6 nm thick AlO_x selected[91]. In addition to that, the constant slope of the junction conductance as function of the PTCDA thickness implies that the probable diffusion of metallic Al on the PTCDA layer, which the authors calculate a maximum reach of 2 nm, have a very small influence on the junction conductance of the spin valve.

1.6.3. Studying molecular dynamics through LFN

Another possible tool of characterization of interfacial molecule dynamics could be LFN.

The motion of organic adsorbates on a surface may lead to fluctuations or switching of the tunneling current. Many studies[93,94] focus in the motion of particles on a surface induced, for example, by thermal activation or by the interaction with the tip of a scanning tunneling microscope (STM). These analysis give insight into dynamics on a single atomic or molecular level but are not normally a useful tool to study dynamics in detail, as STM is intrinsically a slow technique. With the study of LFN, for example, with the characterization of RTN in the signal one could measure the hopping rate, the noise amplitude and the relative occupation of the involved states in single-molecules. In particular, Schaffert *et al.*[95] presents a complete constant-current image of several isolated copper phthalocyanine molecules (CuPc) on Cu(111), ranging from dynamical processes on surfaces to the underlying electronic structure on the single-molecule level. Another study presented by Tsutsui *et al.*[96] makes molecular imaging by measuring the current passing through a molecule, this time its a 1.6-hexanedithiol (HDT) molecule, which is trapped between two Au nanoelectrodes. In this study the authors calculate the effective temperature due to phonon vibrational heating of the molecule using different LFNs, $1/f$ and shot-noise.

Exciting molecules by applying bias induces molecular dynamics which could appear in the form of either vibrational heating or even cooling[86] (local heating/cooling). Those effects remain totally unclear in the case of OMTJs, particularly how the magnetic state of the electrodes could affect molecular vibrational dynamics.

In order to get inside this problem we shall use both tools LFN and IETS to characterize the electron tunneling mechanisms in Perylenetetracarboxylic dianhydride (PTCDA) molecules conforming the barrier of a organic spin-valve (chapter 5). Moreover we will study the magnetic control of over vibrational heating of these molecules by changing the magnetic state of the FM electrodes.

Summarizing the introductory chapter, first we have briefly described the general physical electron tunneling mechanisms regarding magnetic tunnel junctions (MTJs). Second, we have addressed the subject of superconducting spintronics starting with coherent tunneling in epitaxial heterojunctions and explaining how SOC affects the FM electrode's magnetization. Then we have introduced the concept of electronic noise and the different types of LFNs as they are one of the tools we use to measure the MTJs. Finally we explained the other main subject of this thesis which is organic spintronics. With this we conclude the introduction and go to the experimental set-up description in the next chapter.

Chapter 2

Experimental techniques

In this chapter we will describe the different experimental techniques we used to perform the different experiments which mainly have to do with measuring DC voltage versus current (IV curves) and measuring voltage fluctuations (electronic noise) in MTJs. The existent set-ups have been described in detail in the PhD theses of the previous students of the group[97, 13, 2] although during the fulfillment of this thesis, a new room temperature set-up was built. It follows exactly the same electronic schematic as the cryogenic one (described in figure 2.1). One of the purposes of this new set-up is to measure MTJs at room temperature easier than in the cryogenic set-up which is very convenient for example for testing the quality of a MTJ before mounting the samples on the cryogenic system, or, when a measurement involves applying an external magnetic field, the fact that the cryogenic magnetic coils (made of Nb-Ti) are not prepared for working over their critical temperature, etc. Nevertheless the main body of this thesis is still related to cryogenic experiments.

In addition to all the cryogenic set-up configuration the previous PhD students made, there was (and still is) a lot of room for improvement. Automation of an experiment is a basic problem in order to maximize the use of both time and resources. The following sections will briefly illustrate each of these experimental designs in detail, pointing out their improvements or modifications with respect to the

previous configuration. A good example of one of the improvements made is related with the IV curves measurements which have been made much more detailed in this thesis than in the previous ones. We realized that we had to select a fixed range of precision in both the current source and the voltmeter in order to avoid artificial peaks appearing in the conductance appearing always at specific biases when one of the devices had to change its range in order not to overload. This adjustment is not necessary if the selected step of the IV curve is much broader than the minimum step a particular range of the device is capable of.

As important as the experimental tools are the computer programs of analysis to extract the parameters of interest for each particular measurement (Hooge factor, Fano factor, IETS peaks, etc.). A big amount of time has been spent developing and improving the analysis procedures.

2.1. Modeling the low frequency set-up

We are going to describe the set-up system for measuring the drop of voltage across a MTJ as well as the spectral density of the voltage fluctuations as a function of the applied current, the external magnetic field or the temperature, the latter just in the case of the cryogenic system.

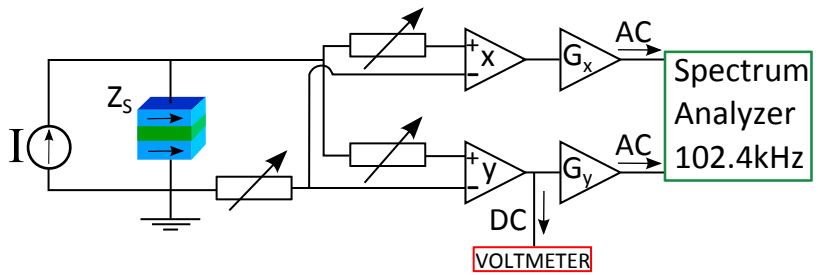

Figure 2.1: Circuit schematic of the low frequency measurement system. Figure adapted from ref.[13]

The experiment consists in measuring a MTJ which has 4 terminals, 2 for running the current through it and 2 where the voltage is read. Both the room temperature set-up and the cryogenic one have the same electronic diagram (figure 2.1), the electron current is supplied by either a Keithley 220 or a Keithley 6221 low noise current sources, this current produces a voltage signal (DC voltage + fluctuations) which is first duplicated and amplified by two nearly identical homemade preamplifiers (design and specifications in ref.[97]). Then, the voltage is registered by a Digital Multimeter PCI Board (DMM-552-PCI) from one of the channels. Each channel, denoted by X and Y, is then amplified a second time by Stanford Research SR560 commercial amplifiers, which additionally filter out the DC part of the signal. These amplifiers also have a bandpass filter with a range from 0 Hz to 1 MHz. Finally both signals, each containing a two-stage amplified and filtered signal, are sent to a Stanford Research SR785 spectrum analyzer which as a bandwidth up to 102.4kHz.

By configuring the amplification gains and filters identically, to the spectrum analyzer will reach two signals which are nearly identical but independent from one another, both channels containing the sample noise signal δV_{R_S} plus a random noise δV_{amp} due to the amplification and filtering stage. The noise due to the electronics of the voltage measuring part is of the same magnitude for both channels but the noise of one channel is uncorrelated (independent) from the noise in the other channel.

Let us model the noise contribution of the amplifying circuit. We consider the voltage and current noise of the preamplifying stage only, since the signal reaches the second amplifying stage with enough amplitude so that the noise from the second amplifiers may be disregarded. The preamplifier is considered to have voltage e_N^2 and current i_N^2 noise sources, so $\delta V_{preamp} = e_N^2 + i_N^2 Z_S^2$, where Z_S is the sample impedance. We will not consider the noise coming from the current source for two reasons: First because we will subtract the value of the power spectral density at zero bias when analyzing the measurement data and second because the current sources has a $1/f$ type of noise, comparing the values given by the manufacturers with the measured noise power, the measurements of our samples have higher noise (sev-

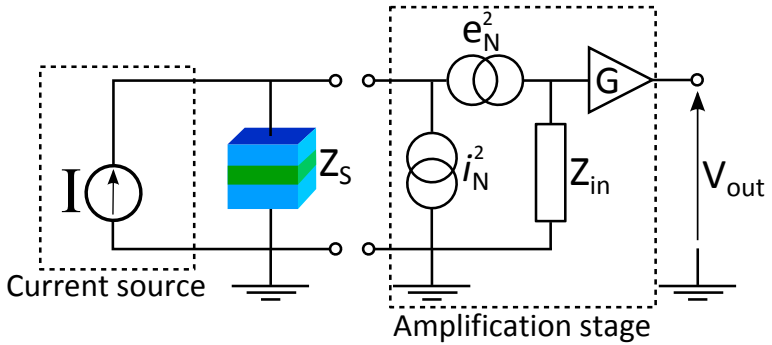

Figure 2.2: Model of the noise sources from the amplifying circuit. Figure adapted from ref.[97]

eral orders of magnitude). Therefore, the circuit is modeled as shown in figure 2.2, where (from left to right): The current source sends a 'noiseless' current to the sample under study (Z_S), then, connected in parallel to the sample is the preamplifier, which has voltage and current noise sources and an input impedance Z_{in} and finally G represents an ideal and noiseless amplifier, containing both the preamplifier and commercial amplifiers gain.

Considering the preamplifiers from both X and Y channels to have the same i_N^2, the total fluctuations reaching the spectrum analyzer will be:

$$S_V = e_{Nx}^2 + e_{Ny}^2 + \delta V_{Z_S} + 2i_N^2 Z_S^2 \tag{2.1}$$

It its clear that the only uncorrelated noise is the noise coming from the sample (δV_{Z_S}), thereby to avoid the correlated noise we use the cross-correlation technique (next subsection). The details of how equation 2.1 is derived and the features of the preamplifier electronics can be found in Ref.[97].

2.1.1. Cross-correlation

The *cross-correlation technique* is, in signal processing, a measure of similarity of two series as a function of the displacement of one rel-

ative to the other. It has applications in pattern recognition, electron tomography, averaging, cryptanalysis, neurophysiology and our case, single particle analysis.

The spectrum analyzer can be configured to directly measure the cross-spectrum (or cross-correlation spectrum) of the two signals $X(t)$ and $Y(t)$ (equation 1.13). Each of the two channels previously mentioned contains the signal of interest V_{Z_S} and the voltage noise of its preamplifier, i.e. $X(t) = V_{Z_S} + X_{pre}(t)$ and $Y(t) = V_{Z_S}(t) + Y_{pre}(t)$. Where X_{pre} and Y_{pre} are independent (uncorrelated) from each other. Thus using 1.13:

$$R_{XX}(\tau) = \lim_{T\to\infty} \frac{1}{2T} \int_{-T}^{T} (V_{Z_S} + X_{pre}(t))^* (V_{Z_S}(t+\tau) + Y_{pre}(t+\tau)) dt =$$

$$\lim_{T\to\infty} \frac{1}{2T} \Big(\int_{-T}^{T} V_{Z_S}^*(t) V_{Z_S}(t+\tau) + \cancelto{0}{\int_{-T}^{T} V_{Z_S}^*(t) X_{pre}(t+\tau)} +$$

$$\cancelto{0}{\int_{-T}^{T} X_{pre}^*(t) V_{Z_S}(t+\tau)} + \cancelto{0}{\int_{-T}^{T} X_{pre}^*(t) Y_{pre}(t+\tau)} \Big)$$

the only nonzero term is the $V_{Z_S}^*(t)V_{Z_S}(t+\tau)$ which is the only term containing only the voltage fluctuations of the sample without any influence from the electronics.

The spectrum analyzer used in the experiments obtains the cross-spectrum, which is given by:

$$\mathcal{F}\{R_{XY}\} = (\mathcal{F}\{X(t)\})^* \cdot \mathcal{F}\{Y(t)\} \tag{2.2}$$

Additionally, the final spectrum measurement is improved by averaging many cross-correlation spectra at each voltage. This procedure reduces the variance of our measurement by $1/N$ (the deviation as $1/\sqrt{N}$), with N the number of averages. The number of averages is chosen so obtaining one averaged spectrum dos not take more than a few seconds, as the time T for taking one average is given by the Δf and f_{max} settings of the spectrum analyzer (see subsection 1.5.2).

The simplest way to check the correct calibration of the setup is by measuring the thermal noise of a resistor. With this procedure we

calibrated the gain values of our homemade preamplifiers, moreover it has been for few years now a lab activity made by undergraduate or master students to estimate the value of Boltzmann's constant. Figure 2.3 shows how a good estimation of k_B can be obtained from the slope of S_V *vs.* RT for just a few resistors.

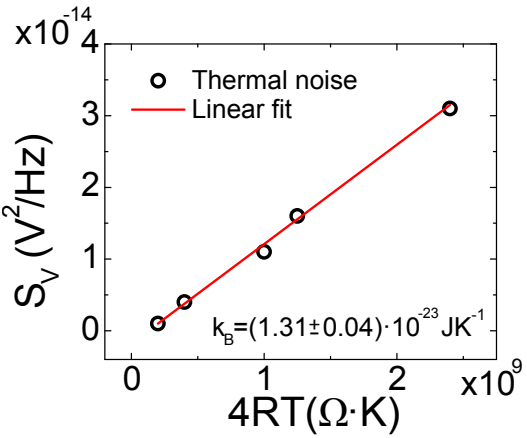

Figure 2.3: Estimation of k_B from the thermal noise of several resistors at room temperature. Figure adapted from ref.[2].

2.2. Room temperature set-up

The aim of making a room temperature set-up (very similar electronically to the one described in figure 2.1) is to simplify the measurement procedure. In the cryogenic set-up it takes about a week to change the samples inside the cryostat due to the time spent in heating up and cooling down. In this set-up one can change the sample in several minutes. The room temperature set-up (figure 2.4) has an add-on which consists in another cylindrical vacuum tube which has an optical window right above the sample position to allow the illumination of the sample. Currently is the only system in our laboratory that combines the LF noise measurements with the illumination in vacuum

conditions. It has been used to measure noise under photo-doping condition in MoS_2 transistors[98], to pre-test samples before putting them inside the cryostat set-up or to measure them at room temperature, and to make the previously mentioned lab activity for master students estimating the Boltzmann's constant.

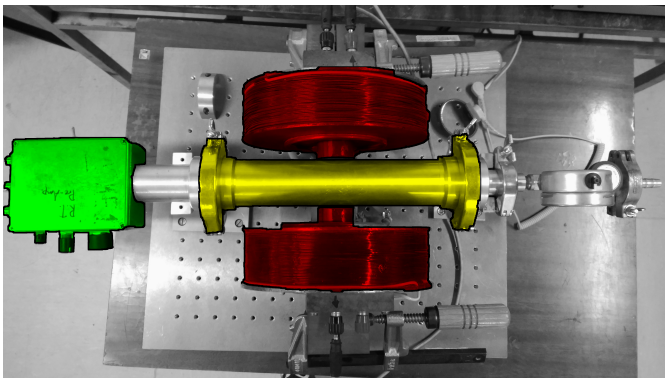

Figure 2.4: Room temperature set up. Highlighted in red are the Helmholtz coils, in green the pre-amplifier and in yellow the vacuum chamber containing the sample.

2.3. Cryogenic set-up

Our cryogenic set-up consists on a Janis cryostat, which has an outer liquid nitrogen reservoir, and an inner liquid ^{4}He reservoir. A ^{3}He (closed-circuit) insert which allows us to cool down samples in vacuum down to $T = 0.3K$.

The basics of the cooling system is the **evaporative cooling**, which consists on reducing the temperature of a liquid by reducing the vapor pressure on top of that liquid. The nitrogen is used only for thermally isolate better the ^{4}He reservoir (and for pre-cooling down from room temperature firstly before siphoning liquid ^{4}He). Focusing in the two working substances (^{4}He and ^{3}He), ^{4}He boiling point is $4.2K$ and with evaporative cooling we decrease the ^{4}He liquid down below

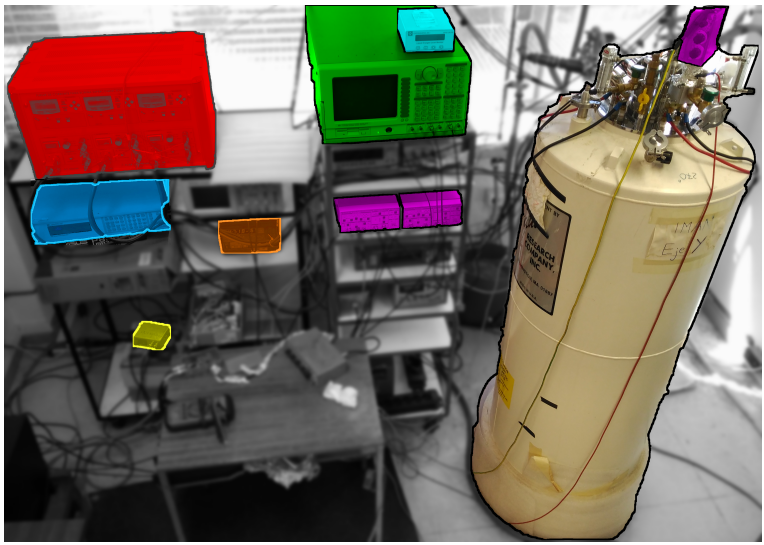

Figure 2.5: Cryogenic set up. Highlighted with its real color is the JANIS cryostat, in purple are the two-stage amplifiers, the 2 channel home-made amplifier is the one on top of the cryostat and one commercial amp. for each channel, in dark green is the spectrum analyzer; on top of it, in light blue, is the Helium level control, in red is the 3D vector superconducting coils current source, in dark blue is the thermometer, in orange is the low noise current source for the sample and finally in yellow is the ARDUINO board for remote control.

$2K$, then comes the part of the ^{3}He, whose boiling point is $3.2K$, and consequently is condensed by the ^{4}He at $2K$ surrounding it. When enough ^{3}He has condensed, an active carbon cryopump which is inside the ^{3}He closed-circuit pumps to make evaporative cooling (this time on the ^{3}He liquid) decreasing the temperature down to $T = 0.3K$.

The external magnetic field is applied to the samples in any direction of space by a 3D superconducting magnet (shown in figure 2.6), composed of a single coil for the Z-axis and two Helmholtz coils for the X and Y axes. The coils were calibrated at $T = 4.2K$ (submerged in liquid ^{4}He). The X, Y and Z axes can produce magnetic fields up to $B = 1T$, $1T$ and $3.5T$ respectively. The field vs. current calibration

can be checked in Ref.[13,2].

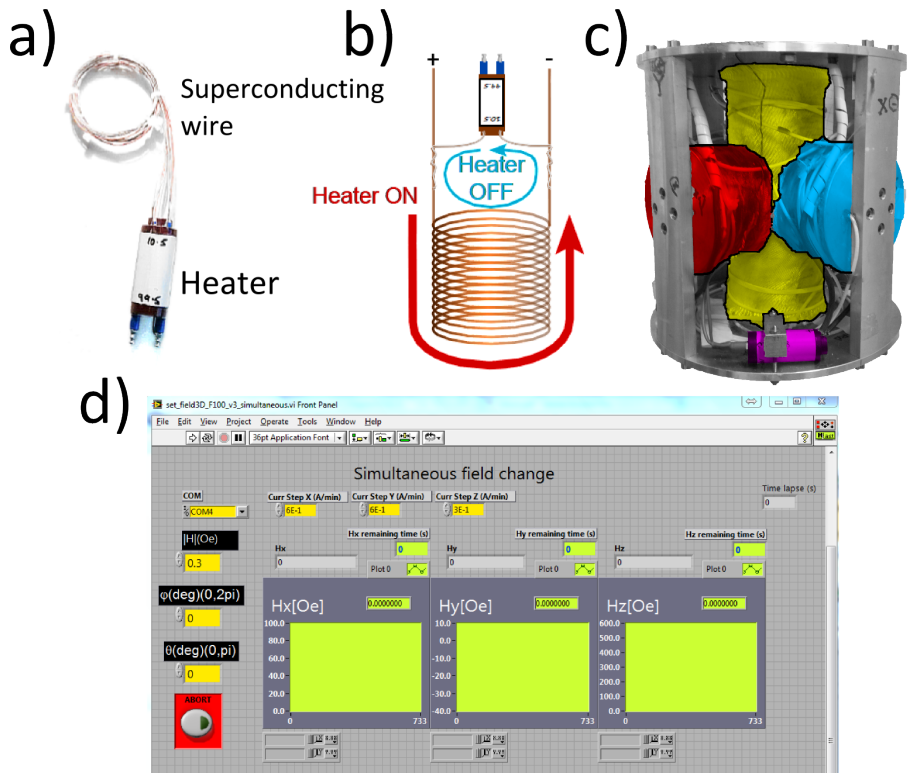

Figure 2.6: a) Photo of one of the superconducting shunts used. b) Electric diagram of the shunt thermal switch. c) 3D vector magnet. Highlighted in yellow is the Z axis 3.5T, and in red and blue are the Y axis and X axis 1T Helmholtz coils respectively. Highlighted in purple is one of the three superconducting shunts. d) LabVIEW window of the program controlling simultaneously the three current sources. Figure adapted from ref.[2]

There was an important modification made in the previous thesis[2] which is the addition of a superconducting shunt (heater) to each coil of the magnet. The function of each shunt is to connect or disconnect each coil to its current source electric circuit by a thermal switch, leaving a permanent electric current inside the superconducting coils.

This is very useful for experiments, in particular for noise experiments, due to the intrinsic electronic noise produced by any running electronic device.

The last upgrade of the set-up is the sample holder. There are samples, in particular PTCDA samples, that should not be exposed to the atmosphere for long due to oxidation of the AlO_X layer (which degrades the sample). This required that the process of contacting them to the sample holder and then attach it to the cryostat must be made in the quickest way possible. With the new configuration of the sample holder, the process of attaching it to the cryostat has been reduced from several minutes (between 10 to 30 minutes) down to a simple *plug-and-play* procedure.

2.4. Automation and remote control

Starting from the developments made by former phD students, in this thesis we have upgraded the cryogenic set-up. Let's address a list of the set-up former issues and the given solutions:

- ✗ Previous to this thesis the 3D vector superconducting magnet had only been used in one direction (Z axis coil in figure 2.6).

- ✓ We have developed a software that controls simultaneously (see figure 2.6 d) the three current sources and ables us to rotate the magnetic field in any direction of the space. Moreover, we chose spherical coordinates to work with because they are more straightforward to our experiments, thus our software directly transform them to the components of each superconducting magnet coil. In addition to this, we take into account possible misalignments between the sample and the 3D superconducting magnet orientation.

- ✓ The thermometer was fully remote controlled already, but some functionalities were not programmed such as automatic cryogenic pump cycle in order to cool down to $T = 0.3K$.

✗ The low noise current source was not used to its full precision. The precision of a current source is the minimum current step the device can vary at a given current range.

✓ In this thesis we have exploit to its maximum the precision of each device. Briefly said, each device's precision depends on the working range selected for the device, if one wants to use a device to its maximum precision the device's range must be adjusted. In the case of the low noise current source in particular the current step also must be adjusted. To further illustrate the importance of this, we acquired a new PCI multimeter card replacing the previous voltmeter (DT330 acquisition board) because its precision limit was not good enough for our purposes.

✗ Finally, there was an issue regarding the fact that our experiments, in particular the noise experiments, are extremely sensitive to electronic noise. All devices produce undesired electronic noise just by the fact of being running, thereby they were, if possible, turned off during experiments. A good example is experiments made with a fixed external magnetic field. As explained above, we can left a constant external magnetic field and switch off the superconducting magnet current source but when we want to make another experiment at a different magnetic field, we need to turn on this current source, change it and switch it off again.

✓ This had to be made by hand until we acquired an ARDUINO board (see figure 2.5) which controls remotely two relays, one switches the 3D magnet current source, and the other the thermometer. Now the student can switch these two devices remotely which has vastly improved the schedule and productivity of the experiments.

2.5. Safety

We have made a small improvement to the cryostat set-up regarding the safety and efficiency of the helium siphoning procedure. Generally cryostats must be often refilled with liquid helium in order to maintain their functionalities, the frequency of this refillings varies from hours to several days depending on their configuration and/or the measurements taking place. In this particular cryostat, the ^{4}He reservoir is closed by a cap (see figure 2.7a). At one point during the siphoning process one must remove the cap and insert the siphon tube. By removing the cap we open the ^{4}He reservoir to the atmosphere therefore the higher pressured ^{4}He evaporated gas will flow out. It is compulsory to wear protection gloves during the siphoning process, however protective gloves reduce the user precision needed for hitting upon the small conduct accurately with the siphon tube, for this reason experienced researchers usually don't wear gloves.

With the new configuration (shown in figure 2.7b) we highly cut down the ^{4}He leakage because the valve is closed while removing the cap and is opened only when the siphon tube is in fact inserted. This avoids ^{4}He to leak out of the reservoir improving the efficiency of ^{4}He losses in addition to avoiding burning injuries (shown in figure 2.7c) which are likely to happen in these type of research laboratories where usually a new inexperienced phD student replaces the experienced old one every few years.

It is of utmost importance to know that the cap is one of the security gas exits of the He reservoir. It will pop out if the inside pressure rises above a threshold level, thereby it is essential that the new security system remains with the valve open at all times besides the siphoning process.

2.6. Data analysis and simulations

The analysis of the experimental raw data provides the information needed to characterize the samples measured, i.e. the conductance curve, IETS, critical temperature, Hooge factor, Fano factor, etc. The

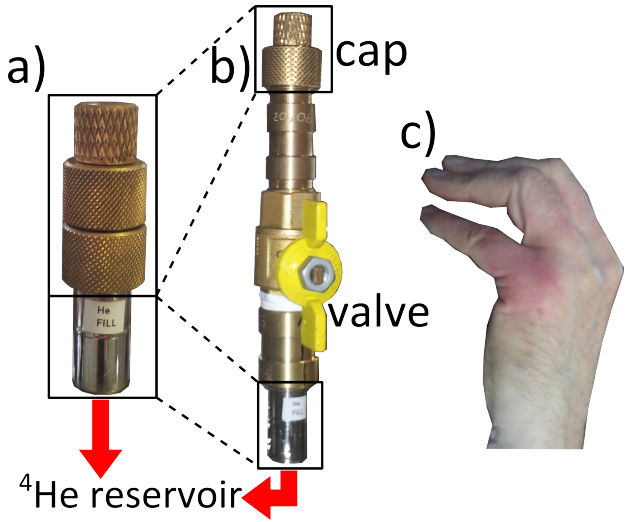

Figure 2.7: a) Previous configuration (simple cap). b) Current configuration (valve + cap). c) Example of a burn made by the cold He gas stream while siphoning.

process of analysis depends on the information we want to obtain and in can have several steps depending on its complexity, i.e. in order to get the energy gap of our superconducting samples, before fitting to the model (equation 1.9) we need to calculate the conductance of the IV curve.

2.6.1. IV curve analysis

The main goal of this measurement is to obtain the conductance of the sample $G = \frac{dI}{dV}$ and the second derivative which provides information about inelastic tunneling mechanisms $IETS = \frac{d^2I}{dV^2}$.

The analysis process begins reading the raw data of the bunch of IV curves measured. After cleaning each IV curve or even deleting some if needed, to derivate each IV curve we use the linear fit (the user selects the amount of points to fit) method which ables us to

derivate and smooth the derivative in the same step. Then we average all the bunch of IV curves and get a single averaged IV curve, its conductance and its IETS.

In the case of study of phonon modes, we then overlap the positive bias part of the conductance (or the IETS) with its negative bias part, to see which modes match and therefore extract the vibrational phonon modes resonant energy.

The course of action has been taking the necessary number of IV curves according to the noise of the sample. The tolerance has been chosen as roughly to get the standard deviation of each voltage point, when the IV curves are averaged, to be a few orders of magnitude lower than the actual voltage value. If a particular study needed more resolution then more IV curves were taken (i.e. in IETS measurements). Each IV curve voltage point was taken after waiting almost 1 or 2 seconds (depending on the voltage step) in order to steady the system after the change of current. Mainly, a single IV curve was selected to last for 2 and a half hours.

2.6.2. MAAR analysis

The magnetoanisotropic Andreev reflection (MAAR) is measured rotating the external magnetic field with the aim of rotating the magnetization of the soft ferromagnet maintaining the hard one fixed. As we have mentioned, there may be some misalignment between the sample and 3D superconducting magnet directions. Measuring this misalignment angles is easy because any perpendicular component of the magnetic field in the superconducting sample affects greatly the superconductivity more than any in-plane field.

To introduce this misalignment in the spherical coordinates given to the current source program, we must beforehand make an Euler angular transformation. Due to our sample's crystallographic symmetry, from the three Euler angles, in aircraft terminology: roll, pitch and yaw, we are only going to consider the out-of-plane angles (with respect to the sample) which are the pitch and yaw (see figure 2.8).

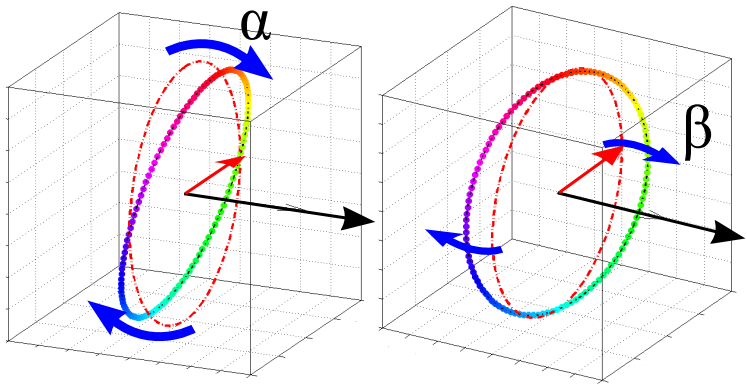

Figure 2.8: Misalignment angles, pitch (α) and yaw (β). The sample plain is rotated from the initial (full-red dashed line) to the corrected one (multicolored dotted line). The black and red arrows are just a guide for the eye referred to the initial plane.

2.6.3. $1/f$ noise analysis

As has been mentioned in section 1.5.5 the $1/f$ noise is described by the Hooge phenomenological function 1.30. From the cross-correlated spectra (raw data) we have:

$$S_V(f) = \frac{\alpha V^2}{A f^\beta} \Rightarrow log(S_V(f)) = log\left(\frac{\alpha V^2}{A}\right) - \beta log(f)$$

so making a linear fit $y(x) = mx + n$ to the logarithm of the power spectrum (where $x = f$), $\alpha = Ae^n/V^2$ and $\beta = -m$. Each parameter is obtained with its standard deviation.

The range of frequencies for which the fit is carried out is user-selected beforehand (see figure 2.9b). Also, the band-pass filtering made by the SR560 amplifiers is undone by dividing the spectra by the filter's transfer function. For this, the high-pass and low-pass cutoff frequencies must be inserted in the analysis program as well. The spectra is cleaned from unwanted peaks (i.e. from the power grid 50Hz and its multiples). In order to do that, the lowest bias spectra is displayed (see figure 2.9a) because the intrinsic peaks coming from

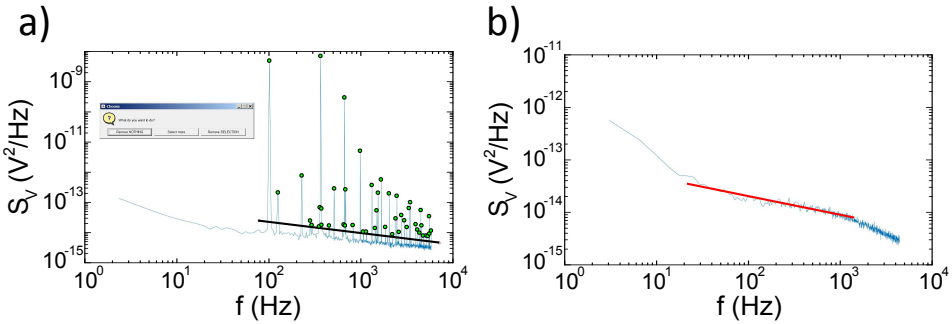

Figure 2.9: Example of a Hooge analysis of a $1/f$ bias dependent measurement. Part a) shows the zero bias noise spectrum from where the electronic circuit peaks will be removed (**green** points) manually by the user drawing a **black** line. Part b) shows a specific bias noise spectrum where the linear fit (red line) will give a value of the Hooge parameter (α). We also check that β is close to 1.

the electronic circuit will be best distinguished when bias dependent noise sources are negligible. The user manually draws a line (black line on figure 2.9a) and all the undesired peaks above (green points) will be automatically removed from the spectrum's data. An example of a successful fitting (red line) is shown in figure 2.9b.

2.6.4. Shot noise analysis

For spectra presenting a frequency independent region (i.e. flat power spectrum), we have two different options for extracting the value of shot noise.

If the spectrum has at low frequency a $1/f$-like behavior and is frequency independent at higher frequencies, we can make a similar study as the $1/f$ analysis:

$$S_V(f) = \frac{\alpha V^2}{A f^\beta} + S_V^{white}(f)$$

where S_V^{white} corresponds to the white noise (shot noise and thermal noise). If we take $\beta = 1$, a fit of the type $y(x) = a/x + b$ yields

$\alpha = aA/V^2$ and $b = S_V^{white}$. An example of this fitting is shown in figure 2.10a.

Another alternative it to calculate the histogram of the spectrum. Since the flat part of the spectrum oscillates around the value corresponding to the white noise amplitude, the resulting histogram is a Gaussian curve centered at S_V^{white}. By fitting the histogram with $y(x) = A \exp -\frac{(x-x_0)^2}{\sigma^2}$, the white noise amplitude is given by x_0 and its standard deviation by σ. An example of this fitting is shown in figure 2.10b.

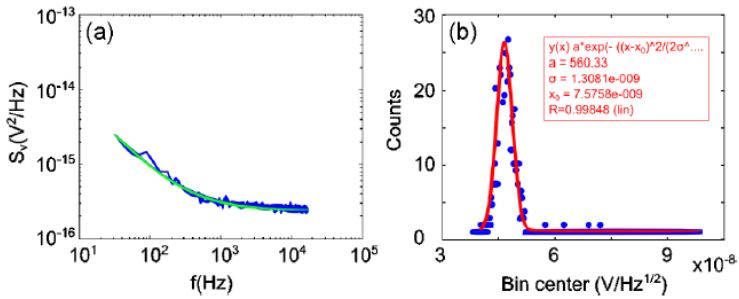

Figure 2.10: Fit of a) Hooge's formula to a spectrum presenting $1/f$ and white noise and b) a Gaussian distribution to the histogram of a flat spectrum presenting shot noise only. Figure adapted from ref. [2]

When we are at low temperatures ($T = 0.3K$) thus $eV \ll k_B T$, then the white noise obtained corresponds to the shot noise from the sample, plus some electronic noise from the experimental setup. Assuming the latter noise contribution constant with the applied bias, we extrapolate the value of noise from the electronics from shot noise measurements. The shot noise must scale linearly with the voltage (eq. 1.22), and must be zero at zero bias. So the noise from the electronics is estimated as the offset which must be subtracted so the noise level at zero bias is zero corresponding to the shot noise behavior. For higher temperatures, also the thermal noise is subtracted from the measurements using again relation 1.22.

2.6.5. Random telegraph noise analysis

As has been described in section 1.5.8 the analysis of the RTN noise consists in fitting the spectra to the Lorentzian function 1.32. The parts of a spectrum that we want to localize are the one showing a humped slope (see figure 2.11).

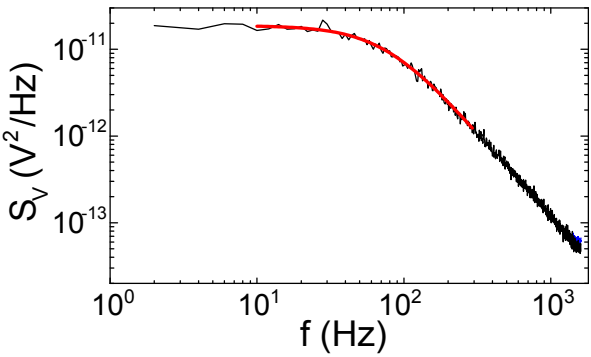

Figure 2.11: Example of a RTN analysis on a specific bias noise spectrum. The humped slope (red curve) is fitted to the Lorentzian function 1.32 to extract the characteristic dwell times (τ_{up} and τ_{down}) and the voltage difference between the two levels (ΔV).

These humped parts of the spectra are selected either directly by the software-user or by a software function which searches for a concave behavior in each spectrum with a particular tolerance. Finally the selected hump is fitted to 1.32 extracting three parameters $\Delta V, \tau_{up}$ and τ_{down}, which are the voltage difference between the two-levels, and the characteristic dwell times of each level respectively. Usually τ_{up} and τ_{down} are similar so we represent the average value (τ) for convenience.

2.6.6. Micro-magnetic simulations

A new computer has been purchased in order to host a brand new TITAN X graphic card (GPU) courtesy of the NVIDIA corp. through their GPU Grant Program. This computer has been used to perform

the new micro-magnetic simulations using MUMAX3 code[99]. With the simulations we have reproduced the magnetic behavior of our 10 nm thick Fe layers conforming the V/MgO/Fe/MgO/Fe/Co multilayer superconducting MTJs. The complete description of the simulation method will be given in the next chapter.

Chapter 3

Normal state conductance and magnetic properties of fully epitaxial MTJs

In this chapter, we start with the original results of the studies made throughout this thesis. We are going to start with MTJs that have one of their electrodes made of Vanadium. Before delving into superconducting spintronics we shall discuss their normal state properties and the control we developed over the magnetization of the FM electrodes. Theoretical predictions straightforwardly relate magnetization orientation, SOI and superconductivity mediated by triplet cooper-pair generation in these type of epitaxial FM/SC junctions[45,52]. The Fe/MgO interfaces under study potentially fulfill the necessary conditions (10 nm thick Fe layer provides competition between magnetic anisotropies, Fe/MgO interfaces show strong SOI and presence of perpendicular to the plane magnetization) for having this type of superconductivity.

In order to independently study magnetization, in this chapter we will focus in normal state measurements (at temperatures above the critical temperature T_C of each sample) which will show only the effect of the magnetization reorientation while in the next chapter we will introduce superconductivity with lower temperature experiments

(below T_C).

After a brief introduction, we will explain the sample growth of the different types of junctions (single and double barrier). The double-barrier (with two FM electrodes) samples are highly sensitive to any change of the relative orientation between their two FM magnetizations. The single-barrier (with one FM electrode) samples however show the more subtle magnetoresistive effects due to the change of their FM magnetization orientation. We will explain the role of the perpendicular magnetic anisotropy (PMA) in the magnetization orientation of all the Fe layers and why having a thickness of 10 nm is optimum for our goals[100].

3.1. Introduction

Magnetic tunnel junctions (MTJs) form the fundamental building blocks of diverse spintronic applications, ranging from magnetic field sensors to spin torque oscillators. Recent trends in spintronics take advantage of the interface related perpendicular magnetic anisotropy (PMA) providing both large tunneling magnetoresistance (TMR), enhanced thermal stability[101], low spin torque switching currents[102,103] and record low lateral sizes[104].

The magnetization of thin FM films, is usually controlled by applying an external magnetic field. Because in our SC-MTJs we have SC layers and FM layers connected through 2 nm thick MgO barriers, we cannot separate the effect of actively controlling the FM magnetization without affecting the SC state at the same time. The solution to avoid using an external field to keep the magnetization aligned in a particular direction is to find the possible remanent (zero applied external field) magnetization configurations. These remanent magnetization states will show different interactions with the superconducting order parameter in the presence of a strong SOC in the FM without the effect of an active external magnetic field suppressing the SC.

Then, to be able to study independently the magnetic effects in FM films we have to work at a range of temperatures over Vanadium's critical temperature. We are going to study mainly two different of mag-

netization states, the in-plane states and the out-of-plane states. In order to do this we shall use the competition between volume/shape and surface anisotropies. The magnetization zero-temperature orientation of thin FM films depends on the film magnetic field history and is a result of the competition between their different magnetic anisotropies (volume/shape, surface, crystalline, etc.) which is normally expressed as a sum of the corresponding terms, $K_{eff} = K_V + K_S/t$ where t is the thickness of the FM thin film.

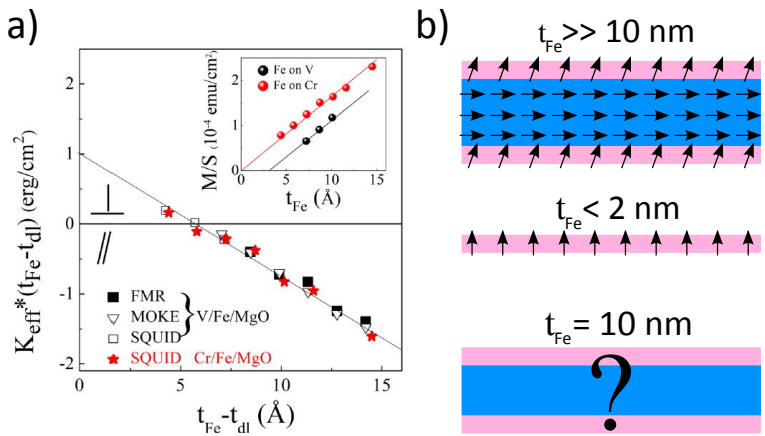

Figure 3.1: Part a) shows the effective anisotropy constant K_{eff} times $t_{eff} - t_{dl}$ as a function of $t_{eff} - t_{dl}$ deduced from SQUID-VSM, FMR, and MOKE measurements at room temperature for both V/Fe/MgO and Cr/Fe/MgO systems. In the inset are plotted the areal magnetization versus Fe thickness showing that $t_{dl} = 0$ for Fe on Cr and $t_{dl} = 3$Å for Fe on V. In part b) we show the magnetization orientation at different limits of the FM layer thickness and the specific case of study $t = 10$ nm (the question mark remarks the challenge of controlling FM magnetization). Figure a) has been adapted from ref.[105]

The investigation made by Lambert *et al.*[105] focuses on the study of this competition in Fe/MgO bilayers grown on top of different materials (V and Cr). When the Fe/MgO bilayer is grown on top of V it shows a deadlayer (not magnetically active) thickness ($t_{dl} = 0.3$

nm) in contrast to the Fe/MgO bilayer grown on top of Cr where ($t_{dl} = 0$) (see figure 3.1a). Essentially the competition between volume and surface anisotropy is calculated, and the authors conclude that the volume anisotropy (K_V) is small compared with the surface anisotropy (K_S) for the thicknesses considered ($t < 2$ nm). Because of this the magnetization of the films studied tend to stay naturally oriented out-of-plane (PMA).

Our Fe/MgO bilayers are made of a 10 nm thick magnetically soft Fe layer (see figure 3.1b) and therefore, further down in this chapter, we are going to study as well the competition between volume and surface anisotropies in section 3.4.3. Micro-magnetic simulations were made using MuMax3[99] taking advantage of the calculated parameters from ref.[105] in order to understand how can we control the remanent FM magnetization orientation applying an external magnetic field.

Now we continue the chapter with the description of the growth and normal state properties of SC-MTJs before the thorough study of the different possible magnetic configurations of the FM electrodes.

3.2. Sample growth and junction types

The fabrication of the epitaxial magnetic tunnel junctions with superconducting electrodes was carried out by the group of professors Coriolan Tiusan and Michael Hehn within a collaboration project between the Magnetrans-UAM group and the Institute Jean Lamour, Nancy Universitè (France). Details on the growth method (for a different type of samples measured also in this laboratory) are described in ref.[106].

The complete structures are, for the single-barrier samples (contacted layers in red):

- MgO(100) substrate/MgO(10 nm)/Cr(2 nm)/V(40 nm)/MgO(2 nm)/Fe(10 nm)/Au(15 nm)

and for the double-barrier samples:

- MgO(100) substrate/MgO(10 nm)/Cr(2 nm)/V(40 nm)/MgO

(2 nm)/Fe(10 nm)/MgO (2 nm)/Fe(10 nm)/Co (20 nm)/Au(15 nm)

- MgO(100) substrate/MgO(10 nm)/Fe(45 nm)/MgO (2 nm)/V(40 nm)/MgO (2 nm)/Fe(10 nm)/Co (20 nm)/Au(15 nm)

The MTJs were elaborated by molecular beam epitaxy (MBE) in a chamber with a base pressure of 1.33×10^{-10} mbar. The samples were epitaxially grown on (100) MgO substrates, previously annealed at 650°C 30 min.

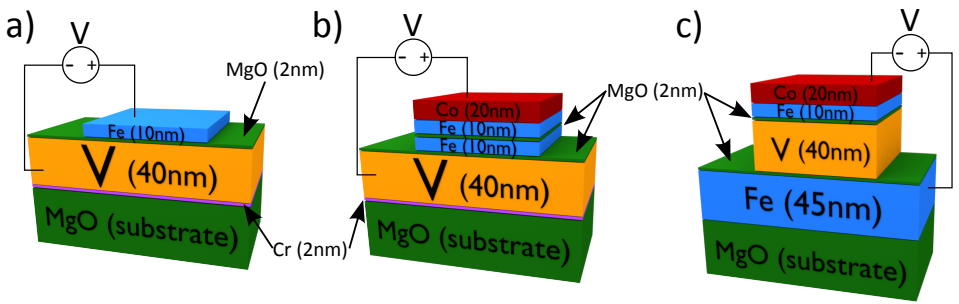

Figure 3.2: Realistic sketch of our SC-MTJs. a) SIF , b) SIFIF and c) FISIF layer configurations.

3.2.1. Single-Barrier junctions

Below we describe in more details the single barrier (SB) junctions. The mentioned first annealing stage (of the MgO substrate) does not completely remove the carbon impurities from the substrate. In order to trap the C on the substrate, a 10 nm thick seed MgO underlayer can be grown at 400°C on the substrate before the deposition of the 2 nm thick Cr layer deposited at 30°C. Then a 40 nm thick V layer is deposited at 28°C and is annealed at 400°C during 10 min and again at 500°C during 30 min to improve the surface quality. After this the 2 nm thick MgO barrier is grown with a Knudsen cell which slow down the deposition rate, from $\sim$ 1Å/s down to few monolayers per minute. In this regime, when growing the tunnel barrier, the thickness

is counted using reflectance high-energy electron diffraction (RHEED) intensity oscillations. Annealing improves the surface quality (see figure 3.3a) indicated as the full continuous lines, in contrast to a rough surface who would appear as dotted lines.

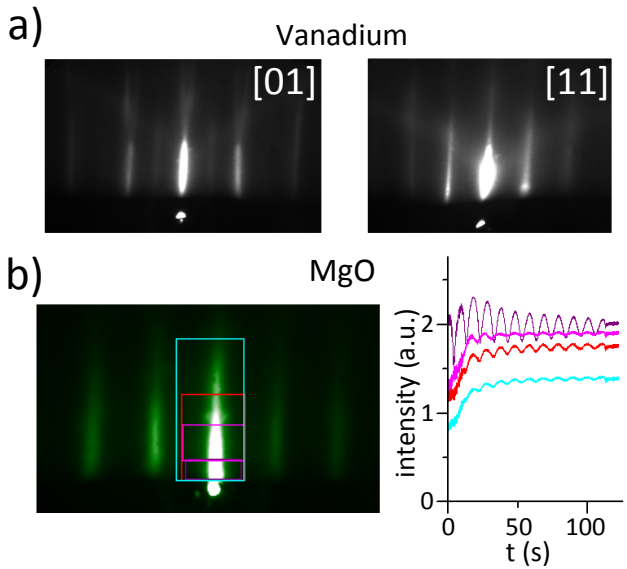

Figure 3.3: Sample growth data from SIF junctions. Reflectance high-energy electron diffraction (RHEED) measurements: a) after annealing the V layer at two different angles of the surface square lattice and b) after the deposition of the MgO insulating barrier. Figures by courtesy of C. Tiusan et al.[107], CNRS IJL Nancy/Technical University of Cluj Napoca.

Then the 10 nm thick Fe layer (soft FM) was grown on top of the insulating MgO barrier at 89°C, and afterwards annealed at 400°C for 20 min. Finally the MTJ stacks are capped with a Au protective layer 15 nm thick grown at 121°C.

The contacted layer configuration is V/MgO/Fe, and is referred to in this thesis as a superconductor/insulator/ferromagnet (SIF) junction (see figure 3.2a). In the particular cases where the experiments are made at temperatures higher than Vanadium's T_C the junction will be named **NIF** (normal-metal/insulator/ferromagnet).

3.2.2. Double-Barrier MTJs

We have measured two types of layered configurations in the double barrier (DB) junctions, one is the V/MgO/Fe/MgO/Fe/Co, which is referred to in this thesis as superconductor/insulator/ferromagnet/ insulator/ferromagnet (SIFIF) junction, and the Fe/MgO/V/MgO/ Fe/Co, which is referred to in this thesis as ferromagnet/insulator/ superconductor/insulator/ferromagnet (FISIF) junction. Again regarding the nomenclature, at above Vanadium's T_C measurements, the samples will be named **NIFIF** and **FINIF**.

Starting with the SIFIF sample, again after the 10 nm underlayer of MgO, a 2 nm thick Cr layer was deposited at 31.7°C, followed by a 40 nm thick V layer grown at 29.1°C. Then the sample is annealed at 500°C for 30 min, and again at 220°C for 45 min (RHEED patterns in figure 3.4a). After this, the first 2 nm thick MgO barrier is deposited (figure 3.4b) at 72°C, then the first 10 nm thick Fe (soft FM) layer is grown at 64.5°C and afterwards annealed at 400°C for 20 min (figure 3.4c). Now the second 2 nm thick MgO barrier is deposited (figure 3.4d) at 80.2°C. After this the second 10 nm thick Fe layer is grown at 72°C and annealed also at 400°C for 20 min. Then a 20 nm Co layer is grown at 97°C, conforming together (the Fe/Co bilayer) the hard FM. Finally the MTJ stacks are capped with a Au protective layer 15 nm thick grown at 80°C.

Ending the growth description with the FISIF sample, after the 10 nm underlayer of MgO, a 45 nm thick first Fe (soft FM) layer is grown at 29.6°C and annealed at 500°C for 30 min (RHEED patterns in figure 3.5a). After this the first 2 nm thick MgO barrier was deposited at 72.8°C (figure 3.5b) followed by the 40 nm thick V layer grown at 67.6°C. Then the sample was annealed at 450°C for 30 min (figure 3.5c). After this the second 2 nm thick MgO barrier was deposited at 106°C (figure 3.5d). Then the second 10 nm thick Fe layer is grown at 89°C and annealed also at 400°C for 20 min and a 20 nm Co layer is grown at 86°C, conforming together (the Fe/Co bilayer) the hard FM. Finally the MTJ stacks are capped with a Au protective layer 15 nm thick grown at 77°C.

After the MBE growth, all the MTJs were patterned with lateral

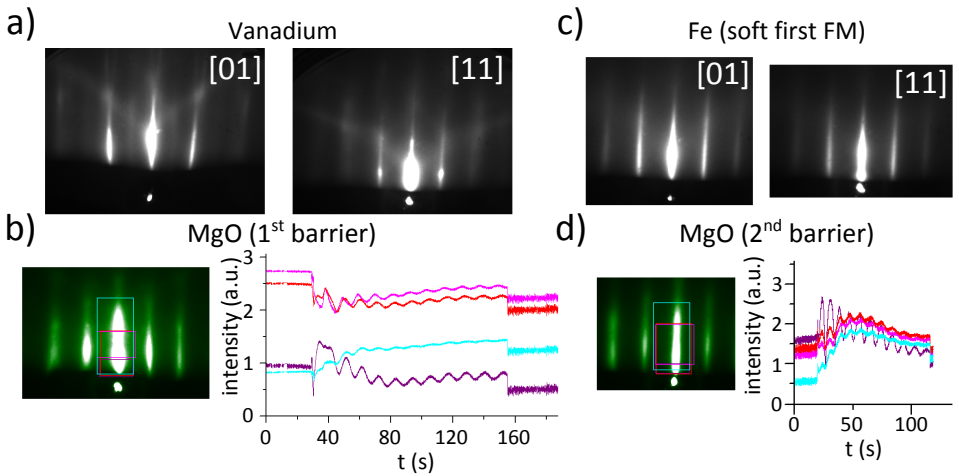

Figure 3.4: Sample growth data from SIFIF samples. Reflectance high-energy electron diffraction (RHEED) measurements: a) after annealing the V layer at two different angles of the surface square lattice, b) after the deposition of the first MgO insulating barrier, c) after annealing the first Fe layer (soft FM) and d) after the deposition of the second MgO insulating barrier. Figures by courtesy of C. Tiusan et al.[107], CNRS IJL Nancy/Technical University of Cluj Napoca.

sizes from 10 to 60 μm by a combination of UV lithography and Ar ion etching, controlled step-by-step *in situ* by Auger spectroscopy[106].

The photo-lithography protocol consists in 4 steps (see figure 3.6). First step consist of patterning the top electrode, the flat sample is covered with a photo-resistive mask using UV lithography and then etched with an Ar ion beam (see figure 3.6a). Second step aims to patterns the bottom electrode, from step 1 the sample is covered again with a photo-resistive mask using UV lithography and then etched with an Ar ion beam (see figure 3.6b). Third step encapsulates the structure with SiO_2, from step 2 the sample is covered with a photo-resistive mask but this time is used to protect the top and bottom electrodes from the SiO_2 sputtering (see figure 3.6c). Finally step 4 consists in sputtering the Al contacts (another photo-resistive mask is used to separate top from bottom contacts) leading to the final

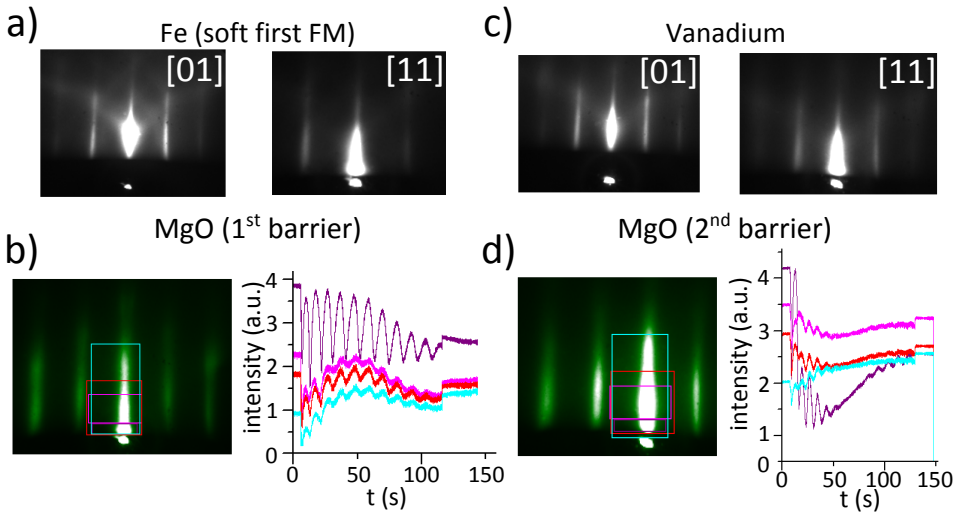

Figure 3.5: Sample growth data from FISIF samples. Reflectance high-energy electron diffraction (RHEED) measurements: a) after annealing the first Fe layer (soft FM) at two different angles of the surface square lattice, b) after the deposition of the first MgO insulating barrier, c) after annealing the V layer and d) after the deposition of the second MgO insulating barrier. Figures by courtesy of C. Tiusan et al.[107], CNRS IJL Nancy/Technical University of Cluj Napoca.

structure (see figure 3.6d).

During the work on this thesis we have measured only samples of the same area ($400\mu m^2$) for an easy comparison with only a few exceptions which we will point out specifically. The selection of that particular area is also because our electronic circuit set-up is designed to measure samples with resistances in the range from about 1kΩ to several 100kΩ (see electronic circuit details in section 2.1).

3.3. Normal state conductance

We start with the discussion of the conductance measurements made above the critical temperature in order to compare the varia-

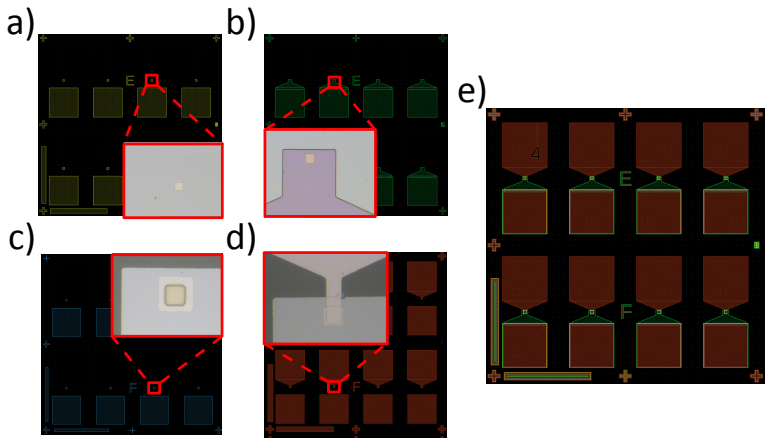

Figure 3.6: Photo-lithography protocol steps: patterning the top a) and bottom b) electrodes (steps 1 and 2), c) SiO_2 encapsulation oxide (step 3), d) sputtering of the metallic contacts (step 4), e) stack of masks. Figures by courtesy of C. Tiusan et al.[107], CNRS IJL Nancy/Technical University of Cluj Napoca.

tion of the conductance with the introduction of a V electrode or when V is inserted in between Fe layers. The introduction chapter explained the concepts of coherent tunneling between different materials (section 1.3.4) when strong SOC is present at their interfaces (section 1.3.5). Magnetism is going to be fully addressed in the following section3.4. All the measurements shown below have been made in the same magnetic state (P state) and at a fixed low temperature above the critical one (typically at 10 K).

A total of 15 samples have been measured: 4 SIF, 5 SIFIF and 6 FISIF samples. We start by comparing the normal state conductance of each of the different types of samples in order to get some statistics. We observe from figure 3.7 that each type of sample shows a very similar bias dependent conductance. This might look obvious but taking into account the amount of particularities of measuring each of them separately this can be taken as one proof of the extreme quality of the fabrication process. In the particular case of the NIF type, the conductace of two of them is very similar whereas one is

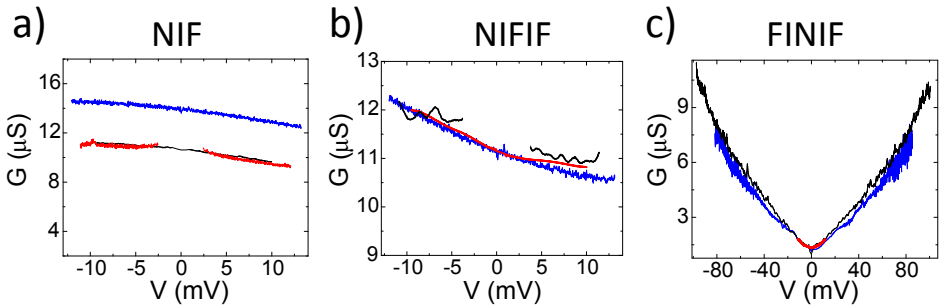

Figure 3.7: Normal state conductance (at T=10K) showing the different sample's statistics for a) the NIF type, b) the NIFIF type and c) the FINIF type. A total of 15 samples have been studied but only in 3 of each type we made proper normal state conductance measurements (colored curves correspond each to a different individual sample).

10% higher. This accounts for the fact that real samples have slightly different behaviors and its very difficult to account for that when they are selected in the stage when they are contacted (previous to their measuring).

Let's now compare them with one another. Looking at the two graphs shown in figure 3.8 it seems clear that the conductance behavior has to be analyzed separately in the low bias and in the high bias regime. The low bias regime shows that the conductance is the lowest in the FINIF sample, being an order of magnitude below in comparison with one of the NIF and the NIFIF samples. These differences could be explained by coherent tunneling. Indeed, looking at the conduction band structure model (see figure 3.9), one observes that near the Fermi level V has only Δ_2 states which are not present in Fe for the majority channel, therefore the conductance is expected to be very low in the barrier when tunneling Fe↔V.

The dramatic decrease of the normal resistivity of our V/MgO/Fe junctions compared to the previously studied Fe/MgO/Fe MTJs[2] is an evidence of the restrictions of MgO filtering added to the non-matching symmetries of this two different materials (see figure 3.9). Such restrictions should be reduced only above 2.3 eV leading to a Δ_1

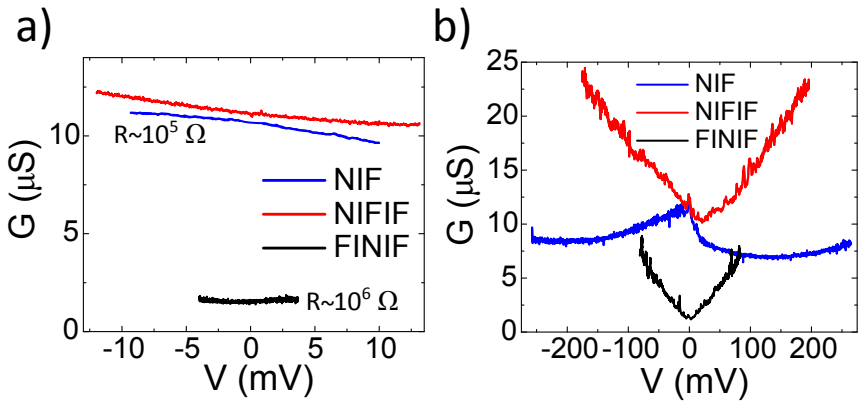

Figure 3.8: Conductance comparison at the a) low bias and b) high bias ranges between the three samples under study. Measurements made at T=10K and in P state (case of NIFIF and FINIF). In part b) the quasi-parabolic dependence of tunneling conductance versus bias can be clearly seen on the three samples in the high bias regime.

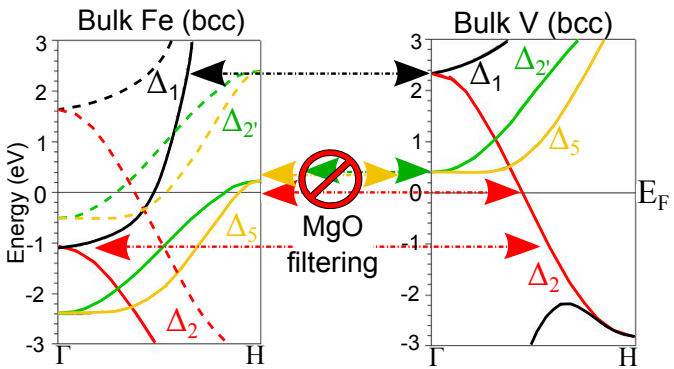

Figure 3.9: Band structure model for electron transport between Fe and V. Inside the bulk Fe, the solid (dotted) lines refer to Fe majority (minority) carriers. MgO filters nearly all symmetries except for Δ_1. Coloured arrows depict symmetry matching. DOS calculation made by C. Tiusan using the program Wien2k.[108]

contribution to conductance which is weakly filtered by the MgO bar-

rier. However, the thin MgO barrier usually can not sustain such high bias and it may break down before (creating a hotspot or a pinhole).

On the other hand, in the high bias regime (figure 3.8b) we can see the expected parabolic conductance behavior typical of MTJs[109–111]. The difference in the parabolas between the SB-MTJs and the DB-MTJs is explained because of sequential tunneling. As the voltage increases sequential tunneling helps electrons to increase their tunnel transparency (case of DB-MTJs). It is not until ranges of more than 1 V when electrons start having open the Δ_2 majority channel in Fe (see figure 3.9). The small increase at low bias of the NIF conductance is understood as due to the defects (which have energy typically in the range of tens of mV) helping the electrons to overcome the barrier.

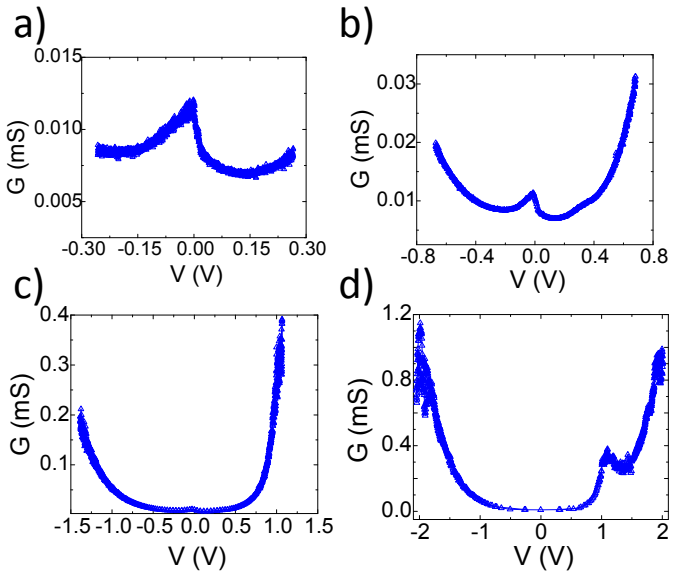

Figure 3.10: NIF conductance increasing the applied voltage step by step with the aim to reach the breakdown threshold. The maximum applied bias for parts (a-d) was correspondingly 0.25, 0.7, 1.2 and 2 V. The sample endured up to 2.2 V. The measurements were made at a base temperature of 5 K.

A very interesting study was made for a NIF sample when we

increased step-by-step the voltage in order to reach the threshold at which the sample would breakdown creating pinholes (see figure 3.10). The sample endured 2.2 V and then the conductance increased suddenly due to the creation of pinholes (high transmitting channels across the barrier). The reproducibility of each curve is really good taking into account that above 1 V the joule effect could increase the sample's temperature a few degrees. The previously mentioned increment of conductance below 150 mV clearly seen in figures 3.10a and b could be linked to an opening of conductance channels due to defect scattering. This scattering is expected to change the orbital symmetry of electrons and may transform Δ_2 channels into highly transmitting Δ_1 channels not filtered by the MgO barrier. At very high voltages the conductance shows a trend towards a parabolic dependence on the voltage (figure 3.10c). When the maximum range of 2 V is used we can see the appearance of the extra peak in conductance followed by a conductance reduction for the positive biases. We attribute this behavior to the appearance at the Fermi level of Δ_2 channel and at the same time disappearance of the Δ_1 conductance channel for the majority Fe carriers (see figure 3.9).

To finish the study of the normal conductance we are going to fit the IV curve for each type of sample to Brinkman's model[9]. The fitting parameters will give us a rough idea of the average height, the asymmetry and the thickness of the barrier. Because of the simplicity of the model it doesn't take into account coherent tunneling, spin filtering, SOC, possible defects, etc. Therefore we will use the obtained information only to have an approximated idea of the barrier parameters. The correlation between the SB-MTJs and the DB-MTJs within Brinkman's model should only be clear in the barrier thickness comparison which should be bigger in the DB-MTJs than in the SB-MTJs.

Looking at the obtained fitting parameters (see figure 3.11) for the NIF and NIFIF samples we see that they roughly agree with the thickness of the barrier (d) in the growth description. This is not the case for the FINIF junctions. If we look at the average height of the barrier ($\bar{\varphi}$) it agrees at high voltages with the fact that the NIF sample has the lowest conductance of the three types of junctions studied (see figure 3.8b). The asymmetry of the barrier ($\Delta\varphi$) is the

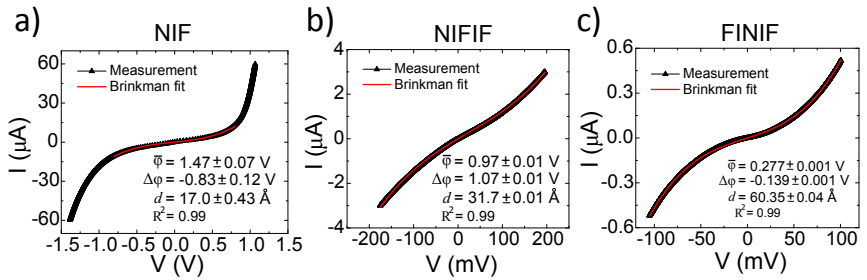

Figure 3.11: Brinkman's fit[9] of a high bias IV curve measurement made at T=5K on a NIS sample. The fitting parameters are the average barrier height ($\bar{\varphi}$), the asymmetry of the barrier ($\Delta\varphi$) and the thickness of the barrier (d).

lowest in the case of the FINIF sample which agrees with the fact that this sample is the only one of the three types which has a symmetric layer configuration.

From this paragraph we conclude on the epitaxial nature of the junctions under study. Low bias excess conductance in SB junctions point out towards orbital symmetry braking at the interface which could be due to SOC among other factors such as surface states. Now we are going to describe the different magnetic states of the FM electrodes studying the competition between their magnetic anisotropies. It is of utmost importance to understand the behavior of the magnetization for the next chapter when superconductivity comes into play.

3.4. Magnetic states

The field of spintronics takes advantage of the conduction electron intrinsic angular momentum (spin) and its associated magnetic moment, in addition to its fundamental electronic charge. One way of interacting with the spin, is through the magnetization of a FM. Electrons traveling through a FM material tend to align their spin with the surrounding FM magnetization defining the magnitude of spin current polarization P (given by expression 1.5). In our experiments

we can change the magnetization of the FM by applying and external magnetic field in any direction of space (3D vector magnet).

The reference system (figure 3.12) for the experiments on the study of the possible remanent states in 10 nm thick Fe electrodes has been chosen following the reference frame of the 3D vector SC magnet. Thereby, the external magnetic field maximum ranges are: $H_{Z-MAX} = 3.5$ T, $H_{X-MAX} = 1$ T and $H_{Y-MAX} = 1$ T. All the experimental data, in reference to the magnetic field application, shown in this thesis has been previously re-calibrated taking into account the possible misalignment explained in section 2.6.2.

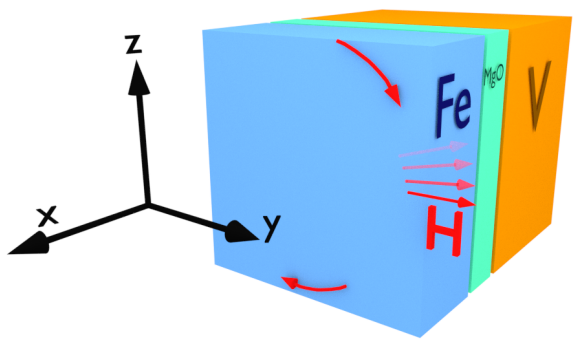

Figure 3.12: Experimental reference axis system in a sketch of a SIF sample, X is the out-of-plane direction and Y and Z the in-plane directions. Illustrated in the sketch is a rotation of the external magnetic field (H) in the YZ plane.

As mentioned, in our DB-MTJs one of the electrodes is made to be a soft FM and the other a hard FM. A typical in-plane TMR of each of the DB-MTJs is shown in Figure3.13. Experimentally, the detection of the magnetic state of the FM magnetization is made by measuring the field dependent conductance (or resistance) across the junction at low biases not exceeding 10 mV.

3.4.1. In-plane magnetization measurements

The magnetization's behavior (remanence, coercive fields, etc) depends on the competition between crystalline, volume (or shape) and surface anisotropies, as well as the interaction between both FM layers (exchange) in the case of the DB-MTJs. Due to the growth of the samples, the plane of the layers and the crystalline Fe bcc easy axis are the same (100)[106]. Because of that, in addition to the shape anisotropy, the coercive fields of the FM layers are lower in the in-plane directions than in the out-of-plane one and thereby the FM magnetization will follow much easily the external magnetic field if its applied in-plane.

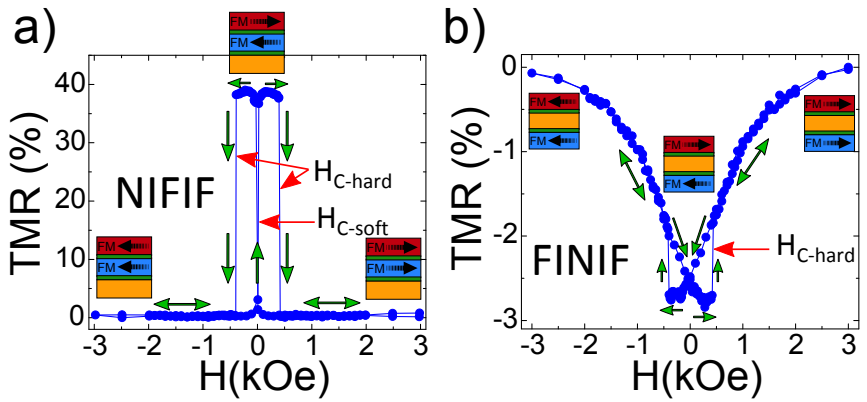

Figure 3.13: Example of a typical in-plane TMR in a NIFIF a) and a FINIF b), both taken at T=5K. In-plane coercive fields are, for the NIFIF $H_{C-soft} \sim 5-10$Oe and $H_{C-hard} \sim 400$Oe, and for the FINIF $H_{C-hard} \sim 400$Oe. The normal TMR in the NIFIF junction contrast with the inverse TMR in the FINIF junction. Green arrows indicate the hysteresis cycle history.

The in-plane TMR measurements have been always the first experiments done in all samples measured. In DB-MTJs TMR measurements also provide an indirect view of the quality of the sample. For our NIFIF samples the estimated maximum value of the TMR is around 40% (see figure 3.13a), and for our FINIF samples it was around -3% (see figure 3.13b). We will address this characteristic in

next section 3.4.2. If the value of the TMR is lower than the mentioned one, it would be a clear sign that the selected sample is of poor quality, normally due to problems during its growth or that some hotspots or pinholes might have appeared. These low quality samples normally had a exceedingly high noise level and a very high conductance most probably because of the presence of highly transmitting channels (no longer in the tunneling regime). Those samples (usually a minority) were directly discarded.

Figure 3.13 demonstrates that the two DB-MTJs have qualitatively different magnetic behaviors. The two FM layers are, in both samples and at low temperatures, anti-ferromagnetically (AF) coupled, which means that the dipole interaction is strong enough to overcome the exchange interaction between them. However, such effects are relatively weak in the NIFIF, where one can achieve a parallel FM configuration without an external field applied (figure 3.13a). In order to achieve a parallel magnetic configuration in the FINIF sample one must apply a strong in-plane field, and the only remanent magnetic configuration possible is anti-parallel (figure 3.13b).

We have already mentioned that to study the interaction between SC and FM (to be introduce in the next chapter), it is important to have the different remanent magnetic configurations available. The in-plane rotation sketched in figure 3.14a in the NIFIF sample, shows the three different in-plane magnetic configurations possible: Parallel (P), Anti-parallel (AP) and perpendicular (Perp.). By making a rotation with an external field lower than the hard FM coercive field, we maintained the hard FM magnetization fixed and rotated only the soft FM magnetization (figure 3.14b). The three in-plane (Perp. state out of plane will be discussed further below) magnetic configurations stay (in the NIFIF sample) remanent during an extended period of time (more than weeks experimentally). It is clear (from figures 3.14b,c) that the soft FM magnetization follows the external field in jumps between four different directions which correspond to the direction of the Fe crystallographic easy axis.

Then, in the NIFIF sample, figure 3.14 demonstrates that the three in-plane magnetic configurations (P, AP and Perp.) can be perfectly controlled with the external magnetic field. As shown in figure 3.13a

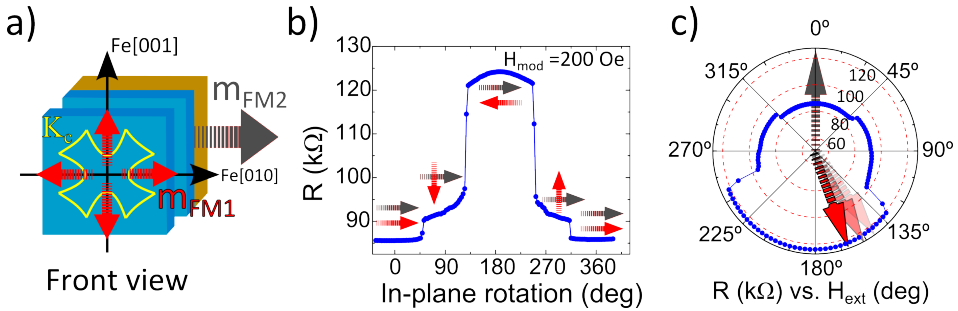

Figure 3.14: In-plane rotation of the magnetization of the soft FM layer in the NIFIF sample. a) Front view sketch of a spin-valve Fe/MgO/FeCo. The magnetization of the FeCo (hard FM2, grey arrow) remain fixed, and the magnetization of Fe (soft FM1, red arrow) rotates. Part b) and c) shows the same rotation made at an external field with a module of 200 Oe in a cartesian and a polar plots respectively.

and in our further experiments these magnetic configurations may remain remanent.

Having demonstrated the existance of those three different magnetic states at low temperatures ables us to apply the Slonczewski formula[112] to evaluate the spin polarization of the FM electrodes (P). The total resistance across the NIFIF sample is the straightforward sum of the resistance across its two tunnel barriers, the NIF and the FIF. If we write it with conductances instead we have:

$$\frac{1}{G_i} = \frac{1}{G_1} + \frac{1}{G_2(1 + P^2 \cos\theta)} \tag{3.1}$$

where $G_{NIF} = G_1$ is constant and $G_{FIF} = G_2(1+P^2\cos\theta)$ depends on θ which is the angle between the two FM magnetizations ($i \rightarrow$ P=0°, AP=180° and Perp.=90°). Solving formula 3.1 for the values from figure 3.14b, we obtain a rough value of the polarization $P \approx 0.7$ which confirms the effective spin filtering made by the MgO barriers.

In the NIF sample, an in-plane rotation does not show any difference in resistance because it only has a single FM layer. But as we

mentioned in 1.3.6 the absolute orientation of the single FM magnetization with respect to the crystallographic axis might show a magnetoresistive effect (TAMR). We can compare the experimental results from Moser *et al.*[24] where they study a Fe/GaAs/Au MTJs with our own V/MgO/Fe samples (shown in figure 3.15). Both are in-plane rotations made at low temperatures using similar external magnetic fields

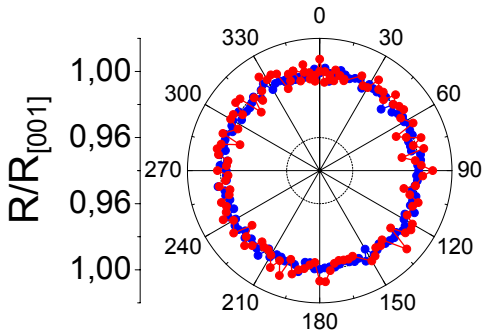

Figure 3.15: In-plane rotations of low bias conductance made on the NIF sample at 10 K. The rotations were me with an external field applied of H_{mod} =0.5kOe (blue) and H_{mod} =2kOe (red). The applied bias was V=5mV. Due to the measurement resolution limit ($\sim$ 1% we can't appreciate any finite TAMR.

Comparing results shown in figures 3.13a and b, we observe that the TMR of the FINIF sample shows a different behavior than the TMR of the NIFIF one. In the FINIF MTJ, the only in-plane remanent magnetic configuration at zero external field is AP. For achieving a P state one must apply a high external magnetic field, on the other hand, the Perp. state is impossible to achieve due to the AF coupling. We will discuss in the next paragraph the behavior of the electrodes magnetization in the FINIF layer configuration.

3.4.2. TMR in FINIF samples

As explained in section 1.2.1, in a TMR measurement in classic FIF junctions, the parallel state (P state) is usually the low resistance

state whereas the anti-parallel state (AP state) is the high resistive one. When P state is the high resistance and AP state the lower one then there is a so called inverse TMR. In the FINIF samples, a polarized electron penetrates into the normal-metal from one of the electrodes but because the thickness of the normal-metal is larger than the spin conservation (spin decay) length, the electron gets depolarized. Indeed, the TMR is decreased from 40% in the NIFIF samples roughly to a 3% shown in the FINIF samples (see figure 3.13).

The inversion of the TMR is an issue that has been addressed in many recent studies[113,114,115,116]. Below we briefly discuss a few possible reasons for the observed inverse TMR.

The investigation made by De Teresa *et al.*[116] and Sunaga *et al.*[114] take into account the possible influence of the density of states (DOS) of the material in the form a peak distortion of the DOS when the junctions in the high bias regime. Other sources of having inverse TMR have been studied by Gao *et al.*[113] in FeCo/MgO interfaces where they found an inverse TMR attributed to the oxidation of the FeCo/MgO interface providing a negative spin polarization.

Finally, one should not exclude that Δ_2 channel blocking of the transport through V to be the origin of the inverse TMR (see sketch in figure 3.16).

In the higher conducting P state where the 2 MgO barrier are transpartent for Δ_1 current and only two SOC events are needed at MgO/V interfaces to provide high current. On the other hand on the AP state Δ_2 and Δ_5 states in Fe are less transparent for the MgO and with one or two scattering events in order a lower current through the device may be expected.

3.4.3. Out-of-plane magnetization and PMA

We have already pointed out that in the absence of metastable states, the equilibrium orientation of the magnetization of a thin FM film is a result of the competition between the crystalline, shape (or volume) and surface anisotropies. The crystallographic axis in our samples matches the plane of the sample thus the competition comes from shape versus surface anisotropies. If the thickness of the ex-

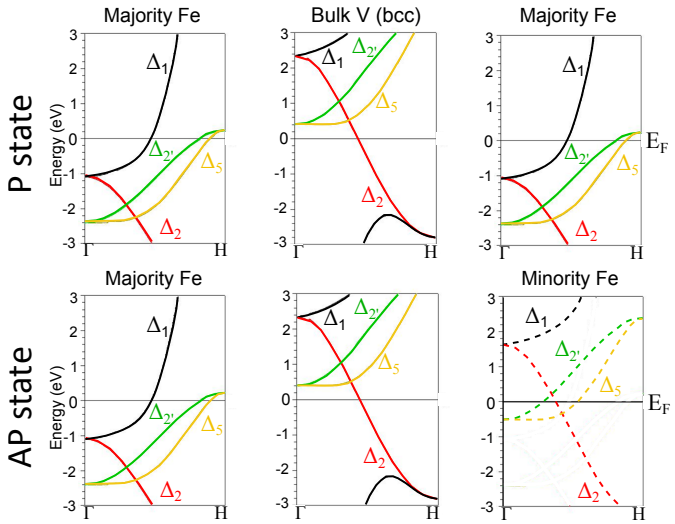

Figure 3.16: Band structure model for electron transport in the FINIF junction. On the P state (upper part), the Δ_2 channel is blocked in both interfaces whereas on the AP state (lower part) the Δ_2 channel is only blocked between the Fe majority channel and V.

tensive FM layer substantially exceeds values of about 10 nm, the shape anisotropy dominates and tends to align the magnetization in-plane. On the contrary if the film is thinner than 2 nm the surface anisotropy tends to align the magnetization out of plane, leading to PMA. Recent trends in spintronics using magnetic tunnel junctions (MTJs) take advantage of PMA to provide large tunneling magnetoresistance (TMR), enhanced thermal stability[101], low spin torque switching currents[102,103] and record small lateral sizes[104].

Previously we have discussed only in-plane measurements. As we show, our 10 nm thick Fe layers ables us to change the magnetization of the film either in-plane or out-of-plane and that the magnetization stays remanent at low temperatures when switching off the external field as it is shown in figure 3.17b. To detect a change in the resistance across the junction we need a sensor, which is the second FM. Thereby we measure in this way the change of the relative orientation between two FM. The sample with the highest TMR is the NIFIF, thus we

are going to study the out-of-plane magnetization behavior with this sample (sketch in figure 3.17a).

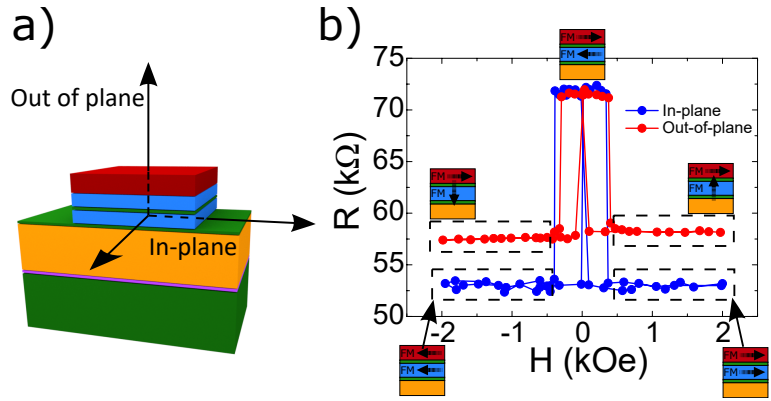

Figure 3.17: Part a) shows a sketch of the NIFIF sample indicating the in-plane and out-of-plane directions. Part b) shows a room temperature TMR made sweeping the field both in-plane and out-of-plane. Three remanent magnetic states are clearly distinguishable P, AP and Perp. states.

One of the main experimental findings of the present work is that the out of plane TMR of the NIFIF sample shows an asymmetric behavior at low temperatures (see figure3.18a). We note that both the out of plane an the in-plane TMR are symmetric at room temperature (see figure3.17b) and the in-plane TMR continues to behave symmetrically at low temperatures (see figure3.18b). On the contrary, the out of plane TMR changes its behavior when the temperature is decreased below 80 K. This is a robust response taking place in all the NIFIF samples measured. Moreover the hysteresis cycle has qualitatively the same asymmetry whichever the sweeping direction of the external magnetic field we choose. Figures 3.18a and 3.19a cycle histories are 0kOe $\rightarrow$ +3kOe $\rightarrow$ -3kOe $\rightarrow$ +3kOe $\rightarrow$ 0kOe, starting from P state (in-plane).

We have planned different measurements with distinct magnetic field histories to figure out the behavior of the out of plane magnetization including changes in the starting magnetization state (P or

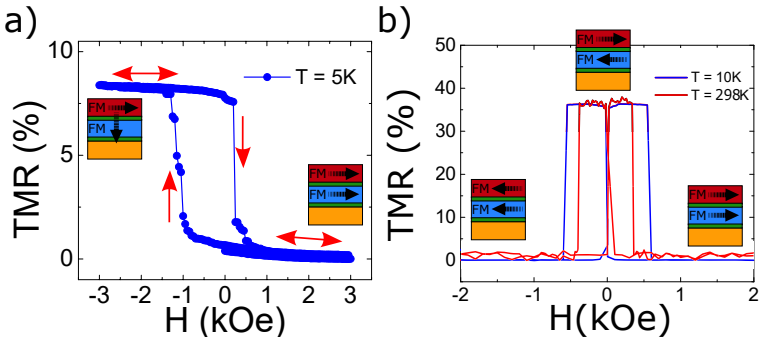

Figure 3.18: Part a) shows a perpendicular asymmetric TMR taken at T=5K. Red arrows indicate the hysteresis cycle history. Part b) shows how the in-plane TMR remains symmetric at low temperatures increasing just the hard coercive fields. All TMRs were measured at V=5mV.

AP in-plane states), and changes in the temperature. For most of the measurements we even repeated them but with opposite sweeping history (see figure 3.19b) and the cycle remains with the same asymmetry just changing the switching fields (soft FM out-of-plane coercive field). Moreover, we made measurements up to H_{ext} = 7kOe (the limit of our SC magnets is 10kOe) with the idea of looking if the switching field for the positive direction of the external magnetic field wasn't reached at 3kOe (figure 3.18a) and the result is that it should be higher than 7kOe.

Figure 3.20 shows the comparison between high field perpendicular TMRs starting from P (figure 3.20a) and AP (figure 3.20b) states at high (T=80 K) and low temperatures (T=0.3 K) (the measurements are different from the one shown in figure 3.19). Even with an external perpendicularly applied field of H_{ext} = 7kOe there is no switch on the magnetization of the soft FM layer, which remains parallel to the hard one. A strong magnetization asymmetry in the angle between the soft and hard layers is evident. Only in the negative perpendicular direction there is a change in the relative orientation between the two magnetizations. First the soft layer switches to a Perp. state (step with about a 10% of TMR). Such Perp. state however, due to the

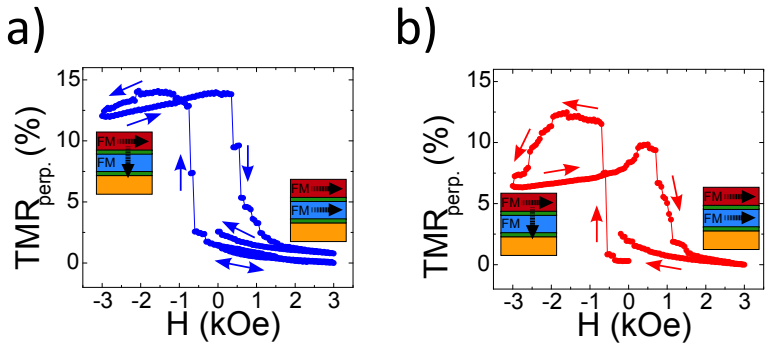

Figure 3.19: Perpendicular TMRs made at 5 K. Hysteresis cycle history of: a) 0kOe → +3kOe → -3kOe → +3kOe → 0kOe and b) 0kOe → -3kOe → +3kOe → -3kOe → 0kOe.

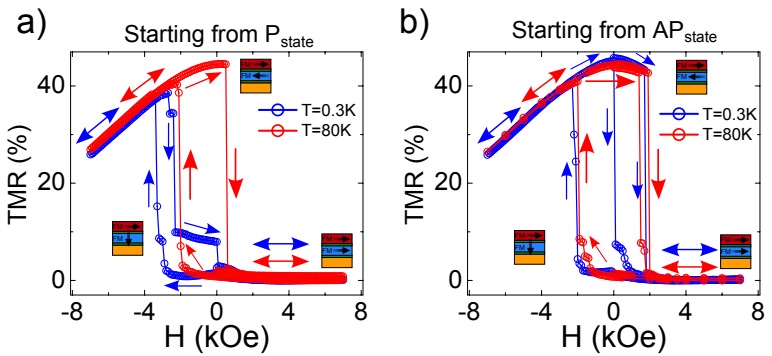

Figure 3.20: High field perpendicular TMRs at different temperatures and for a different sample from the one shown in figure 3.18a. Starting the measurement from a) P state and b) AP state. Colored arrows indicate the hysteresis magnetic field sweep history. Three remanent magnetic states are achievable: P, AP (in-plane states), and Perp. (out-of-plane state). The latter can only be achieved by applying a negative external magnetic field. Hysteresis cycle history: 0kOe → +7kOe → -7kOe → +7kOe → 0kOe

antiferromagnetic coupling of the electrodes, becomes unstable when continuing the increase of the field and ends switching into AP state.

The difference in the switching field value to from in-plane states (P or AP) to Perp. if compared with the previous figure 3.18a could be attributed to the increment on the saturating fields used in addition to the fact that the low temperature (T=0.3 K) measurement was made below the critical temperature of V, thereby the magnetic field becomes nonuniform and might contribute to this effect.

Additionally the Perp. state becomes more robust (even remanent at zero field) at low temperatures which agrees with our T=0K simulations discussed below. As expected, in the limit of higher negative fields, the relative angle between magnetization of the soft and hard layers reduces approaching gradually towards P state which is expected to occur above 16 kOe which is outside our experimental range. Heating up to 80 K substantially suppresses the metastable Perp. state for the initial P alignment while it stays present for the initial AP alignment. We tentatively link this difference to the following idea. Domain walls probably present in the AP state may stabilize a metastable Perp. state even at high temperatures.

In the FINIF sample we observe that the AF coupling is much stronger that the influence of PMA, thus its effect could be neglected. As shown in figure 3.21 there is no hysteresis in the cycle when sweeping the external magnetic field out of plane. At zero field the ground magnetic state is AP state (due to AF coupling). When an out-of-plane external field is applied, at the beginning (0-4kOe) there is just a small rotation of the AP state and if the field continues to increase (above 4kOe) then the soft FM starts to rotate to a Perp. state but as there is no jump-like transition it is difficult to assert the exact value of the external field for reaching a full Perp. state.

3.5. Simulations of PMA

In order to understand deeper the mechanism behind different magnetization orientations due to competing anisotropies we have carried out micromagnetic simulations. Although the simulations were done for the structure which consisted of two FM layers (one of then soft and the other hard), we concentrate here mainly on the case when

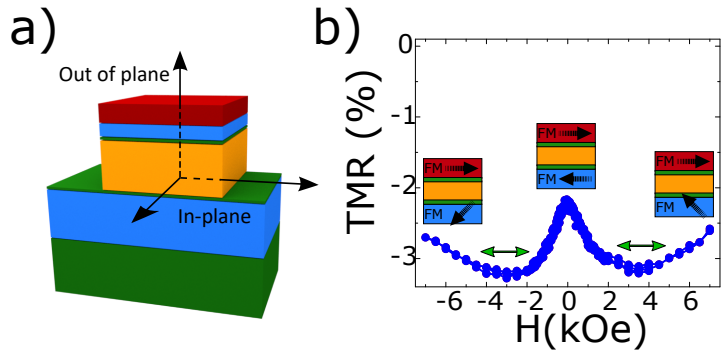

Figure 3.21: Part a) shows a sketch of the FINIF sample indicating the in-plane and out-of-plane directions. Part b) shows a perpendicular TMR measured at T=5K normalized by the P state resistance taken from figure 3.13b. Green arrows indicate the hysteresis cycle history.

the coupling between them is negligible. This allows us to better understand the grund and metastable states of the single FM layer with the competing anisotropies and with the possibility of having broken symmetry at one of the interfaces. In order to thoroughly investigate the behavior of the soft FM layer magnetization, we have simulated its magnetic field dependence at T=0K by using MuMax3 code[99]. The PMA is characterized by an effective anisotropy constant (K_{eff}) that has a volume contribution (K_V) and a surface or interface contribution (K_S).

$$K_{eff} = K_V + K_S^{(I)}/t + K_S^{(II)}/t$$

where $K_S^{(I)}$ and $K_S^{(II)}$ are the surface anisotropies at the interfaces (I) and (II) respectively, and t is the FM layer thickness. As mentioned, the competition between volume and surface anisotropies is the key factor to manipulate the FM thin layer magnetization (see figure 3.22).

Surface anisotropies K_S may range between $K_S \approx 1 \times 10^{-3}\mathrm{J/m}^2$ in ultrathin Co, Fe and Ni films[117] and $K_S \approx 3 - 4 \times 10^{-3}\mathrm{J/m}^2$ in CoFeB/Pt interfaces[118]. It appeared that MgO/Fe interfaces show PMA substantially exceeding the values reported for the prototype

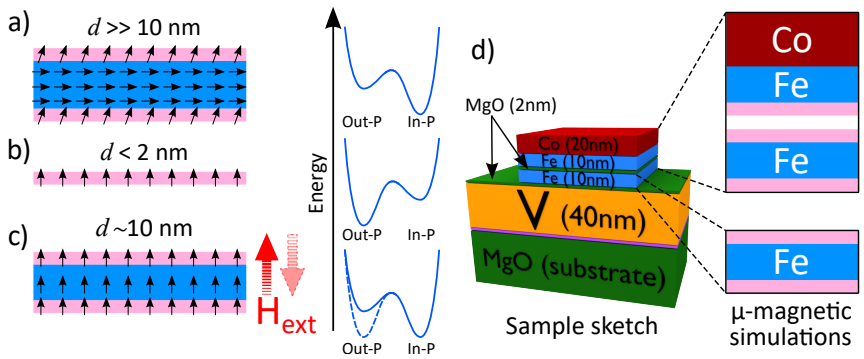

Figure 3.22: Competition between shape and surface anisotropies dependence on the film thickness. Part a) shows an in-plane magnetization in the limit of thick FM films, part b) an out-of-plane magnetization in the limit of thin FM films and part c) shows how with 10 nm thick films one can switch with an external magnetic field between the magnetization directions in-plane and out-of-plane. Part d) shows the sketch describing the system used in the micro-magnetic simulations. Pink stripes indicate the presence of PMA within the FM (at the interfaces).

Co/Ni(111) system[119]. First-principles calculations give values of K_S ranging between 1.5×10^{-3}J/m^2 and 1.8×10^{-3}J/m^2 (see ref.[120]) in reasonable agreement with experiments[101,121,105]. The main source of the PMA at MgO/Fe interface has been suggested to be the SOC emerging from the reduced interfacial symmetry of the Fe d-orbitals and O p-orbitals. Changing the nature of the normal-metal in NM/Fe/MgO (NM=V;Cr)[105], the transition between in-plane and out-of-plane anisotropy remains between 4 and 6 Fe monolayers. The critical thickness of the spin reorientation transition[101] is difficult to increase above a few nm without the need of a permanent application of an external magnetic field stimulus[122]. Reducing the bulk magnetization through doping with V or Cr impurities the bulk Fe reduces the easy-plane demagnetizing energy and moves slightly the critical thickness of the spin reorientation transition[123]. Decreasing the temperature down to 5K has rather limited impact on the critical thickness for the spontaneous

out-of-plane magnetization alignment and leads to the PMA and the saturation magnetization enhancement[124,125]. The most common ferromagnetic thin film used is grown by Molecular Beam Epitaxy (MBE) and typically incorporate 10 nm thick Fe (or FeCo) soft (or hard) FM layers usually separated by MgO barriers[110,106], this thickness allows the magnetization of the film to be controlled due to the competition between its magnetic anisotropies.

Figure 3.22d shows the simulated soft Fe layer interfaced by two MgO barriers. The simulation parameters used for Fe are: saturation magnetization $M_s = 1700 \times 10^3 \mathrm{A/m}$, exchange stiffness $A_{exch} = 21 \times 10^{-12} \mathrm{J/m}$, damping $\alpha = 0.02$ and cubic anisotropy $K_c = 4.8 \times 10^4 \mathrm{J/m^3}$, the interfacial layers with PMA include the surface anisotropy term K_S. The results are independent on whether the MgO is represented as vacuum or as a weakly (with a susceptibility of 10^{-7}) diamagnetic material. The parameters used for Cobalt are: $M_s = 1400 \times 10^3 \mathrm{A/m}$, exchange stiffness $A_{exch} = 30 \times 10^{-12} \mathrm{J/m}$, damping $\alpha = 0.02$. To simulate the extensive in-plane dimension (in conparison with the thickness), the simulated structure is set to $50 \times 50\ \mathrm{nm^2}$ with periodic boundary conditions. The space was discretized in $16 \times 16 \times 147$ cells. With this discretization we have solved the micromagnetic problem using different models (see figure 3.23) of the interface anisotropies.

The spin reorientation transition has been simulated in different ways. One is model M1 which uses a single step variation of the PMA within the first atomic layer 3.23. This corresponds to the vacuum/Fe/vacuum case discussed in ref.[120]. The other model M2(i-iii) allows different PMA variations in steps of half a lattice period $a/2$ (i.e. Fe atomic layer). The model M2i, which shows an oscillatory decay of PMA inside the Fe is the closest to the numerical predictions for the MgO/Fe/MgO structure[120].

Model M2i uses the following uniaxial surface anisotropy K_S distribution in percentages: 65% for the first layer of Fe atoms and 30% for the second one. The third layer, following the DFT results[120], has a uniaxial in-plane anositropy (instead of out-of-plane) of roughly 10% (shown as a "negative" contribution in figure 3.23). Finally 5% is assigned to the forth layer. In general, the concentration of the

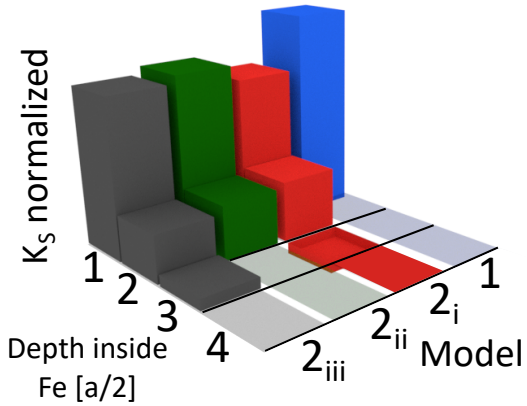

Figure 3.23: Sketch of the different possible distributions of the surface anisotropy K_S explored in simulations. The blue prism represents the PMA variation within model M1, in this case, all concentrated in the first interfacial atomic layer. There are three other configurations within model M2(i-iii) represented by red, green and grey prisms. The total energy corresponding to PMA has been kept constant.

surface anisotropy K_S within the first four atomic Fe layers qualitatively follows the DFT results[120]. It also introduce the predicted Friedel-like decay of the surface anisotropy between in-plane and out-of-plane (PMA) anisotropies. The other versions of the model M2(ii and iii) modify the Friedel-type PMA decay in a more monotonous PMA variation.

In figure 3.24 we see the different magnetization reorientation transitions (magnetization jumps) when simulating the effect of an external perpendicular magnetic field on the 10 nm thick Fe layer. The different models keep the total PMA energy fixed. The introduction of the Friedel-like PMA variation[120] (model M2i) softens the reorientation transition with respect to models M2ii-iii. Although the M1 PMA distribution softens also the reorientation transition, it reduces the nonvolatility of the zero field remanent magnetic state, in contrast to the experimental observations.

Few factors may contribute to some discrepancies between experiments and simulations. The presence of asymmetrically located inter-

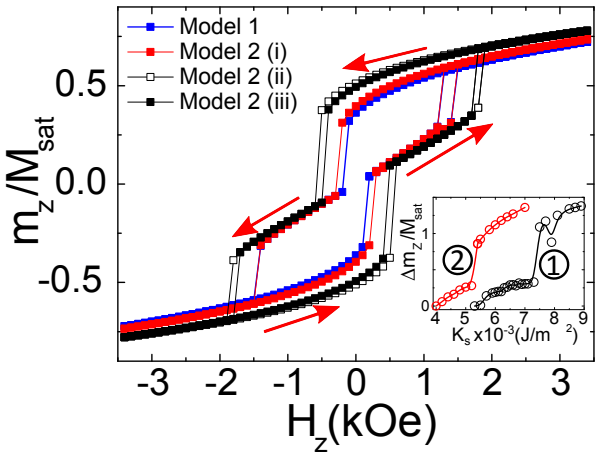

Figure 3.24: Simulation of the normalized, by the saturation moment (M_{sat}), perpendicular (z) component of the magnetization of the interfacial first layer of the 10 nm thick Fe using the different models. The inset represents the variation of the maximum (normalized by the saturation magnetization) jump in the z component magnetization during the spin reorientation transition (K_S) when simulated with model M2i for two different spatial distributions of the saturation magnetization. Red arrows indicate the magnetic field sweep history.

facial defects could lead to a higher order contribution to the PMA [126]. Among other possible sources of the discrepancies could be the value of the effective Fe moment in the proximity to the Fe/MgO interface. Some reports point towards an enhanced (up to 25% [127,128]) interfacial magnetic moment at the ferromagnet/oxide interface. Our simulations however show that critical values of the surface anisotropy K_S, needed for the spin reorientation transition, are closer to those obtained by DFT once we reduce the saturation magnetization (M_{sat}) only at the first interfacial atomic layers at both interfaces (see inset to figure 3.26). Looking at the inset of figure 3.24, the curve 1 uses a constant value of $M_{sat} = 1700 \times 10^3$ A/m while curve 2 is obtained by using a 25% reduced interfacial values of M_{sat}. The first plateau in both dependences correspond to a transition between near in-plane

to near out of plane magnetizations while the second plateau corresponds to magnetization jumps between two opposite close to out of plane magnetizations. Additionally looking at curve 1 (on the inset of figure 3.24), we see that the magnetization full flip (from up to down or viceversa out-of-plane) does not happen for PMA values below approximately $K_S = 5 \times 10^{-3}\mathrm{J/m^2}$. If we use $K_S > 6.4 \times 10^{-3}\mathrm{J/m^2}$ the reorientation transition tends to take place directly between two nearly perpendicular magnetization states, i.e. without locking the magnetization in the intermediate (close to in-plane) state (shown in the inset of figure 3.24 in the part where $\Delta m_Z/M_{sat} > 1$). Simulations show that the spin flip transition is rather weakly affected by the presence of the Fe layer cubic anisotropy (see figure 3.27). This demonstrates that it is mainly a demagnetization energy competing with PMA which provides the spin reorientation transition.

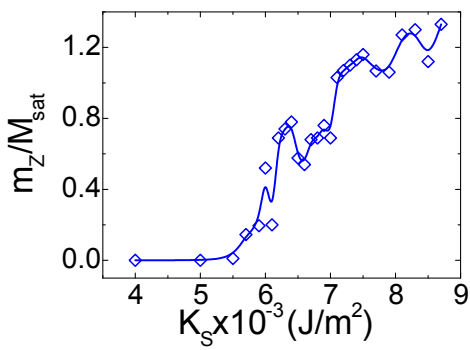

Figure 3.25: Simulation of the complete MgO/Fe/MgO/Fe/Co system. Variation of the magnetization jump on the 10nm thick soft Fe layer, using model M1 with the soft Fe layer ferromagnetically coupled to the hard Fe/Co layer with an energy density of RKKY= $10^{-2}\mathrm{J/m^2}$. Blue solid line serves as a guide for the eye.

Regarding the interaction between the soft FM (Fe layer) and the hard FM (FeCo layer), the spin reorientation transition could be affected by either a ferromagnetic (see figure 3.25) or an antiferromagnetic (see figure 3.26) coupling between the two electrodes. For the simulations shown in figures 3.25 and 3.26 we used an energy density of

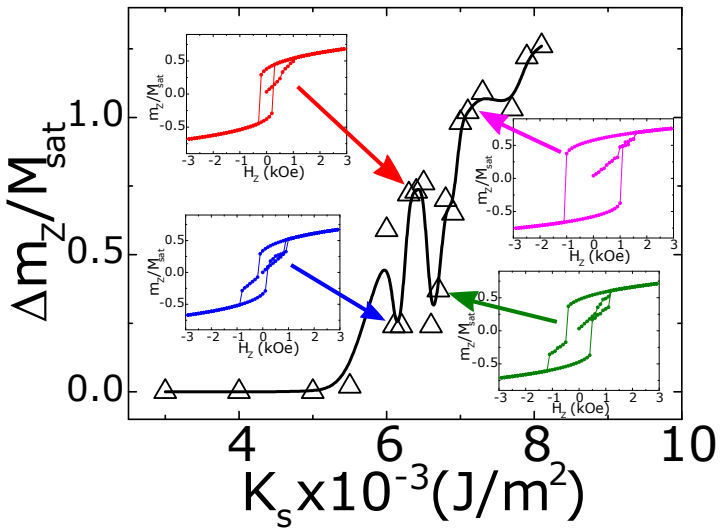

Figure 3.26: Simulation of the complete MgO/Fe/MgO/Fe/Co system. Variation of the magnetization jump on the 10nm thick soft Fe layer, using model M1 with the soft Fe layer antiferromagnetically coupled to the hard Fe/Co layer with an energy density of RKKY= 10^{-2}J/m^2. Insets show some representative hysteresis loops obtained upon increasing the PMA. Black solid line serves as a guide for the eye.

$RKKY = 1 \times 10^{-2}$J/m^2 (RKKY stands for Ruderman Kittel Kasuya Yosida interaction). In the case of the ferromagnetic coupling, there is roughly a smooth reorientation of the magnetization towards the perpendicular orientation as the surface anisotropy increases whereas if the coupling is antiferromagnetic there is an instability for values of $K_S = (6-7) \times 10^{-3}$J/m^2. In the simulations (at T=0K) of the single FM film (figure 3.24) and the complete soft and hard FM system (insets of figure 3.26) we see that the spin reorientation transition (magnetization of the soft FM jump) is symmetric, i.e. it occurs both at positive and negative external magnetic fields.

Simulations still have to address the fact that the experimental field dependence of the out-of-plane magnetization has an asymmetric behavior at low temperatures. We consider two possible scenarios,

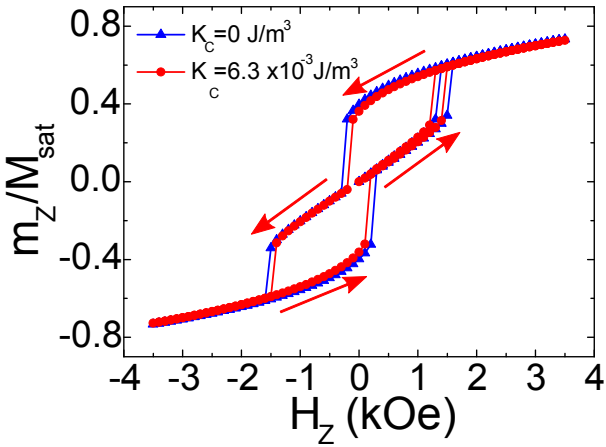

Figure 3.27: Spin reorientation transition simulated for the Fe layer with and without cubic anisotropy (K_c). Simulations have been done for the symmetric MgO/Fe/MgO structure within model $M1$ and by using a PMA value of $K_S = 6.3 \times 10^{-3}\mathrm{J/m}^2$. Red arrows indicate the magnetic field sweep history.

sketched in figure 3.28a, which are based on the difference in the interfacial disorder between the bottom and the top Fe/MgO interfaces. One is that such a difference in the structural disorder influences the Rashba field making it non-equal at the two interfaces (sketched in left part of figure 3.28a). The alternative scenario is that a higher order interfacial uniaxial anisotropy (e.g. second order) (K_{S2}) could show up at disordered interfaces. Already back to 1994 Dieny and Vedyayev showed analytically[129] that spatial fluctuations on the film thickness with $K_{S1} = Const.$ and period of the fluctuations lower than the exchange length on the FM may lead to a higher $K_{S2}\cos^4(\Theta)$ contribution to the PMA in addition to the $K_{S1}\cos^2(\Theta)$ term. Here Θ is the angle between the magnetization and the perpendicular to the interface axis. This possibility has been confirmed recently[126] showing that the magnetization reversal could be substantially modified for the opposite K_{S1} and K_{S2} signs.

In order to account for such a possibility, we have modified the

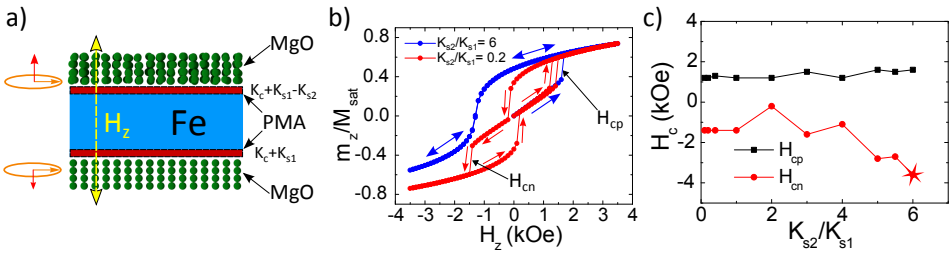

Figure 3.28: The left side of part a) explains the presence of the net perpendicular to the interface Rashba field component. The right side of part) is the alternative possibility for the appearance of the second order surface anisotropy at the more disordered (top) interface. Part b) shows two simulated magnetization loops (within model M2i) with different ratios between the second order (K_{S2}) and the first order (K_{S1}) interfacial anisotropy terms. The colored arrows (related to the blue and red cycles respectively) show the magnetic cycle step by step sweep. Part c) shows how the asymmetry of the positive (H_{cp}) and negative (H_{cn}) coercive fields corresponding to the transition between the near in-plane and near out-of-plane magnetizations emerges with the increase of the relative contribution of K_{S2} at the Fe/MgO interface. The point marked as a star shows the negative coercive field out of the actual field range.

simulations within model M2i (see figure 3.28b) introducing that the interfacial anisotropies K_{S1} and K_{S2} have opposite signs. The second order term K_{S2} has been introduced only at the upper Fe/MgO interface which is, by the growth history, the more disordered of the two. With such modification of the model, we observe a strong asymmetry in the magnetization hysteresis cycle for the negative K_{S2} values a few times higher than K_{S1} corresponding to a switch from near in-plane to near out-of-plane direction which resembles the experiment (figure 3.18a).

In figure 3.28c we have represented the variation of the positive H_{cp} and negative H_{cn} coercive fields with the increasing K_{S2}/K_{S1} ratio. The last point marked with a star (maximum negative) is taken as just exceeding the maximum negative applied field. This is because the

magnetization reorientation transition does not take place in that case (within the field range used) and the magnetization just returns along the same trajectory which is the asymmetry in the field magnetization response observed experimentally. Although the asymmetry in the magnetization reorientation transition appears only for $K_{S2}/K_{S1} > 5$, the critical condition for this ratio is around 0.2-0.4. This is because the reorientation takes place at angles about $\Theta \approx 1.37$ rad where the relation between the angular dependent factors $[\cos^4(\Theta)] \ll [\cos^2(\Theta)]$ is about 0.04. We note that a more uniform distribution of the K_{S2} along the four (instead of the single) interfacial cells does not alter substantially the simulation results.

Finally, one could also speculate on the above mentioned perpendicular component of the Rashba field induced by the oxygen defects inside the MgO and/or the lattice mismatch at Fe/MgO interface. Both things can increase the interfacial in-plane component of the electric field E. Since the Rashba field is proportional to the cross product of the electron momentum and the electric field $B_R = k \times E$, then depending on the local interface disorder of the interface, the perpendicular to the interface Rashba field component could be different. The presence of such a bias field could explain the existence of the field induced reorientation transition of the magnetization for one of the external magnetic field directions only (at least within the field range under study).

Despite the general qualitative agreement between the experiment and simulations, a certain number of open questions remain yet to be answered. Our simulations show that the magnetization flip to a not fully perpendicular to the interface orientation occurs at the fields around 1-2 kOe (see figure 3.24). The switching field is nearly independnet on the upper saturation field when varied in the range of 3.5-7 kOe (not shown). On the other side, the experiments reveal a near in-plane to near out of plane magnetization jump near 1 kOe (see figure 3.18a). Other issue is that a somewhat larger than the reported PMA values are needed to reproduce the abrupt magnetization switch in the perpendicular field.

Several factors not present in the simulations could be responsible for such differences. Among them are the (i) presence of defects, (ii)

modified interfacial saturation magnetization and/or (iii) presence of finite temperature in the experiments among others. Some reduction of the lateral size of the simulated structure affects the competing anisotropies leading to a suppression of the robustness in the simulation results. Our discussion is centered mainly around physical effects and omit the possible influence of chemical bonding on PMA[130] because the latest numerical studies minimize the effect of Fe-O $p-d$ hybridization on PMA[131].

Regarding the possible influence of the electrodes coupling on the results. If the hard FM layer was magnetostatically and/or weakly exchange coupled to the soft Fe layer under study, this would give rise to a more complex magnetization reversal (see figure 3.26) with other possible states[132] well beyond those simplest three relative magnetization states observed and discussed above for the uncoupled MgO/Fe/MgO.

An additional source of PMA values discrepancy could be the lattice mismatch (stress) providing interfacial electric fields[120] and stronger pinning of interfacial magnetic moments[122]. Just a small as 0.5% reduction of the lattice parameter is expected to increase (K_S) from $(1-2)\times 10^{-3}\mathrm{J/m^2}$ to $(5-6)\times 10^{-3}\mathrm{J/m^2}$ at the MgO/(Fe/Co) interface. Moreover, PMA for the individual Fe atoms deposited on MgO (100) thin films could increase (K_S) in the same order of magnitude[133]. So far the PMA has been investigated in about 1-2 nm thick FM layers mainly as long as only ultrathin magnetically soft layers provided the conditions for the room temperature operation of MTJs with PMA[134].

Finishing the chapter before the conclusions, one important thing we have considered from the simulation's data is that we have checked the stray fields exiting the FM layer which go into the Vanadium layer. This is important for the superconductivity (next chapter). Our simulations show that the stray field that exit the FM are very weak ($< 10Oe$), thus they can be neglected regarding any suppression of the superconducting state.

3.6. Conclusions

In this chapter we have studied the electron transport and the magnetization behavior of three different epitaxial magnetic tunnel junctions (MTJs): V/MgO/Fe, V/MgO/Fe/MgO/Fe and Fe/MgO/V/MgO/Fe. The measurements have been made above the critical temperature (T_C) of the superconducting transition of Vanadium in order to not have superconductivity interfering. Micro-magnetic simulations have been carried out to investigate the reorientation phase transition of the magnetization of a 10 nm thick Fe layer conforming a MgO/Fe/MgO stack.

The conductance above T_C (normal conductance) has been investigated to check important parameters of the junctions such as their barrier height and width. The substantial difference between band structures close to the Fermi level of the materials on use (Fe and V) essentially decrease their normal state conductance compared to other non-epitaxial normal-metal/insulator/ferromagnetic junctions or seminal epitaxial ferromagnetic/insulator/ferromagnetic (spin-valve) junctions made of the same materials (e.g. Fe/MgO/Fe).

In the spin-valve double barrier junctions (V/MgO/Fe/MgO/Fe) we have investigated the different possible quasi-equilibrium states of the magnetization orientation of the 10 nm thick Fe soft layer. By applying an external magnetic field at temperatures below 80 K, three different remanent magnetic configurations can be achieved: parallel (P state), anti-parallel (AP state) and perpendicular to the plane (Perp. state). We have observed a reproducible perpendicular magnetoresistance asymmetry at low temperatures (below 80 K). We have also verified that within our experimental set-up range of magnetic fields ($\pm$7 kOe) the perpendicular magnetization remains asymmetric. The possibility of controlling those three stable magnetizations indicates the competition between the perpendicular (out of plane) magnetic anisotropy (PMA) located at the interfaces of the soft Fe layer and the shape (or volume) anisotropy which tends to align the magnetization in-plane. In the Fe/MgO/V/MgO/Fe junction, due to the antiferromagnetic coupling between the two Fe electrodes, the only remanent magnetic state possible is AP state.

We have investigated, using micro-magnetic simulations, the magnetization behavior of a 10 nm thick Fe layer conforming a MgO/ Fe/MgO stack. We have simulated perpendicular to the plane magnetic hysteresis cycles up to 3 kOe and reproduced the magnetization reorientation transition. The experimental asymmetry on the perpendicular magnetization has been qualitatively recreated by introducing a second order anisotropy term in one of the two interfaces of the simulated Fe layer. The origin of the perpendicular magnetization asymmetry at low temperatures (below 80 K) comes from the difference in disorder at the two Fe layer interfaces due to the growth procedures.

Chapter 4

Towards superconducting spintronics in epitaxial magnetic tunnel junctions

On the previous chapter we introduced the magnetic control over the magnetization of the FM electrodes of our superconducting magnetic tunnel junctions (SC-MTJs). With that basis we continue the path towards fully coherent superconducting spintronics and study the electron tunneling mechanisms when the temperature drops below the critical temperature of our SC-MTJs. The interaction between superconductivity and ferromagnetism order parameters mediated by strong spin-orbit interaction (SOI) is the novel direction of research investigated in this thesis. Additionally the spin-active MgO barrier separating the SC and the FM makes the hybridization in the presence of a strong electron symmetry filtering. We will start motivating the subject, after that we will go to the sample description where we will introduce a control sample (the rest of the junctions are the same as in the previous chapter 3).

4.1. Introduction

The main motivation to investigate the interaction of SC and FM are two recent theoretical proposals[45,52] predicting the generation of long range triplet (LRT) correlations in the proximity of a spin-active interface with strong SOC separating a SC from a single FM. The theory from Bergeret *et al.*[52] is general, formulated in the diffusion limit, and only predicts how LRT diffusion length changes with the FM magnetization orientation. The theory from Högl *et al.*[45], using the ballistic approach, suggests a tool to verify the theoretical prediction of LRT by investigating the zero bias conductance as a function of the FM magnetization direction.

In the last decades a wide class of physical systems ranging from spintronics, to topological insulators[135] to Bose Einstein condensates[136] exploit the spin degree of freedom. The creation and manipulation of spin triplet Cooper pairs capable of penetrating long ranges into FM is a central aspect of study in superconducting spintronics[137,49]. Although the main research activity in superconducting spintronics still focuses in fundamental aspects, a growing number of applications are starting to emerge in the direction of novel kinds of non-dissipative spintronic devices[138,139,140].

The currently accepted agreement is that the transition from singlet to triplet pairing in superconducting spintronics with long range triplet (LRT) penetration[141] will not take place if the magnetization of the FM (in contact with the SC) is fully collinear[142]. Probably the most important search in superconducting spintronics is indeed having two FM with a relative magnetization angle close to 90° contacting the superconductor[143]. With few exceptions (spiral Holmium FM[144] and the CrO_2 half metal[47]), the main experimental efforts in the last decade have concentrated on optimizing the effectiveness of such multilayer structures[145,146,147,148]. Eschrig *et al.* introduced spin-active interfaces with spin-sensitive reflection and broken spin-rotation symmetry at SC/half metal or SC/strongly polarized FM as a source of LRTs[149,150,151]. More recently it has been demonstrated the crucial influence of spin-orbit interaction (SOI) for the LRT currents penetrating into a single FM[51,52,152].

For their practical realization it is usually suggested the incorporation of normal metals with strong Rashba-type SOI in the SC/FM/N[52] or SC/N/FM[153] systems with the FM being homogeneous. However, the perspectives of introducing to modern spin-filtering based spintronics[18,17] the considered superconducting spintronics structures is still a long run.

Summarizing, the aim of this chapter is to study the possible generation and control with SOC of LRT correlations in our SC-MTJs. The main characteristics of SC-MTJs for being able to produce LRT correlations are that they need a spin-active interface providing SOC, and at least one strong polarized FM capable of having its magnetization oriented perpendicular to the interface.

However, before focusing on the goal of the LRT detection, we have thoroughly characterized some superconducting properties of our samples for example measuring their critical temperature, the influence of the magnetic field orientation in the superconductivity, critical fields, etc.

4.2. Sample growth and junction types

The growth procedures and the description of the different types of MTJs has already been explained in section 3.2 on the previous chapter although we didn't address then the V/MgO/Au junction in order not to spoil the plan.

Here we introduce V(100)/MgO(100)/Fe(100) (SIF) junctions as the building block for future coherent superconducting spintronics. Our epitaxial junctions between a superconductor (V) and a symmetry-filtering based FM (MgO/Fe) incorporate the key requisites for LRT generation such as high spin polarization and interfacial SOC.

We have studied the electron tunneling procedures in the previously mentioned SC-MTJs, namely: V/MgO/Fe (SIF), V/MgO/Fe/MgO/Fe (SIFIF) and Fe/MgO/V/MgO/Fe (FISIF). In addition, we have studied another type of tunnel junction which instead of having a ferromagnetic material, they have a normal metal instead (SIN). Because this new type of junctions don't present effects related to the

magnetization, we have taken these sample as "control samples" when studying superconducting spintronics.

4.2.1. Control samples V/MgO/Au

The fabrication of these samples has been carried out by the same group that made the samples mentioned in section 3.2. They were made by the group of professors Coriolan Tiusan and Michael Hehn within a collaboration project between the Magnetrans-UAM group and the Institute Jean Lamour, Nancy Universitè (France).

These control samples have a single-barrier and their complete structures are (contacted layers in red):

- MgO(100) substrate/MgO(10 nm)/Cr(2 nm)/V(40 nm)/MgO(2 nm)/Au(15 nm)

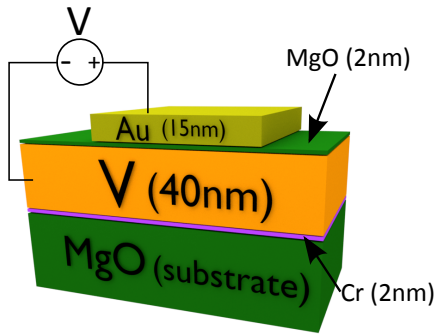

Figure 4.1: Realistic sketch of the control SC-TJs (SIN)

The control samples (see sketch in figure 4.1) were elaborated by molecular beam epitaxy (MBE) with the same procedure described in section 3.2. However these control samples are probably not epitaxially grown. It is difficult to assume that the gold specifically has been grown epitaxially on top of the MgO. The problem is that the Au has a very good thermal conductivity and when heated by electrons in the crucible it may start to evaporate with a very high deposition rate abruptly. This give rise often to a polycrystalline phase rather

than epitaxial. In order to crystallize, one should make further annealing which is not suitable because the barrier can be damaged in the process.

Having said this, we have studied two of these control samples which will be named as superconductor/insulator/normal metal (SIN) junctions. However we have to take into account that not being epitaxial implies that the tunneling through the junctions will not be coherent. SIN junctions have not been introduced in the previous chapter 3 because it was focused on ferromagnetism.

4.3. Experimental results

A total of 19 SC-MTJs have been measured in the course of this thesis. We start the description of the main experimental results by the basic experiment of IV curves in our samples to see how the conductance behaves in each of the three samples. Due to the experimental set-up particularities the chosen temperatures for most of the measurements have been 0.3 K (below T_C) and 10 K (above T_C). Nevertheless we have made a thoroughly study of the critical temperature of each of the samples, which is indeed shown after the conductance measurements. After that we will investigate the critical fields in order to understand better the measurements of magnetoanisotropic andreev reflection (MAAR) shown afterwards. The experimental results will finish with a discussion on the conductance anomalies observed on the DB-MTJs.

We will show the conductance values instead of the usual normalization by the normal (above gap) conductance in order to make a full comparison between them. Because we have already explained in the previous chapter 3.3 how the normal conductance behavior of these junctions is, we will concentrate in this chapter in the conductance below the superconducting gap. Bulk Vanadium has a superconducting gap value of $\Delta = 1.6$ meV[33] at $T = 0$ K. We need to recall also that the application of an external magnetic field will suppress the superconductivity (more in the out-of-plane direction than in the in-plane one) as well as changing the magnetization orientation of the

FM. Thereby some experiments have been specifically done at zero magnetic field.

4.3.1. Subgap electron transport

As it has been described in section 1.4, the electron transport in SC-TJs at energies near the Fermi level is the Andreev Reflection (AR) conductance mechanism (explained in section 1.4.3). Regarding the particles having a role in the conductance, the conventional AR involves singlet Cooper pairs (antiparallel spin alignment) whereas the unconventional AR involves triplet Cooper pairs (parallel spin alignment). We will try to differentiate between these two types of conduction mechanisms throughout this chapter.

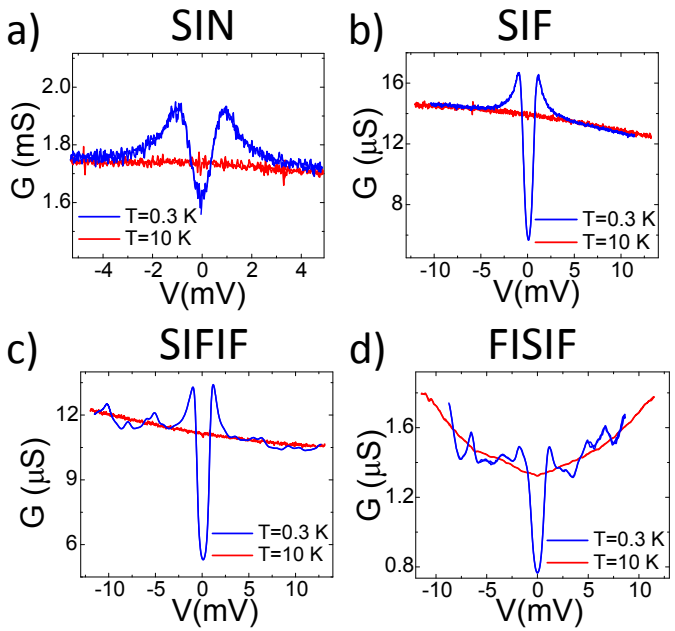

Figure 4.2: Conductance from each type the SC-MTJs measured at temperatures below and above T_C. The measurements were made at zero magnetic field and with the FM layers aligned parallel in-plane.

The conductance of the four different types of junctions measured

is shown in figure 4.2. All of them present a superconducting gap whose width is very similar around $\Delta \approx 1$ mV which is totally suppressed by temperature at $T = 10$ K. Regarding the overgap conductance, the differences between SIF, SIFIF and FISIF have been explained in section 3.3. The difference of three orders of magnitude between, for example the SIF junction (see figure 4.3), and the control SIN junction is due to the mentioned fact that the SIN junction is not epitaxial, thus coherent tunneling doesn't take place and there is neither symmetry filtering nor symmetry matching issues involved. Additionally the SIN junction has a much noisier conductance measurements preventing shot noise measurements being made in these type of samples. Because of this issues we will use the SIN junction only on exceptional comparisons and our main investigation will be focused on the SC-MTJs (SIF, SIFIF and FISIF). Brinkman's fits[9] made on SIN junctions give similar values as the ones shown in the previous chapter for SIF junctions of the barrier thickness and the barrier height.

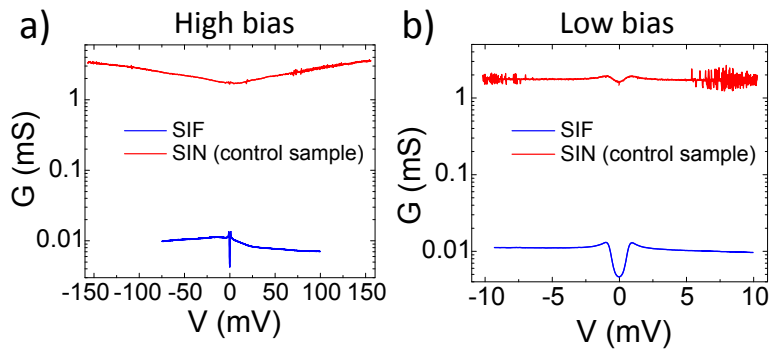

Figure 4.3: Conductance comparison between SIF and SIN junctions in the a) high bias and b) low bias regimes. The measurements were made at $T = 0.3$ K, at zero bais magnetic field and with the FM layer of the SIF junction aligned in-plane.

There are conductance anomalies in both the DB-MTJs that don't seem to be present on the SB junctions (SIN or SIF). We presume that their presence is related to triplet superconductivity and thereby we

are going to address them in a separate paragraph below. The depth of the conductance gap is different for each sample. For the case of the control sample (see figure 4.2a) the explanation for having a ratio between the normal state conductance (G_N) and the zero bias conductance (G_0) of $G_0/G_N = 0.9$ is attributed to the fact that the transparency of the barrier (see figure 1.16) is much higher (compared to the other samples) because the sample is not epitaxial. The depth of the gap in the other samples is much more pronounced (see figure 4.2b, c and d). On average the conductance ratio is roughly $G_0/G_N \approx 0.4$. Such a ratio is in principle not the expected of transport devices on the tunneling regime. We can try to fit conductance curves from the SB junctions to formula 1.9 from ref.[44] and formula 1.8 from ref.[38] which account for the conductance on a SIF and a SIN junctions respectively.

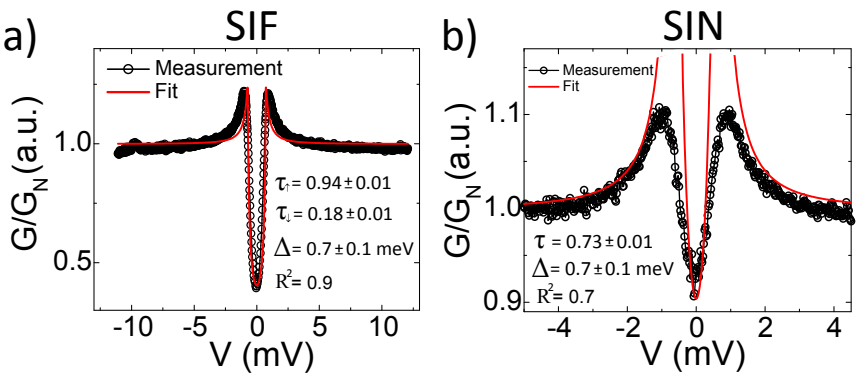

Figure 4.4: Conductance measurements (normalized by G_N) taken at $T = 0.3$ K on a) a SIF junction with fit to formula[44] 1.9 and b) a control SIN junction with fit to formula[38] 1.8 at zero magnetic field with the FM aligned in-plane.

The fitting values obtained on the SIF sample (see figure 4.4a) are, for the spin-up electron transmission $\tau_\uparrow = 0.94 \pm 0.01$, for the spin-down electron transmission $\tau_\uparrow = 0.18 \pm 0.01$ and the SC gap value $\Delta = 0.7 \pm 0.1$ meV. On the SIN sample where there's no spin degree of freedom involved (see figure 4.4b) the parameters are, for the electron transmission $\tau = 0.73 \pm 0.01$ and the SC gap value $\Delta = 0.7 \pm 0.1$ meV.

While the value of the SC gap roughly agrees with the measured one, the values of the transmission are near those of a metallic contact junction (direct contact $\tau \sim 1$). With the SIF transmission values we can calculate the spin current polarization $P = |\tau_\uparrow - \tau_\downarrow|/(\tau_\uparrow + \tau_\downarrow) = 68\%$ which agrees with the experimental values calculated on the previous chapter (see formula 3.1). We attribute the disagreement between Cueva's models[38,44] and the experimental results to the fact that the models don't take into account SOC interactions, which can flip the spin orientation, or coherent tunneling in the case of the SIF junction. In the case of the SIN junction, the poor quality of the interface in addition to being at finite temperature could be the reasons for the disagreement.

Now focusing only on the MTJs, we may summarize the discrepancies for the conductance measurements made at 0.3 K (the lowest we achieve in our set-up) and without any external magnetic field applied. The observed relatively large zero bias conductance in a junction with a high spin polarized Fe/MgO tunneling interface could be linked to the presence of spin-orbit fields. However, there could be other sources for spin-flip scattering such as e.g. magnetic impurities. Further below we will also refute the possibility of having poor quality junctions with the experimental results of the shot-noise measurements which show a perfect Fano factor$\sim$ 1 (see section 4.3.7) which corresponds to a Poissonian tunneling current.

Continuing the investigation we are going to study two important parameters of superconducting devices which are their critical temperature (T_C) and their critical field (H_C).

4.3.2. Critical temperature vs. magnetic state of the FM electrodes

The critical temperature (T_C) of a sample is an essential parameter which determines the temperature, without any external magnetic field applied, at which the superconducting material (Vanadium in this case) changes from superconductor to a normal metal. As we mentioned, bulk V has $T_C = 5.38K$[33]. Because we have investigated SC-MTJs, we are going to study the possible influence of the mag-

netization of the FM in the value of the T_C of each of the different junctions.

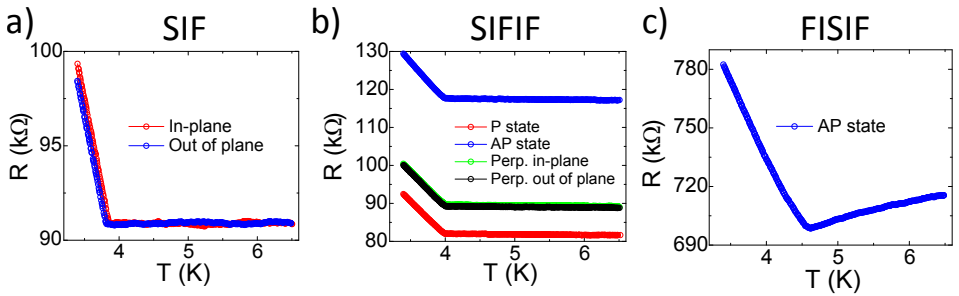

Figure 4.5: Resistance versus temperature measurements taken at zero magnetic field and at $V = 0.7$ mV on a) SIF, b) SIFIF and c) FISIF junctions. The legends indicate the magnetization orientation of the FM electrode(s).

Figure 4.5 shows the resistance of each type of sample dependence on temperature. Usually these measurements are taken at $V = 0.7$ mV in order to be in the subgap bias regime. The measurements were made by heating the sample up to 6.5 K. After that we wait for stabilizing temperature for 5 minutes. Finally we turn off the heater and let the sample cool down slowly at a temperature decrease rate of roughly 2 K/h. If we would do it the other way around which is starting from low temperature and heating up the sample we have thermoelectric effects that influence the results. In order to not influence the critical temperature transition, the measurements shown in figure 4.5 were made without any external magnetic field applied, thereby all the magnetic states indicated on the legends are remanent states.

In order to calculate the value of T_C we average several resistance vs temperature curves (see figure 4.5). Then we calculate the two slopes below and above the T_C value and from its intersection we obtained the value of T_C with a precision of $< 1\%$ (see figure 4.6). The results on the critical temperature show that the lowest T_C value is for the SIF, then the SIFIF and the highest is for the FISIF junction. The difference between SIF and SIFIF critical temperature is just about $0.1 - 0.2$ K however the difference between them and the FISIF junction is a

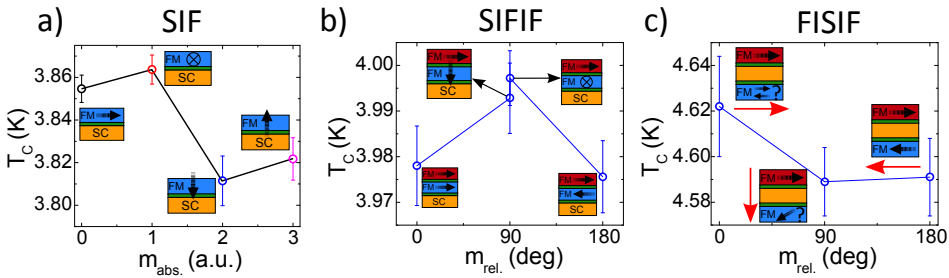

Figure 4.6: Critical temperature on each of the three types of SC-MTJs studied. Each point and its corresponding standard deviation has been taken averaging curves such as those on figure 4.5. Part a) shows T_C dependence on the absolute magnetization orientation on SIF. Part b) shows T_C dependence on the relative magnetization orientation on SIFIF. Part c) shows T_C on the FISIF junction, the red arrows depict the saturation field applied before removing the external magnetic field. Question marks indicate that the magnetization orientation is not clear on these two situations because on the FISIF junction the only possible remanent magnetization is AP state.

bit more than 0.5 K. We attribute this difference to the analysis of RHEED patterns (growth procedure 3.2) which show that the V has a better structural crystalline quality when grown in a sandwich between the two MgO barriers (FISIF) than when is not (SIF and SIFIF).

If we concentrate now in the individual types of samples, on the SIF samples (see figure 4.6a) T_C is clearly higher when the absolute magnetization is in-plane than when its out of plane. The reduction of T_C due to triplet pair generation is a standard explanation when a SC is attached to a spin-valve[148]. More studies show this reduction of T_C when the magnetization orientation is perpendicular to the junction's plane[154].

In the case of the SIFIF junction (see figure 4.6b) the highest T_C value is when the relative magnetization is perpendicular. This occurs when both magnetizations are perpendicular in-plane and if they are perpendicular out of plane. The increment of T_C comes from the fact that the perpendicularly magnetized FM soft layer layer has

more inhomogeneous magnetization when magnetized perpendicular than when magnetized in P or AP states[155]. When the temperature is decreased below T_C, the superconductivity is expected to first nucleate at the location where the stray field is minimum, that is, at the domain wall[156].

In the case of the FISIF junction as the remanent magnetization is the AP state, the value of T_C doesn't change very much depending on the saturation state previous to removing the external field. Differences on T_C in this type of junctions should be related to a slightly different remanent magnetic domain structure of the soft FM.

Summarizing, for the SC-MTJs where the remanent magnetization can be controlled (SIF and SIFIF), the critical temperature (T_C) clearly depends on the FM magnetization orientation. This dependence of the critical temperature is one of the best fingerprints of having LRT correlations in SC-MTJs[148]. The dependence of T_C on the magnetization may vary according to the particular characteristics (materials, layer arrangement, etc) of the structure studied[143].

4.3.3. Anisotropy of critical magnetic fields

We have obtained the critical fields on a SIF sample applying an external magnetic field and measuring IV curves at increasing external fields until the superconducting gap was fully suppressed. The results for this SIF junction showed that the critical field in the in-plane direction is $H_{c,\parallel} = 12$ kOe and for the out of plane direction $H_{c,\perp} = 4$ kOe (see figure 4.7a). The normalization of the conductance was $G_{Norm.} = (G_0(H) - G_0(H = 0))/(G_N - G_0(H = 0))$ where G_0 is the zero bias conductance and G_N is the zero bias conductance in the normal state.

Although we have only fully measured the critical magnetic fields on the SIF junction, we have partial measurements (see figure 4.7b) made on the SIN junction, which are very useful to compare the same effect of superconducting suppression but in a sample without the ferromagnetic interaction. From our results we can only indicate that the out of plane field dependence shows a very similar behavior whereas on the in-plane direction the gap seems to start increasing the first

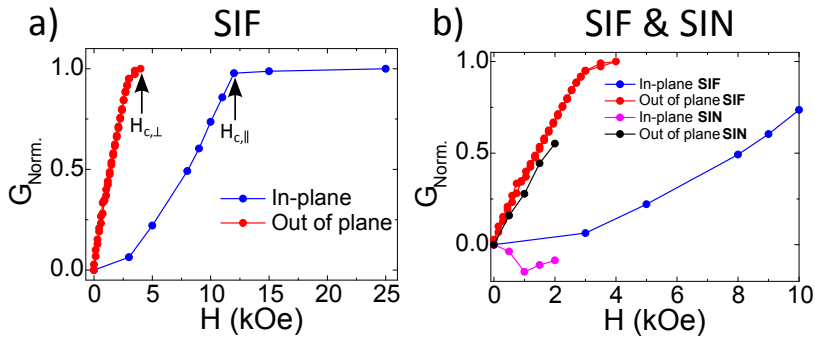

Figure 4.7: Normalized conductance dependence on the external magnetic field applied in a) SIF junction and b) in a SIN junction (SIF for comparison). Normalization is given by $G_Norm. = (G(H) - G_{min.})/(G_{max.} - G_{min.})$ where $G_{max.}$ is the normal conductance and $G_{min.}$ is the zero bias conductance without any magnetic field applied. The critical fields for the in-plane ($H_{c,\parallel} = 12$ kOe) and out of plane ($H_{c,\perp} = 4$ kOe) orientations are indicated with black arrows. Measurements taken at T=0.3 K.

point to quickly start suppressing following the same trend as the SIF junction.

4.3.4. Anisotropy of the zero bias conductance in SIF junctions in the presence of an external magnetic field

In order to prove long range triplet (LRT) correlations, we explore the zero bias conductance anisotropy between the superconductor and the ferromagnet with two different competing zero field magnetization states (in-plane or out-of-plane[100]). The observation of magnetic anisotropy is a true fingerprint of SOC. With the help of the model developed by Petra et al.[45], which describes the magnetization direction control over the LRT correlations, we suggest how these LRT conductance channels as well as normal quasiparticles contribute to the conductance.

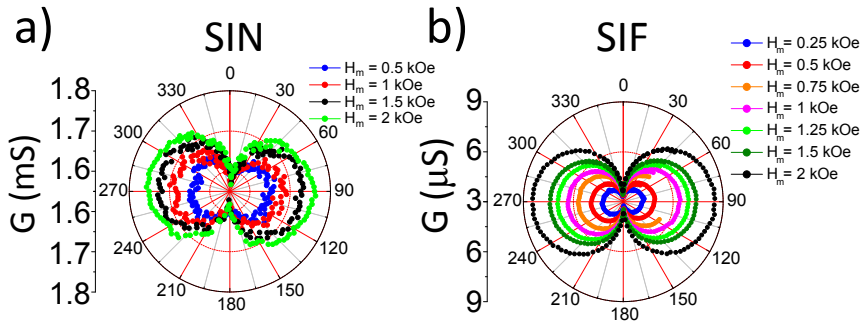

Figure 4.8: Zero bias conductance dependence on a constant magnetic field rotation along the XZ plane on a) the SIN and b) the SIF junctions. Measurements taken at $T = 0.3$ K.

When the magnetization is rotated out of plane, the electron's probability to scatter depends on the relative angle between the SOC field and their spin (oriented along the magnetization direction). So the conductance depends on the out of plane angle and leads to the magnetoanisotropic Andreev reflection (MAAR) whereas for an in-plane rotation there is almost no effect of the (relatively small compared to $H_{c,\parallel}$) external magnetic field on the SC (see figure 4.9). When rotating the field in-plane, larger fields in module might cause a small shifting of the conductance due to a possible small misalignment ($< 2°$) of the external magnetic field with the plane of the sample. We can see how at temperatures above T_C there is a barely noticeable effect of the misalignment because there is no superconductivity suppression (see figure 4.9b). Zooming up to the resolution limit of the measurement ($\sim 0.03\%$) we start observing a TAMR effect (see figure 4.9c) which is expected to be below our resolution limit ($\sim 0.01\%$)[45].

As we have mentioned, in order to change the magnetization orientation we need to apply an external magnetic field. From a measurement of the zero bias conductance dependence on the magnetic field rotation (see figure 4.8) we can see a symmetrical response. Figure 4.8 shows an out of plane rotation, in this case along the XZ plain, we can see how perpendicular magnetic fields suppress the superconductivity for both SIN and SIF junctions.

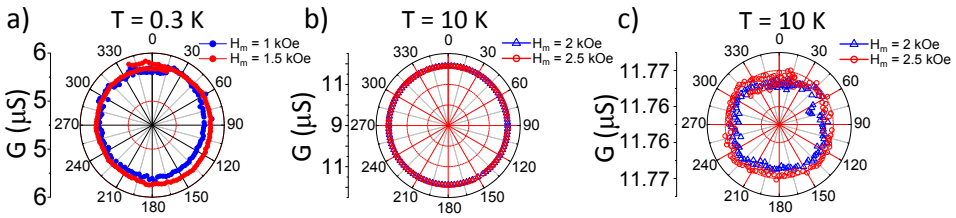

Figure 4.9: Zero bias conductance dependence on a constant magnetic field rotation along the YZ plane on the SIF junction. Part a) shows measurements taken at $T = 0.3$ K at two different magnetic fields. Part b) shows measurements taken at $T = 10$ K at two different magnetic fields. Part c) zooms the zero bias conductance at $T = 10$ K to the limit of resolution of the measurement ($\sim 3 \cdot 10^{-4} \mu$S). A partial suppression of the superconductivity due to a small misalignment of the field plane rotation is present and only seen in part a).

4.3.5. Anisotropy of the zero bias conductance in SIF junctions without an external magnetic field

Ideally, we would compare the external magnetic field rotation of the SIF junction (see figure 4.8b) straightforward with the MAAR as shown in figure 1.20 from ref.[45]. However the MAAR accounts for the magnetoresistance dependence on the magnetization orientation. By applying an external field we are, at the same time changing the magnetization orientation and suppressing the superconductivity. Thereby we have designed an experiment on the SIF junction taking advantage of the fact that we have studied the magnetic remanent states of our FM electrodes (see figure 4.10). The experiment consists in applying a strong saturating magnetic field, then removing the field leaving the magnetization saturated and start measuring from zero field increasing it slowly to see the magnetization behavior with almost no interaction on the superconductivity.

The results from figure 4.10 clearly show that the in-plane measurements are practically unaltered whereas the out of plane measurements show a difference which we attribute to the magnetization asymmetry

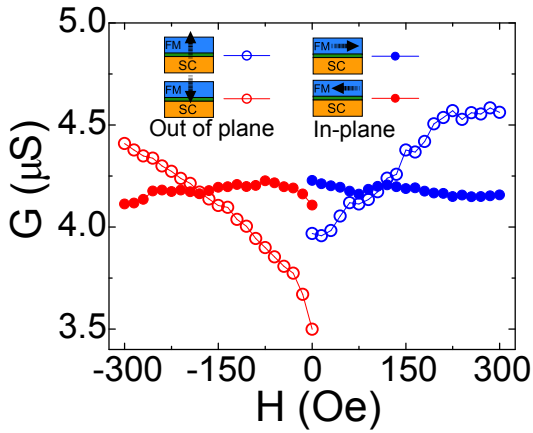

Figure 4.10: Zero bias conductance measurement on the SIF junction taken at $T = 0.3$ K. Full (empty) dots are for in-plane (out of plane) applied magnetic fields. Blue (red) dots correspond to a positive (negative) magnetic field direction. The black arrows on the junction sketches depict the remanent magnetization orientation.

explained in the previous chapter. As we discussed, the magnetization at low temperatures in these type of MTJs has an asymmetry when applying perpendicular fields (see figure 3.18). Therefore, the out of plane magnetization in figure 4.10 is only effective for negative applied fields (red full and empty dots). From the zero bias conductance values at zero external magnetic field we obtain a MAAR $\approx 17\%$ which agrees with the theoretical calculations shown below. Moreover, focusing now on the remanent in-plane and out of plane magnetization for the negative fields (red dots from figure 4.10), the out of plane zero bias conductance is lower than the in-plane zero bias conductance. The lower the conductance the more robust the superconductivity of the junction is, thereby there's an increment of the strength of the superconductivity when the magnetization is oriented out of plane which totally agrees with the theoretical prediction of having LRTs[52].

Additionally to the MAAR results, the LRT coherent pair penetration and confinement has been reflected in the magnetic state dependence of the finite bias conductance resonances observed in the SIFIF

structure.

4.3.6. Above gap conductance anomalies (CAs)

This section discusses in more details the above gap conductance anomalies (CAs) as an alternative source of information on LRT transport in epitaxial superconducting spintronic devices.

As we have mentioned, conductance curves in DB-MTJs (4.2c and d) show some conductance anomalies (CAs) that don't seem to appear in SB-MTJs (4.2b) or in SIN junctions (4.2a). We observe that CAs appear when there's a SIF structure having the Fe sandwiched between two MgO layers. On the SIFIF junction the middle FM is sandwiched between the MgO barriers, and in the case of the FISIF junction the soft Fe layer is sandwiched between the buffer MgO layer (substrate) and the first MgO barrier. In order to verify the possible relation between those CAs and LRT correlations, we are going to analyze the CAs features as a function of temperature, relative orientation of the FM electrodes and applied magnetic field for both DB-MTJs (SIFIF and FISIF).

We'll start discussing the results obtained on the SIFIF junctions which have a TMR about 40%. The magnitude of these highly reproducible CAs depend on the relative magnetic alignment of the electrodes (see figure 4.11a). One could control the position of CAs in the SIFIF system as long as applied bias re-distributes between P and AP alignments. The CAs amplitude decrease with increasing temperature up through T_C being hardly detected at temperatures twice the critical temperature (see figure 4.11b).

Looking now at figure 4.11c one observes the normalized CAs to be reduced in the AP state and maximum in the saturated P state. Interestingly, the normalized CAs amplitude notably depends on the type of perpendicular magnetic orientation, being stronger when the soft FM is oriented out of plane with respect to the in-plane orientation. Such observation is in line with the interpretation of the CAs as originated from electron-hole (e-h) interference within MgO/Fe/MgO. Indeed the reduced zero bias conductance for the corresponding (out of plane) magnetic alignment as observed in zero field MAAR (see figure

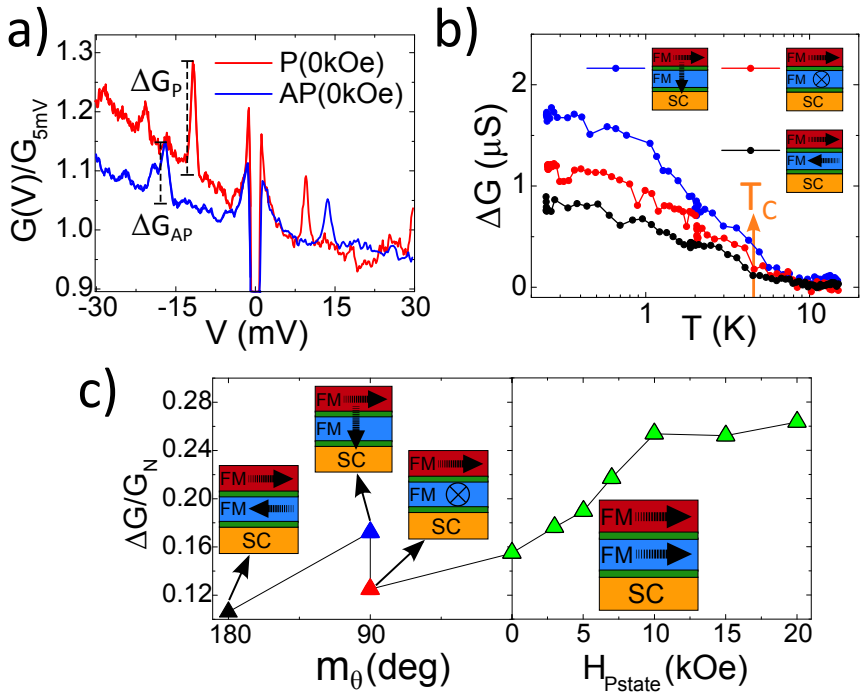

Figure 4.11: Conductance anomalies on the SIFIF junction. Part a) shows the conductance normalized (by G_N) at P and AP states at T=0.3 K. The selected peaks ΔG_P and ΔG_{AP} for the analysis are at biases around $-[10..15]$ mV. Part b) shows the temperature dependence of the selected CA peak amplitudes for different remanent magnetic states. Part c) shows the magnetic field dependence, as a function of the magnetic state and the applied magnetic field, of the CA amplitudes normalized by G_N at T=0.3 K.

4.10) provides higher effective barrier at the SIF interface. Therefore stronger CAs as a consequence of higher interference probatility from the multiple *e-h* or electron reflections. The presence of a saturation of the normalized CAs amplitude with no suppression behavior even at very strong magnetic fields applied (up to 20 kOe) suggests that the superconducting quasiparticle implicated in the CAs generation is not much affected by the intensity of the external magnetic field. This fact supports the possibility of having triplet Cooper pairing penetrating

into the FM (LRTs).

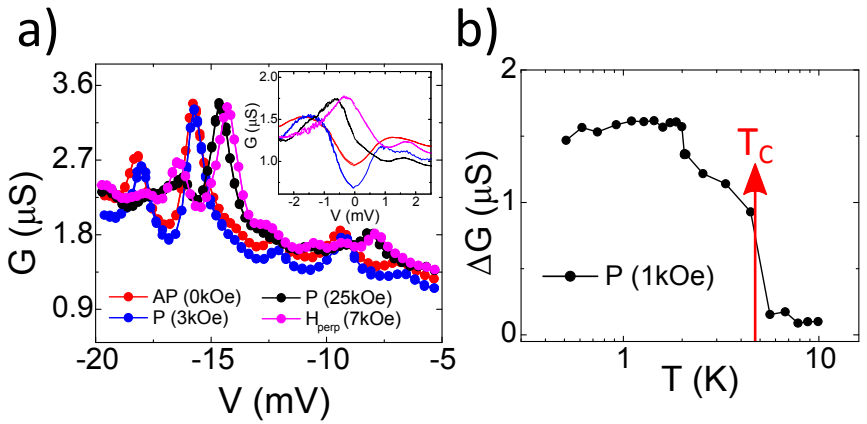

Figure 4.12: CAs on the FISIF junction at T=0.3 K. Part a) shows the most pronounced CAs at different magnetic states and with different external field intensities. Inset zooms the below gap conductance region for the corresponding external fields remarked by the same coloured lines. Part b) shows the temperature dependence of the main CA peak amplitude measured in the P state with 1 kOe field applied. The vertical red arrow points out the junction's superconducting T_C.

On the other side, CAs in the FISIF structures show a much weaker dependence on the magnetic state (P vs. AP), seemly due to the above discussed antiferromagnetic coupling between electrodes (see figure 4.12a). In figure 4.12a one can see the CAs even when the magnetic field suppresses the SC gap (see inset of figure 4.12a). Figure 4.12b shows how the CAs emerge with decreasing temperature at values below the the FISIF superconducting transition (T_C). The evolution with temperature of the CAs amplitude is in general similar to what we have discussed in the case of the SIFIF structure. However, due to the strong antiferromagnetic coupling through the superconducting Vanadium, the soft Fe electrode direction could not be reoriented in small fields the same way as it was done in the SIFIF junction.

We have not yet been able to model theoretically the behavior of the CAs. Therefore we are going to discuss their possible physical

origin looking at a similar behavior taking place in other epitaxial superconducting-magnetic junctions (SC-MJs). There is an extensive study developed by Visani *et al.*[39,50] where quasiparticle and electron interference effects in the conductance across SC/FM metallic interfaces directly demonstrate the LRT correlations. In their experiments they study different structures involving a high T_C *d*-wave SC ($YBa_2Cu_3O_7$) in direct contact with a half-metallic ferromagnet ($La_{0.7}Ca_{0.3}MnO_3$).

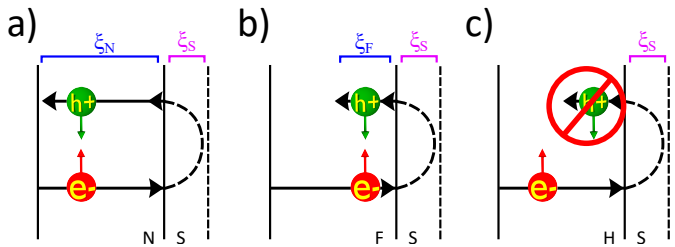

Figure 4.13: Propagation of the phase-correlated particles according to the conventional Andreev reflection in the case of a) a normal metal (long-range), b) a ferromagnetic metal (short-range), c) a half metal (forbidden). Figure adapted from ref.[39].

The authors in ref.[39] find resonances in conductance which are due to interactions between particles of the same species. If the CAs appear due to the interaction between electrons (or holes) inside the normal metal or FM they are McMillan-Rowell resonances[157,158] (MMR). However, if the CAs apper due to the interference of SC quasiparticles inside the SC film they are Tomasch resonances[159,160] (TR).

When a SC and a FM are brought together, the *proximity effect* influences both parts of the interface, the FM interface becomes somewhat superconducting and the SC interface becomes ferromagnetic due to the FM exchange splitting. Moreover, when two FM layers are present, the relative magnetization of the two FM electrodes can be used as a magnetoresistive probe to study the characteristics of the SC-MTJ. From a conventional Andreev reflection point of view, depending if the metal is normal (NM), ferromagnetic (FM) or half metal (HM) (100% spin polarization), the propagation of particles is

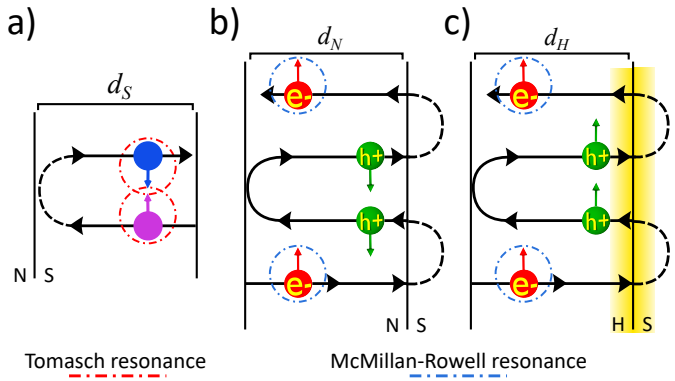

Figure 4.14: Interferences occur only between two particles of the same species (hole-hole, electron-electron or between two quasiparticles). a)TR at a N/S interface. b)MRR at a N/S interface and c) at a H/S interface. The interfering particles are enclosed in dot-dashed circles. The shaded area in c) means that the interface is spin-active. Note that in the non-superconducting side (N or H) particles have 'pure' electron (or hole) character, conversely that in the superconducting side each quasiparticle is a 'mixture' of both electron and hole states (although one predominant over the other). Figure adapted from ref.[39].

respectively long-rage ξ_N, short-range ξ_F or forbidden. In clean metals, at low temperatures, ξ_N can be micrometers long whereas in weak ferromagnets ξ_F is only a few nanometers[39] (see figure4.13). In the extreme case of a HM, Andreev reflection is strictly forbidden owing to the zero DOS at the Fermi level within the minority spin band, thereby hindering the penetration of superconducting correlations (see figure 4.13c). However, in the case of having a so-called 'spin-active' S/F interface, this produces spin-flip and spin-mixing processes which permits the flip of the leaving hole particle (see figure 4.14c).

The authors in ref. find experimentally two distinct sets of geometrical resonances in SFS junctions (see figure 4.15), a long-period and a short-period one, which they identified respectively as TR and MMR. As mentioned, the TR result from quasiparticle interferences in the SC side of the interface (see figure 4.14a). The incident electron-like

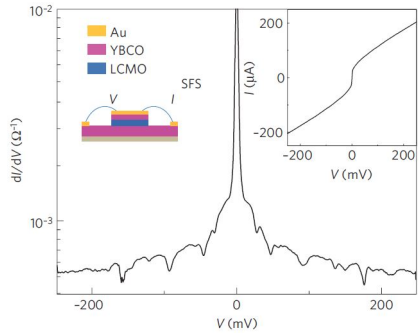

Figure 4.15: Differential conductance as a function of the voltage for a trilayer YBCO (15 nm)/LCMO (12 nm)/YBCO (30 nm) (SC/HM/SC) junction. The inset shows the IV curve from which the conductance has been obtained. Figure adapted from ref.[39].

quasiparticle (a 'mixture' of a hole and an electron in which the latter is predominant[161]) and its hole-like counterpart. The energy at which the quasiparticles interfere is given by:

$$V_n = \sqrt{\Delta^2 + (nh\nu_F^S/2d_S)^2}; \quad \text{with } n = 0, 1, 2, \ldots$$

where Δ is the energy gap, ν_F^S is the Fermi velocity in the SC and d_S its thickness. This interference thereby appears as a nearly periodic series of oscillations[161]. Conversely, the MMR arise as a consequence of resonances in the non-SC side of the interface (see figure 4.14b,c). The interactions in this side of the interface come from electron-electron or hole-hole interactions (particles of the same species). Therefore, for the interference to occur in the normal-metal (or FM), the Andreev-reflected hole must subsequently travel a distance d_N to the opposite interface and, after being normal-reflected, propagate back to the SC/NM interference to undergo a second Andreev reflection. Here the electron-electron (hole-hole) interference is given by:

$$V_m = V_0 + mhv_F^N/4d_N; \quad \text{with } m = 0, 1, 2, \ldots$$

where v_F^N is the Fermi velocity in the NM and d_N its thickness[157].

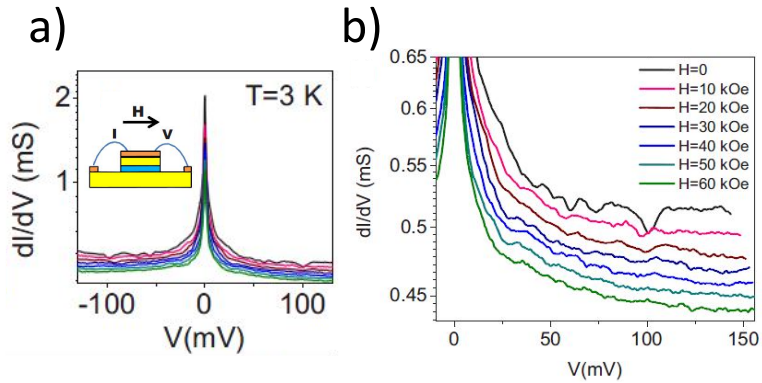

Figure 4.16: Part a) shows the differential conductance across a Au/YBCO(15 nm)/LCMO (12 nm)/YBCO (30 nm) junction (area 32 μm^2), measured at $T = 3$ K for different magnetic field applied parallel to the film plane. Inset depicts the junction structure. Part b) zooms the curves shown in a). Figure adapted from ref.[50].

In the following study made by Visani *et al.*[50] they study the magnetic field influence on the proximity effect on the same YBaCuO/LaCaMnO (SC/HM) structures. The authors found that the conductance features that evidence long-range proximity effects are essentially insensitive to moderate magnetic fields (see figure 4.16). Moreover, this spectral fingerprints of the long-range proximity effect fade away for magnetic fields well above the critical field of the SC used (LCMO). This is consistent with our own experimental results where we don't see a suppression of the CAs when applying a moderate/strong (20 kOe) magnetic field (see figure 4.11).

To conclude this section, although the CAs on our Vanadium's SC-MTJs don't seem to present any periodicity, their source could well be MMR and TR. Also CAs could appear from just the interference of coherent quasiparticles within a bounded structure. Among such mechanisms could be even some interference phenomena inside the MgO barrier[17]. Possibly the fact that electrons tunnel coherently, having a spin-active interface and spin-orbit interaction interferes with the periodic nature of MRRs and TRs. Before finishing the experimental

results section we will discuss a little of the shot noise measurements performed in our SC-MTJs.

4.3.7. Barrier quality characterization through shot noise

The aim of analyzing shot noise in these SC-MTJs is to demonstrate the high quality of the barriers conforming the epitaxially grown junctions. Doubts on the barrier quality might arise when one observed the finite zero bias conductance in our SC-MTJs. The first impression would be to attribute this just to pinholes inside the barrier. Additionally we will demonstrate how the shot noise can be used as a source of characterization of the samples, in particular obtaining the TMR from shot noise measurements at different magnetic states.

The shot noise through a DB junction with FM electrodes can be calculated using a model of sequential tunneling[111,162]. The influence of resonant tunneling is not taken into consideration. The experimental Fano factor for the P and AP magnetic configurations could be used to calculate the TMR ratio. The corresponding value shows a good agreement with the experimental TMR (in the limit of strong spin relaxation). Following the calculation of shot noise in the presence of spin relaxation[163], the Fano factor is given by:

$$F = \frac{R_{2\uparrow}R_{2\downarrow}(R_{1\uparrow}+R_{1\downarrow})^2 + R_{1\uparrow}R_{1\downarrow}(R_{2\uparrow}+R_{2\downarrow})^2}{[R_{1\uparrow}R_{1\downarrow}(R_{2\uparrow}+R_{2\downarrow}) + R_{2\uparrow}R_{2\downarrow}(R_{1\uparrow}+R_{1\downarrow})]^2}$$

where R is the partial resistance of each of the two barriers (indices 1,2) and of each of the spin directions (up $\uparrow$ and down $\downarrow$).

In the case of a SIFIF structure the two barriers separate different systems. The SIF barrier resistance (for bias above the SC gap) is not influenced by the magnetic configuration of the FM electrodes. On the other side, the FIF barrier will have different resistances for the P and AP configurations. Defining $\alpha_{P,AP} = R_{FIF}^{P,AP}/R_{SIF}$ and the total resistance being:

$$R_T = R_{FIF} + R_{SIF} = (\alpha_{P,AP} + 1)R_{SIF}$$

The Fano factor is given by:

$$F_{P,AP} = \frac{1 + \alpha_{P,AP}^2}{(1 + \alpha_{P,AP})^2}$$

And the TMR is then:

$$TMR = 100 \cdot \frac{\alpha_{AP} - \alpha_P}{1 + \alpha_P}$$

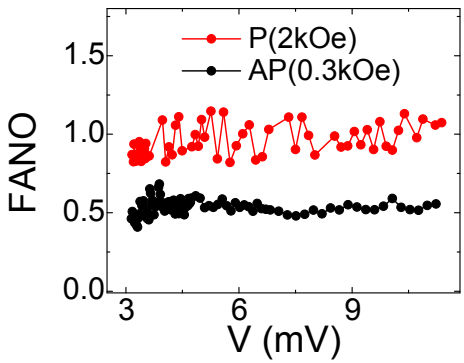

Figure 4.17: Bias dependence of the Fano factor in P state (2 kOe) and AP state (0.3 kOe) for the SIFIF sample measured at T=0.3 K for biases above the SC gap.

By using values of the averaged over bias Fano factors for different magnetic states shown in figure 4.17 with $F_P = 0.94 \pm 0.1$ and $F_{AP} = 0.58 \pm 0.1$, one gets an evaluation for the TMR of about 40% which is reasonably close to the TMR experimentally measured from conductance.

The fact that the Fano factor is close to 1 indicates that electrons tunneling follow a Poissonian distribution, which confirms that the sample has a high quality and that it has been grown fully epitaxial. The Fano factor is presented only for biases above the SC gap where in principle the Andreev reflection conductance is negligible.

With this we conclude the experimental results part and now we address the theoretical model which aims to simulate the conductance

behavior of electrons tunneling at energies below the SC gap and the MAAR dependence on the FM magnetization and the external magnetic field.

4.4. Modeling spin-triplet transport generated by a single FM in the presence of spin-orbit interaction

Historically, the first theoretical proposal of LRT generation inside a SC/FM structure in the presence of SOC was given by Bergeret *et al.*[52] as we mentioned in the introduction chapter. The proposal studies the long range triplet transport in the diffusive transport regime where it accounts for a deeper penetration of the superconducting quasiparticles inside the FM layer if the particles are triplet cooper pairs in contrast to the classical cooper pairs. The proposed system consists in a superconductor-ferromagnet hybrids which present SOC resulting from either an intrinsic property of materials without inversion symmetry or from interfaces between different materials[51]. The main conclusion from ref.[52] is that in order to have LRT correlations in SC/FM junctions, the presence of SOC is necessary as well as the possibility to have a perpendicular to the interface magnetization.

Because ref.[52] does not propose any particular experimental observation of LRT, we have followed the work of Högl *et al.*[45] which accounts for a change in the mangetoanisotropic Andreev reflection due to having LRT correlations.

4.4.1. Modeling conductance anisotropy in ballistic transport regime

The following theoretical model has been developed by the groups of Prof. Jaroslav Fabian with the help of Petra Högl (University of Regensburg) in Germany, Prof. Alex Matos-Abiague and Prof. Igor Zutiċ (University at Buffalo) in USA. The numerical model aims to simulate SIF structures in the presence of spin-orbit interaction (SOI).

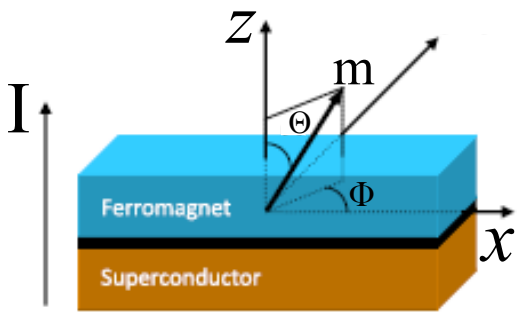

Figure 4.18: Theoretical model sketch showing the reference system used (which is rotated from the experimental one). Figure adapted from ref.[45]

To model the SIF tunnel junction, considering epitaxial-quality junctions in which ballistic transport regime is applicable, the general BTK formalism[45] has been used. The FM and SC layers are described by two semi-infinite regions at $z < 0$ and $z > 0$, respectively. At $z = 0$ there's a flat interface that accounts for the insulating MgO layer which includes a delta-like potential barrier $V_0 d\delta(z)$, with effective height V_0 and width d (see figure 4.18). For the clarification of the reader, the model's coordinate system depicted in figure 4.18 is rotated from the experimental one. The full theoretical formalism is described further below.

As we have mentioned, the observed relatively large zero bias conductance in a SIF junction with a highly spin polarized Fe/MgO tunneling interface could be linked to the presence of SOC fields. When searching for these SOC fields, the true fingerprint is the observation of magnetic anisotropies. In figure 4.19a one can see the zero bias conductance when the magnetization is rotated in a plane perpendicular to the interface at 0.3 K. The corresponding out of plane MAAR[45], which is defined as:

$$MAAR(\Theta) = \frac{G(0) - G(\Theta)}{G(\Theta)} \tag{4.1}$$

is presented in figure 4.19b. It exhibits a huge out of plane MAAR

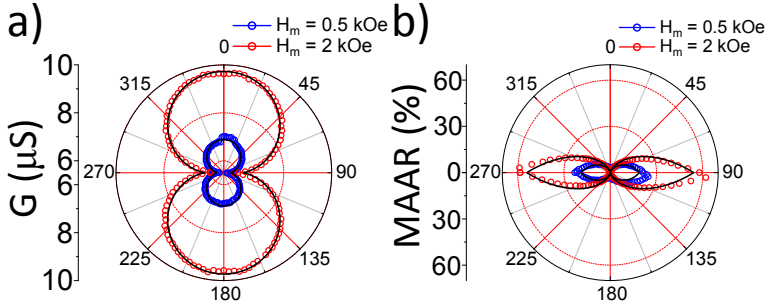

Figure 4.19: a) Out of plane zero bias conductance anisotropy measured at T=0.3 K applying a field of $H_m = 0.5$ kOe (empty blue dots) and $H_m = 2$ kOe (empty red dots) compared to the fits from the phenomenological model including magnetic field effects (**black** lines). b) Out of plane MAAR angular dependence measured at T=0.3 K applying a field of $H_m = 0.5$ kOe (empty blue dots) and $H_m = 2$ kOe (empty red dots) compared to the fits from the extended BTK[32] model with $\alpha = 34.5$ eVA^2 (**black** lines) and the phenomenological model including magnetic field effects (red and blue lines).

amplitude up to 60% and isotropic conductance with respect to in-plane rotations. From this one can conclude that a Rashba SOC field is present at the tunneling interface due to the structure inversion asymmetry of the tunnel junction and the corresponding potential gradient along the z-direction. The field is of the form:

$$\boldsymbol{w}_R = (\alpha k_y, -\alpha k_x) \tag{4.2}$$

with α the Rashba SOC parameter and $\boldsymbol{k}_{\parallel} = (k_x, k_y)$ the in-plane wave vector. It lies in a plane parallel to the interface and is rotationally symmetric in the plane. Therefore, the scattering probability is independent of the orientation of the magnetization in-plane. When the magnetization is rotated out of plane, the electron's probability to scatter depends on the relative angle between the SOC field and their spin (oriented along the magnetization direction). So the conductance depends on the out of plane angle Θ and leads to the MAAR.

The calculated angular dependence of the conductance and MAAR

are presented in figures 4.19a and 4.19b respectively. The SOC parameter α in eq. 4.2 as been used as the fitting parameter and realistic model parameters. From the phenomenological model has been derived analytical expressions for the angular dependence of the conductance:

$$G(\Theta) = G_0 + g_\alpha^{(2)}\alpha^2(1 - \cos 2\Theta) \tag{4.3}$$

and the MAAR:

$$MAAR(\Theta) = \frac{g_\alpha^{(2)}\alpha^2(\cos 2\Theta) - 1}{G_0 - g_\alpha^{(2)}\alpha^2(\cos 2\Theta) - 1} \tag{4.4}$$

which are valid up to second order in SOC and contain the real, SOC independent coefficient $g_\alpha^{(2)}$. Focusing on the angular dependence of the MAAR there is a clear discrepancy between theory and experiment. From the result of the phenomenological model its extracted that the agreement is improved if $g_\alpha^(2)\alpha^2$ is large enough so that it is no longer negligible compared to G_0 in the denominator of eq. 4.4. However, fitting the full model shows that this situation is not reached even with large SOC parameters. Instead it gives $g_\alpha^(2)\alpha^2 \ll G_0$ and $MAAR(\Theta) \approx g_\alpha^(2)\alpha^2/G_0(\cos 2\Theta - 1)$ for the angular dependence. The reason for the deviation of the model from the experimental results is that it does not take into account effects of the external magnetic field apart from aligning the magnetization orientation. **There are two effect which play a role namely orbital effects on the charge carriers and partial destruction of superconductivity due to creation of vortexes**.

Let's start with the **orbital effects**. Charge carriers in a magnetic field, which is perpendicular to their propagation direction, experience Lorentz force which compels them on cyclotron orbits. When the magnetic field is tilted away from perpendicular direction, these orbits become helicoids around the magnetic field direction and finally vanish when field and propagation directions are parallel. The deflection from their initial propagation in z-direction reduces their kinetic energy in that direction and increases the one in the x and y directions which effectively increases the tunnel barrier. This effect has been included

in the model by shifting the initial wave vectors in x and y directions in the Andreev reflection probability and the SOC field (details shown further below). The shift depends on the magnitude and the direction of the field and introduces and additional contribution to the conductance which depends linearly on the Rashba SOC α and the magnetic field H and has an extra angular dependence:

$$G_{orbital} = g_{\alpha}^{(1)} \alpha H (1 - \cos 2\Theta) \tag{4.5}$$

with $g_{\alpha}^{(1)}$ the real expansion coefficient. The orbital contribution increases linearly with the magnetic field for in-plane orientations and vanishes for an out of plane field. The quadratic terms in H are neglected.

Now let's consider the effect of the **external magnetic field on superconductivity**. V is a type II superconductor so its penetration depth is larger than the coherence length and therefore vortexes can be formed. This means that SC is partially destroyed where a magnetic flux quantum enters but around the vortex superconducting currents keep the field out and SC is preserved there. In a thin SC film there are two different critical field values which has been measured experimentally, the critical perpendicular field $H_{c,\perp} = 4$ kOe and the parallel critical field $H_{c,\parallel} = 12$ kOe. So, for the experimentally applied fields shown in figure 4.19, in the out of plane configuration is already large enough to partially suppress SC whereas for the in-plane orientation almost no effect of the external field on the SC should be present. The partial destruction of superconductivity by magnetic flux quanta can be modeled by considering two conduction channels, a superconducting one G_S and a normal one G_N, where the superconducting (normal) channels decreases (increases) linear with the applied field[164]. To account for the different on-set of this effect for perpendicular and parallel fields an angular dependence has been included and the appearance of vortexes for in-plane fields has been neglected:

$$G(V, \Theta, h) = h|\cos\Theta| G_N + (1 - h|\cos\Theta|) G_S \tag{4.6}$$

with $h = H/H_{c,\perp}$ and $G_{N/S}(V, \Theta) = G_0^{N/S}(V) + G_{\alpha}^{N/S}(V)(1 -$

$cos2\Theta$). Combining eqs. 4.3 and 4.5 one can get $G_{\alpha}^{N/S}(V) = g_{\alpha,N/S}^{(1)}\alpha H + g_{\alpha,N/S}^{(2)}\alpha^2$ for normal (N) and superconducting (S) channels. From the experimental data in figure 4.8b (SIF junction) one can assume for the zero bias conductance that $G_{0/\alpha}^{N} \approx 2G_{0/\alpha}^{S}$ and arrive to the final results from the phenomenological model (dropping the superscript S from now on) for zero bias conductance:

$$G_{ZB}(\Theta, h) \approx G_0 + G_\alpha(1 - \cos 2\Theta) + h|\cos\Theta|(G_0 + G_\alpha - G_\alpha \cos 2\Theta) \tag{4.7}$$

and out of plane MAAR:

$$MAAR(\Theta, h) = \frac{hG_0 - h|\cos\Theta|(G_0 + G_\alpha - G_\alpha\cos 2\Theta) + G_\alpha(\cos 2\Theta - 1)}{h|\cos\Theta|(G_0 + G_\alpha - G_\alpha\cos 2\Theta) + G_0 - G_\alpha(\cos 2\Theta - 1)} \tag{4.8}$$

in the presence of orbital effects and vortex creation in the SC due to the external magnetic field. As mentioned, figure 4.19a shows the results of fitting the conductance from eq. 4.7 to the experimental data. There are three fitting parameters h, G_0 and G_α so by using the data points at $G(0°)$, $G(45°)$ and $G(90°)$ the parameters are determined for two values of the magnetic field ($H = 0.5$ kOe: $h = 0.155$, $G_0 = 6.06\ \mu S$, $G_\alpha = -0.144\ \mu S$; $H = 2$ kOe: $h = 0.745$, $G_0 = 5.51\ \mu S$, $G_\alpha = 0.290\ \mu S$). The MAAR is computed using eq 4.8 and is presented in figure 4.19b. Both, conductance and MAAR angular dependence exhibit a very good agreement with the experiment. The fitting parameter h indicates how close the applied field is to the critical perpendicular field. Comparing the extracted rations of 16% and 75% for $H = 0.5$ and $H = 2$ kOe respectively, to the measured value of the critical perpendicular field ($H_{c,\perp} = 4$ kOe) one can get a reasonable estimation for the influence of the vortexes. From the fitting parameters for the unperturbed conductance G_0 and the one induced by SOC and orbital effects G_α we see $G_\alpha \ll G_0$, which is the reason why almost no increase of the conductance is observed for in-plane and SOC and orbital effects alone do not cause the deviation of

the angular dependence from $MAAR(\Theta) \propto \cos 2\Theta - 1$. Note that G_α changes sign when the field dependent orbital contribution (eq. 4.5) becomes larger than the quadratic SOC term $g_\alpha^{(2)}\alpha^2$. Control measurements in SIN junctions support the presence of both orbital effects and vortexes since we observe still uniaxial out of plane anisotropy. If magnetic fields are not included the spin imbalance of a FM is necessary to have finite MAAR. In a non-magnetic tunnel junction, orbital effects can introduce a similar angular dependence. Furthermore we also see a linear increase of the out of plane conductance with increasing field and the anisotropy amplitude (see figure 4.8a) which we get from the angular dependent two channel model:

$$ASR(90°, h) = \frac{hG_0 - 2G_\alpha}{G_0 + 2G_\alpha} \tag{4.9}$$

when $G_\alpha \ll G_0$ and now $G_\alpha(V) = g_\alpha^{(1)}\alpha H$. This effect has been called anisotropic superconducting resistance (ASR). As mentioned, the quality of the SIN junction is worse than the SIF junction and the data is more noisy but the main trends confirm a clear ASR magnitude about 5-20%.

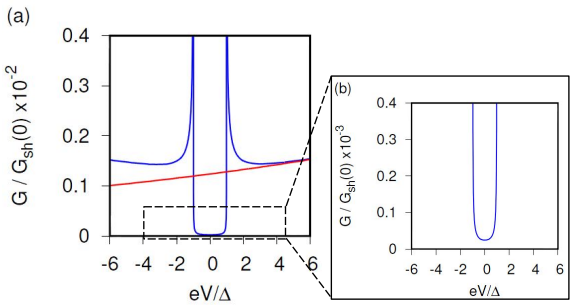

Figure 4.20: Calculated conductance normalized by the Sharvin conductance (G_{sh}) of the SIF structure from the extended BTK model for the FM magnetized in-plane. The modeling parameters are discussed in text.

The calculated normalized conductance for the superconducting and normal state is shown in figure 4.20. The normalization has been

made dividing by the Sharvin conductance value (G_{sh})which corresponds to the conductance on the ballistic regime. The modeling parameters used are: Fermi wave vectors $k_F = 0.805 \times 10^8$ cm^{-1} for Fe and $q_F = 0.66 \times 10^8$ cm^{-1} for V, the effective masses are $m_{Fe} = m_0$ and $m_V = 4.3m_0$ with m_0 the free electron mass, the spin polarization of Fe is given by $P = (\Delta_{xc}/2)/\mu_{Fe} = 0.7$, where $\mu_{Fe} = \hbar^2 k_F^2/(2m_{Fe})$, the SC pair potential is $\Delta = 1.6$ meV, the barrier height $V_0 = 1.47$ eV and width $d = 1.7$ nm and the Rashba SOC is $\alpha = 34.5$ eVA^2. Figure 4.20 and its inset shows that the extended BTK model gives a similar voltage dependence as observed in experiments. The magnitude of the zero bias conductance is about 300 times smaller than the experimental one ($G_{exp} \approx 0.08G_{sh}$) and the ratio between the normal and superconducting zero bias conductance is 50 compared to roughly 2 in experiments. This is because the model assumes zero temperature at which quasiparticle tunneling is completely forbidden and the conductance at eV$< \Delta$ is exclusively determined by Andreev reflection.

4.4.2. Numerical model of SIF structures

As mentioned, the model of the SIF tunnel junction is based on the generalized BTK formalism[45]. The FM and SC layer are described by two semi-infinite regions at $z < 0$ and $z > 0$ respectively. At $z = 0$ there is a flat interface accounting for the insulating MgO layer included as a delta-like potential barrier $V_0 d\delta(z)$ with effective height V_0 and width d. Since the in-built electric field due to SIA inducing Rashba SOC is largest at interfaces, the Rashba SOC field $\boldsymbol{w}_R = (\alpha k_y, -\alpha k_x)$ (eq. 4.2) is also considered to be delta-like. The Bogoliubov-de Gennes equation[37] reads:

$$\begin{pmatrix} \hat{H}_e & \hat{\Delta} \\ \hat{\Delta}^\dagger & \hat{H}_h \end{pmatrix} \boldsymbol{\Psi}(\boldsymbol{r}) = E\boldsymbol{\Psi}(\boldsymbol{r}) \tag{4.10}$$

with quasiparticle states $\boldsymbol{\Psi}(\boldsymbol{r})$ of energy E. The single-particle Hamiltonian for electrons is $\hat{H}_e = -(\hbar^2/2)\nabla[1/m(z)]\nabla - \mu(z) - (\Delta_{xc}/2)$ $\Theta(-z)\boldsymbol{m}\cdot\hat{\sigma} + (V_0 d + w\cdot\hat{\sigma})\delta(z)$ and for holes $\hat{H}_h = -\hat{\sigma}_y \hat{H}_e^* \hat{\sigma}_y$. They contain the effective mass $m(z)$, the chemical potential $\mu(z)$, and the

exchange spin splitting Δxc. The unit magnetization vector in the xz-plane is $\boldsymbol{m} = (\sin\Theta, 0, \cos\Theta)$ and $\hat{\sigma}$ are Pauli matrices. The s-wave superconductor V is modeled by the pair potential $\hat{\Delta} = \Delta\Theta(z)\mathbb{1}_{2\times 2}$ with the isotropic gap Δ. Due to conservation of in-plane wave vector $k_\parallel$, we can write $\boldsymbol{\Psi_\sigma(r)} = \boldsymbol{\Psi_\sigma(z)}e^{i\boldsymbol{k}_\parallel \boldsymbol{r}_\parallel}$. We find the solution in the FM layer for incoming electrons with spin σ:

$$\Psi_\sigma^F = \frac{1}{\sqrt{k_\sigma^e}} e^{ik_\sigma^e z}\chi_\sigma^e + r_{\sigma,\sigma}^e e^{-ik_\sigma^e z}\chi_\sigma^e$$
$$+ r_{\sigma,-\sigma}^e e^{-ik_{-\sigma}^e z}\chi_{-\sigma}^e + r_{\sigma,-\sigma}^h e^{ik_{-\sigma}^h z}\chi_{-\sigma}^h + r_{\sigma,\sigma}^h e^{ik_\sigma^h z}\chi_\sigma^h \tag{4.11}$$

with electron-like $\chi_\sigma^e = (\chi_\sigma, 0)^T$ and hole-like $\chi_\sigma^h = (0, \chi_{-\sigma})^T$ spinors, where:

$$\chi_\sigma^T = \left(\sigma\sqrt{1+\sigma\cos\Theta}, \sqrt{1-\sigma\cos\Theta}\right)/\sqrt{2} \tag{4.12}$$

and $\sigma = 1(-1)$ corresponds to the spin parallel (antiparallel) to $\hat{\boldsymbol{m}}$. The electron-like (hole-like) wave vectors in the FM region are $k_\sigma^{e(h)} = \sqrt{k_F^2 + 2m_F/\hbar^2[-E + \sigma\Delta_{xc}/2] - k_\parallel^2}$. The superconducting scattering states are:

$$\Psi_\sigma^S = t_{\sigma,\sigma}^e e^{iq^e z}\begin{pmatrix} \mathrm{u} \\ 0 \\ \nu \\ 0 \end{pmatrix} + t_{\sigma,-\sigma}^e e^{iq^e z}\begin{pmatrix} 0 \\ \mathrm{u} \\ 0 \\ \nu \end{pmatrix}$$
$$+ t_{\sigma,\sigma}^h e^{-iq^h z}\begin{pmatrix} \nu \\ 0 \\ \mathrm{u} \\ 0 \end{pmatrix} + t_{\sigma,-\sigma}^h e^{-iq^h z}\begin{pmatrix} 0 \\ \nu \\ 0 \\ \mathrm{u} \end{pmatrix} \tag{4.13}$$

with superconducting coherence factors $u^2 = 1-\nu^2 = (1+\sqrt{E^2-\Delta^2}/E)/2$. The wave vectors are given by $q^{e(h)} = \sqrt{q_F^2 + (-)2m_S/\hbar^2\sqrt{E^2-\Delta^2} - k_\parallel^2}$. Applying charge current conservation one can compute the differential conductance at zero temperature:

$$G = \frac{e^2 A}{(2\pi)^2 h} \sum_{\sigma} \int d^2 k_{\parallel} [1 + R^h_{\sigma}(-eV) - R^e_{\sigma}(eV)] \tag{4.14}$$

The probability amplitudes in the FM region $R^{e(h)}_{\sigma}(E, k_{\parallel}) = \mathrm{Re}\left(k^{e(h)}_{\sigma} |r^{e(h)}_{\sigma,\sigma}|^2 + k^{e(h)}_{-\sigma} |r^{e(h)}_{\sigma,-\sigma}|^2 \right)$ contain the scattering coefficients for specular and Andreev reflection with and without spin flip. Bias voltage is denoted by V and A is the interfacial area. To tescribe the Fe/MgO/V tunnel junction we use the Fermi wave vectors $k_F = 0.805 \times 10^8$ cm^{-1} for Fe and $q_F = 0.66 \times 10^8$ cm^{-1} for V, the effective masses are $m_{Fe} = m_0$ and $m_V = 4.3 m_0$ with m_0 the free electron mass, the spin polarization of Fe is given by $P = (\Delta_{xc}/2)/\mu_{Fe} = 0.7$, where $\mu_{Fe} = \hbar^2 k_F^2/(2m_{Fe})$, the SC pair potential is $\Delta = 1.6$ meV, the barrier height $V_0 = 1.47$ eV and width $d = 1.7$ nm. The SOC parameter α is used as fitting parameter. The results in figure 4.20 are obtained by applying boundary conditions:

$$\Psi^F_{\sigma}|_{z=0^-} = \Psi^S_{\sigma}|_{z=0^+} \tag{4.15}$$

$$\frac{\hbar^2}{2m_S} \frac{d}{dz} \eta \Psi^S_{\sigma}|_{z=0^+} = \begin{pmatrix} \boldsymbol{w} \cdot \hat{\sigma} & 0 \\ 0 & -\boldsymbol{w} \cdot \hat{\sigma} \end{pmatrix} \Psi^F_{\sigma}|_{z=0^-} + \left(\frac{\hbar^2}{2m_F} \frac{d}{dz} + V_0 d \right) \eta \Psi^F_{\sigma}|_{z=0^-} \tag{4.16}$$

with

$$\eta = \begin{pmatrix} \mathbb{1}_{2\times 2} & 0 \\ 0 & \mathbb{1}_{2\times 2} \end{pmatrix} \tag{4.17}$$

numerically solving for the scattering coefficients and performing the integration in eq. 4.14. Note that for bias voltage $eV < \Delta$ quasiparticle transmission is prohibited and we get V probability current conservation $R^e_{\sigma}(eV) = 1 - R^h_{\sigma}(-eV)$, which leads to:

$$G = \frac{e^2 A}{(2\pi)^2 h} \sum_{\sigma} \int d^2 \boldsymbol{k}_{\parallel} [2 R^h_{\sigma}(-eV)] \tag{4.18}$$

Thus, zero bias conductance depends only on Andreev reflection probability amplitude.

4.4.3. Phenomenological model of SIF structures in the presence of SOC and magnetic field

To get insight into the physical mechanisms behind the angular dependence of the conductance and MAAR, the following phenomenological model has been considered which was developed earlier for TAMR[23,165] and also applied to MAAR[45]. The model is based on general symmetry arguments. It identifies two preferential directions in the system for given $\boldsymbol{k}_\parallel$, namely $\mathbf{m}$ and $\boldsymbol{w}(\boldsymbol{k}_\parallel)$. Therefore, a scalar quantity as the Andreev reflection probability can be expanded in powers of $\boldsymbol{m} \cdot \boldsymbol{w}(\boldsymbol{k}_\parallel)$. Up to second order in SOC we get for the conductance:

$$G = \frac{e^2 A}{(2\pi)^2 h} \sum_\sigma \int d^2\boldsymbol{k}_\parallel 2\Big[R_\sigma^{h,(0)}(-eV) + R_\sigma^{h,(1)}(-eV)[\boldsymbol{m} \cdot \boldsymbol{w}(\boldsymbol{k}_\parallel)] + R_\sigma^{h,(2)}(-eV)[\boldsymbol{m} \cdot \boldsymbol{w}(\boldsymbol{k}_\parallel)]^2\Big] \tag{4.19}$$

The linear term vanishes after integration due to $\boldsymbol{w}(\boldsymbol{k}_\parallel) = -\boldsymbol{w}(-\boldsymbol{k}_\parallel)$ and with eq. 4.2 we arrive at:

$$G(\Theta) = G_0 + g_\alpha^{(2)} \alpha^2 (1 - \cos 2\Theta) \tag{4.20}$$

which contains the SOC independent conductance $G_0 = e^2 A/(2\pi)^2/h \sum_\alpha \int d^2\boldsymbol{k}_\parallel 2R_\sigma^{h,(0)}(-eV)$ and the SOC dependent part with the expansion coefficient $g_\alpha^{(2)} = e^2 A/(2\pi)^2/h \sum_\alpha \int d^2\boldsymbol{k}_\parallel 2R_\sigma^{h,(0)}(-eV) k_y^2$. So far the external field, which is applied to rotated the orientation magnetization in the XZ-plane, has been neglected. The radius of the cyclotron orbits, whereby charge carriers are forced by a magnetic field perpendicular to their propagation direction, are assumed to be much smaller than the width of the MgO tunnel barrier. For a cyclotron orbit comparable to the barrier width of $d \approx 2$ nm a magnetic flux density of $B \approx 500$ T is needed. By applying kOe magnetic field this condition is reached for a relative permeability $\mu_r \approx 5000$ since $B \approx \mu_r 0.1$

T. So for Fe-based tunnel junctions, the orbits can reach a comparable radius to the barrier width in the present external magnetic fields with $0.5 - 2$ kOe and magnetic field effects should be taken into account. They have been included to the phenomenological model for out of plane rotation of the magnetic field in a similar way as it was proposed for in plane fields[166]. A magnetic field is introduced to the model Hamiltonian via minimal coupling $\boldsymbol{p} = -i\hbar\nabla \rightarrow \pi = -i\hbar\nabla + e\mathbf{A}$. The magnetic flux density is given by $\boldsymbol{B} = B\boldsymbol{m}$ so we can choose the gauge $\mathbf{A}= (-yB\cos\Theta, -zB\sin\Theta, 0)$ for the vector potential $\mathbf{A}$ and relate it to the magnetic field via $\boldsymbol{B} = \mu_r\mu_0\boldsymbol{H}$ with the vacuum permeability μ_0. With the substitution for the momentum above, the kinetic energy and Rashba SOC parts of the single-particle Hamiltonian $\hat{H}_e$ are modified to $\hat{H}_{kin} = 1/2\pi[1/m(z)]\pi$ and $\hat{H}_R = \alpha/\hbar[(\pi_y, -\pi_x, 0)\cdot\hat{\sigma}]\delta(z)$ respectively. Instead of numerically solving this problem the goal is to study the physics behind. The strategy is to again expand the Andreev reflection probability in powers of magnetization direction and SOC field. This is still possible, however, the expansion coefficients and SOC field depend now on the magnetic field. So the way forward consist to approximate the field dependent quantities $R^{h,(n)}_{\sigma,H}(-eV)$ and $\boldsymbol{w}_H(\boldsymbol{k}_\parallel)$ by the previous independent ones valid up to linear order in H.

Let's first focus on the kinetic energy term. In the absence of a magnetic field the Andreev reflection is largest at $\boldsymbol{k}_\parallel = 0$ since for finite $\boldsymbol{k}_\parallel$ a part of the total kinetic energy of an incoming electron is in the parallel direction to the interface which effectively increases the barrier height. When $H \neq 0$ the maximum Andreev reflection is shifted to an in-plane wave vector $\boldsymbol{k}_{\parallel,0}$ which fulfills $\left\langle [k_{x,0} - e\mu_0 H_y/\hbar\cos\Theta]^2 \right\rangle = 0$ and $\left\langle [k_{y,0} - e\mu_0 H_z/\hbar\sin\Theta]^2 \right\rangle = 0$, performing a quantum mechanical average $\langle\ldots\rangle$. So the electrons feel effectively the smallest barrier for $k_{\parallel,0} = [b_1 H\cos\Theta, b_2 H\sin\Theta, 0]$, where b_1 and b_2 are constants that depend on $\langle y\rangle$ and $\langle y^2\rangle$ or $\langle z\rangle$ and $\langle z^2\rangle$, respectively. Thus, we approximate $R^{h,(n)}_{\sigma,H}(\boldsymbol{k}_\parallel) \approx R^{h,(n)}_{\sigma}(\sqrt{(k_x - k_{x,0})^2 + (k_y - k_{y,0})^2})$. This shift can be related to the Lorentz force which sends the charge carriers on helicoids depending on the orientation of magnetization. Higher order effects from the magnetic field on the Andreev reflection ampli-

tude are neglected. The spin-orbit field experiences also a momentum shift $\boldsymbol{w}_H(\boldsymbol{k}_\parallel) \approx \boldsymbol{w}(k_x - b_3 H\cos\Theta, k_y - b_4 H\sin\Theta)$ with the coefficients b_3 and b_4 respectively depending on $\langle y\rangle$ and $\langle z\rangle$ because momentum appears linearly in the SOC field. In the presence of an out of plane magnetic field, the Hamiltonian is not anymore translationally invariant in the y-direction. Assuming those terms as small perturbations ables to still compute the conductance from eq. 4.18 plugging in the expansion of the Andreev reflection probability in powers of SOC with H-dependent expansion coefficients. The SOC independent term is the same upon integration as in the absence of magnetic field. Conductance corrections to the second order term are neglected since they are quadratic in H. From the first order term, which vanishes without magnetic field, we get and additional contribution to the conductance:

$$G_{orbital} = \frac{e^2 A}{(2\pi)^2 h}\sum_\sigma \int d^2\boldsymbol{k}_\parallel 2R_\sigma^{h,(1)}(-eV)[\boldsymbol{m}\cdot\boldsymbol{w}(\boldsymbol{k}_\parallel)] = g_\alpha^{(1)}\alpha H(1-\cos 2\Theta) \tag{4.21}$$

which is linear in H and contains the coefficient $g_\alpha^{(1)} = e^2A/(2\pi)^2/h\sum_\sigma \int d^2\boldsymbol{k}'_\parallel 2R_\sigma^{h,(1)}(\boldsymbol{k}'_\parallel)(b_2 - b_4)$ with $\boldsymbol{k}'_\parallel = \boldsymbol{k}_\parallel - \boldsymbol{k}_{\parallel,0}$. So orbital effects in the presence of a Rashba SOC field induce an angular dependence which is of the same form as the one from the second order SOC term in the absence of an external magnetic field.

With this we finish the theoretical model explanation and now we are going to summarize the conclusions of these chapter.

4.5. Conclusion

To our knowledge this is the first study that has thoroughly characterized the tunneling mechanisms on epitaxial superconducting magnetic tunnel junctions (SC-MTJs) with spin-active interfaces with spin-orbit interaction. We have characterized the superconducting properties of three different types of epitaxial magnetic tunnel junctions: V/MgO/Fe, V/MgO/Fe/MgO/Fe, Fe/MgO/V/MgO/Fe and a non-epitaxial one made out of V/MgO/Au taken as the "control sample". We have measured their critical temperature (T_C) value with

a precision of ±10 mK, their superconducting gap width, their critical magnetic fields both in parallel and perpendicularly applied with respect to the junction's plane and the above gap shot noise.

We found that, in two types of junctions, T_C depends on the magnetic state of the electrodes. In the V/MgO/Fe junction, the reduction of T_C when the magnetization is oriented perpendicular to the interface points towards the possible explanation of triplet pair generation[148]. On the other side, in the V/MgO/Fe/MgO/Fe junction, the increase of T_C when the relative magnetization is oriented perpendicular out of plane could be due to the nucleation of superconductivity starting at domain walls[156]. In the Fe/MgO/V/MgO/Fe junction, due to the antiferromagnetic coupling of the electrodes, the only remanent magnetization is AP state. Therefore there is no possibility of measuring T_C at different magnetic states without actively applying an external magnetic field.

The zero bias conductance anisotropy in the V/MgO/Fe system at 0.3 K has been thoroughly studied by using two methods: (i) establishing three different remanent magnetization orientations of the Fe layer and (ii) performing a rotation, perpendicular to the junction's plane, of the external magnetic field and changing the magnetization of the Fe layer. Through method (i) we observed a change in the relative value of the zero bias conductance anisotropy between the in-plane and out of plane remanent magnetizations of roughly a 10%. By applying an external magnetic field modulus of 2 kOe, method (ii), the observed relative value of the zero bias conductance anisotropy rises to 60% due to the suppression of the superconductivity. From method (i) we observe a reduction of the zero bias conductance anisotropy when the remanent magnetization is oriented out of plane with respect to when its in-plane. This indicates the possible presence of long-range triplet correlations which have a deeper penetration length into the ferromagnet than the singlet (conventional) Cooper pairs[52].

We have carried out shot noise measurements for biases above the gap at 0.3 K on all the epitaxial SC-MTJs in order to verify the quality of the barrier. These experiments show the high quality of the tunnel MgO barriers as long as shot noise in single barriers gives a Fano factor close to 1.

In both double-barrier structures (V/MgO/Fe/MgO/Fe and Fe/MgO/V/MgO/Fe) we have observed reproducible above gap conductance anomalies (CAs) at temperatures around and below T_C. The CAs peak amplitudes depend on the magnetic state of the FM electrodes. Additionally, CAs are not suppressed by moderate/high magnetic fields (up to $\sim$ 20 kOe) at a temperature of 0.3 K and even survive 1 or 2 K above T_C. This features adds weight to the idea of having LRT correlations in our SC-MTJs.

Our main experimental results on the zero bias conductance anisotropy have been described with a theoretical model developed in collaboration with the groups of prof. Jaroslav Fabian and Petra Högl, from the University of Regensburg (Germany), prof. Alex Matos-Abiague and prof. Igor Zutić, from the University at Buffalo (USA). The model calculates the magnetoanisotropic Andreev reflection (MAAR) through the zero bias conductance anisotropy when the magnetization is remanent and when there is an external magnetic field actively applied. In the case when the magnetization is remanent the model gives a MAAR value of 17% and when there is an external magnetic field applied the MAAR value is 57%. Moreover the model also explains the finite subgap conductance at temperatures much below T_C.

Chapter 5

Organic Magnetic Tunnel Junctions with PTCDA

In this chapter we move from investigating the spin control of superconducting pairing to the exploration of the possible spin control of phonons. The research has been carried out on organic magnetic tunnel junctions (OMTJs) where the organic barrier is made of Perylenetetracarboxylic dianhydride (PTCDA) molecules. We will use low frequency noise (LFN) and inelastic electron tunneling spectroscopy (IETS) measurements to characterize the electron-phonon interactions when electrons tunnel through an organic barrier. In addition we will investigate the possibility of magnetic control over vibrational heating of the molecules by varying the magnetic state of the devices. Vibrational heating refers to the local excitation of the molecules in the way that part of the molecules conforming the barrier vibrate or bend[167]. The thermal noise associated with the overall temperature remains constant and vibrational heating will be studied through the LFN anomalies coming from a small fraction of excited molecules.

One of the possible ways to characterize vibrational heating independently is using surface-enhanced Raman emission which determines the effective temperature for both the vibrational modes and the flowing electrons in biased metallic molecular junctions[168]. Our

experimental set-up is not prepared to make such optical measurements. Besides optic signals would have to cross metallic electodes weakening in that way the Raman signal. Therefore we cannot associate an effective temperature directly to the detection of vibrational modes. However we will use the vibrational spectroscopy of Raman studies[169–171] to compare qualitatively the activation energy of the vibrational modes detected.

5.1. Introduction

Since last decades, the problems of downscaling inorganic electronics due to both physical limitations and increment of the fabrication costs has boosted the search of alternative concepts to provide electronic devices at reasonable costs. The concept of using single molecules or small groups of molecules conducting electrical current between two electrodes is among the most promising candidates to create future devices capable of substituting the traditional silicon based electronics. Organic spintronics has attracted considerable attention in recent years[82,83,85,93,94,96,167,172,173]. As it was presented in the introduction, the use of organic molecules as the insulating spacer is a relatively new trend in material fabrication which is nowadays commonly used in new technology (i.e. OLEDs, OFETs, photovoltaic cells, etc). However, despite the extensive research carried out in this field, the behavior of spin-polarized electrons tunneling through thin organic barriers remains mostly unexplored.

In molecular electronics and spintronics vibration induced heating and breakdown is one of the major obstacles in the advances of their application[86,174–176]. Some recent studies suggest that interfacial vibrons play an important role in the spin relaxation dynamics[177,178]. On the experimental side, only the work from Galbiati *et al.*[84] using Alq_3 as the organic spacer uses TMR and IETS measurements to study the spin-tunneling mechanisms but without delving in the control of the magnetic configuration of the electrodes. To our knowledge, the work presented in this thesis is the first study of spin-dependent transport in OMTJs which investigates the possibility of magnetic control over

vibrational heating of the organic spin-valves by taking advantage of the combination of LFN, TMR and IETS measurements.

This chapter presents a detailed investigation of spin current dependent dynamics through an organic spacer, in particular for different PTCDA thin thicknesses (1.2 - 6 nm). After describing the junctions briefly we will present the results for the control sample which has no PTCDA layer. Then we will present the experimental results obtained for OMTJs describing the different tools used to study the vibrational modes. The study of the LFN dependence with temperature has been made at a broad temperature range from 0.3 K to 100 K and as a function of the magnetic state. Finally we will describe a model based on vibrational heating in the presence of spin dependent vibron excitation and relaxation which explains qualitatively the observed effects. With these tools we investigate the possibility of the **magnetic control of the vibrational modes** with the magnetic state of the FM electrodes separated by an organic (PTCDA) barrier.

5.2. Sample growth

The PTCDA samples have been grown in the group of prof. Minn-Tsong Lin in a collaboration project with the National Taiwan University (NTU). The collaboration has permitted a visit abroad to the NTU's laboratory where the author of this thesis learned about the growth procedures of the OMTJs investigated. The growth procedure is described in detail in ref.[179]. The layer sequence of the OMTJs is: NiFe(25 nm)/CoFe(15 nm)/AlO_x(0.6 nm)/PTCDA(1.2-5 nm)/AlO_x(0.6 nm)/CoFe(30 nm). The structure was deposited onto a glass substrate in a high-vacuum environment with a base pressure lower than $10^{-8} mbar$. The metallic layers were deposited by sputtering at an Ar working pressure of 5×10^{-3} mbar. The bottom NiFe/CoFe layer is the soft FM and the top CoFe layer is the hard FM. The PTCDA layers were grown by thermal evaporation at 10^{-8} mbar, with a deposition rate of 0.1 nm/s. Thin AlO_x buffer layers were grown between the PTCDA layer and both FM layers by partially oxidizing Al in oxygen plasma for 5s. X-ray Photoelectron

Spectroscopy (XPS) measurements of the Co/PTCDA interface have revealed that the addition of a buffer layer prevents the hybridization between both layers[179], preserving an effective spin injection into the organic spacer. The PTCDA molecules have been found to lie essentially flat over both AlO_x/Co or Co, with a tilt angle of $12° \pm 3°$[179]. The area of all samples is $3.8971 \times 10^4 \mu m^2$ and the PTCDA molecule size is 9.2Å × 14.2Å which, taking into account the tilting deposition angle 1 nm thick layer corresponds roughly to 3 monolayers of PTCDA (sketched in figure 5.1).

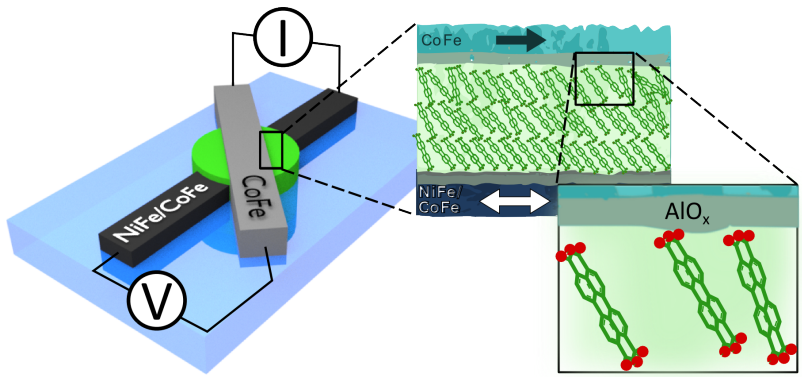

Figure 5.1: Sketch of the OMTJs with a first zoom of the cross section of the PTCDA barrier highlighting the deposition angle of the PTCDA molecules. The second zoom highlights how interfacial molecules could be contact or not with the AlO_x electrode due to its roughness. Arrows indicate that the CoFe layer is the hard FM electrode and the NiFe/CoFe layer is the soft FM electrode.

As long as aluminum is not fully oxidized, these samples continue to oxidize if they are more than a few hours in contact with the atmosphere. Because of this, the samples are grown in high-vacuum conditions and after they are extracted from the chamber they are vacuum sealed for their transport (from Taiwan to Spain). When they arrive to the laboratory we have vacuum chambers to contain these type of sensitive samples. Then, the process of contacting the samples is made always as quickly as possible and finally the sample is

inserted in the high-vacuum insert chamber of the cryostat. All in all, the samples are exposed to the atmosphere no more than few hours overall.

We have measured a total of 23 samples with thicknesses that range from absent PTCDA barrier (control sample) to (1.2-6) nm thick PTCDA. The statistics of the experiments are not perfectly robust, meaning that for the same thickness different samples could have slightly different tunneling behaviors. We attribute this issue to differences in the growth and as a result of the transport and the different contacting time lapses or if the sample has being measured more than once. Having said this the dependence of samples resistances and TMRs on thickness have a perfectly clear trend (see figure 5.5).

5.2.1. Control Sample (without PTCDA)

The control sample layer sequence is NiFe (25 nm)/CoFe (15 nm)/ AlO_x (1.2 nm)/CoFe (30 nm). Is it therefore the same previously mentioned structure but without the PTCDA layer deposition step. Comparing the samples with PTCDA with the control sample is necessary to investigate the role of the organic molecules in the tunneling and related dynamic process.

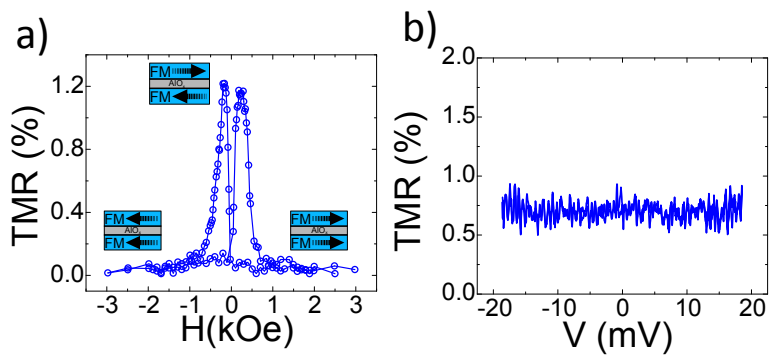

Figure 5.2: TMR dependence on a) magnetic field (taken at V=0.7 mV) and b) bias of the control sample. Measurements taken at $T = 0.3$ K.

The very small magnetoresistance signal coming from the control sample (see figure figure 5.2) demonstrates that the partially oxidized Al layer (AlO_x) alone does not act as an effective spin-transport barrier. More comparisons with the samples with PTCDA will be shown further on this chapter. But before delving into the experimental results, it's worth noting the annealing process we performed in all PTCDA samples before starting to measure them.

5.3. Annealing with voltage

One particular characteristic we found in these OMTJs is that at the beginning of measuring, the "fresh" (newly inserted) samples slightly changed the shape of their conductance because by applying a voltage we were annealing the PTCDA molecules contacting the electrodes. We presume that this annealing consists in a rearrangement of the PTCDA molecular conformation. We found that this annealing procedure improved the measurements. As general trend, after annealing each of the measured samples we have seen an increment of the TMR value (see figure 5.3). Besides, the low frequency noise of the sample has been reduced after annealing and the reproducibility of the measurements improved.

The process of annealing is made by taking a few IV curves (slowly increasing the applied current). In figure 5.3 there's the TMR ratio of a 3 nm thick PTCDA sample measured at 0.3 K after different annealing sweeps. It is clearly seen how the TMR improves with increasing the annealing maximum voltage (see figure 5.3b). However, we found that annealing the sample higher than 300 mV did not improve so much the TMR value and on the contrary it provoked an increment of the noise of the sample which could be attributed to a small degradation of the barrier. Because of this observation on the measurements shown, further on we have **always annealed the samples up to 100 or 150 mV before start conductance and noise measurements**.

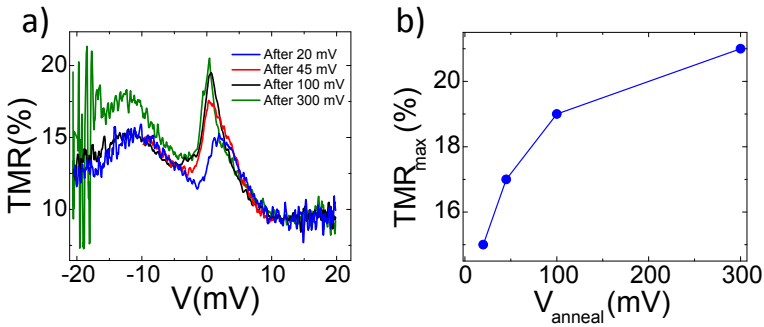

Figure 5.3: Annealing effect on the sample's TMR ratio at T=0.3K in the 3 nm thick PTCDA. Part a) shows the annealing procedure increasing the applied bias. Part b) shows the maximum TMR value after each annealing process. Maximum applied bias range (positive or negative) while measuring has been kept constant (±20 mV).

5.4. Experimental results

We are going to start by summarizing our main observations which will be further detailed throughout this chapter (see figure 5.4). Most of the measurements have been made at low temperatures, typically at 0.3 or 10 K (two of the stationary temperatures of our cryogenic set-up). The external magnetic field applied, in order to change the FM magnetization, has only been applied in the sample's plane (in-plane). Thereby we will consider only two different magnetic configurations of the electrodes which are the parallel (P) and the antiparallel (AP) states. We found no evidence of any influence of the strength of the external in-plane magnetic field in our experimental results. For this reason, we are not going to continuously specify the value of the external magnetic field in a particular magnetic state configuration. For the P state we have chosen a saturating in-plane field of 3 kOe but for selecting the AP state however, a starting TMR measurement (see example in figure 5.4a) has always been made at the beginning of the experiments time period in order to know the corresponding field value of the AP state configuration. Note that the characteristic field at which AP state is reached (with maximum magnetoresistance)

could vary with temperature.

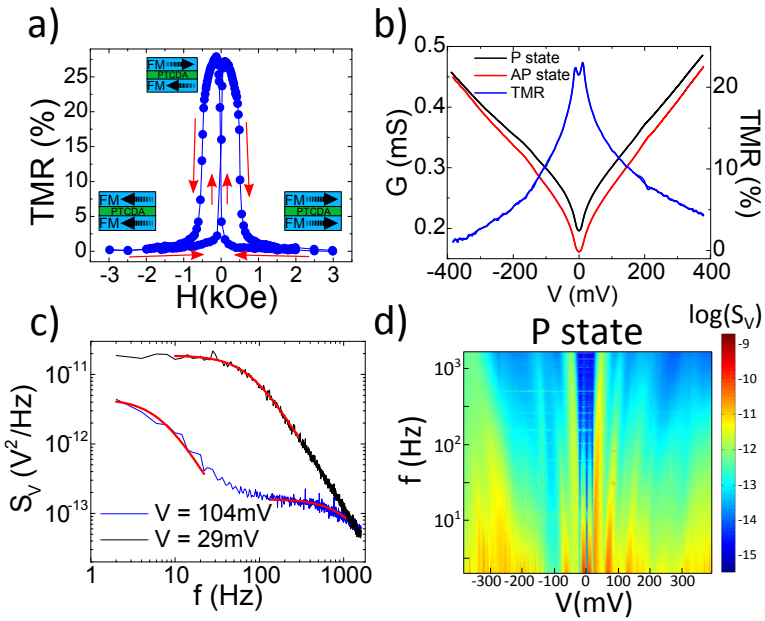

Figure 5.4: Organic barrier characterization measurements on a 1.2 nm thick PTCDA sample taken at 10 K. Part a) shows a typical positive TMR vs magnetic field where the red arrows depict the magnetic field sweep history. Part b) shows the parabolic dependence of conductance in P and AP states and the TMR vs bias. Part c) shows two spectra at specific biases where RTN and $1/f$ show up. Part d) shows a 3D plot of the bunch of noise spectra in P state to study the LFN dependence with bias.

In order to characterize the conductance mechanisms for electrons tunneling through an OMTJ we always start by measuring the TMR dependence on the magnetic field (see figure 5.4a). By making the TMR we have the P and AP states determined. Then we thoroughly study at the same time conductance (see figure 5.4b) and low frequency noise (see figure 5.4c and d) taking into account that the sample can be annealed while it's being measured (applying a high enough bias).

The experimental results will be presented starting with the discus-

sion on the electron transport dependence on the PTCDA thickness followed by the LFN analysis at the different magnetic configurations. Afterwards the IETS analysis will be shown and finally the dependence of the different LFN with temperature will be presented.

5.4.1. Electron transport vs PTCDA thickness

Indeed a variety of factors determine the electron transport through organic tunnel junctions (OTJs)[86]. The most important are the molecular and electrode electronic structures followed by molecular vibrations and electron-vibron coupling particularly of the bonds modified by the proximity to the interfaces. The electron spin is a relevant factor for controlling transport in OMTJs[79–81,180–184]. Moreover, the magnetic state of the interfacial molecules could be qualitatively changed by the electron coupling to the electrodes[185,186]. The interplay between spin and phonons in molecular spintronics remained however obscured. Only very recent studies pointed out that such a possibility might exist[176,177]. Charge-vibron related non-equilibrium transport and its current fluctuations flowing through molecular interfaces has been recently explored for non-destructive characterization of molecular barriers through inelastic electron tunneling spectroscopy (IETS)[170] and low frequency noise (LFN) based molecular imaging[95] in *single molecules*. After the general example of measurements shown in figure 5.4, let's take a look at the general behavior of transport vs. thickness (see figure 5.5).

First of all, these samples show an exponential increment of resistance with the PTCDA thickness (see figure 5.5a), which is a sign of the good quality of the barrier[82]. Second, the TMR signal comes from the organic spacer clearly (see figure 5.5b) and will be corroborated further on with IETS measurements. The $1/f$ noise analyzed through the Hooge factor (α), which will be discussed further below, clearly shows that the noise level of the control sample is several orders of magnitude lower than the noise level of the samples with PTCDA. In addition to the IETS, the LFN will be a key tool to analyze the magnetic state dependence on the vibrational heating.

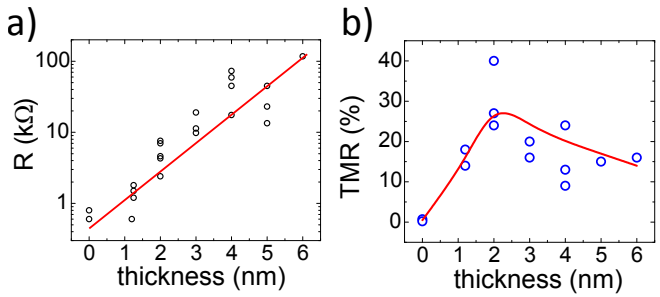

Figure 5.5: Part a) shows the dependence of the junctions resistances on thickness at room temperature. Part b) studies the sample's TMRs dependence on thickness at 10 K. Red lines are a guide for the eye.

5.4.2. Dependence of LFN on electrode's magnetic state

In this section we are going to study the effect of the magnetic state in the noise power spectra which for the case of PTCDA samples is additionally going to be analyzed through the RTN characteristic frequencies.

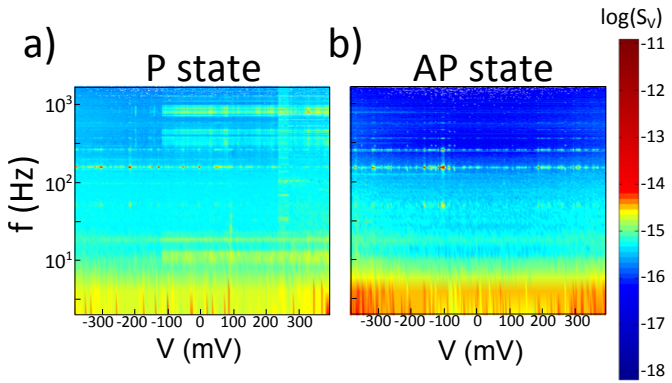

Figure 5.6: LFN spectra measured on the control sample a) in P state and b) in AP state. Measurements were made at 10 K.

To check the source of the LFN anomalies, we can directly com-

pare the noise power spectra of the control sample and a sample with a PTCDA barrier (figures 5.6 and 5.7 respectively). The control sample shows a clear $1/f$ noise dependence in the full bias range whereas the 1.2 nm thick PTCDA junction (see figure 5.7) shows LFN anomalies which corresponds to a RTN type at specific biases. To further corroborate this, we show LFN for the control sample in both the P and AP states (see figure 5.6 a and b). Both measurements show no special difference in the LFN spectra.

On the other hand comparing the noise spectra on a PTCDA junction between the P with the AP state (figures 5.7a and b respectively) the LFN features, in the form of bias triggered RTN, are clearly visible. One can see a difference both in their characteristic threshold bias positions and in their amplitude. By looking at their difference in absolute value we highlight the noise spectra peaks (see figure 5.7c). Each noise maximum tends to drift to higher voltage and we observe that in AP state the activation energy of the peak is slightly higher than in P state.

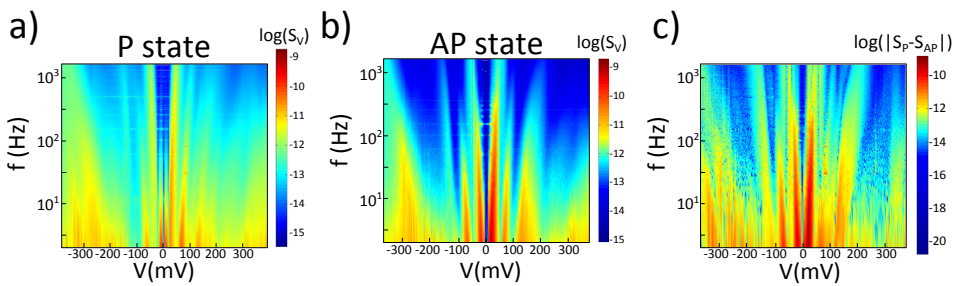

Figure 5.7: Noise power spectra in OMTJs with 1.2 nm thick PTCDA measured at 10 K in a) P state and b) AP state. Part c) shows the absolute value of the difference between the noise power in P and AP states.

The LFN peak evolution has been corroborated in the RTN analysis (see figure 5.8) where each RTN mode (humped slope of the spectrum in figure 5.4c) appears at low voltages and then shows a nearly linear dependence to higher frequencies as the voltage is increased. When increasing the PTCDA thickness there's an additional $1/f$ con-

tribution probably due to the increased background barrier disorder which complicates the detection of RTN signals. One can see that the RTN vs. bias dependence on thickness (comparing figures 5.8a and b) shows a similar behavior as the $1/f$ noise (see figure 5.10). This behavior consists in a spreading of the maximums in the case of the Hooge analysis and an increment in the distance between different RTN modes. Regarding the effect of the magnetic state, from the RTN analysis is difficult to extract any assertion. What we can say is that most of the RTN modes appear in both magnetic states at roughly the same energies, however there's a few number of modes that appear in one state (either P or AP state) but not in the other.

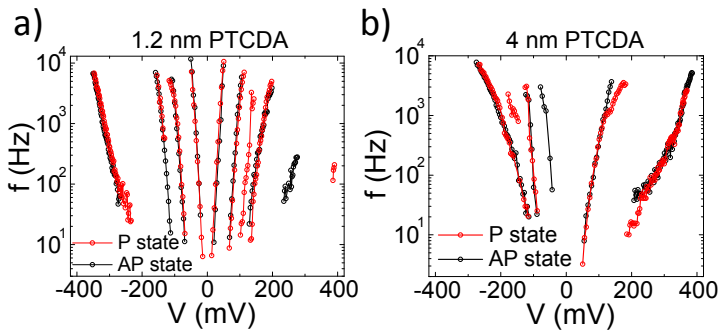

Figure 5.8: RTN analysis made at 10 K showing the characteristic frequencies in P and AP states for a) a 1.2 nm and b) a 4 nm thick PTCDA samples.

In order to further clarify the question if the magnetic state influence in the noise level is strictly due to the difference of resistance between P and AP states we made a comparison between the spin-dependent integrated normalized LFN and the TMR. The spin-dependent vibrational noise has been calculated using the integrated noise (S_{int}) over the span of frequencies of the spectrum (1-1600 Hz). With the integrated noise we calculate the so-called tunnel magnetic noise (TMN) as the ratio between the integrated noise at the different magnetic states divided by the integrated noise in the P state $TMN = (S_{int-AP} - S_{int-P})/S_{int-P}$.

The comparison (see figure 5.9) demonstrates that spin-dependent vibrational heating changes the noise level well above the expected variation from the fluctuation-dissipation theorem (with variation of the noise proportional to variation of resistance). A similar conclusion can be reached by analizing the spin-dependent noise power in comparison with the one expected from the difference in the thermal resistance between P and AP states. Indeed, at a temperature of 0.3 K and maximum resistance change between P and AP states of a few kΩ, the expected noise power changes should be less than $S_V = 4k_BT(R_{AP} - R_P) \approx 10^{-19}V^2/Hz$, i.e. a few orders of magnitude below the experimentally observed variation in figure 5.7c.

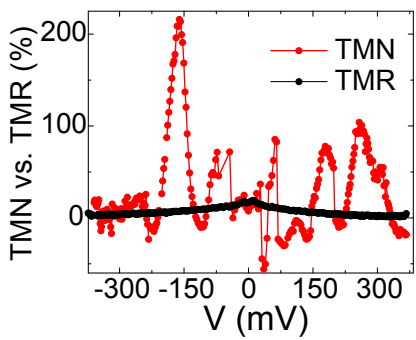

Figure 5.9: Comparison between tunneling magnetic noise TMN and TMR for the OMTJs with 1.2 nm PTCDA thick barrier at T=10K.

If we explore now the $1/f$ noise dependence on thickness, taking a look at figure 5.10 one have to take into account Hooge's phenomenological law 1.30 from where the Hooge parameter α is extracted. The model assumes a $1/f$ noise dependence which is the case of the control sample (see figure 5.6), however in the case of having PTCDA barrier RTN appears at certain voltages with a Lorentzian dependence on the frequency and Hooge analysis could not be quantitatively correct.

Therefore for a comparison between the control and the PTCDA samples, figure 5.10 has to be considered only qualitatively, and the quantitative comparison must be made comparing the noise level of the control sample (figures 5.6a,b) with the noise level of the sample

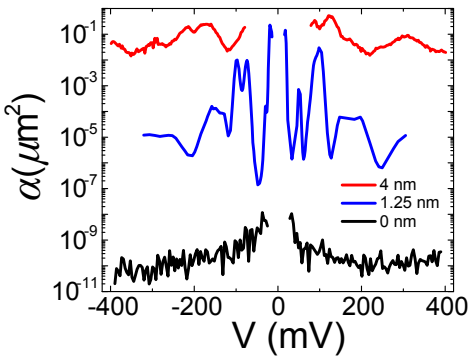

Figure 5.10: Dependence of the Hooge factor (α) on the PTCDA thickness at 10 K. The control sample (no thickness) shows a negligible TMR and the Hooge factor (α) is several orders of magnitude lower than the junction with the thinnest PTCDA barrier (1.2 nm).

with PTCDA barrier (figure 5.7). The junction with the thinnest (1.2 nm) PTCDA barrier shows a clear patron of vibrational modes in the LFN spectra with a higher noise level (see figure 5.7c). This contrast to the control sample where the magnetic state doesn't appear to affect the $1/f$ noise very much (see figures 5.6a and b).

The reproducibility of the measurements has been checked also (see figure 5.11). The major part of the samples measured show a great reproducibility after they have been annealed (up to a voltage range of $\pm$100 mV). The IV curves, which will be addressed in the next paragraph, in addition to figure 5.11 where 4 different noise measurements analyzed and represented for simplicity using the Hooge factor follow smoothly the same trend illustrating the high degree of measurement reproducibility.

For the spectroscopy of vibrons we have additionally used the IETS analysis. We are going to explain now the steps to analyze an IV curve in order to extract the characteristic phonon energies using IETS that afterwards will be compared with the LFN analysis.

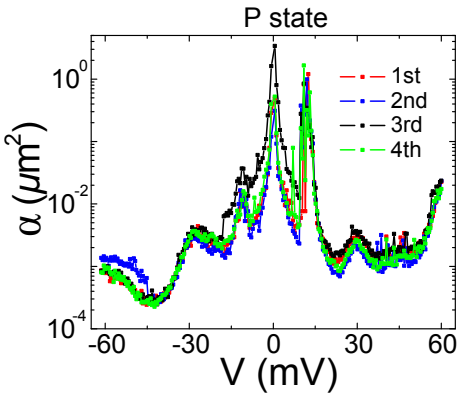

Figure 5.11: Reproducibility of bias dependent noise analyzed through the Hooge factor in P state at T=10K in an annealed OMTJ with 1.2 nm thick PTCDA.

5.4.3. Inelastic electron tunneling spectroscopy

The inelastic electron tunneling spectroscopy (IETS) is an experimental tool that is extensively used for studying the vibrations of molecular adsorbates on metal plates. Sending current through tunnel junctions and measuring their voltage response, one can record a **I-V characteristic curve** (see figure 5.12a). The first derivative gives the conductance (see figure 5.12b) which provides information about the local density of states (LDOS) in both electrodes and the transmission probability (as described in eq.1.2). The second derivative gives information about the vibrational modes of the insulating molecular layer through electron-phonon interactions which will appear as dips and peaks on the second derivative of the IV curve[187] (see figure 5.12c). The negative bias part of the second derivative is changed of sign in order to facilitate the vibrational mode comparison.

Generally, studies of molecular vibrational spectroscopy using IETS have been made in the energy range of hundreds of mV[84,91]. In the high bias regime (up to 0.5 V) the phonon contribution to the conductance comes mainly from interfacial molecules while at low bias (up to 20 mV) the phonon contribution comes mainly from the inner

molecules inside the barrier where collective vibrations (*librons*) can be studied. In our low bias measurements, because the energy width of the phonons is at least roughly 1 mV, in order to facilitate the visualization of the modes, a smooth of 0.5 mV has been made on the IETS curves. For the high bias measurements the smoothing is around 1 mV.

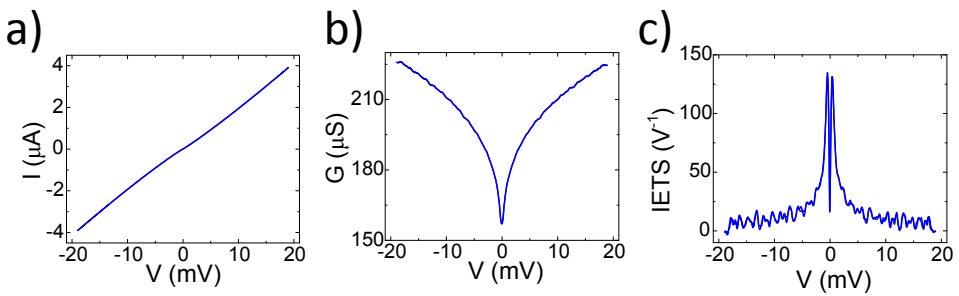

Figure 5.12: Example of how molecular vibrations could be observed in a particular IETS curve. a) Typical IV characteristic curve measurement. b) Conductance (dI/dV). c) IETS module and normalized by the conductance ($d^2I/dV^2(dI/dV)^{-1}$). Measurements taken on a OMTJ with 2 nm PTCDA barrier at 0.3 K.

To characterize the electron-phonon interactions we will compare our IETS peaks with the Raman spectrum of the PTCDA[188,189,169]. Through IETS we will only detect the strongest vibrations whereas the Raman spectrum shows a more detailed vibrational landscape (see figure 5.13). The energy unit conversion is $1cm^{-1} = 124\mu$V.

Vibrational modes are usually differentiated in internal vibrations of a single molecule (*phonons*, figure 5.13b) and collective vibration of several molecules (*librons*, figure 5.13a) which conforms the molecular lattice. Typically librons have a weaker activation energy (< 10 mV) than phonons (> 10 mV) which are dominant at high energies. To check that our IETS peaks correspond to a real vibrational mode we overlap the positive and negative parts of the IETS spectrum because peaks must appear symmetric in voltage (see figure 5.14).

Figure 5.14 correspond to a PTCDA sample (2 nm thick) which was the one with the highest quality we have measured. The particu-

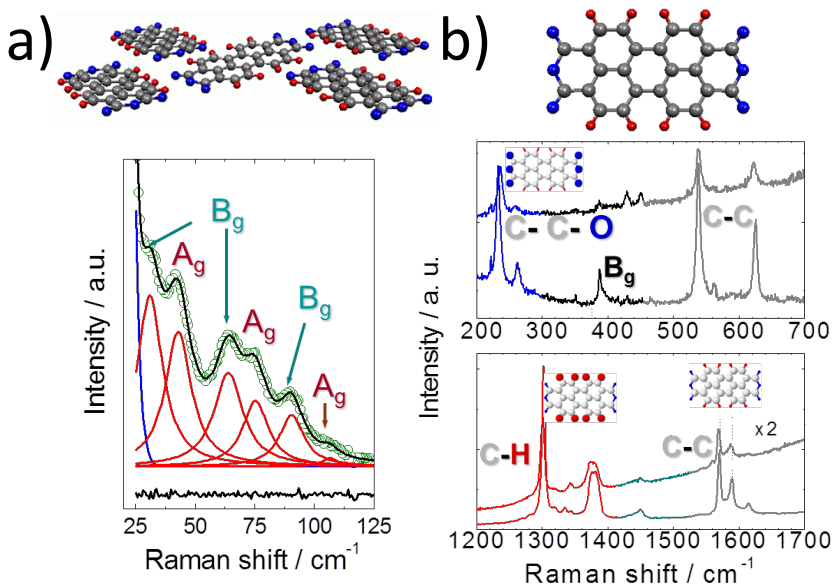

Figure 5.13: Raman spectroscopy of librons a) where A_g and B_g are different collective vibrational orientations and phonons b) where individual internal molecular vibrations appear at different specific energy ranges. Figure adapted from ref.[171]

larly good matching in the overlap of the IETS positive and negative branches where we can even distinguish in some peaks that they are formed by individual phonons or librons (agrees with Raman spectroscopy shown in figure 5.13) accounts for the high quality. Comparing the phonon modes (see figures 5.14 a and b) we demonstrate how the activation energy of the phonon modes of the molecule can be controlled with the magnetic state of the electrodes. We can compare P state with AP state normalized by the TMR value in order to make them overlap (see figure 5.14c). One can observe a splitting of the libron related peaks which could be related to a small change of the effective thickness of the PTCDA barrier through the magnetostriction of the electrodes[190,191]. The dependence of the phonons with thickness is not so clear. Because at low energies the entire section of molecules conforming the barrier contributes to the conductance,

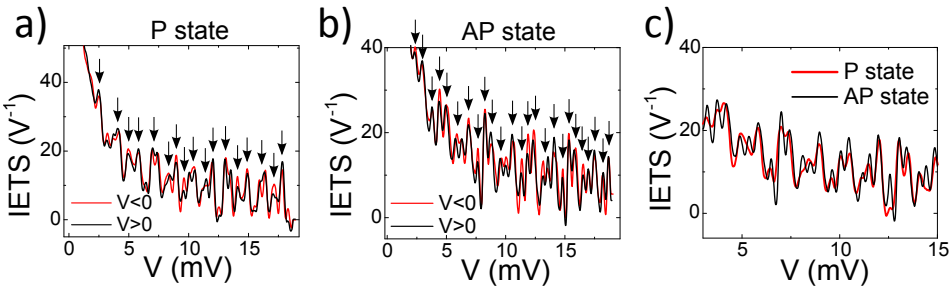

Figure 5.14: Magnetic field control over the vibrational spectra in a) P state and b) AP state. The IETS negative (red) and positive (black) voltage curves are overlapped to check which peaks match (vibrational modes) in parts a) and b). Black arrows indicate the phonon modes energy. Part c) shows only the $V < 0$ part with AP state normalized by the TMR value in order to overlap with P state in order to see the splitting of the vibrational modes. The measurements were made in a 2 nm thick PTCDA sample at 0.3 K.

the quality of the sample is essential to make a good IETS analysis. One could compare the previously mentioned high quality 2 nm thick sample (see figure 5.15a) with another of the double thickness (see figure 5.15b)) and with one of triple thickness (see figure 5.15c)). The experimental result show that the 4 nm thick junction appears to have very few phonon modes which in addition don't match perfectly, in contrast to the 6 nm thick where there's clearly a better phonon spectra. What happens is that due to the increment in the number of molecular layers as the thickness increases, the individual phonon energies start overlapping and the peaks start to spread.

What we extract from the different tools used study vibrational spectroscopy of these samples is that there are some molecular vibrations that contribute more to the noise spectra, others to the conductance spectra, and occasionally to both. For example in a 2 nm thick PTCDA (see figure 5.16) we can see how there is a peak on the IETS near 200 mV clearly appearing as an increment in the power spectral noise whereas other peaks in the noise (near 300 mV) are not reflected in the IETS measurement.

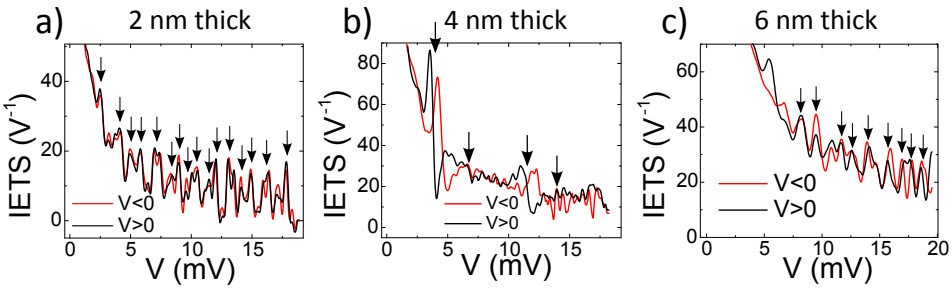

Figure 5.15: Dependence of the phonon spectra with the PTCDA thickness. Black arrows indicate the phonon modes energy. The measurements were made in P state at 0.3 K.

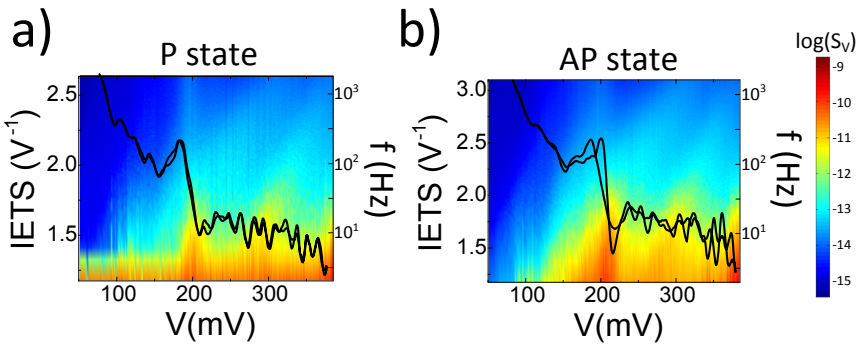

Figure 5.16: LFN vs. IETS comparison for a 2 nm thick PTCDA sample at 10 K in a) P state and b) AP state.

5.4.4. Vibrational modes dependence on temperature

Now we are going to take a look at the influence of temperature in the LFN. The main effect of temperature is to lower the activation energy of the vibrational modes because of the thermal energy of the molecules. We observe from the Hooge factor analyzed from $1/f$ noise (shown in figures 5.16a and b) and from the RTN (shown in figures 5.16c) that the activation energy of the vibrations is lower at 10 K than at 0.3 K. The effect is much clearly seen in long-lasting experiments

we used to perform at the end of the experiments time period taking advantage of the gradual warming up of the cryostat (see figure 5.16d), each black arrow indicate the position of one those Hooge maximums and how it shifts towards lower energies as the temperature rises.

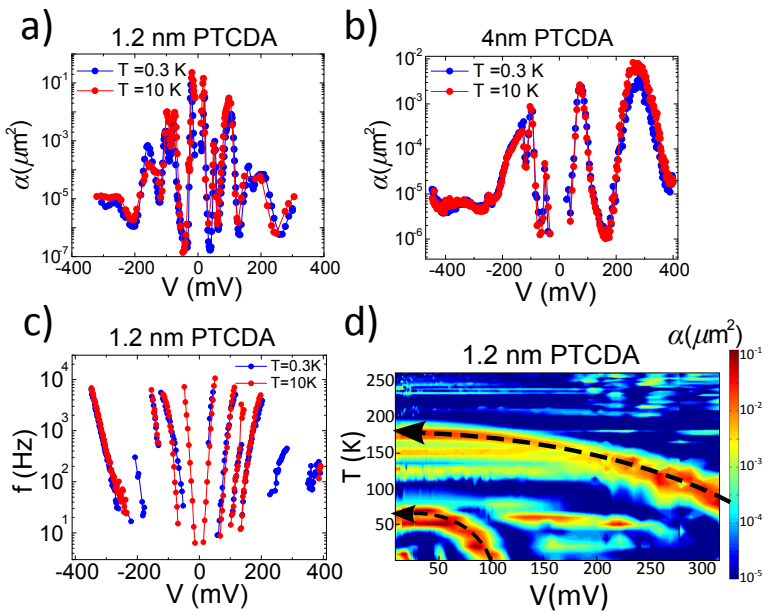

Figure 5.17: LFN dependence on temperature in P state. Parts a) and b) are the Hooge factor (α) analysis from a 1.2 nm and 4 nm thick PTCDA barrier respectively. Part c) shows the RTN characteristic frequency from a 1.2 nm thick PTCDA sample. Part d) is a long-lasting experiment of the Hooge factor vs temperature slowly leaving the cryostat warming up to room temperature. The black arrows highlight the decrease of the activation energy of the LFN anomaly as the temperature rises.

5.5. Theoretical model

Following the theoretical fremework of refs.[167,173,192,193], in the so-called vibrational heating mechanism for atom transfer proposed in-

dependently by Gao *et al.*[192] and Walkup *et al.*[194], the interfacial molecule gathers energy to overcome the potential barrier by inelastic scattering of the tunneling electron with vibrations of the molecule. Simultaneously the molecule loses energy to electron-hole pairs and other processes. Brumme *et al.*[195] applied such ideas to describe the switching of the carboxylic oxygen in a PTCDA scanning tunneling microscope (STM) junction (see figure 5.18).

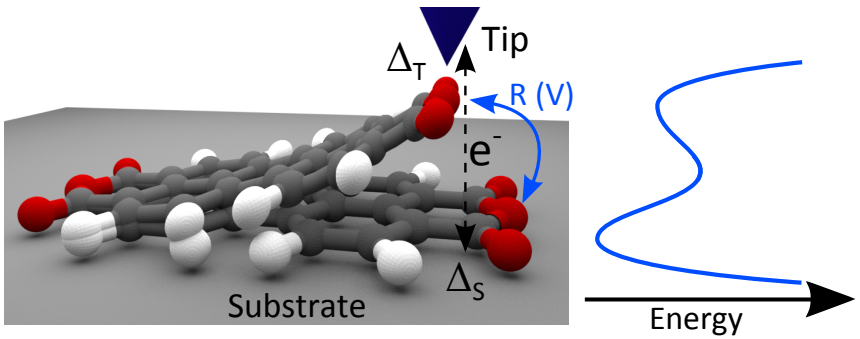

Figure 5.18: Schematic representation of a single-molecule switching rate ($R(V)$) in an STM junction in which the molecule is asymmetrically coupled to the surface of the STM tip ($\Delta_S > \Delta_T$). The molecule gathers energy to overcome the potential barrier between the two stable positions by inelastic scattering of the tunneling electron. Figure adapted from ref.[167]

The nearly symmetric character of the LFN anomalies points toward their link with vibrational excitations rather than to be originated from resonant electron tunneling[87] where broad LFN features are expected for one of the bias polarities only. Is interesting how the enhancement of the LFN power at specific biases (e.g. 5.4d) is accomplished (up to a few orders of magnitude) by the limited impact on the conductance (e.g. figure 5.4b). We suggest that a great majority of the molecular conductance channels in our OMTJs comes from the well established contacts between molecules an the electrode. At the same time, a negligibly small part of the conductance channels, estimated to be of the order of $10^{-2} - 10^{-3}$ (see figure 5.9), contribute to the RTN (see sketch in figure 5.19).

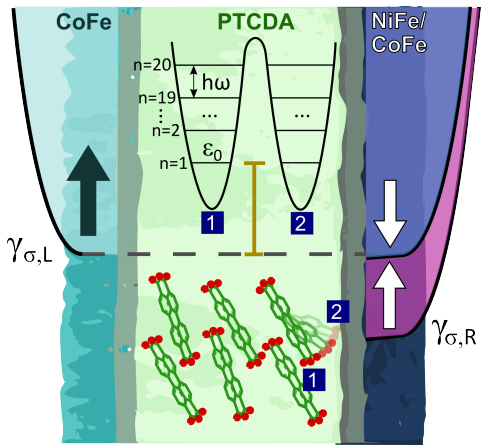

Figure 5.19: Model and parameters used: symmetric junction in the off-resonant regime (ϵ_0) $= 10\gamma_L = 10\gamma_R = 1$ eV), reaction order $n = 20$ and coupling strength $\chi = 1$ meV. The non-bended state of the molecule is number 1 and the bended state is number 2. The electrode spin polarization (σ) is depicted by the vertical arrows.

Based on this scenario, with the help of prof. T. Frederiksen[196] a model for explaining the resonant enhancement of LFN for some specific biases has been made. The standard adsorbate resonance model Hamiltonian for a metal-molecule-metal tunnel junction is:

$$H_0 = \epsilon_0|M\rangle\langle M| + \sum_L \epsilon_L|L\rangle\langle L| + \sum_R \epsilon_R|R\rangle\langle R|$$
$$+ \sum_L (V_{LM}|L\rangle\langle M| + h.c.) + \sum_R (V_{RM}|R\rangle\langle M| + h.c.) + \hbar\Omega(b^\dagger b + 1/2),$$

written in terms of the one-particle electron states $|M\rangle, |L\rangle$ and $|R\rangle$ of molecule and left/right electrode respectively and their corresponding one-electron energies ϵ_0, ϵ_l and ϵ_R. $V_{LM}(V_{RM})$ describes the hopping integrals between the left L and right R electrodes and the molecular level respectively. The vibrational energy quantum is $\hbar\Omega$. We further consider that the vibrational mode couples linearly to the central resonance:

$$H' = \chi(b^\dagger + b)|M\rangle\langle M|,$$

where χ is the electron-vibration coupling matrix element and $b(b^\dagger)$ are the corresponding vibration annihilation (creation) operators. The system is therefore described by the following Hamiltonian:

$$H = H_0 + H'$$

In the considered model, the conductance channels (I-Ch) are interrupted at small enough bias due to unavoidable interface roughness (see figure 5.19). These channels are suggested to become unstable (similar to single molecular switches[167]) under the applied bias due to transitions between unbent (1) and bent (2) molecular conformal configurations. The rest of the stable conduction channels contribute to the average conductance and provide common $1/f$ noise. The model sketch (see figure 5.19) depicts the vibrational heating of one of the molecules forming I-Ch either in the P or AP states. Following the spinless vibrational heating model[167] we suggest that I-Ch contribute to the excess of the RTN above certain biases by opening conductance channels due to inelastic relaxation of the applied bias through molecular phonons. Considering the spin degree of freedom, we write the partial density of states $\rho_{\sigma,\alpha}$ from electrode α and spin channel σ as:

$$\rho_{\sigma,\alpha}(\epsilon) = \frac{1}{2\pi}\frac{\gamma_{\sigma,\alpha}}{(\epsilon - \epsilon_0) + (\gamma_\sigma/2)^2}$$

and the total density of states as $\gamma_\sigma = \gamma_{\sigma,L} + \gamma_{\sigma,R}$ in the wide-band approximation. We consider the Fermi-Dirac occupation function ($n_F(\epsilon)$) in the low-temperature limit as it becomes a step function in order to simplify the vibrational excitation rates $\Gamma^{\alpha,\beta}_{\uparrow,\downarrow}$ in terms of electrons initially in a state in electrode $\alpha \in \{L, R\}$ and ending up in a final state in electrode $\beta \in \{L, R\}$. The full math development can be checked in the supplementary material from ref.[196].

Let's further define the spin-averaged DOS of the electrode α as:

$$2\gamma_\alpha = \gamma_{\uparrow,\alpha} + \gamma_{\downarrow,\alpha}$$

and the electrode polarization as:

$$P_\alpha = \frac{\gamma_{\uparrow,\alpha} - \gamma_{\downarrow,\alpha}}{2\gamma_\alpha}$$

in this way $P_\alpha = 0$ when $\gamma_{\uparrow,\alpha} = \gamma_{\downarrow,\alpha}$, $P_\alpha \to 1$ when $\gamma_{\uparrow,\alpha} \gg \gamma_{\downarrow,\alpha}$ and $P_\alpha \to -1$ when $\gamma_{\uparrow,\alpha} \ll \gamma_{\downarrow,\alpha}$.

As we mentioned, following ref.[167] we compute the switching rate R and the noise spectrum S for a two-level system driven by inelastic excitations of a vibrational mode Ω by a spin-polarized electronic current. The reaction transfer rate out of a given atomic configuration (λ) is given by the product of the quasi-stationary population P_{n-1} for the corresponding oscillator level $n-1$ and the excitation rate out of this state ($n\Gamma_\uparrow$), which is:

$$R_\lambda = n\Gamma_\uparrow \left(\frac{\Gamma_\uparrow}{\Gamma_\downarrow}\right)^{n-1} \tag{5.1}$$

where it is evident that the reaction rate scales as the electron-vibration coupling squared ($R_\lambda \propto \chi^2$). For simplicity we have used a value of $\Omega = 20$ meV which is not far from the lowest frequency Raman-active internal vibrational mode[197] (see figure 5.13) of a single PTCDA molecule (233 cm^{-1}).

At zero temperature the (elastic) electronic current through the single level is given by:

$$I = \frac{e}{h} \sum_\sigma 2 \frac{\gamma_{\sigma,L}\gamma_{\sigma,R}}{\gamma_\alpha} \times \left(\arctan \frac{2(\mu_L - \epsilon_0)}{\gamma_\sigma} - \arctan \frac{2(\mu_R - \epsilon_0)}{\gamma_\sigma} \right)$$

where $\mu_{L,R}$ is the chemical potential at the L, R electrode respectively. Then, the tunneling magnetoresistance is defined as:

$$TMR(V) = \frac{|I_P - I_{AP}|}{min(|I_P|, |I_{AP}|)} \tag{5.2}$$

For the considered model parameters we find that the reaction yield $Y = R/I$ (spin polarized current I) is practically the same for unpolarized and parallel (P) electrode spin alignment, whereas the anti-parallel (AP) alignment results in a significantly lower yield. This effect can be understood as originating from a suppressed excitation

rate $\Gamma_\uparrow$ (involving only DOS products $\rho_L\rho_R$ of *different* electrodes per spin channel) in the AP configuration, while the deexcitation rate $\Gamma_\downarrow$ (involving $\rho_L\rho_R$, ρ_L^2 and ρ_R^2 per spin channel) always has a large term for both alignments. The reduced yield in AP should thus be a generic effect related to the phase space of inelastic electron scattering.

Finally the noise power is calculated following Machlup[193] model for a two-parameter random signal ($\tau_1 = 1/R_1$ and $\tau_2 = 1/R_2$).

$$S(\omega) = \frac{1}{\pi}\frac{\tau_1\tau_2}{(\tau_1+\tau_2)^2}\frac{1/\tau_1 + 1/\tau_2}{\omega^2 + (1/\tau_1 + 1/\tau_2)^2} = \frac{1}{\pi}\frac{R_1R_2}{(R_1+R_2)^3 + (R_1+R_2)\omega^2}$$

assuming $\tau_1 = \tau_2 = 1/R$ this reduces to:

$$S(\omega) = \frac{1}{\pi}\frac{R}{8R^2 + 2\omega^2}$$

as well as in frequency notation ($f = \omega/2\pi$):

$$S(f) = \frac{2\pi R}{(4\pi R)^2 + f^2} \tag{5.3}$$

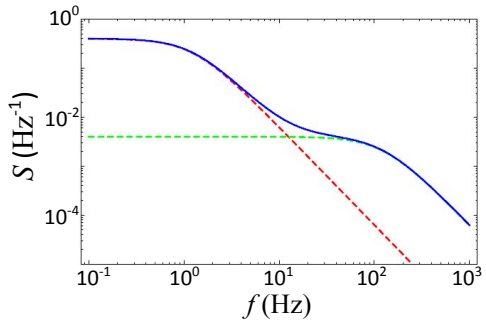

Figure 5.20: Example of the noise spectrum corresponding to two characteristic frequencies $f_1 = 0.1$ Hz (red dashed line) and $f_2 = 10$ (green dashed line) Hz.

Let us first understand the noise spectrum $S(f)$ (see figure 5.21). To obtain a signal similar to the experimental frequency range $f \approx 1-1000$ Hz we are looking for switching rates that are about an order of magnitude slower, i.e., $R \approx 1-100$ Hz. The integrated noise power over a finite frequency range $[f_1, f_2]$ leaves equation 5.3 as:

$$S(f) = \int_{f_1}^{f_2} df S(f) = \frac{1}{2}\left[\operatorname{arccot}\frac{4\pi R}{f_2} - \operatorname{arccot}\frac{4\pi R}{f_1}\right] \tag{5.4}$$

An example of the noise spectrum with two characteristic frequencies of $f_1 = 0.1$ Hz and $f_2 = 10$ Hz is shown in figure 5.20. The shape qualitatively agrees with the example of a spectrum taken at 104 mV having two RTN (blue curve in figure 5.4c). We have performed the calculations of the TMR and switching rate for the case of a symmetric junction in the off-resonant regime ($\epsilon = 10\gamma_L = 10\gamma_R = 1$ eV) at two different spin polarizations, provided that the reaction order is about $n = 20$ and the electron-phonon coupling energy $\chi = 1$ meV (see figure 5.21a,b,d,e). We note that the different rates for P and AP states originates from different reaction yields. This is due to the suppressed excitation rates $\Gamma_\uparrow$ in the AP state.

We explored the magnetic state dependent noise spectrum $S = S(V, f)$ as a function of bias voltage V and frequency f for different realistic bias dependent TMR and associated spin polarizations. By the eye its hard to appreciate the difference between P and AP states so we performed the quantity $log(\mathrm{ABS}(S_P - S_{AP}))$ (see figures 5.21c,f). Using as reference the experimental TMR (shown in figure 5.4b) and the RTN (shown in figure 5.8a) corresponding to one of our highest quality samples (1.2 nm thick PTCDA), the value of the zero bias spin polarization $P = 0.32$ gives the best agreement between theory and experiment. For this zero bias spin polarization we get a similar zero bias TMR value ($TMR \approx 20\%$) and the switching rate is slightly different between P and AP states, therefore we deduce that our modeling reproduce qualitatively well the main experimental observations.

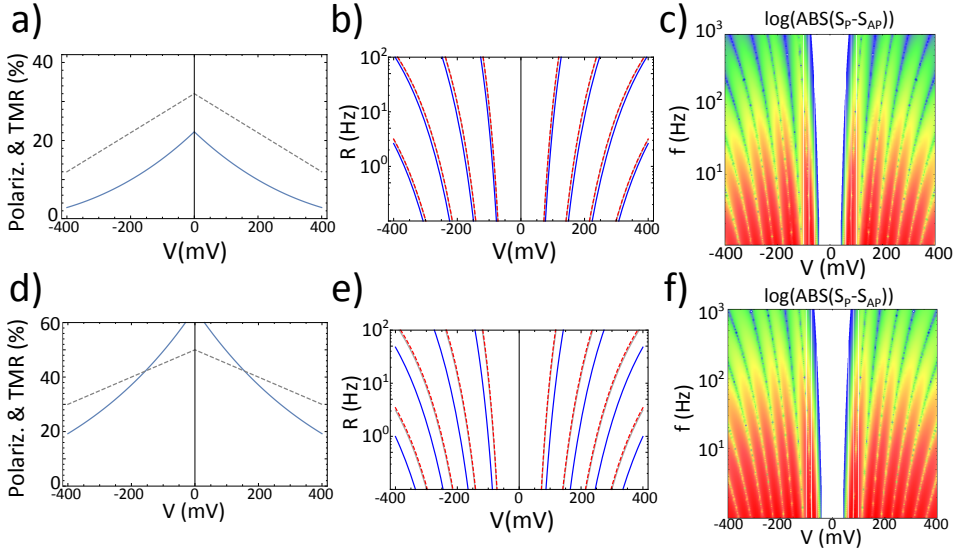

Figure 5.21: LFN modeling for zero-bias spin polarization $P = 0.32$ (top figures) and $P = 0.5$ (bottom figures). Parts a) and d) show the suggested spin current polarization (dotted line) and TMR (solid line). Parts b) and e) present the switching rate in P (dotted red line) and AP (full blue line) and without spin polarization (full grey line). Parts c) and f) show the power noise spectrum difference between P and AP states in absolute value.

5.6. Conclusions

This chapter presented an experimental study demonstrating the possibility of spin-control over phonon excitations and relaxations. Low frequency noise (LFN) and inelastic electron tunneling spectroscopy (IETS) were used to investigate the excitation of vibrational modes in organic magnetic tunnel junctions with barriers made of Perylenetetracarboxylic dianhydride (PTCDA). The measurements were made in junctions with barrier thicknesses ranging from no PTCDA (control sample) up to 6 nm and taken at temperatures from 0.3 K to 100 K. The control sample's experiments corroborate that the main signal attributed to electron-phonon interaction comes from the PTCDA

molecules within the barrier.

We have observed, through LFN measurements, the fluctuations in voltage caused by the vibrations of the PTCDA molecules. The related random telegraph noise (RTN) was observed to be symmetric in voltage. The characteristic frequencies of RTN features appear at low biases and increase their frequency with increasing bias. The dependence of the $1/f$ noise with temperature shows how the activation energy of phonons decreases as the temperature rises. The phonon-related noise changes between the parallel and anti-parallel magnetic states is a few orders of magnitude bigger than the one expected from the fluctuation-dissipation theorem.

We have performed IETS experiments where we have observed the vibrational modes of the PTCDA molecules by overlapping the voltage positive and negative parts of the second derivative of IV curves at different bias ranges. At the lower range (up to 20 mV) we observe the collective vibrational modes called "librons". When the voltage is increased the fluctuations correspond to individual vibrations, namely phonons, which we observe up to the range of 400 mV. The phonon detection was better measured for the thin PTCDA thicknesses (1.2 and 2 nm) where the signal comes from the molecules contacting the electrodes, whereas for the thicker barriers the molecules in the middle molecules smooth the signal by increasing its noise.

The experimental results have been qualitatively corroborated by a spin-dependent vibrational heating model developed in collaboration with prof. Thomas Frederiksen, which calculates several magnitudes such as the TMR, the switching rate or the noise spectrum in the low-temperature regime.

We have experimentally demonstrated that we can exert the magnetic control over the vibrational heating in molecular spin valves. Our finding contribute towards a better understanding of low frequency noise mechanisms in molecular spintronics needed to optimize their signal to noise ratio.

Chapter 6

General conclusions

To conclude, this thesis opens new lines of research in spintronics. We have investigated the spin-dependent electron transport and its fluctuations (*noise*) in epitaxial superconducting spintronics and in molecular spintronics with the aim to understand deeply the mechanisms which govern the electron transport in these types of tunnel junctions. The measurements were carried out on an existing cryogenic set-up, at temperatures down to 0.3 K and using a 3D vector magnet, and on a newly made room temperature set-up. The low frequency noise measurements were taken at a frequency range below 100 kHz.

In order to fulfill the objectives we have improved the existing cryogenic set-up, reaching almost a complete automation of the measuring tasks as well as for the first time using the 3D vector magnets to apply magnetic field in all directions. A new software has been created to control the prefect rotation of the external magnetic field which uses the Euler angle's notation. The conductance measurements required more precision than the previous set-up configuration had, therefore we replaced the old digital PCI multimeter board with a new one with more measurement precision. A new room temperature set-up has been built from scratch. The existing data analysis algorithms have been improved and new ones have been created to analyze the newest measurements. A new simulation work-post has been created

(with the participation of other members of the lab.) to carry out micro-magnetic simulations using the MuMax3 program. The main experimental results and conclusions in this manuscript are:

1. We have studied, with both experiments and simulations, the behavior of the electron transport and magnetization on 3 types of epitaxial superconducting magnetic tunnel junctions (SC-MTJs) with the following layer configurations: V/MgO/Fe, V/MgO/Fe/MgO/Fe, Fe/MgO/V/MgO/Fe and a non-epitaxial one made out of V/MgO/Au taken as the "control sample". The measurements have been made at temperatures above and below the critical one (T_C) of each junction in the $[0.3 - 300]$ K range.

2. In the spin-valve double barrier sample (V/MgO/Fe/MgO/Fe) we have investigated the different possible stable states of the magnetization direction of the 10 nm thick Fe soft layer with competing shape and surface anisotropies in the MgO/Fe(100)/MgO stack. We have used tunneling magnetoresistance as a sensor at temperatures above the critical temperature of the superconducting transition of Vanadium. We have experimentally observed, through a change in the sample's resistance, three different remanent magnetic states corresponding to the possible orientations of the soft Fe layer magnetization: parallel (P state), anti-parallel (AP state) and perpendicular to the plane (Perp. state). We have also observed a reproducible perpendicular magnetoresistance asymmetry at low temperatures (below 80 K). We have verified that within our experimental set-up limit range of magnetic fields (± 7 kOe) the perpendicular magnetization remains asymmetric. The possibility of controlling those three stable magnetizations of the Fe layer at temperatures below 80 K is explained through the competition between shape (or volume) and surface anisotropies. This competition between anisotropies indicates that the system under study has perpendicular magnetic anisotropy (PMA). The presence of these three different remanent magnetic states could be a key property in the design and fabrication of new types of spintornic multilevel devices.

3. We have investigated, using micro-magnetic simulations, the reorientation phase transition of the magnetization of a 10 nm thick

Fe layer conforming a MgO/Fe/MgO stack. We have simulated perpendicular to the Fe layer magnetic hysteresis cycles in order to study the magnetization reorientation field transitions up to 3 kOe. We have observed in simulations approximately similar values of the magnetization's reorientation phase transition as the ones observed in the experiment. In order to reproduce the asymmetry of the low temperature perpendicular magnetization we have introduced in the simulations a second order anisotropy term in one of the two interfaces of the Fe layer. The origin of the perpendicular magnetization asymmetry at low temperatures (below 80 K) has been explained from the difference in the second order anisotropy which is controlled by the difference in disorder at the two Fe layer interfaces.

4. We have characterized the superconducting properties of our SC-MTJs by measuring their critical temperature (T_C) value with a precision of ± 10 mK, their superconducting gap and their critical magnetic fields in both in-plane and out of plane orientations. We found that, in two types of junctions, T_C depends on the magnetization orientation of the electrodes. In the V/MgO/Fe junction, the reduction of T_C when the magnetization is oriented perpendicular to the interface agrees with the possible explanation of having triplet pair generation. In the V/MgO/Fe/MgO/Fe junction the increment of T_C when the relative magnetization is oriented perpendicular could be due to the nucleation of superconductivity starting at domain walls. In the last case of the Fe/MgO/V/MgO/Fe junction, as the only remenant magnetic configuration is AP state, there is no possibility of measuring T_C at different magnetization states without actively applying an external magnetic field.

5. We have studied the zero bias conductance anisotropy in the V/MgO/Fe system at 0.3 K by using two methods: (i) establishing three different remanent magnetization orientations of the Fe layer and (ii) rotating the external magnetic field and thus changing the magnetization of the Fe layer. Through method (i), the observed relative value of the zero bias conductance anisotropy between the in-plane and out of plane remanent magnetizations is roughly 10%. By applying an external magnetic field of 2 kOe, method (ii), the

observed relative value of the zero bias conductance anisotropy rises to 60%. From method (i), we observe that the zero bias conductance is lower when the remanent magnetization is out of plane than when the remanent magnetization is in-plane oriented. This indicates the possible presence of long-range triplet (LRT) correlations which have a deeper penetration length into the ferromagnetic material.

6. We have performed shot noise measurements at 0.3 K in order to verify the quality of the barrier in these epitaxially grown SC-MTJs. These experiments prove the high quality of the tunnel MgO barriers as long as shot noise may be described within a model considering pinhole free barriers.

7. In the two double-barrier structures (V/MgO/Fe/MgO/Fe and Fe/MgO/V/MgO/Fe) we have observed reproducible above gap conductance anomalies (CAs) at temperatures close to and below T_C. The CAs amplitudes depend on the relative orientation of the FM electrodes. Moreover CAs are not suppressed by moderate/high magnetic fields (up to $\sim$ 20 kOe) at a temperature of 0.3 K and even survive 1 or 2 K above T_C. These results point towards a high crystalline quality and indirectly add more consistency to the possibility of having LRT correlation happening on our SC-MTJs.

8. Our main experimental results on the zero bias conductance anisotropy have been described with a theoretical model developed in collaboration with the groups of prof. Jaroslav Fabian and Petra Högl, from the University of Regensburg (Germany), prof. Alex Matos-Abiague and prof. Igor Zutić, from the University at Buffalo (USA). The model has been developed for both cases when the magnetization is remanent (i) and when the magnetization is oriented by the active application of an external magnetic field (ii). In case (i) the numerical model gives a value of the magnetoanisotropic Andreev reflection (MAAR) of 17% and in case (ii), applying a 2 kOe external magnetic field, the value is 57%. Thereby, the theoretical model supports the experimental results in terms of the MAAR effect. Moreover the model also explains the finite subgap conductance at temperatures much below T_C.

9. We have carried out a detailed investigation of the electron transport through organic magnetic tunnel junctions (OMTJs) whose barrier is made of PTCDA. We have used several tools such as conductance measurements, inelastic electron tunneling spectroscopy (IETS) and low frequency noise (LFN) taken at low temperatures down to 0.3 K and as a function of the magnetic state of the electrodes. The thicknesses of the samples range from no PTCDA (control sample) up to 6 nm. The measurements have been made in the temperature range from 0.3 K to 100 K.

10. The LFN measurements, particularly fitting the spectra to a random telegraph noise (RTN) behavior, shows a reproducible phonon landscape symmetric in voltage. The RTN appear at low biases and increase their characteristic frequency as the bias increases. Regarding the effect of the magnetic state, from the RTN analysis the bias shift is relatively small and is difficult to extract any conclusion. The control sample shows only $1/f$ noise spectra which is several orders of magnitude lower than the thinnest PTCDA barrier (1.2 nm). This corroborates that the noise fluctuations come from the molecules conforming the organic barrier. When the thickness of the barrier increases, more molecules inside the barrier add more background noise to the system, smoothing the phonon amplitude signal. The $1/f$ dependence with temperature shows a relative reduction of the phonon activation energy as the temperature rises. The variation of the phonon-dependent noise with the magnetic state exceeds in a few orders of magnitude the one expected from the fluctuation-dissipation theorem.

11. The IETS experiments have been made through the second derivation of several highly detailed IV curves at different bias ranges. At the lower bias range (up to 20 mV) we observe the collective vibrational modes called "librons". At the high bias range (up to 400 mV) the signal comes from the individual molecular vibrations, namely phonons. We observed a shift in the bias position of the phonon-related molecular vibrations controlled by the magnetic state of the electrodes. The phonon detection was better measured in the junctions with lower PTCDA thicknesses (1.2 and 2 nm) where the signal comes mainly from the interfacial molecules in contrast to the thicker

barriers were the intermediate molecules contribute adding noise to the signal. We have demonstrated that we can exert magnetic control over the vibrational heating in molecular spin valves at low temperatures below 10 K.

12. The main experimental results on LFN in OMTJs have been explained with a spin-dependent vibrational heating model developed in collaboration with prof. Thomas Frederiksen. Our findings contribute towards a better understanding of low frequency noise mechanisms in molecular spintronics.

Conclusiones generales

En conclusión, en esta tesis se abren nuevas lineas de investigación en el campo de la espintrónica. Hemos investigado el transporte electrónico dependiente del espín y sus fluctuaciones (*ruido*) en voltaje en uniones túnel magnéticas superconductoras epitaxiales y uniones túnel magnéticas moleculares con el propósito de entender mejor los mecanismos que gobiernan el transporte electrónico en estos tipos de uniones. Las medidas experimentales se han realizado en un sistema criogénico, a temperaturas bajas hasta los 0.3 K y usando un imán vectorial, y en un sistema nuevo a temperatura ambiente. Las medidas de ruido a baja frecuencia se han hecho en el rango por debajo de los 100 kHz.

Para poder cumplir con los objetivos de la tesis se ha mejorado el sistema criogénico experimental existente, casi alcanzando la completa automatización de las medidas experimentales y se ha implementando por primera vez la funcionalidad de aplicar campo en todas las direcciones del espacio usando el imán vectorial. Se ha creado un software nuevo para controlar la rotación del campo magnético externo de manera precisa usando la notación de los ángulos de Euler. Las medidas de conductancia han requerido más precisión que la que tenía el sistema experimental previo, para lo cual se adquirió una nueva tarjeta multímetro PCI con más precisión de medida. El nuevo sistema experimental a temperatura ambiente ha sido montado desde cero. Los algoritmos existentes de análisis de datos se han mejorado y se han creado nuevos para analizar nuevos tipos de medidas. Se ha creado un nuevo puesto de simulación (con la participación de otros miembros del laboratorio) para llevar a cabo simulaciones micro-magnéticas usando el programa MuMax3. Los resultados experimentales principales y las conclusiones de este trabajo son:

1. Se ha estudiado, con experimentos y simulaciones, el comportamiento del transporte electrónico y la magnetización en 3 tipos de uniones túnel magnéticas epitaxiales superconductoras (SC-MTJs) con la siguiente configuración: V/MgO/Fe, V/MgO/Fe/MgO/Fe, Fe/

MgO/V/MgO/Fe y otra no epitaxial conformada por V/MgO/Au tomada como muestra de "control". Las medidas se han realizado a temperaturas por encima y por debajo de la temperatura crítica (T_C) de cada muestra en el rango de $[0.3 - 300]$ K.

2. En las uniones tipo válvula de espín con doble barrera (V/MgO/Fe/MgO/Fe) hemos investigado los distintos posibles estados de la imanación en la película de Fe de 10 nm de espesor, donde se produce la competición entre anisotropía de forma y de superficie, que conforma el sistema MgO/Fe(100)/MgO. Hemos usado la magnetoresistencia túnel como sensor a temperaturas por encima de la temperatura crítica de la transición superconductora del Vanadio. Se ha observado experimentalmente, mediante el cambio de la resistencia de la muestra, tres estados magnéticos distintos remanentes correspondientes a las posibles orientaciones de la imanación de la capa blanda de Fe: estado paralelo (P state), anti-paralelo (AP state) y perpendicular al plano (Perp. state). También se ha observado una asimetría en la magnetoresistencia perpendicular perfectamente reproducible a bajas temperaturas (por debajo de 80 K). Hemos verificado que, dentro del rango experimental de aplicación de campo magnético (± 7 kOe), la magnetoresistencia perpendicular se mantiene asimétrica. La posibilidad de controlar estos tres estados estables de la imanación de la capa blanda de Fe a temperaturas por debajo de 80 K se explica a través de la competición entre la anisotropía de forma (o de volúmen) y la de superficie. Esta competición entre anisotropías indica que el sistema tiene anisotropía magnética perpendicular (PMA). La presencia de estos tres distintos estados magnéticos remanentes podría ser una propiedad clave en el diseño y fabricación de nuevos tipos de dispositivos espintrónicos multinivel.

3. Usando simulaciones micro-magnéticas hemos estudiado la transición de reorientación de la imanación de una capa de Fe de 10 nm de espesor que conforma el sistema MgO/Fe/MgO. Hemos simulado ciclos de histéresis magnéticos perpendiculares a la capa de Fe para estudiar la transición de reorientación hasta campos de 3 kOe. Las simulaciones dan valores similares de la transición de reorientación de la imanación a los observados experimentalmente. Para reproducir la

asimetría a bajas temperaturas de la imanación perpendicular hemos introducido en las simulaciones un término de segundo orden en la anisotropía para una de las dos interfaces de la capa de Fe. El origen de la asimetría a bajas temperaturas (por debajo de 80 K) de la imanación perpendicular se explica a través de la diferencia en el término de segundo orden de la anisotropía que está controlado por la diferencia en el desorden estructural entre las dos interfaces de la capa de Fe.

4. Hemos caracterizado las propiedades superconductoras de las SC-MTJs midiendo su temperatura crítica (T_C) con una precisión de $\pm$10 mK, el valor del gap superconductor y los campos críticos tanto en el plano como en la dirección perpendicular. En dos tipos de uniones, T_C depende de la orientación de la imanación de los electrodos. En la unión formada por V/MgO/Fe, la disminución de T_C cuando la imanación está orientada perpendicular a la interfaz concuerda con la posibilidad de que exista generación de pares de Cooper del tipo triplete. En la unión del tipo V/MgO/Fe/MgO/Fe, el incremento de T_C cuando la imanación relativa está orientada perpendicular podría deberse a que la nucleación de la superconductividad se origina cerca de parades de dominio. En el último caso de la muestra de Fe/MgO/V/MgO/Fe, debido a que el único estado magnético remanente es AP state, no hay posibilidad de medir T_C en distintos estados magnéticos sin aplicar activamente un campo magnético externo.

5. Se ha investigado la anisotropía de la conductancia a voltaje cero en la muestra V/MgO/Fe a 0.3 K usando dos métodos: (i) estableciendo tres orientaciones distintas de la imanación remanente de la capa de Fe y (ii) rotando el campo magnético externo con lo que controlamos la imanación de la capa de Fe. Con el método (i) se observa un valor relativo de la anisotropía de conductancia a voltaje cero entre las imanaciones en plano y fuera del plano de un 10% aproximadamente. Aplicando un campo externo de 2 kOe en módulo, método (ii), se obtiene un valor relativo de la anisotropía de conductancia a voltaje cero de un 60%. Por el método (i) observamos que la anisotropía de conductancia a voltaje cero es menor cuando la imanación remanente se encuentra orientada fuera del plano de cuando está orientada en

el plano. Esto indica la posible presencia de correlaciones triplete de largo alcance (LRT) dado que estas partículas tienen una longitud de penetración más grande que los pares singlete en el ferromagnético.

6. Se han realizado medidas de ruido de disparo a 0.3 K para verificar la calidad de la barrera en las uniones SC-MTJs epitaxiales. Estos experimentos prueban la alta calidad de las barreras túnel de MgO en tanto que el ruido de disparo puede describirse dentro de un modelo para barreras sin la presencia de defectos.

7. En las uniones con doble barrera (V/MgO/Fe/MgO/Fe and Fe/MgO/V/MgO/Fe) hemos observado anomalías reproducibles en la conductancia (CAs) a energías por encima del gap a temperatures cercanas y por debajo de T_C. La amplitud de las CAs depende de la orientación relativa de la imanación de los electrodos FM. Además las CAs no se suprimen al estar sometidas a campos magnéticos moderados/altos (hasta $\sim$ 20 kOe) a temperaturas de 0.3 K y hasta sobreviven 1 o 2 K por encima de T_C. Estos resultados apuntan hacia una estructura cristalina altamente ordenada y añade consistencia a la posibilidad de tener correlaciones LRT en nuestras SC-MTJs.

8. Los resultados principales con respecto a la anisotropía de la conductancia a voltaje cero se han descrito mediante un modelo teórico desarrollado en colaboración con los grupos del prof. Jaroslav Fabian y Petra Högl, de la Universidad de Regensburg (Alemania), el prof. Alex Matos-Abiague y el prof. Igor Zutič de la Universidad de Buffalo (USA). El modelo se ha desarrollado para ambos casos, cuando la imanación es remanente (i) y cuando la imanación es variada mediante la aplicación de un campo magnético externo (ii). En el primer caso (i) el modelo numérico da un valor de la magnetoanisotropic Andreev reflection (MAAR) del 17% y en el segundo caso (ii), aplicando un campo externo de 2 kOe en módulo, el valor es del 57%. Por lo tanto, el modelo teórico corrobora los resultados experimentales en términos del efecto MAAR. Además el modelo también explica el hecho de tener un valor de la conductancia subgap finito a temperaturas mucho menores de T_C.

9. Se ha llevado a cabo una investigación detallada del transporte

electrónico a través de uniones túnel magnéticas orgánicas (OMTJs) cuya barrera está compuesta por moléculas de PTCDA. Hemos utilizado diversas herramientas tales como medidas de conductancia, espectroscopía de túnel inelástico (IETS) y ruido a baja frecuencia (LFN) medido a temperaturas bajas hasta los 0.3 K y en función del estado magnético de los electrodos. Los espesores utilizados en estas muestras varían desde no tener PTCDA (muestra de control) hasta los 6 nm. Las medidas se han realizado en el rango de temperaturas entre los 0.3 K y los 100 K.

10. Los experimentos de LFN, particularmente los que estudian el ruido aleatorio telegráfico (RTN), enseñan un comportamiento reproducible simétrico en voltaje de los fonones. El RTN aparece a voltajes bajos y su frecuencia característica aumenta según lo hace el voltaje. En cuanto al efecto del estado magnético, el análisis del RTN muestra un desplazamiento en voltaje relativamente pequeño para extraer ninguna conclusión. En la muestra de control se ve solo ruido del tipo $1/f$ varios órdenes de magnitud menor que el que se observa en la muestra con la barrera de PTCDA más fina (1.2 nm). Esto corrobora que el origen de las fluctuaciones son las moléculas orgánicas que conforman la barrera. Cuando más gruesa sea la barrera, más moléculas habrá y mayor nivel de ruido se mide en el sistema de forma que la señal de los fonones se suaviza. La dependencia del ruido $1/f$ con la tempratura muestra una reducción relativa de la energía de activación de los fonones según aumenta la temperatura. La variación del ruido de los fonones dependiente del estado magnético excede en unos pocos órdenes de magnitud a la magnitud esperada según el teorema de fluctuación-disipación.

11. Los experimentos de IETS se han realizado derivando dos veces un promedio de varias curvas IV con alto nivel de detalle a distintos rangos de voltaje. En el rango de voltajes bajos (hasta 20 mV) se observan vibraciones colectivas moleculares llamadas “librones”. En el rango de altos voltajes (hasta 400 mV) la señal viene de modos de vibración de las moléculas individuales, los fonones. Se observa un desplazamiento en la posición en voltaje de los fonones que puede ser controlado con el estado magnético de los electrodos. La detección de

los fonones es más precisa para las barreras de PTCDA finas (1.2 y 2 nm) donde la señal proviene principalmente de las moléculas interfaciales en contraste con las barreras gruesas donde las moléculas intermedias contribuyen aumentando el nivel de ruido de la señal. Hemos demostrado que podemos ejercer control sobre el calentamiento vibracional en válvulas de espín moleculares a temperaturas por debajo de 10 K.

12. Los resultados principales de LFN en las OMTJs han sido explicados con un modelo de calentamiento vibracional dependiente del espín desarrollado con la ayuda del prof. Thomas Frederiksen. Nuestros resultados contribuyen hacia la mejor comprensión de los mecanismos de ruido a bajas frecuencias en el campo de la espintrónica molecular.

Bibliography

[1] W. Thomson, Proc. Roy. Soc. London **8**, 546 (1856).

[2] J. P. Cascales, "Conductance and noise in magnetic tunnel junctions with inorganic and organic barriers," (Ph.D. thesis, Universidad Autónoma de Madrid, Spain, 2015).

[3] G. Binasch, P. Grünberg, F. Saurenbach, and W. Zinn, Phys. Rev. B **39**, 4828 (1989).

[4] M. N. Baibich, J. M. Broto, A. Fert, F. N. Van Dau, F. Petroff, P. Etienne, G. Creuzet, A. Friederich, and J. Chazelas, Phys. Rev. Lett. **61**, 2472 (1988).

[5] P. Grünberg, R. Schreiber, Y. Pang, M. B. Brodsky, and H. Sowers, Phys. Rev. Lett. **57**, 2442 (1986).

[6] A. Cebollada, J. L. Martnez, J. M. Gallego, J. J. de Miguel, R. Miranda, S. Ferrer, F. Batallán, G. Fillion, and J. P. Rebouillat, Phys. Rev. B **39**, 9726 (1989).

[7] D. Herranz, R. Guerrero, R. Villar, F. G. Aliev, A. C. Swaving, R. A. Duine, C. van Haesendonck, and I. Vavra, Phys. Rev. B **79**, 134423 (2009).

[8] J. G. Simmons, Journal of Applied Physics **34**, 1793 (1963).

[9] W. F. Brinkman, R. C. Dynes, and J. M. Rowell, Journal of Applied Physics **41**, 1915 (1970).

[10] M. Julliére, Physics Letters A **54**, 225 (1975).

[11] J. M. De Teresa, A. Barthélémy, A. Fert, J. P. Contour, F. Montaigne, and P. Seneor, Science **286**, 507 (1999).

[12] S. Yuasa and D. D. Djayaprawira, Journal of Physics D: Applied Physics **40**, R337 (2007).

[13] D. Herranz, "Electron transport and noise in magnetic tunnel junctions with mgo barriers," (Ph.D. thesis, Universidad Autónoma de Madrid, Spain, 2012).

[14] E. Tsymbal and I. Zutic, "Handbook of spin transport and magnetism," (Taylor & Francis, 2011).

[15] W. H. Butler, X.-G. Zhang, T. C. Schulthess, and J. M. MacLaren, Phys. Rev. B **63**, 054416 (2001).

[16] J. Mathon and A. Umerski, Phys. Rev. B **63**, 220403 (2001).

[17] S. Yuasa, T. Nagahama, A. Fukushima, Y. Suzuki, and K. Ando, Nature Materials **3**, 868 (2004).

[18] S. S. P. Parkin, C. Kaiser, A. Panchula, P. M. Rice, B. Hughes, M. Samant, and S.-H. Yang, Nature Materials **3**, 862 (2004).

[19] O. Wunnicke, N. Papanikolaou, R. Zeller, P. H. Dederichs, V. Drchal, and J. Kudrnovský, Phys. Rev. B **65**, 064425 (2002).

[20] V. L. Moruzzi, J. Janak, and A. R. Williams, "Calculated electronic structure of metals," (Pergamon, Elmsford, NY, 1978).

[21] G.-X. Miao, A. V. Ramos, and J. S. Moodera, Phys. Rev. Lett. **101**, 137001 (2008).

[22] I. Žutić, J. Fabian, and S. Das Sarma, Rev. Mod. Phys. **76**, 323 (2004).

[23] J. Fabian, A. Matos-Abiague, C. Ertler, P. Stano, and I. Žutić, Acta Phys. Slovaca **57**, 565 (2007).

[24] J. Moser, A. Matos-Abiague, D. Schuh, W. Wegscheider, J. Fabian, and D. Weiss, Phys. Rev. Lett. **99**, 056601 (2007).

[25] S. E. Barnes, J. Ieda, and S. Maekawa, Scientific Reports **4** (2014), 10.1038/srep04105.

[26] C. Fowley, K. Rode, K. Oguz, H. Kurt, and J. M. D. Coey, Journal of Physics D: Applied Physics **44**, 305001 (2011).

[27] C. Gould, C. Rüster, T. Jungwirth, E. Girgis, G. M. Schott, R. Giraud, K. Brunner, G. Schmidt, and L. W. Molenkamp, Phys. Rev. Lett. **93**, 117203 (2004).

[28] L. Brey, C. Tejedor, and J. Fernández-Rossier, Appl. Phys. Lett. **85**, 1996 (2004).

[29] L. E. Nistor, B. Rodmacq, S. Auffret, A. Schuhl, M. Chshiev, and B. Dieny, Phys. Rev. B **81**, 220407 (2010).

[30] J. Hinken, "Superconductor electronics: Fundamentals and microwave applications," (Springer-Verlag Berlin, 1989).

[31] S. Ruggiero, "Superconducting devices," (Rudman, D.A., 1990).

[32] G. E. Blonder, M. Tinkham, and T. M. Klapwijk, Phys. Rev. B **25**, 4515 (1982).

[33] K. Charles, "Introduction to solid state physics 8th edition," (John Wiley & Sons, Inc, 2005).

[34] I. Giaever, Phys. Rev. Lett. **5**, 147 (1960).

[35] T. Klapwijk, G. Blonder, and M. Tinkham, Physica B+C **109**, 1657 (1982).

[36] M. Octavio, M. Tinkham, G. E. Blonder, and T. M. Klapwijk, Phys. Rev. B **27**, 6739 (1983).

[37] P. de Gennes, "Superconductivity of metals and alloys," (W.A. Benjamin, New York, 1966).

[38] J. Cuevas, "Electronic transport in normal and superconducting nanocontacts," (Universidad Autónoma de Madrid, 1999).

[39] C. Visani, Z. Sefrioui, J. Tornos, C. Leon, J. Briatico, M. Bibes, A. Barthelemy, J. Santamaria, and J. E. Villegas, Nat Phys **8**, 539 (2012).

[40] A. Andreev, Soviet Physics JETP **19**, 1823 (1964).

[41] Z. Kresin and S. Wolf, "Fundamentals of superconductivity," (Plenum Press, New York, 1990).

[42] K. A. Yates, L. A. B. Olde Olthof, M. E. Vickers, D. Prabhakaran, M. Egilmez, J. W. A. Robinson, and L. F. Cohen, Phys. Rev. B **95**, 094516 (2017).

[43] J.-D. Pillet, C. H. L. Quay, P. Morfin, C. Bena, A. L. Yeyati, and P. Joyez, Nature Physics **6**, 965 (2010).

[44] F. Pérez-Willard, J. C. Cuevas, C. Sürgers, P. Pfundstein, J. Kopu, M. Eschrig, and H. v. Löhneysen, Phys. Rev. B **69**, 140502 (2004).

[45] P. Högl, A. Matos-Abiague, I. Žutić, and J. Fabian, Phys. Rev. Lett. **115**, 116601 (2015).

[46] J. Bardeen, L. N. Cooper, and J. R. Schrieffer, Phys. Rev. **106**, 162 (1957).

[47] R. S. Keizer, S. T. B. Goennenwein, T. M. Klapwijk, G. Miao, G. Xiao, and A. Gupta, Nature **439**, 825 (2006).

[48] J. Linder, M. Cuoco, and A. Sudbø, Phys. Rev. B **81**, 174526 (2010).

[49] E. Matthias, Rep. Prog. Phys **78**, 104501 (2015).

[50] C. Visani, F. Cuellar, A. Pérez-Muñoz, Z. Sefrioui, C. León, J. Santamaría, and J. E. Villegas, Phys. Rev. B **92**, 014519 (2015).

[51] F. S. Bergeret and I. V. Tokatly, Phys. Rev. Lett. **110**, 117003 (2013).

[52] F. S. Bergeret and I. V. Tokatly, Phys. Rev. B **89**, 134517 (2014).

[53] R. Brown and D. Mazey, Philosophical magazine **4**, 161 (1828).

[54] H. B. Callen and T. A. Welton, Phys. Rev. **83**, 34 (1951).

[55] H. Nyquist, Phys. Rev. **32**, 110 (1928).

[56] G. Durin, P. Falferi, M. Cerdonio, G. A. Prodi, and S. Vitale, Journal of Applied Physics **73**, 5363 (1993).

[57] J. B. Johnson, Phys. Rev. **32**, 97 (1928).

[58] R. J. Schoelkopf, P. J. Burke, A. A. Kozhevnikov, D. E. Prober, and M. J. Rooks, Phys. Rev. Lett. **78**, 3370 (1997).

[59] Y. Blanter and M. BÃijttiker, Physics Reports **336**, 1 (2000).

[60] R. Landauer, Phys. Rev. B **47**, 16427 (1993).

[61] L. Callegaro, American Journal of Physics **74**, 438 (2006).

[62] S. MacEarchern, "Kendall's advanced theory of statistics. vol 2b: Bayesian interference. anthony o'hagan, edward arnold," (John Wiley and Sons, London, 1997).

[63] C. E. Carroll, "Statistical physics, vol. 5: course of theoretical physics: L.d. landau and e.m. lifshitz, 2nd rev." (Elsevier Science, New York, 1971).

[64] P. Dutta and P. M. Horn, Rev. Mod. Phys. **53**, 497 (1981).

[65] S. Kogan, "Electronic noise and fluctuations in solids," (Cambridge University Press, 1996).

[66] F. K. Du Pré, Phys. Rev. **78**, 615 (1950).

[67] A. V. D. Ziel, Physica **16**, 359 (1950).

[68] F. N. Hooge, T. G. M. Kleinpenning, and L. K. J. Vandamme, Reports on Progress in Physics **44**, 479 (1981).

[69] K. S. Ralls and R. A. Buhrman, Phys. Rev. Lett. **60**, 2434 (1988).

[70] G. A. Prodi, S. Vitale, M. Cerdonio, and P. Falferi, Journal of Applied Physics **66**, 5984 (1989).

[71] S. Vitale, R. Tommasini, M. Cerdonio, M. Bonaldi, A. Cavalleri, and G. Durin, Journal of Applied Physics **72**, 4820 (1992).

[72] H. T. Hardner, M. B. Weissman, M. B. Salamon, and S. S. P. Parkin, Phys. Rev. B **48**, 16156 (1993).

[73] R. Guerrero, F. G. Aliev, R. Villar, R. Ortega-Hertogs, W. K. Park, and J. S. Moodera, Journal of Physics D: Applied Physics **35**, 1761 (2002).

[74] A. N. Grigorenko and D. J. Mapps, Journal of Physics D: Applied Physics **36**, 791 (2003).

[75] E. Paperno and B. Z. Kaplan, IEEE Transactions on Magnetics **31**, 3161 (1995).

[76] L. S. Kirschenbaum, C. T. Rogers, S. E. Russek, and S. C. Sanders, IEEE Transactions on Magnetics **31**, 3943 (1995).

[77] K. K. Hung, P. K. Ko, C. Hu, and Y. C. Cheng, IEEE Electron Device Letters **11**, 90 (1990).

[78] B. Mann and H. Kuhn, Journal of Applied Physics **42**, 4398 (1971).

[79] V. Dediu, M. Murgia, F. Matacotta, C. Taliani, and S. Barbanera, Solid State Communications **122**, 181 (2002).

[80] Z. H. Xiong, D. Wu, Z. Valy Vardeny, and J. Shi, Nature **427**, 821 (2004).

[81] T. S. Santos, J. S. Lee, P. Migdal, I. C. Lekshmi, B. Satpati, and J. S. Moodera, Phys. Rev. Lett. **98**, 016601 (2007).

[82] J. J. H. M. Schoonus, P. G. E. Lumens, W. Wagemans, J. T. Kohlhepp, P. A. Bobbert, H. J. M. Swagten, and B. Koopmans, Phys. Rev. Lett. **103**, 146601 (2009).

[83] C. Barraud, P. Seneor, R. Mattana, S. Fusil, K. Bouzehouane, C. Deranlot, P. Graziosi, L. Hueso, I. Bergenti, V. Dediu, F. Petroff, and A. Fert, Nature Physics **6**, 615 (2010).

[84] M. Galbiati, S. Tatay, S. Delprat, H. L. Khanh, B. Servet, C. Deranlot, S. Collin, P. Seneor, R. Mattana, and F. Petroff, Applied Physics Letters **106**, 082408 (2015).

[85] W. Wang, T. Lee, and M. A. Reed, Reports on Progress in Physics **68**, 523 (2005).

[86] M. Galperin, M. Ratner, and A. Nitzan, Journal of Physics Condensed Matter **19** (2007), 10.1088/0953-8984/19/10/103201.

[87] S. Shi, F. Liu, D. L. Smith, and P. P. Ruden, Journal of Applied Physics **117**, 085501 (2015).

[88] G. Szulczewski, H. Tokuc, K. Oguz, and J. M. D. Coey, Applied Physics Letters **95**, 202506 (2009).

[89] J.-W. Yoo, H. W. Jang, V. N. Prigodin, C. Kao, C. B. Eom, and A. J. Epstein, Phys. Rev. B **80**, 205207 (2009).

[90] S. Kowarik, A. Gerlach, and F. Schreiber, Journal of Physics: Condensed Matter **20**, 184005 (2008).

[91] K.-S. Li, Y.-M. Chang, S. Agilan, J.-Y. Hong, J.-C. Tai, W.-C. Chiang, K. Fukutani, P. A. Dowben, and M.-T. Lin, Phys. Rev. B **83**, 172404 (2011).

[92] Y. Hirose, A. Kahn, V. Aristov, P. Soukiassian, V. Bulovic, and S. R. Forrest, Phys. Rev. B **54**, 13748 (1996).

[93] L. Gao, Q. Liu, Y. Y. Zhang, N. Jiang, H. G. Zhang, Z. H. Cheng, W. F. Qiu, S. X. Du, Y. Q. Liu, W. A. Hofer, and H.-J. Gao, Phys. Rev. Lett. **101**, 197209 (2008).

[94] C. Nacci, S. FÃűlsch, K. Zenichowski, J. DokiÄĞ, T. Klamroth, and P. Saalfrank, Nano Letters **9**, 2996 (2009), pMID: 19583246.

[95] J. Schaffert, M. C. Cottin, A. Sonntag, H. Karacuban, C. A. Bobisch, N. Lorente, J.-P. Gauyacq, and R. Möller, Nature Materials **12**, 223 (2012).

[96] M. Tsutsui, M. Taniguchi, and T. Kawai, Nano Letters **1**, 138 (2010).

[97] R. Guerrero, "Conductancia y ruido en uniones túnel magnéticas," (Ph.D. thesis, Universidad Autónoma de Madrid, Spain, 2007).

[98] I. Martinez, M. Ribeiro, P. Andres, L. E. Hueso, F. Casanova, and F. G. Aliev, Phys. Rev. Applied **7**, 034034 (2017).

[99] A. Vansteenkiste, J. Leliaert, M. Dvornik, M. Helsen, F. Garcia-Sanchez, and B. V. Waeyenberge, AIP Advances **4**, 107133 (2014).

[100] I. Martinez, C. Tiusan, M. Hehn, M. Chshiev, and F. G. Aliev, Scientific Reports **submitted** (2018).

[101] S. Ikeda, K. Miura, H. Yamamoto, K. Mizunuma, H. D. Gan, M. Endo, S. Kanai, J. Hayakawa, F. Matsukura, and H. Ohno, Nat Mater **9**, 721 (2010).

[102] J. C. Leutenantsmeyer, V. Zbarsky, M. von der Ehe, S. Wittrock, P. Peretzki, H. Schuhmann, A. Thomas, K. Rott, G. Reiss, T. H. Kim, M. Seibt, and M. Münzenberg, MATERIALS TRANSACTIONS **56**, 1323 (2015).

[103] Y.-C. Lau, D. Betto, K. Rode, J. M. D. Coey, and P. Stamenov, Nat Nano **11**, 758 (2016).

[104] J. Igarashi, J. Llandro, H. Sato, F. Matsukura, and H. Ohno, Applied Physics Letters **111**, 132407 (2017).

[105] C.-H. Lambert, A. Rajanikanth, T. Hauet, S. Mangin, E. E. Fullerton, and S. Andrieu, Applied Physics Letters **102**, 122410 (2013).

[106] C. Tiusan, F. Greullet, M. Hehn, F. Montaigne, S. Andrieu, and A. Schuhl, Journal of Physics: Condensed Matter **19**, 165201 (2007).

[107] C. Tiusan, A. Dullard, F. Greullet, and J. Vincent F., "Private communication regarding RHEED thickness measurement," (2017).

[108] P. Blaha, K. Schwarz, G. Madsen, D. Kvasnicka, and J. Luitz, "Wien2k, an augmented plane wave local orbitals program for calculating crystal properties," (Technical University of Wien, Austria, 2017).

[109] T. Nozaki, A. Hirohata, N. Tezuka, S. Sugimoto, and K. Inomata, Applied Physics Letters **86**, 082501 (2005).

[110] R. Guerrero, D. Herranz, F. G. Aliev, F. Greullet, C. Tiusan, M. Hehn, and F. Montaigne, Applied Physics Letters **91**, 132504 (2007).

[111] J. P. Cascales, L. Martin, A. Dulluard, M. Hehn, C. Tiusan, T. Szczepański, V. K. Dugaev, J. Barnaś, and F. G. Aliev, IEEE Transactions on Magnetics **49**, 4047 (2013).

[112] J. C. Slonczewski, Phys. Rev. B **39**, 6995 (1989).

[113] X. Gao, Q. Li, S. Li, J. Xu, Y. Qin, X. Shi, S. Yan, and G. Miao, Journal of Alloys and Compounds **662**, 79 (2016).

[114] K. Sunaga, M. Tsunoda, K. Komagaki, Y. Uehara, and M. Takahashi, Journal of Applied Physics **102**, 013917 (2007).

[115] T.-S. Kim, Phys. Rev. B **72**, 024401 (2005).

[116] J. M. De Teresa, A. Barthélémy, A. Fert, J. P. Contour, R. Lyonnet, F. Montaigne, P. Seneor, and A. Vaurès, Phys. Rev. Lett. **82**, 4288 (1999).

[117] P. Bruno, Phys. Rev. B **39**, 865 (1989).

[118] d.-t. Quach, D. Handoko, S.-H. Lee, J.-H. Shim, T. Phan, T. Pham, K.-M. Lee, J.-R. Jeong, D.-T. Ngo, and D.-H. Kim, *IEEE Transactions on Magnetics*, **51**, 1 (2015).

[119] M. Gottwald, S. Andrieu, F. Gimbert, E. Shipton, L. Calmels, C. Magen, E. Snoeck, M. Liberati, T. Hauet, E. Arenholz, S. Mangin, and E. E. Fullerton, Phys. Rev. B **86**, 014425 (2012).

[120] A. Hallal, H. X. Yang, B. Dieny, and M. Chshiev, Phys. Rev. B **88**, 184423 (2013).

[121] J. W. Koo, S. Mitani, T. T. Sasaki, H. Sukegawa, Z. C. Wen, T. Ohkubo, T. Niizeki, K. Inomata, and K. Hono, Applied Physics Letters **103**, 192401 (2013).

[122] A. Koziol-Rachwal, W. Skowroński, T. Ślezak, D. Wilgocka-Ślezak, J. Przewoźnik, T. Stobiecki, Q. H. Qin, S. van Dijken, and J. Korecki, Journal of Applied Physics **114**, 224307 (2013).

[123] A. Hallal, B. Dieny, and M. Chshiev, Phys. Rev. B **90**, 064422 (2014).

[124] Y. Fu, I. Barsukov, J. Li, A. M. GonÃğalves, C. C. Kuo, M. Farle, and I. N. Krivorotov, Applied Physics Letters **108**, 142403 (2016).

[125] M. S. Gabor, T. Petrisor, O. Pop, S. Colis, and C. Tiusan, Journal of Magnetism and Magnetic Materials **392**, 79 (2015).

[126] A. A. Timopheev, R. Sousa, M. Chshiev, H. T. Nguyen, and B. Dieny, Scientific Reports **6**, 26877 (2016).

[127] E. Jal, J. B. Kortright, T. Chase, T. Liu, A. X. Gray, P. Shafer, E. Arenholz, P. Xu, J. Jeong, M. G. Samant, S. S. P. Parkin, and H. A. DÃijrr, Applied Physics Letters **107**, 092404 (2015).

[128] T. Ueno, J. Sinha, N. Inami, Y. Takeichi, S. Mitani, K. Ono, and M. Hayashi, Scientific Reports **5**, 14858 (2015).

[129] B. Dieny and A. Vedyayev, EPL (Europhysics Letters) **25**, 723 (1994).

[130] E. MÅĆyÅĎczak, K. Freindl, N. Spiridis, and J. Korecki, Journal of Applied Physics **113**, 024320 (2013).

[131] D. Odkhuu, W. S. Yun, S. Rhim, and S. C. Hong, Journal of Magnetism and Magnetic Materials **414**, 126 (2016).

[132] F. C. Ummelen, A. FernÃąndez-Pacheco, R. Mansell, D. Petit, H. J. M. Swagten, and R. P. Cowburn, Applied Physics Letters **110**, 102405 (2017).

[133] S. Baumann, F. Donati, S. Stepanow, S. Rusponi, W. Paul, S. Gangopadhyay, I. G. Rau, G. E. Pacchioni, L. Gragnaniello, M. Pivetta, J. Dreiser, C. Piamonteze, C. P. Lutz, R. M. Macfarlane, B. A. Jones, P. Gambardella, A. J. Heinrich, and H. Brune, Phys. Rev. Lett. **115**, 237202 (2015).

[134] H. Meng, R. Sbiaa, S. Y. H. Lua, C. C. Wang, M. A. K. Akhtar, S. K. Wong, P. Luo, C. J. P. Carlberg, and K. S. A. Ang, Journal of Physics D: Applied Physics **44**, 405001 (2011).

[135] M. Z. Hasan and C. L. Kane, Rev. Mod. Phys. **82**, 3045 (2010).

[136] T. Oshima and Y. Kawaguchi, Phys. Rev. A **93**, 053605 (2016).

[137] J. Linder and J. W. A. Robinson, Nature Physics **11**, 307 (2015).

[138] N. Banerjee, J. Robinson, and M. G. Blamire, Nature Communications **5**, 4771 (2014).

[139] B. Baek, W. H. Rippard, S. P. Benz, S. E. Russek, and P. D. Dresselhaus, Nature Communications **12**, 564 (2016).

[140] E. C. Gingrich, B. M. Niedzielski, J. A. Glick, Y. Wang, D. L. Miller, R. Loloee, W. P. Pratt Jr, and N. O. Birge, Nature Physics **5**, 3888 (2014).

[141] V. T. Petrashov, I. A. Sosnin, I. Cox, A. Parsons, and C. Troadec, Journal of Low Temperature Physics **118**, 689 (2000).

[142] F. S. Bergeret, A. F. Volkov, and K. B. Efetov, Phys. Rev. Lett. **86**, 4096 (2001).

[143] Y. V. Forminov, A. A. Golubov, T. Y. Karminskaya, M. Y. Kupriyanov, R. G. Deminov, and L. R. Tagirov, JETP Letters **91**, 329 (2010).

[144] A. Di Bernardo, S. Diesch, Y. Gu, J. Linder, G. Divitini, C. Ducati, E. Scheer, M. Blamire, and J. Robinson, Nature Communications **6**, 8053 (2015).

[145] V. I. Zdravkov, J. Kehrle, G. Obermeier, D. Lenk, H.-A. Krug von Nidda, C. Müller, M. Y. Kupriyanov, A. S. Sidorenko, S. Horn, R. Tidecks, and L. R. Tagirov, Phys. Rev. B **87**, 144507 (2013).

[146] A. A. Jara, C. Safranski, I. N. Krivorotov, C.-T. Wu, A. N. Malmi-Kakkada, O. T. Valls, and K. Halterman, Phys. Rev. B **89**, 184502 (2014).

[147] X. L. Wang, A. Di Bernardo, N. Banerjee, A. Wells, F. S. Bergeret, M. G. Blamire, and J. W. A. Robinson, Phys. Rev. B **89**, 140508 (2014).

[148] A. Singh, S. Voltan, K. Lahabi, and J. Aarts, Phys. Rev. X **5**, 021019 (2015).

[149] M. Eschrig and T. Löfwander, Nature Physics **4**, 138 (2008).

[150] M. Eschrig, J. Kopu, J. C. Cuevas, and G. Schön, Phys. Rev. Lett. **90**, 137003 (2003).

[151] R. Grein, M. Eschrig, G. Metalidis, and G. Schön, Phys. Rev. Lett. **102**, 227005 (2009).

[152] C. R. Reeg and D. L. Maslov, Phys. Rev. B **92**, 134512 (2015).

[153] S. H. Jacobsen, I. Kulagina, and J. Linder, Scientific Reports **6**, 23926 (2016).

[154] S. H. Jacobsen, J. A. Ouassou, and J. Linder, Phys. Rev. B **92**, 024510 (2015).

[155] M. Iavarone, S. A. Moore, J. Fedor, S. T. Ciocys, G. Karapetrov, J. Pearson, V. Novosad, and S. D. Bader, Nature Communications **5**, 4766 (2014).

[156] A. I. Buzdin and A. S. Mel'nikov, Phys. Rev. B **67**, 020503 (2003).

[157] J. M. Rowell and W. L. McMillan, Phys. Rev. Lett. **16**, 453 (1966).

[158] J. M. Rowell, Phys. Rev. Lett. **30**, 167 (1973).

[159] W. J. Tomasch, Phys. Rev. Lett. **16**, 16 (1966).

[160] W. L. McMillan and P. W. Anderson, Phys. Rev. Lett. **16**, 85 (1966).

[161] T. M. Klapwijk, Journal of Superconductivity **17**, 593 (2004).

[162] J. P. Cascales, D. Herranz, F. G. Aliev, T. Szczepański, V. K. Dugaev, J. Barnaś, A. Duluard, M. Hehn, and C. Tiusan, Phys. Rev. Lett. **109**, 066601 (2012).

[163] T. Szczepański, V. K. Dugaev, J. Barnaś, J. P. Cascales, and F. G. Aliev, Phys. Rev. B **87**, 155406 (2013).

[164] Y. Miyoshi, Y. Bugoslavsky, and L. F. Cohen, Phys. Rev. B **72**, 012502 (2005).

[165] A. Matos-Abiague and J. Fabian, Phys. Rev. B **79**, 155303 (2009).

[166] M. Wimmer, M. Lobenhofer, J. Moser, A. Matos-Abiague, D. Schuh, W. Wegscheider, J. Fabian, K. Richter, and D. Weiss, Phys. Rev. B **80**, 121301 (2009).

[167] T. Brumme, R. Gutierrez, and G. Cuniberti, Journal of Physics: Condensed Matter **24**, 394003 (2012).

[168] D. R. Ward, D. A. Corley, J. M. Tour, and D. Natelson, Nature Nanotechnology **6**, 33 (2011).

[169] D. A. Tenne, S. Park, T. U. Kampen, A. Das, R. Scholz, and D. R. T. Zahn, Phys. Rev. B **61**, 14564 (2000).

[170] A. B. S. Elliott, R. Horvath, and K. C. Gordon, Chem. Soc. Rev. **41**, 1929 (2012).

[171] D. R. Zahn, "Spectroscopy of hybrid inorganic/organic interfaces vibrational spectroscopy," `http://slideplayer.com/slide/5816577/`.

[172] W. J. M. Naber, S. Faez, and W. G. van der Wiel, Journal of Physics D: Applied Physics **40**, R205 (2007).

[173] T. Frederiksen, M. Paulsson, and H. Ueba, Phys. Rev. B **89**, 035427 (2014).

[174] Y. Dubi and M. Di Ventra, Rev. Mod. Phys. **83**, 131 (2011).

[175] L. Simine and D. Segal, Phys. Chem. Chem. Phys. **14**, 13820 (2012).

[176] S. Weiss, J. Brüggemann, and M. Thorwart, Phys. Rev. B **92**, 045431 (2015).

[177] A. Droghetti, I. Rungger, M. Cinchetti, and S. Sanvito, Phys. Rev. B **91**, 224427 (2015).

[178] A. Lunghi, F. Totti, R. Sessoli, and S. Sanvito, Nature Communications **8**, 14620 (2017).

[179] J.-Y. Hong, K.-H. O. Yang, B.-Y. Wang, K.-S. Li, H.-W. Shiu, C.-H. Chen, Y.-L. Chan, D.-H. Wei, F.-H. Chang, H.-J. Lin, W.-C. Chiang, and M.-T. Lin, Applied Physics Letters **104**, 083301 (2014).

[180] A. R. Rocha, V. M. GarcÃŋa-suÃąrez, S. W. Bailey, C. J. Lambert, J. Ferrer, and S. Sanvito, Nature Materials **4**, 335 (2005).

[181] S. Sanvito, Chem. Soc. Rev. **40**, 3336 (2011).

[182] J. S. Jiang, J. E. Pearson, and S. D. Bader, Phys. Rev. Lett. **106**, 156807 (2011).

[183] R. Vincent, S. Klyatskaya, M. Ruben, W. Wernsdorfer, and F. Balestro, Nature **488**, 357 (2012).

[184] T. D. Nguyen, E. Ehrenfreund, and Z. V. Vardeny, Science **337**, 204 (2012).

[185] S. Sanvito, Nature Physics **6**, 562 (2010).

[186] S. Lach, A. Altenhof, K. Tarafder, F. Schmitt, M. E. Ali, M. Vogel, J. Sauther, P. M. Oppeneer, and C. Ziegler, Advanced Functional Materials **22**, 989 (2012).

[187] M. A. Reed, Materials Today **11**, 46 (2008).

[188] K. Akers, R. Aroca, A. M. Hor, and R. O. Loutfy, The Journal of Physical Chemistry **91**, 2954 (1987).

[189] S. R. Forrest, Chemical Reviews **97**, 1793 (1997), pMID: 11848893.

[190] D. Hunter, W. Osborn, K. Wang, N. Kazantseva, J. Hattrick-Simpers, R. Suchoski, R. Takahashi, M. L. Young, A. Mehta, L. A. Bendersky, S. E. Lofland, M. Wuttig, and I. Takeuchi, Nature Communications **2**, 518 (2011).

[191] D. E. Parkes, L. R. Shelford, P. Wadley, V. Holý, M. Wang, A. T. Hindmarch, G. van der Laan, R. P. Campion, K. W. Edmonds, S. A. Cavill, and A. W. Rushforth, Scientific Reports **3**, 2220 (2013).

[192] S. Gao, M. Persson, and B. I. Lundqvist, Phys. Rev. B **55**, 4825 (1997).

[193] S. Machlup, Journal of Applied Physics **25**, 341 (1954).

[194] R. E. Walkup, D. M. Newns, and P. Avouris, Phys. Rev. B **48**, 1858 (1993).

[195] T. Brumme, O. A. Neucheva, C. Toher, R. Gutiérrez, C. Weiss, R. Temirov, A. Greuling, M. Kaczmarski, M. Rohlfing, F. S. Tautz, and G. Cuniberti, Phys. Rev. B **84**, 115449 (2011).

[196] I. Martinez, J. Cascales, J. Y. Hong, C. F. Hung, M. T. Lin, T. Frederiksen, and F. G. Aliev, **to be submitted** (2018).

[197] G. Salvan and D. R. T. Zahn, EPL (Europhysics Letters) **67**, 827 (2004).